The Role of Excited-State Energy Landscapes in Directing Electron and Proton Motion for Light Harvesting Applications

Emily Rabe

A dissertation

submitted in partial fulfillment of the

requirements for the degree of

Doctor of Philosophy

University of Washington

2020

Reading Committee:

Cody Schlenker, Chair

Brandi Cossairt

Munira Khalil

Program Authorized to Offer Degree:

Chemistry

University of Washington

Abstract

The Role of Excited-State Energy Landscapes in Directing Electron and Proton Motion for Light Harvesting Applications

Emily Rabe

Chair of the Supervisory Committee:
Professor Cody Schlenker
Department of Chemistry

To meet the increasing global demand for energy we need to innovate new ways to harness and convert renewable energy sources. Solar energy provides a huge potential to meet these demands, but there is still a plethora of unanswered questions surrounding how photons interact with organic molecules and materials, particularly in the field of photovoltaics and photochemistry. The low dielectric constant of these organic materials causes them to behave differently than their inorganic counterparts. Chapter 2 provides background for the variety of applications of organic optoelectronic materials and common techniques used to study them.

In recent years, the aza-aromatic material carbon nitride, and its monomer unit, heptazine, has seen a surge in popularity to mediate photochemical transformations, particularly hydrogen evolution. Yet despite the thousands of publications in this field, there are few fundamental

photophysical studies, which are critical to enable new reaction pathways. This work describes a series of photophysical explorations into a molecular heptazine derivative, 2,5,8-tris(4-methoxyphenyl)-1,3,4,6,7,9,9b-heptaazaphenalene (TAHz). Chapter 3 provides an overview of the photophysical and electrochemical properties of TAHz, including the unusual inversion of the lowest singlet and triplet state. Chapter 4 provides the first experimental evidence for excited-state proton-coupled electron transfer (ES-PCET) from water to a heptazine chromophore using time-resolved photoluminescence and radical scavenging. This first step of water oxidation opens a new range of possible photochemical reactions to harness solar energy. Chapter 5 proposes design rules for increasing reaction efficiency of ES-PCET with heptazine chromophores by studying reaction rates with a series of phenol derivatives. By adding electron-donating groups on phenol, increased reactivity and support the corollary: adding electron-withdrawing groups to heptazine could increase reaction efficiency with water. Chapter 6 considers another aspect of chromophore design by studying hydrogen bonding and how the local excited-state landscape is modulated by hydrogen-bond strength. Together, this work presents a holistic picture of heptazine's photophysics with implications for tailoring organic chromophores to meet unique photochemical demands.

TABLE OF CONTENTS

LIST OF FIGURES

LIST OF TABLES

ACKNOWLEDGEMENTS

I am very grateful to my advisor, Prof Cody Schlenker, for the mentorship, encouragement, and freedom to pursue this degree through every twist and turn. Beyond providing scientific insight, thank you for reminding me that “nothings breaks if you never go into lab,” not to apologize for my results, and not to “hope” for any specific outcome; I am a far better scientist for having spent 5 years in your lab.

I thank my committee members past and present. I am grateful to Prof Brandi Cossairt for serving on both my general and final exam committees and including me in a fun collaboration. But I am also grateful for your support of WCS/InCS; and for beginning a presentation with a image of an ice cream cone stuck to the forehead of a horse, along with the words “Fake It ‘Til You Make It." I still find that reassuring. I would like to thank Prof Munira Khalil for all the thoughtful comments from spectroscopy group meetings and for serving on my final exam committee even while transitioning to department chair. I thank Prof Corie Cobb for serving as my GSR for my final exam and for the mentorship around technical consulting. I am grateful to Prof David Ginger for serving on two exam committees; I appreciated your constructive criticism (though I may still use an offense number of slides). I am grateful for Prof Mike Heinekey for not only serving on my general exam committee but for two quarters of the best teaching assignment. I also thank Prof Xiaosong Li and Prof Gary Drobny for serving on my second-year committee.

I cannot thank the Schlenker group members enough, both past and present. I chose this lab for the camaraderie, and that camaraderie saw me to the end. I am continuously grateful to Dr. Dana Sulas for being such an amazing mentor to me in my first couple years; beyond PIA and sublimation purification, you taught me how to have fun with science, laugh off failures, and make really good presentations. Thank you for always emphasizing teamwork (e.g. Team PhD); your

friendship and encouragement helped immensely. Dr. Katie Corp, thank you for being a mentor to me before even I started; you taught me everything from how to solder to how to function in the department. I'm grateful for our years of scientific collaboration and friendship. Dr. Jarred Olson, thank you for the never-ending support and encouragement you gave me; our office chats and wine Wednesdays made grad school a much more pleasant experience. Tim Pollock, thank you for setting the tradition of drinking together after group meeting, the lab would not have been the same without you encouraging us all to go to College Inn or initiating a game of office soccer. Sarah Pristash, I am so grateful for all the laughing-induced tears you brought to the lab. I loved turning around in my chair to bounce around ideas whether they be about science, InCS, or anything else. Emma Cave, I am so grateful for both the fun and seriousness you brought to the lab; you have taken on so much lab responsibility, but still goof off with all of us. Ryan Flores, it is hard to thank you enough for joining the lab and taking on whatever crazy synthesis projects we threw at you, and for being a source for such fun and joy in the lab. Liam Wrigley, thank you being so kind and eager. And thank you for filling your group meeting presentations with funny pictures. And to the knee-scooter, I will always be grateful you allowed me to continue lab work while continuously injuring myself climbing.

I want to thank my cohort and friends outside of UW for supporting me outside the lab. From cranking out quantum mechanics homework to climbing mountains, you all made grad school fun and Seattle feel like home. Thank you to everyone involved in WCS, InCS, Mentorship Network, and Grad Club, those organizations grounded me. To everyone in Doofhaus, I appreciate our three years together and I was grateful to have you all during quarantine.

And finally, I thank my family for encouraging me to pursue a career in science and supporting me throughout the process. I am so grateful for a mother who was always on my side and always

coming out to see me. I'm thankful you taught me how to cut corners, but also when I shouldn't. I'm so thankful to my brother, Phil, for sparking my interest in chemistry, and continually talking with me about it for the next couple decades. I loved having a brother who was so passionate about science. I thank my father for taking every opportunity to teach me something new and always having faith in my potential. You are a great role model for a successful career built on the love of science and technology. To Harrison, my chosen family, I cannot thank you enough for your never-ending support. During the past five years you have been my friend, roommate, adventure buddy, partner, and co-author; there is no aspect of the last five years that wasn't made better by your presence.

DEDICATION

To my father, a brilliant chemistry dropout.

Chapter 1. Introduction

1.1 Motivating Clean Energy Research

1.1.1 *Increasing Global Energy Demand*

Not only is the global demand for energy increasing, but the rate of the change in demand is also increasing.[1] When talking about energy, there are seemingly infinite possible units used to express energy: British thermal units, watt hours, tones of oil equivalents, etc. As a way to visualize energy consumption, I will use 16-oz jars of peanut butter as an energy unit, as I frequently use it to fuel activities such as backpacking or writing this thesis. In 2017, according to the US Energy Information Administration, the US primary energy consumption per person per day was equivalent to 77 jars of peanut butter on a caloric basis. This highlights how much of our energy consumption is indirect; about 34 jars is used by the industrial sector (making our cars, houses, appliances, etc.) and nearly 22 jars are used by the transportation sector which brings those items as well as our food to us. But to really understand a big driving force behind the increasing energy consumption, it is important to compare the US's energy consumption to developing countries: China uses about 18 jars/person/day and India only uses 6 jars/person/day. It is clear to see that the energy consumption not evenly spread. As more of the global population demands energy-intensive comforts such as building heating/cooling, the demand will continue growing for the foreseeable future.

While we do not use peanut butter as our primary energy source, we do use carbon-based fuels such as coal, oil, and gas which all share CO_2 as a byproduct. This poses a dilemma to the rapidly increasing energy demand as excess CO_2 has been correlated to global warming.[2] According to a recent IPCC report, human-induced warming has already reached rough 1°C since pre-industrial

times.[3] The central aim of the Paris Agreement is to keep the global temperature rise below 2°C above pre-industrial levels while pursuing a smaller rise of only 1.5°C. This goal requires drastic action seeing as the current rate of warming is roughly 0.2°C per decade.

Putting these pieces together, the rising demand for energy and rising global temperatures from our current energy consumption, paint a dire picture. Fortunately, there are more energy sources available to us besides coal, oil, gas, and peanut butter. It will require scientific and technology advancements in order to harness and utilize enough solar, wind, geothermal, and tidal energy to meet the growing demand.

1.1.2 *Solar Energy Potential*

A 2000 World Energy Assessment conducted by the United Nations Development Programme concluded the amount of potentially usable solar energy intercepted by the Earth is roughly three orders of magnitude higher than annual global energy use.[4] While the potential is huge, solar photovoltaics (PV) and solar thermal only accounted for roughly 1% of global energy supply in 2017 according to IEA global data.[5] The percentage is roughly the same for US energy consumption, meaning that of the 77 jars of peanut butter/person/day, less than one jar comes from solar energy.[6] Fortunately, the solar energy is an actively growing sector; the percentage of US electricity produced by solar PV increased by an order of magnitude from 2011 to 2017.[7] This impressive jump was made possible by the dramatic cost reduction of utility-scale solar down to $0.06/kWh, which is approaching the cost of coal-powered electricity at roughly $0.03/kWh.[7] Further advancements to increase efficiency and decrease cost of solar panels are expected to allow solar energy to capture a greater share of the electricity generation. For the first time, in 2019, renewable sources eclipsed coal use for generating electricity.[8] This growth is encouraging but will need to continue to meet the IPCC's call for limiting global temperatures to less than 2°C.

Regarding mitigation strategies, the IPCC proposes growing the energy output from wind and solar 10x from 2020 to 2050.[2]

While this is promising for decreasing the CO_2 emissions for the growing electricity sector, large chunks of our emission come from energy uses outside of electricity. As an example, Julian Allwood's book *Sustainable Materials with Both Eyes Open* dives into the industry sector, which accounts for roughly 35% of global CO_2 emissions. The book highlights how increasing electricity generation by solar and wind will not necessarily be enough to decarbonize this sector; steel manufacturing makes up 25% of industrial emissions, and less than 40% of the energy used is from electricity. Interestingly, coal is used directly as a reactant in the chemical reduction of iron oxide releasing CO_2. Tackling sectors like steel manufacturing will require more knowledge about how drive chemical reactions either photo- or electrochemically to utilize the immense potential of solar energy and will be discussed in the following sections.

1.1.3 *Global Hydrogen Production*

Often, hydrogen production is thought of in the context of clean energy for fuel cell cars or energy storage applications. However, approximately 60 Mt of hydrogen is currently produced globally each year.[9] It is used in the production of nitrogen-rich fertilizers and methanol, as well as in hydro-treatment in petroleum refining. Roughly only 6% of hydrogen produced is used for fuel cells, both stationary cells and in cars. If global hydrogen production were a country, it would be the 6th largest CO_2 emitter (Wood MacKenzie), highlighting the energy-intensive nature of chemical production, and a reliance on fossil fuels not easily replaced directly by electricity from solar power.

Currently, about 96% of the 60 Mt of H_2 is produced from sources such as methane, coal, and liquid hydrocarbons.[9] All of these processes result in significant release of CO_2. The other 4% is

made electrochemically from water, which could have zero carbon emissions if powered exclusively by renewable energy sources such as solar panels. However, this is not currently economically feasible as low utilization of expensive electrolyzers drive the cost significantly above conventional fossil fuel methods, even including the cost of carbon capture.[9]

This has motivated massive research efforts into creating lower cost electrolyzers[10-13] and exploring new methods, such as photocatalytic production, which is discussed in the next section. Particularly in the context of chemical transformations, it is interesting to consider designing a route to directly use solar energy to drive reactions, rather than first converting it to electricity and transmitting it to an electrolyzer.

1.2 PHOTOCATALYTIC REACTIONS

While photovoltaic (PV) and electrolyzer technologies are currently commercialized and generally better understood, the possibility of using an all-in-one photoelectrochemical system can present some advantages. A technoeconomic analysis of water splitting systems by Nate Lewis and coworkers suggest that the costs of earth-abundant photoelectrochemical systems could be significantly lower than the combination of PV and electrolysis.[14] However, these systems are far less well-studied particularly for the water oxidation reaction, which requires the motion of four electrons and four protons to produce oxygen from water. Coordinating this complex reaction will require a deep understanding of how to design the photoelectrode to direct the motion of these

protons and electrons. This section will provide an overview of the proton reduction reaction, and the proton-coupled electron transfer, being the first step in water oxidation.

1.2.1 *Hydrogen Evolution*

Much of the literature on photocatalytic hydrogen production focuses on proton reduction half reaction ($2H^+ + 2e^- \rightarrow H_2$); this is especially true for the carbon nitride literature discussed below. In the simplest case, a chromophore absorbs a photon and transfers the photoexcited electron to a proton in solution, then two hydrogen atoms come together to form H_2. However, researchers will often use co-catalysts, such as Pt nanoparticles, to accept the photoexcited electron and perform the proton reduction and bond formation steps. Regardless of whether a co-catalyst is used, it is important to recognize that this is only a half reaction and leave the chromophore in an oxidized state. Frequently in the literature, a sacrificial electron donor (or hole acceptor) is used to regenerate the chromophore to its neutral state. Common electron donors are triethanolamine, methanol, and sodium sulfite.[15] It is important to remember that this is not regenerated and results in a waste product. Alternatively, if the other half reaction is water oxidation, this avoids the need for an additional reagent and ideally the waste product from the oxidation is oxygen. However, it is very challenging to mediate the four-electron oxidation from water to oxygen. To tackle this half, coupling the motion of protons and electrons is critical to efficient catalysis, and is the subject of the following section.[16]

1.2.2 *Proton-Coupled Electron Transfer*

Proton-coupled electron transfer (PCET) reactions are scientifically and technologically relevant for characterizing and controlling energy conversion and storage processes.[17-20] Figure 1-1 A shows the classic square scheme used to illustrate the possible pathways for proton and electron

transfer. While this diagram shows the proton and electron moving to the same acceptor, that does not have to be the case. Dempsey and co works have an excellent review regarding the different PCET categories.[18] Regardless of direction, the concerted movement of protons and electrons avoid charged intermediates, unlike proton reduction discussed previously. This feature is particularly important for facilitating multi-proton and multi-electron reactions as the highly charged intermediates would pose energy barriers too high for efficient conversion. Due to this efficiency, PCET reactions are ubiquitous in nature from respiration to evolving oxygen in Photosystem II.[21-22]

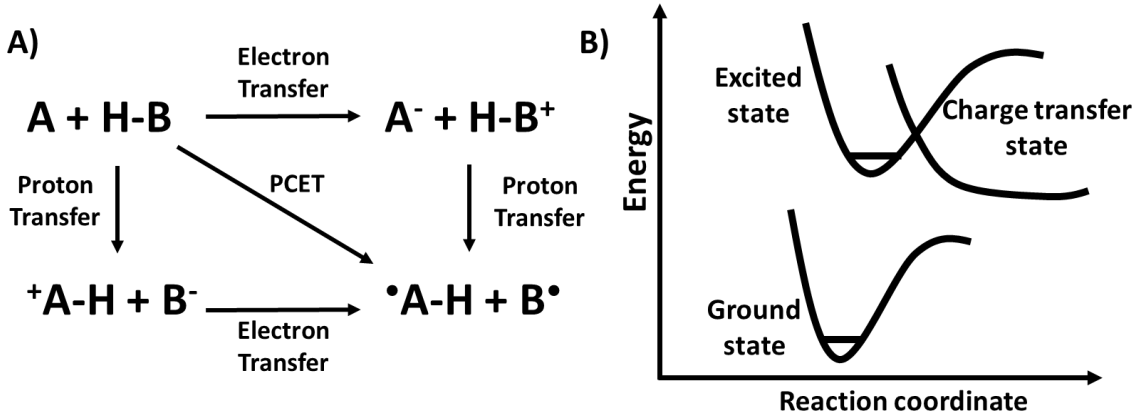

Figure 1-1. PCET pathways and landscape

A) Traditional square scheme used to describe pathways for proton and electron transfer, illustrating how coupled motion avoids charged intermediates. B) A cartoon of an excited-state potential energy surface showing the existence of a charge transfer state that is highly dependent on proton motion.

As we look for ways to convert solar energy into fuel, there is no better role model than plant's photosynthesis, refined by millions of years of evolution.[23] In fact, photosynthesis is responsible for the energy in our coal, oil, and peanut butter. However, if we want different fuels (such as hydrogen) we will have to manipulate the fundamental reactions. Since we do not have millennia

to solve our energy crisis, rationally designed catalysts, rather than trial-and-error, will be necessary.

Currently, the majority of intermolecular PCET literature to date focuses on metal-containing complexes,[17-19, 24] with fewer examples of all organic materials,[25-27] this despite photophysical properties of aza-aromatics being extensively studied over the past century.[26, 28-29] Exhibiting increased intersystem crossing rates and photochemical reactivity, heteroaromatics are prevalent in organic light emitting diodes[30-32] and photochemical redox applications.[33-35] Historically, researchers have heavily debated the nature of the excited state responsible for the photochemical reactivity of these compounds, both the orbitals involved and the spin of the excited state.[28, 36] Recent computational studies suggest intermolecular excitations involving photon-initiated electron transfer from H-bonded water to aza-aromatics facilitate H-atom abstraction to form neutral radicals.[26, 37-38] These studies open the discussion beyond strictly localized $n\rightarrow\pi^*$ and $\pi\rightarrow\pi^*$ excited states and introduced the idea of a charge transfer state, shown in Figure 1-1 B. While the charge transfer energy represents electron transfer, the energy of that state varies with the position of the proton illustrating how to the motion of the two are connected. While in reality, the potential energy surface with be more complicated with avoided crossings, this simplified diagram is still useful for visualizing the landscape.

1.3 History of Carbon Nitride and Heptazine

While carbon nitride first entered the spotlight in 2008 for photocatalyic hydrogen evolution,[39] it has a long history stretching back to 1834 when it was first made by Justus von Liebig.[40] However, the molecular structure was not fully understood until the 1930's when Edward C. Franklin gave Linus Pauling carbon nitride-like crystals (at this time it was $C_6N_7O_3Na_3\cdot 3H_2O$) to

study with X-ray spectroscopy.[41] Pauling proposed the three fused ring structure (tri-s-triazine) we know today as heptazine shown in Figure 1-2 A, but went unconfirmed until the 1982.[42] This heptazine is the monomer unit of carbon nitride, which is commonly connected by nitrogen atoms, shown in Figure 1-2 B.

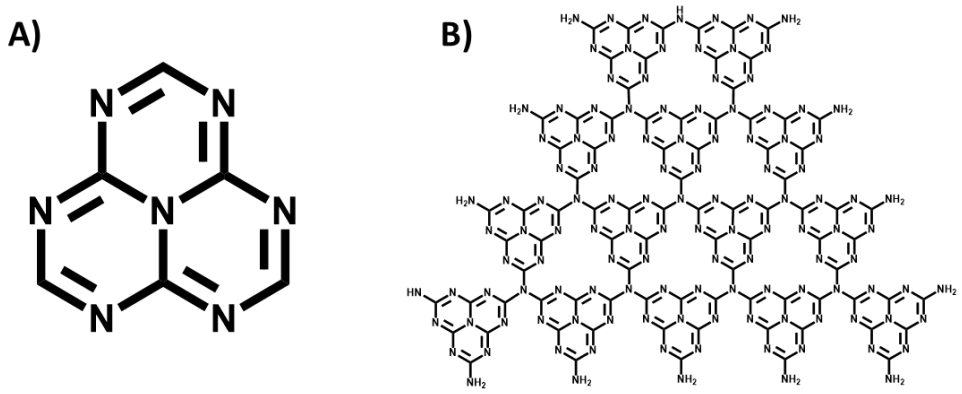

Figure 1-2. Heptazine (A) and carbon nitride (B) structures.

The report of visible light-driven photocatalytic hydrogen evolution using carbon nitride in 2008 kicked off a huge body of research studying the material.[39, 43-44] Two main advantages of carbon nitride are 1) it is metal-free and 2) very easily synthesized from earth-abundant precursors via pyrolysis.[45-50] While the ease of this synthetic procedure is advantageous in many ways, the resulting material will contain a variety of defects and overall structurally ambiguous.[51] This ambiguity has led to many debates in the literature. Despite thousands of publications concerning carbon nitride photocatalysts, there are few fundamental photophysical studies. As a result, there is still an active debate over whether the material should be thought of as a molecular material[43, 52-53] or more akin to inorganic semiconductors.[54-55] Work done by the Lotsch group has shown that small oligomer and molecular heptazine units are capable of photocatalytically producing hydrogen.[51-52] While these studies helped give weight to the argument to think of carbon nitride as

a molecular material, the intricacies of hetpazine's photophysics had yet to be explored in detail, and will be a major focus of this work.

1.4 REFERENCES

1. IEA *Global Energy & CO2 Status Report 2019*; Paris, 2019.
2. Rogelj, J., D. Shindell, K. Jiang, S. Fifita, P. Forster, V. Ginzburg, C. Handa, H. Kheshgi, S. Kobayashi, E. Kriegler, L. Mundaca,; R. Séférian, a. M. V. V. *Mitigation Pathways Compatible with 1.5°C in the Context of Sustainable Development*; 2018.
3. Allen, M. R., O.P. Dube, W. Solecki, F. Aragón-Durand, W. Cramer, S. Humphreys, M. Kainuma, J. Kala, N. Mahowald,; Y. Mulugetta, R. P., M.Wairiu, and K. Zickfeld *Framing and Context. In: Global Warming of 1.5°C. An IPCC Special Report on the impacts of global warming of 1.5°C above pre-industrial levels and related global greenhouse gas emission pathways, in the context of strengthening the global response to the threat of climate change, sustainable development, and efforts to eradicate poverty*; 2018.
4. Programme, U. N. D., *World Energy Assessment and the Chanllenge of Sustainable Energy*. New York, 2000.
5. Agency, I. E., Data and Statistics. 2017.
6. Administration, U. S. E. I., Total Energy Monthly Review. 2020.
7. Office of Energy Efficiency & Renewable Energy: New Solar Opportunities for a New Decade. https://www.energy.gov/eere/solar/sunshot-2030.
8. Administration, U. S. E. I., Electric Power Monthly. 2019.
9. Parkinson, B.; Balcombe, P.; Speirs, J. F.; Hawkes, A. D.; Hellgardt, K., Levelized cost of CO2 mitigation from hydrogen production routes. *Energy Environ. Sci.* **2019,** *12* (1), 19-40.
10. Zheng, Y.; Jiao, Y.; Zhu, Y.; Li, L. H.; Han, Y.; Chen, Y.; Du, A.; Jaroniec, M.; Qiao, S. Z., Hydrogen evolution by a metal-free electrocatalyst. *Nat. Comm* **2014,** *5* (1), 3783.
11. Mallouk, T. E., Divide and conquer. *Nature Chemistry* **2013,** *5* (5), 362-363.
12. Zou, X.; Zhang, Y., Noble metal-free hydrogen evolution catalysts for water splitting. *Chem. Soc. Rev.* **2015,** *44* (15), 5148-5180.
13. Mohammed-Ibrahim, J.; Sun, X., Recent progress on earth abundant electrocatalysts for hydrogen evolution reaction (HER) in alkaline medium to achieve efficient water splitting – A review. *Journal of Energy Chemistry* **2019,** *34*, 111-160.
14. Hu, S.; Xiang, C.; Haussener, S.; Berger, A. D.; Lewis, N. S., An analysis of the optimal band gaps of light absorbers in integrated tandem photoelectrochemical water-splitting systems. *Energy Environ. Sci.* **2013,** *6* (10), 2984-2993.
15. Wang, M.; Shen, S.; Li, L.; Tang, Z.; Yang, J., Effects of sacrificial reagents on photocatalytic hydrogen evolution over different photocatalysts. *Journal of Materials Science* **2017,** *52* (9), 5155-5164.

16. Tommos, C.; Babcock, G. T., Proton and hydrogen currents in photosynthetic water oxidation. *Biochem. Biophys. Acta* **2000,** *1458* (1), 199-219.
17. Concepcion, J. J.; Brennaman, M. K.; Deyton, J. R.; Lebedeva, N. V.; Forbes, M. D. E.; Papanikolas, J. M.; Meyer, T. J., Excited-State Quenching by Proton-Coupled Electron Transfer. *J. Am. Chem. Soc.* **2007,** *129* (22), 6968-6969.
18. Lennox, J. C.; Kurtz, D. A.; Huang, T.; Dempsey, J. L., Excited-State Proton-Coupled Electron Transfer: Different Avenues for Promoting Proton/Electron Movement with Solar Photons. *ACS Enery Lett.* **2017,** *2* (5), 1246-1256.
19. Weinberg, D. R.; Gagliardi, C. J.; Hull, J. F.; Murphy, C. F.; Kent, C. A.; Westlake, B. C.; Paul, A.; Ess, D. H.; McCafferty, D. G.; Meyer, T. J., Proton-Coupled Electron Transfer. *Chem. Rev.* **2012,** *112* (7), 4016-4093.
20. Gagliardi, C. J.; Vannucci, A. K.; Concepcion, J. J.; Chen, Z.; Meyer, T. J., The role of proton coupled electron transfer in water oxidation. *Energy Environ. Sci.* **2012,** *5* (7), 7704-7717.
21. Hammarström, L.; Styring, S., Proton-coupled electron transfer of tyrosines in Photosystem II and model systems for artificial photosynthesis: the role of a redox-active link between catalyst and photosensitizer. *Energy Environ. Sci.* **2011,** *4* (7), 2379-2388.
22. Kaila, V. R. I., Long-range proton-coupled electron transfer in biological energy conversion: towards mechanistic understanding of respiratory complex I. *Journal of The Royal Society Interface* **2018,** *15* (141), 20170916.
23. Reece, S. Y.; Nocera, D. G., Proton-Coupled Electron Transfer in Biology: Results from Synergistic Studies in Natural and Model Systems. *Annu. Rev. Biochem* **2009,** *78* (1), 673-699.
24. Damrauer, N. H.; Hodgkiss, J. M.; Rosenthal, J.; Nocera, D. G., Observation of Proton-Coupled Electron Transfer by Transient Absorption Spectroscopy in a Hydrogen-Bonded, Porphyrin Donor−Acceptor Assembly. *J. Phys. Chem. B* **2004,** *108* (20), 6315-6321.
25. Eisenhart, T. T.; Dempsey, J. L., Photo-induced Proton-Coupled Electron Transfer Reactions of Acridine Orange: Comprehensive Spectral and Kinetics Analysis. *J. Am. Chem. Soc.* **2014,** *136* (35), 12221-12224.
26. Liu, X.; Karsili, T. N.; Sobolewski, A. L.; Domcke, W., Photocatalytic Water Splitting with the Acridine Chromophore: A Computational Study. *J. Phys. Chem. B* **2015,** *119* (33), 10664-72.
27. Reimers, J. R.; Cai, Z.-L., Hydrogen Bonding and Reactivity of Water to Azines in Their S1 (n,pi*) Electronic Excited States in the Gas Phase and in Solution. *Phys. Chem. Chem. Phys.* **2012,** *14* (25), 8791-8802.
28. Whitten, D. G.; Lee, Y. J., Photochemistry of Aza Aromatics. Identification of the Reactive Intermediate in the Photoreduction of Acridine. *J. Am. Chem. Soc.* **1971,** *93* (4), 961-966.
29. Peon, J.; Tan, X.; Hoerner, J. D.; Xia, C.; Luk, Y. F.; Kohler, B., Excited State Dynamics of Methyl Viologen. Ultrafast Photoreduction in Methanol and Fluorescence in Acetonitrile. *J. Phys. Chem. A* **2001,** *105* (24), 5768-5777.
30. Hosokai, T.; Matsuzaki, H.; Nakanotani, H.; Tokumaru, K.; Tsutsui, T.; Furube, A.; Nasu, K.; Nomura, H.; Yahiro, M.; Adachi, C., Evidence and mechanism of efficient thermally activated delayed fluorescence promoted by delocalized excited states. *Sci. Adv* **2017,** *3* (5).
31. Li, J.; Nakagawa, T.; MacDonald, J.; Zhang, Q.; Nomura, H.; Miyazaki, H.; Adachi, C., Highly Efficient Organic Light-Emitting Diode Based on a Hidden Thermally Activated Delayed Fluorescence Channel in a Heptazine Derivative. *Adv. Mater.* **2013,** *25* (24), 3319-3323.

32. Goushi, K.; Yoshida, K.; Sato, K.; Adachi, C., Organic light-emitting diodes employing efficient reverse intersystem crossing for triplet-to-singlet state conversion. *Nat. Photon.* **2012,** *6*, 253.
33. Sartor, S. M.; McCarthy, B. G.; Pearson, R. M.; Miyake, G. M.; Damrauer, N. H., Exploiting Charge-Transfer States for Maximizing Intersystem Crossing Yields in Organic Photoredox Catalysts. *J. Am. Chem. Soc.* **2018,** *140* (14), 4778-4781.
34. Theriot, J. C.; Lim, C. H.; Yang, H.; Ryan, M. D.; Musgrave, C. B.; Miyake, G. M., Organocatalyzed Atom Transfer Radical Polymerization Driven by Visible Light. *Science* **2016,** *352* (6289), 1082-6.
35. Korvinson, K. A.; Hargenrader, G. N.; Stevanovic, J.; Xie, Y.; Joseph, J.; Maslak, V.; Hadad, C. M.; Glusac, K. D., Improved Flavin-Based Catalytic Photooxidation of Alcohols through Intersystem Crossing Rate Enhancement. *J. Phys. Chem. A* **2016,** *120* (37), 7294-7300.
36. Chen, Y.; Wang, B.; Lin, S.; Zhang, Y.; Wang, X., Activation of n → π* Transitions in Two-Dimensional Conjugated Polymers for Visible Light Photocatalysis. *J. Phys. Chem. C* **2014,** *118* (51), 29981-29989.
37. Ehrmaier, J.; Karsili, T. N. V.; Sobolewski, A. L.; Domcke, W., Mechanism of Photocatalytic Water Splitting with Graphitic Carbon Nitride: Photochemistry of the Heptazine–Water Complex. *J. Phys. Chem. A* **2017,** *121* (25), 4754-4764.
38. Ehrmaier, J.; Janicki, M. J.; Sobolewski, A. L.; Domcke, W., Mechanism of photocatalytic water splitting with triazine-based carbon nitrides: insights from ab initio calculations for the triazine-water complex. *Phys. Chem. Chem. Phys.* **2018,** *20* (21), 14420-14430.
39. Wang, X.; Maeda, K.; Thomas, A.; Takanabe, K.; Xin, G.; Carlsson, J. M.; Domen, K.; Antonietti, M., A Metal-Free Polymeric Photocatalyst for Hydrogen Production from Water Under Visible Light. *Nat. Mater.* **2008,** *8*, 76.
40. Liebig, J., Uber einige Stickstoff - Verbindungen. *Annalen der Pharmacie* **1834,** *10* (1), 1-47.
41. Pauling, L.; Sturdivant, J. H., The Structure of Cyameluric Acid, Hydromelonic Acid and Related Substances. *Proceedings of the National Academy of Sciences* **1937,** *23* (12), 615-620.
42. Hosmane, R. S.; Rossman, M. A.; Leonard, N. J., Synthesis and structure of tri-s-triazine. *J. Am. Chem. Soc.* **1982,** *104* (20), 5497-5499.
43. Ong, W.-J.; Tan, L.-L.; Ng, Y. H.; Yong, S.-T.; Chai, S.-P., Graphitic Carbon Nitride (g-C3N4)-Based Photocatalysts for Artificial Photosynthesis and Environmental Remediation: Are We a Step Closer To Achieving Sustainability? *Chem. Rev.* **2016,** *116* (12), 7159-7329.
44. Darkwah, W. K.; Oswald, K. A., Photocatalytic Applications of Heterostructure Graphitic Carbon Nitride: Pollutant Degradation, Hydrogen Gas Production (water splitting), and CO2 Reduction. *Nanoscale Research Letters* **2019,** *14* (1), 234.
45. Liu, J.; Zhang, Y.; Lu, L.; Wu, G.; Chen, W., Self-regenerated solar-driven photocatalytic water-splitting by urea derived graphitic carbon nitride with platinum nanoparticles. *Chem. Commun.* **2012,** *48* (70), 8826-8.
46. Xu, J.; Li, Y.; Peng, S.; Lu, G.; Li, S., Eosin Y-sensitized graphitic carbon nitride fabricated by heating urea for visible light photocatalytic hydrogen evolution: the effect of the pyrolysis temperature of urea. *Phys Chem Chem Phys* **2013,** *15* (20), 7657-65.
47. Huang, J.; Ho, W.; Wang, X., Metal-free disinfection effects induced by graphitic carbon nitride polymers under visible light illumination. *Chem Commun (Camb)* **2014,** *50* (33), 4338-40.

48. Zheng, Y.; Lin, L.; Wang, B.; Wang, X., Graphitic Carbon Nitride Polymers toward Sustainable Photoredox Catalysis. *Angew Chem Int Ed Engl* **2015,** *54* (44), 12868-84.
49. Koryakin, A.; Galperin, V.; Sarbaev, A.; AI, F., Thermography of urea and its pyrolysis products. *Zh. Org. Khim.* **1971,** *7* (5), 972-&.
50. Khabashesku, V. N.; Zimmerman, J. L.; Margrave, J. L., Powder synthesis and characterization of amorphous carbon nitride. *Chem. Mater.* **2000,** *12* (11), 3264-3270.
51. Lau, V. W.; Moudrakovski, I.; Botari, T.; Weinberger, S.; Mesch, M. B.; Duppel, V.; Senker, J.; Blum, V.; Lotsch, B. V., Rational design of carbon nitride photocatalysts by identification of cyanamide defects as catalytically relevant sites. *Nat Commun* **2016,** *7*, 12165.
52. Lau, V. W.; Mesch, M. B.; Duppel, V.; Blum, V.; Senker, J.; Lotsch, B. V., Low-molecular-weight carbon nitrides for solar hydrogen evolution. *J. Am. Chem. Soc.* **2015,** *137* (3), 1064-72.
53. Corp, K. L.; Schlenker, C. W., Ultrafast Spectroscopy Reveals Electron-Transfer Cascade That Improves Hydrogen Evolution with Carbon Nitride Photocatalysts. *J. Am. Chem. Soc.* **2017,** *139* (23), 7904-7912.
54. Godin, R.; Wang, Y.; Zwijnenburg, M. A.; Tang, J.; Durrant, J. R., Time-Resolved Spectroscopic Investigation of Charge Trapping in Carbon Nitrides Photocatalysts for Hydrogen Generation. *J. Am. Chem. Soc.* **2017,** *139* (14), 5216-5224.
55. Yang, W.; Godin, R.; Kasap, H.; Moss, B.; Dong, Y.; Hillman, S. A. J.; Steier, L.; Reisner, E.; Durrant, J. R., Electron Accumulation Induces Efficiency Bottleneck for Hydrogen Production in Carbon Nitride Photocatalysts. *J. Am. Chem. Soc.* **2019,** *141* (28), 11219-11229.

Chapter 2. Background

This chapter will provide some background knowledge for understanding how we think about photophysical events in organic materials, ways to measure and analyze these systems, and some implications for organic solar energy conversion devices.

2.1 PHOTOPHYSICS OF ORGANIC MOLECULES

This section will provide a brief overview of fundamental principles governing how light interacts with organic molecules. The following chapters will focus on how these fundamental photophysical principles relate to photochemistry. Nicholas Turro's *Modern Molecular Photochemistry* is an excellent resource for a more detailed discussion.[1]

2.1.1 *Absorption of Light*

In general chemistry, we are introduced to the concept of molecular orbitals to describe how atoms are connected by shared electron density. The most important molecular orbitals for understanding photophysical processes are the highest occupied molecular orbital (HOMO) and lowest unoccupied molecular orbital (LUMO), and the orbitals close to those in energy (i.e. HOMO-1, LUMO+1, etc.). When a molecule interacts with a photon of sufficient energy, an electron can be promoted from the HOMO to the LUMO, as shown in Figure 2-1A. Figure 2-1B shows how these transitions are commonly represented in a state diagram where the energies of transitions are all depicted relative to the ground state energy. The nature of the molecular orbitals involved influence the likelihood of that transition. If the transition is perfectly symmetric, the transition dipole is zero, which cannot interact with the oscillating electric field of the photon making the transition symmetry-forbidden. An example of this is the $\pi\pi^*$ transition of benzene,

Figure 1-1C and seen in heptazine discussed in later sections. Additionally, if there is no spatial overlap between the molecular orbitals, the transition is also overlap-forbidden, transitions from n- to π^*- orbitals, and spatially separated charge-transfer transitions.

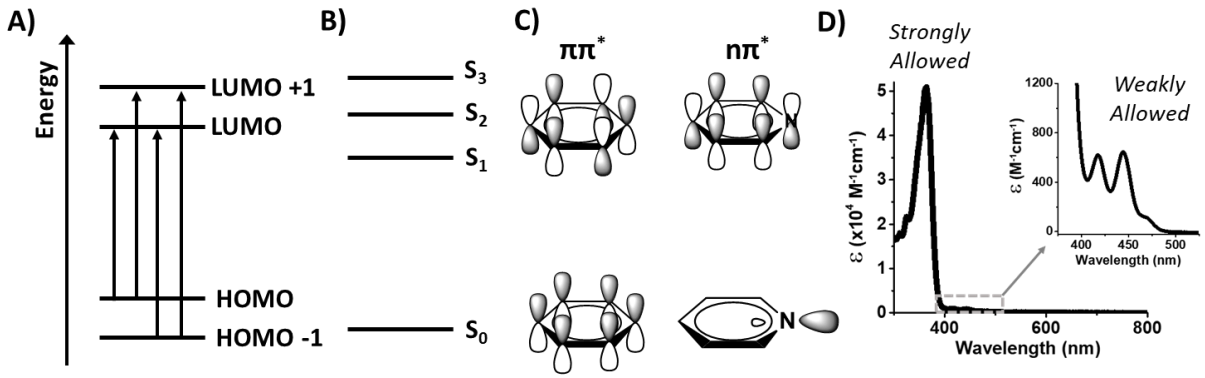

Figure 2-1. Relating molecular orbitals to light absorption

A) Energy levels of molecular orbital levels determine the energy of possible transitions within a molecule. B) State diagrams are useful to illustrate the energies of transitions relative to the ground state. C) Visual depiction of $\pi\pi^*$ and $n\pi^*$ transitions that are formally forbidden. D) Molar extinction spectra showing the differing values for strongly allowed transitions and weakly allowed transitions.

Of course, in the real world, molecular vibrations and interactions with the surrounding environment can relax these constraints and therefore result in weakly-allowed transitions. Experimentally, the "allowedness" of a transition is generally quantified using a molar extinction coefficient (ε) given by rearranging Beer's law: $\varepsilon = A/lc$, where A is the absorption in optical density (OD) at a given wavelength, l is the path length, and c is the concentration.[2] It generally reported in units of $cm^{-1}M^{-1}$, but it is important to remember this quantity is area/mole, because M is really mole/volume. A fully allowed transition will have a peak absorption (ε_{max}) on the order of 10^4-10^5 $cm^{-1}M^{-1}$ while very weakly allowed transitions can have ε_{max} on the order of 10 $cm^{-1}M^{-1}$. By

looking at absorption spectra wherein the y-axis is ε, it is possible to gain insight into the types of transitions being observed.

As opposed to atoms, molecules within an electronic state have many molecular configurations accessible through molecular vibrations. To pictorially depict this, we typically draw the electronic state as a well with numerous horizontal lines depicting the vibrational energy levels for a certain nuclear coordinate, Figure 2-2. When considering absorption of a photon, it is important to remember that electrons move significantly faster than nuclei, so it is a fair assumption that an electronic excitation will occur within the same nuclear configuration, a result of the Born-Oppenheimer approximation. Pictorially, we represent this as vertical transition in energy along a nuclear coordinate x-axis, as shown in Figure 2-2. For a more quantum mechanical discussion of these process, see Chapter 4 of *Modern Molecular Photochemistry* by Nicholas Turro.

2.1.2 ***Photoluminescence***

After absorbing a photon, the molecule is now in an excited state away from equilibrium. One decay pathway is for the molecule to radiate energy back in the form of a photon, termed photoluminescence. However, the altered electron density in the excited state can result in a different nuclear configuration to be lowest in energy. The new molecular configuration is illustrated by a shifted electronic potential well relative to the ground state as shown in Figure 2-2. This means the vertical absorption transition can excite a higher-energy vibrational state within the electronic well. The molecule can release energy in the form of heat as the molecule rearranges to this lower energy configuration, illustrated with a curvy arrow in Figure 2-2. This process of internal conversion is expected to be faster than the rate of fluorescence, so the steady-state fluorescence observed will be from the lowest vibrational state of the excited electronic well, aside from the temperature-dependent Boltzmann distribution of vibrational excited states. The overlap

of the wavefunctions in the ground and excited state determines the probability of any transition. This can result in transitions to multiple vibrational energy levels resulting in spectra showing a distinct vibronic progression, commonly referred to as the Franck-Condon progression. Analyzing this progression can give insight in which vibrational modes are most strongly coupled to the electronic transitions and the extent to which the relaxed excited-state geometry is distorted relative to the ground-state geometry.

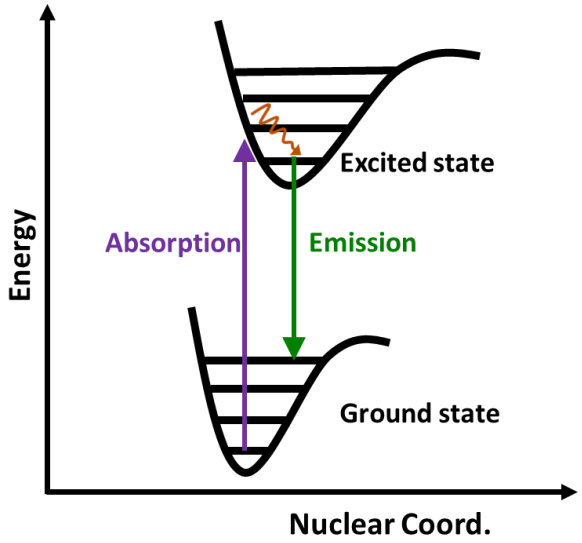

Figure 2-2. Potential energy landscape for organic molecules

Along some nuclear coordinate, the wells represent the energy of the electronic state with quantized vibrational states shown as horizontal lines. Absorption is represented as a vertical transition (purple arrow) from the lowest vibrational state in the ground state, vibrational cooling is represented as a curvy arrow (red) down to the lowest vibrational state of the electronic excited state, and emission is represented as a vertical transition (green) to the ground state. The displacement of the excited state electronic well relative to the ground state well represented nuclear distortion in the excited state, results in the emitted photon having lower energy than the absorbed photon.

The same properties governing the probability of an absorption between two states occurring effect the luminescence probability. Meaning that if the absorption probability was high, or the rate of absorption was fast, then the probability and rate of emission will also be fast in the absence of other non-radiative processes. The overall photoluminescence quantum yield (PLQY) is the

ratio of photons emitted to photons absorbed. This quantity is ultimately determined by the rates of all other competing non-radiative processes (to be discussed below) relative to the rate of emission.

2.1.3 *Non-radiative rates*

In addition to radiative decay, an excited state can transition to lower energy electronic states by converting electronic energy into kinetic energy through the motion of nuclei, as mentioned for the vibrational cooling within an electronic excited state. If this process does not involve a change in spin multiplicity (e.g. $S_3 \rightarrow S_2$) it is termed internal conversion (IC). If the process does involve a change in spin multiplicity (e.g. $S_1 \rightarrow T_1$) it is termed intersystem crossing (ISC). The process of intersystem crossing and the corresponding driving forces are discussed more thoroughly in Chapter 3.4 of this dissertation and in Chapter 3 and 6 of Nicholas Turro's *Modern Molecular Photochemistry*.[1]

In some organic molecules, such as heptazine-based chromophores, the most strongly allowed transition is not the lowest energy transition. In this case, the rate of internal conversion (k_{IC}) for states close in energy is expected to be around 10^{12}-10^{15} s^{-1}. This is often faster than the rate of fluorescence, which typically on the order of 10^{8}-10^{10} s^{-1}. Because of this difference in rates, the majority of luminescence will occur from the lowest-lying excited state (Kasha's Rule), with some notable exceptions such as azulene, which Kasha himself addresses.[3] Additionally, chemical reactions typically occur on even slower timescales indicating that most photochemistry will take place from the lowest-lying excited state, particularly if diffusion is first required.

The quantum yield of fluorescence (Φ_f) is defined by $\Phi_f = \frac{k_f}{k_f + k_{IC} + k_{ISC}}$, where k_f is the rate of fluorescence, k_{IC} is the rate of internal conversion to the ground state, and k_{ISC} is the rate of

intersystem crossing to the triplet manifold. Additionally, the lifetime of fluorescence (τ_f) is defined as $\tau_f = \frac{1}{k_f + k_{IC} + k_{ISC}}$. These quantities are in the absence of an external quenching source (e.g. a reactant in a photochemical transformation). When an external quencher is present, Stern-Volmer analysis can be used to determine the rate of collision-based quenching (k_Q), which is another form of a non-radiative decay. Stern-Volmer analysis involved monitoring the photoluminescence intensities or lifetimes as a function quencher concentration [Q]. By plotting $\frac{I_0}{I} = 1 + \frac{k_Q}{k_f}[Q]$ or $\frac{1}{\tau} = k_f + k_Q[Q]$, the k_Q for an excited state reaction can be found from the slope of the line.

2.2 Methods for Studying Optoelectronic Materials

In this section, a variety of measurement and analysis techniques used throughout this dissertation will be discussed.

2.2.1 *Lock-in Amplification*

Measuring a small number of excited states with finite lifetime in a sea of ground-state chromophores presents a challenge for studying energy storage processes in optoelectronic materials. To overcome a low signal-to-noise ratio, we use amplitude-modulated excitation and lock-in amplification. By modulating either a source of photoexcitation (e.g. LED or laser diode) or an electrical input (e.g. voltage) we are able to selectively extract the resulting signals that show the same modulated frequency. Two techniques used in our lab using lock-in detection are photoluminescence (PL) and charge-modulation spectroscopy (CMS).

Photoluminesence

In the simplest scenario, a sample is irradiated with a modulated LED excitation source. The modulation is accomplished either by a chopper wheel or a function generator (Aligent 33120A arbitrary waveform generator), the modulation frequency is typically 200 Hz. Spectra are resolved using an Acton monochromator and a photodiode which can be changed depending on the wavelength region of interest. The signal is amplified with a Stanford Research Systems SR570 low-noise current preamplifier and measured with a Stanford Research Systems SR830 lock-in amplifier. The phase is typically set using reflected pump light such that the signal is positive in X-channel (in-phase) with the Y-channel being as close to zero as possible. Photoluminescence spectra should be corrected for detector response using a calibrated LS-1-CAL Ocean Optics light source. The calibration filed used should match not only the detector of the measurement but also the slit size of both the entrance and exit slit of the monochromator.

Charge Modulation Spectroscopy

To obtain absorption spectra for polarons in organic thin films, we can use charge-modulation spectroscopy (CMS), where instead of modulating a light source, a voltage is modulated to inject charges into a device. Traditionally CMS measurements have been performed on field-effect transistors or charge-accumulation devices for the selective accumulation of either positive or negative charges.[4-6] However, in order to perform device-relevant transmission measurements with measurable current densities, it is useful to fabricate current-carrying hole-only or electron-only devices with semi-transparent Al electrodes (~30 nm).

Typically, an AC bias at 200Hz with a DC offset is applied to devices where the DC is set just below the current onset. The setup for this measurement is shown in Figure 2-3A. Devices are loaded into a home-built device chamber and kept under static vacuum during the measurement.

A DC bias from a Keithly 2400 Sourcemeter with an AC perturbation from a function generator is applied to the device's electrical contacts using a summing amplifier. Light generated by a halogen lamp is dispersed onto the grating of a monochromator and focused onto the sample at each wavelength. The transmitted light through the sample is collected through another monochromator and detected using a SiInGaAs detector or a UV-enhanced silicon photodiode. The resulting current is converted to voltage using a pre-amplifier and recorded as the steady-state transmission. Simultaneously, the amplified signal was demodulated using a lock-in amplifier referenced to the AC frequency (200Hz). This allows for selectively detecting small changes in absorption signal due to the applied bias.

In order to confirm the spectroscopy setup, I measured poly(3-hexylthiophene-2,5-diyl) (P3HT) in a charge-accumulation device to replicate the CMS spectra of Brown and coworkers.[4] The results in Figure 2-3B show that the polaron spectrum obtained from our CMS setup (black) exhibits the same peak positions as in literature (blue). In these spectra, positive features correspond to increased transmission of light, in this case representing the ground state bleach of P3HT. Negative features indicate less transmission, in this case attributed to the absorption of injected charge carriers. The difference in relative intensities between the two spectra is likely a result from different polymer morphologies due to different processing conditions.[7] The

discrepancy at 1.26 eV could also be a result of the diminishing silicon photodiode response around 1.24 eV (silicon's band edge).

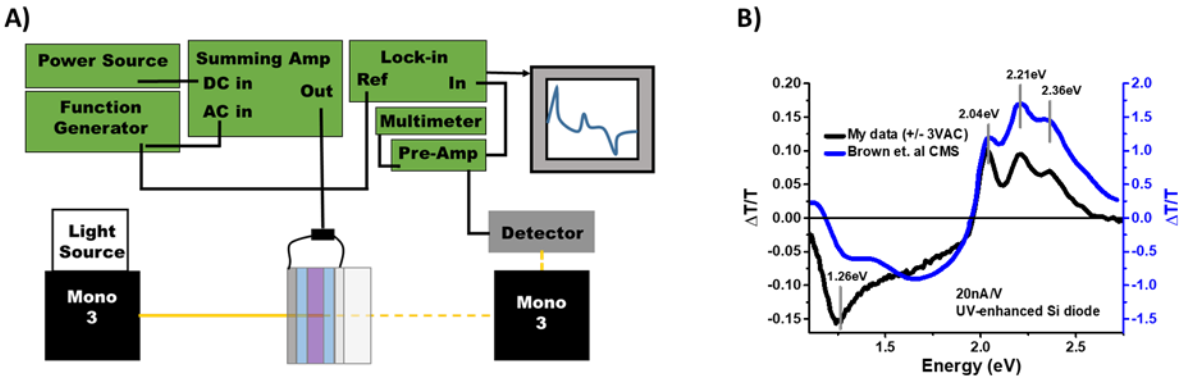

Figure 2-3. CMS setup and verification

A) Pictorial diagram of CMS setup. The sample is connected to a summing amplifier which sums the DC and AC signal from the power supply and function generator respectively. Differential absorbance spectra were recorded using lock-in techniques. B) The confirm the proper functioning of the CMS setup, a spectrum taken in lab (blue) is compared to literature (black).[4]

2.2.2 *Time-Resolved Photoluminescence*

Time-resolved photoluminescence (TR-PL) is useful to characterize the rates of formation and decay of luminescent excited states. For photochemistry, it is a useful probe on the disappearance of reactant and calculate quenching rate constants as mentioned previously.

Discussed here are two measurement techniques for measuring the lifetime of photoluminescence: time-correlated single photon counting (TCSPC) or detection with a streak camera. TCSPC is a simpler method which does not provide spectral resolution. In this technique, a pulsed laser diode is used to excite that sample at some repetition rate. Emission is collected through a long-pass filter to remove scattered laser light. The excitation intensity must be such that only a single photon of PL is detected after each pulse. By precisely counting time in between each pulse and the arrival of a photon, a time-dependent concentration trace is constructed. The resulting trace can be fit to an exponential decay, or sum of exponential decays, to determine the

fluorescence lifetime (τ_f) Because there is no grating, there is no wavelength dependence to this decay trace, aside from the long-pass filter. Additionally, the resolution of the PicoQuant FluoTime 100 system is about 300 ps.

Alternatively, time-resolved photoluminescence using a streak camera provides both spectral and temporal resolution with instrument response down to tens of picoseconds. Our setup uses roughly 50 fs pulses and collected with a Hammatsu streak camera (further details in Chapter 4.4). Figure 2-4A shows a schematic of how the streak camera collects data. Briefly, the sample is irradiated with a pulsed laser, and the orthogonal luminescence is focused through a lens and dispersed onto a grating, providing spectral resolution. The dispersed light then hits a photocathode which converts photons into electrons and enters the streak tube, where a voltage is triggered by the laser pulse and swept as a function of time, effectively changing the path of the electrons as a function of time. The electrons then strike a phosphor screen and are converted back into photons. The resulting image is captured by a CCD camera wherein the vertical axis corresponds to time and the horizontal axis corresponds to wavelength.

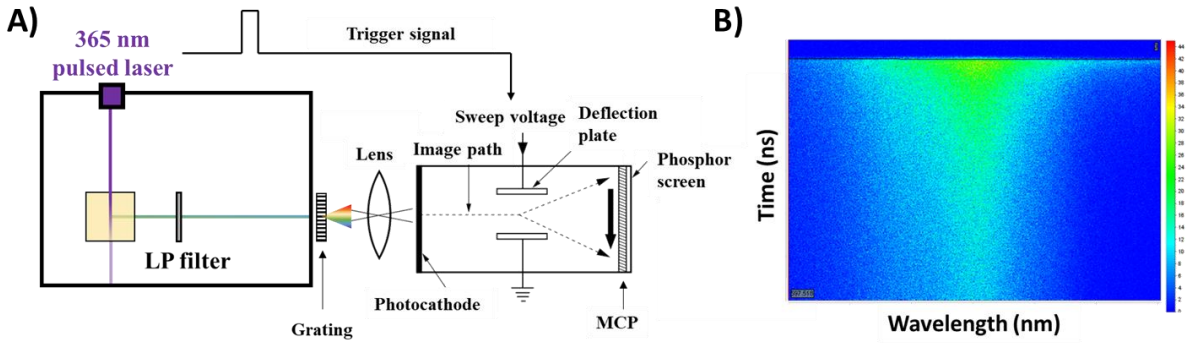

Figure 2-4. Streak camera operation
A) A diagram of the set for using a streak camera to collect TR-PL. B) An example dataset of luminescence intensity as a function of both time and wavelength.

Our lab has two different streak tubes: one operates on the nanosecond to millisecond time range (slow sweep unit) and operates at a faster picosecond to nanosecond time range (synchroscan).

The synchroscan camera continuously sweeps the voltage between pulses – forward to collect data and backward while clearing the phosphor screen. If the radiative species is not entirely decayed after half the time between pulses of the laser (6.25 ns in our system) the tail of the luminescence will become convoluted with the data. This is obvious to notice by elevated counts prior to time zero with the same spectral shape as the luminescence. This problem can be overcome with a pulse picker (also known as a shift blanking unit) which allows laser pulses to be skipped and thus the radiative species can fully relax before the next voltage sweep and data collection.

2.3 Global Analysis

TR-PL is especially powerful when used in concert with global analysis to extract distinct components from overlapping signals. For example, if there are two luminescing species which partially overlap in the emission wavelength but decay at different rates, global analysis can pull out the spectral component of related to each decay rate. This is not possible with either steady-state photoluminescence measurements. While TCSPC can pull out different decay rates, it cannot provide any spectral information which is useful for understanding the nature of the excited state.

Briefly, global analysis is able to model the time- and wavelength-dependent spectrum , $\psi(t,\lambda)$, shown in Figure 2-4 B as a function of a time-dependent concentration of the associated species, $c_i(t)$, and a wavelength-dependent spectrum, $\sigma_i(\lambda)$, for the i^{th} species, such that $\psi(t,\lambda) = \sum c_i(t)\sigma_i(\lambda)$. When analyzing emission spectra, the resulting wavelength-dependent spectra are termed decay-associated emission spectra (DAES) or species-associated emission spectra (SAES). Our lab uses Glotaran,[8] a graphical user interface for the R-package TIMP, to perform global and target analyses. For some datasets, it is important to either add physical constraints to the model or allow for more complex interactions between states. For these cases, target analysis is used by

constructing a K matrix. In Chapter 4, the K matrix is used to allow each spectral trace, $\sigma_i(\lambda)$, to have multiple decay rates, $c_i(t)$, by using five components but forcing the spectra to be equal for two of the components, and the other three must also share a spectral trace. Additionally, we were able to force the $\sigma_i(\lambda)$ to zero at certain wavelengths, justified by prior knowledge. In general, target analysis is a powerful tool as long as one has a physical model to test. The article published on the software package, provides a helpful example of drawing a diagram to represent a hypothesis and creating a K-matrix from the diagram to test that hypothesis.

2.4 Excited State Energies Drive Charge Transfer in Organic Materials

Adapted with permission from "Excited State Energies Drive Charge Transfer in Organic Semiconductors" by Emily J. Rabe, and Cody W. Schlenker, Franky So (editor), Copyright 2018, World Scientific.

2.4.1 *Introduction*

Understanding and controlling the energy landscape of organic materials is paramount to driving electricity generation or solar fuel production. This chapter will specifically focus on energy landscapes for organic photovoltaic (OPV) devices; however, the same principles apply to organic materials for any solar energy harvesting system. While it is tempting to apply the same formalisms used to describe covalent crystalline inorganic materials and represent this landscape using band models, organic materials act as weakly coupled molecular systems.[9] To signify this difference, many researchers have replaced the terms valence band and conduction band with highest occupied molecular orbital (HOMO) and lowest unoccupied molecular orbital (LUMO), respectively. Intense experimental and theoretical research efforts have focused on tailoring molecular structure

to tune these HOMO and LUMO levels for optimizing charge-transfer in OPV systems.[10-13] This approach has been successful in achieving high efficiency devices in many cases and can provide valuable insight into rational materials design. However, using ground-state energy levels does not account for the role of excitons in charge-transfer and can lead to incorrect predictions regarding the thermodynamic driving force for charge separation. It has become common in the literature to use terms such as conduction band, LUMO, transport level, and optical LUMO interchangeably; however, this is physically inaccurate and can be misleading for the synthetic chemist aiming to design new classes of materials or the electrical engineer targeting next-generation device architectures.[14] A number of studies correlating energy level alignment with charge-transfer and device performance on small molecule/fullerene, polymer/fullerene and polymer/quantum dot blends have highlighted the importance of accurate energy level diagrams. This chapter will discuss how to represent the energetic driving force for charge-transfer in OPV systems in a physically meaningful way, methods for determining these values, and how to apply this strategy for designing advanced organic device architectures.

2.4.2 *Depicting the Energy Landscape of OPV's*

Conventional inorganic semiconductors are covalent crystalline materials with very high dielectric constants that support nearly instantaneous generation of charge carriers upon photoexcitation since the exciton binding energies are on the order of the thermal energy available at room temperature.[15-17] In this case, the free-electron approximation is appropriate, leading to the band structure shown in Figure 2-5 for a typical inorganic *p*-*n* junction diode. From this diagram, it is intuitive to visualize how photoexcitation leads to current generation: electrons from the valence band (VB) are promoted into the conduction band (CB) and the conjugate charges are swept apart by the electric field in the depletion region of the device that is established between

the *p* and the *n* regions. This charge separation process allows the photovoltaic device to deliver electrical power to an external load.

The picture for organic semiconductor systems is substantively different because organic materials behave as weakly coupled molecular systems with low dielectric constants.[9] This results in photoexcitations that are primarily excitonic in nature. Additionally, the equilibrium electric field across the donor/acceptor interface is often vanishingly small. Due to strong covalent bonds existing only within molecules and the solid-state structure being held together by significantly weaker intermolecular interactions, it is common to replace the conduction and valence band labels with the labels corresponding to the molecular orbital energy levels, HOMO and LUMO respectively, as shown in Figure 2-5.[18]

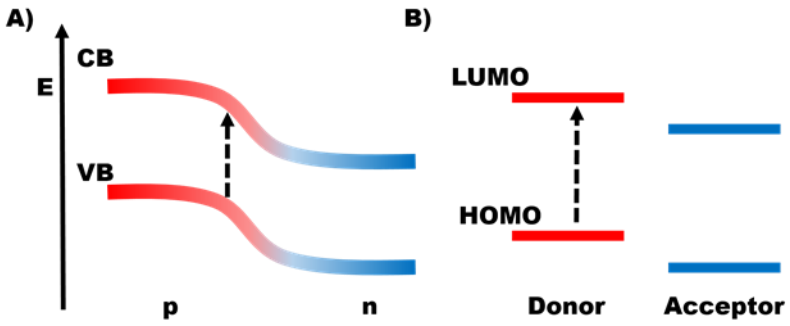

Figure 2-5. Energy diagram comparison for PV materials

A) Conventional energy band diagram representation of a p-n junction solar cell where the dashed line represents photoexcitation. B) A common, but incomplete energy landscape diagram for OPVs where CB and VB are replaced with HOMO and LUMO levels, respectively. While it would appear this would lead to favorable electron-transfer to the acceptor and hole-transfer to the donor, it does not take into account the exciton binding energy.

While this is conceptually attractive and generally a convenient convention, the ground-state energy level offsets between the donor and acceptor ($HOMO_D/HOMO_A$ and $LUMO_D/LUMO_A$) do not contain sufficient information to predict whether charge-transfer will be exothermic. Photocurrent can be generated via electron-transfer between a donor exciton and ground-state

acceptor, or hole-transfer between ground-state donor and an acceptor exciton. As mentioned above, the low dielectric constant of these materials leads to exciton binding energies on the order of 0.5-1.5 eV.[19] Therefore, these quasi-particles no longer have the same energetic landscape as the single-particle ground-state levels. To predict charge-transfer one must consider these excited-state potentials for both the donor and the acceptor materials. Adding these levels to the HOMO/LUMO diagram shown above is not simple, as this involves comparing single particle and quasi-particle levels.

In order to construct a physically meaningful energy level diagram consisting of both exciton and ground-state energy levels for weakly coupled molecular systems, it is useful to replace HOMO and LUMO with ionization potential (IP) and electron affinity (EA) respectively. It should be noted this is common practice in the photoelectrochemistry community, but is far less common in the materials synthesis and device engineering literature for OPVs.[20-24] The IP is defined as the energy required to remove an electron from the material to create a cation ($M \rightarrow M^+ + e^-$). The energy of this process is associated with the energy of the HOMO orbital in a molecular system. Conversely, EA is associated with the energy released upon the capture of an electron by the material to form an anion ($M + e^- \rightarrow M^-$), corresponding to the molecular LUMO. Typically, one considers only the IP and EA values associated with the ground-state of the molecule. However, it is particularly useful to also consider the IP and EA values associated with the molecular excited states. Exciton ionization potentials and electron affinities can be denoted as IP* and EA*, respectively. One can readily distinguish further between ionization potentials of excitons with different values of the total spin quantum number (S) by indicating the spin multiplicity ($2S + 1$) as $^{2S+1}$IP*. It follows that electron affinities of excitons with different spin character can be denoted as $^{2S+1}$EA*. These quantities can be estimated for ground-state and excited-state measurements

using methods discussed in the next section. This formalism allows one to plot these energy levels on the same axis for useful comparison as demonstrated in Figure 2-6.

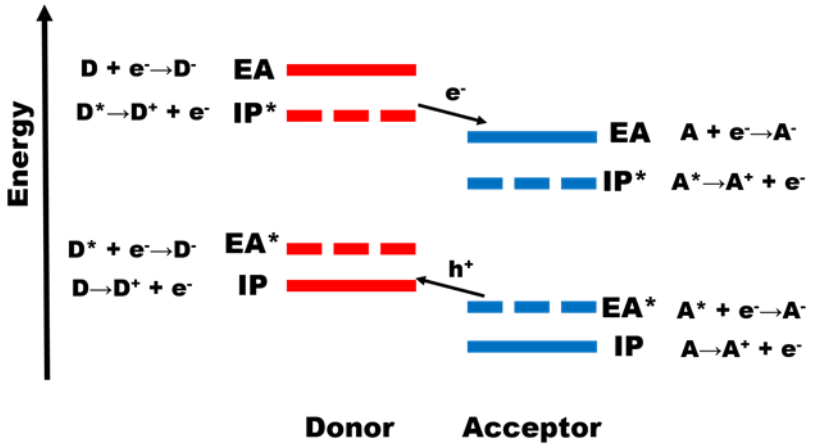

Figure 2-6. Excited-state IP and EA energy diagram

Relevant energy landscape for determining the driving force for charge-transfer using ionization potentials (IP) and electron affinities (EA). For electron-transfer from an excited donor to a ground-state acceptor molecule, the donor IP* must be above that of the acceptor EA. Conversely, for hole-transfer from an excited acceptor molecule to ground-state donor, the acceptor EA* must be lower in energy than the donor IP.

Electron-transfer events that are enthalpically driven for a donor exciton to a ground-state acceptor (i.e. $D^* + A \rightarrow D^+ + A^-$) can be represented by the value of the donor IP* being higher in energy (less negative with respect to vacuum level) than the value of the acceptor EA. While this is often considered to be the primary mechanism for photocurrent generation, one must also ensure that efficient hole-transfer can occur from acceptor excitons to ground-state donor molecules ($D + A^* \rightarrow D^+ + A^-$). Acceptor excitons can be formed either through direct photoexcitation or via Förster energy-transfer from a donor exciton.[25] Favorable hole-transfer from an acceptor exciton

is also shown in Figure 2-6, with the value of the acceptor EA* lower in energy than that of the ground-state donor IP.

A key advantage of this diagram is the ability to plot IP and EA values for any excited-state on the same axis, for example, triplet states (T_n), singlet states (S_n), or charge-transfer states (CT_n). A process for constructing an energy level diagram encompassing these states has recently been addressed by X.-Y. Zhu.[18] The ability to visualize these excited-state energy levels is useful in designing a variety of device architectures. For example, converting singlet excitons to triplets has been identified as one strategy to increase the exciton diffusion length in organic materials.[26] The thickness of the donor layer in a bilayer device is ultimately limited by this diffusion length. So, while thicker layers can absorb more light, increasing the thickness significantly beyond the exciton diffusion length results in diminishing photocurrent response. By integrating a triplet sensitizer into the donor layer, Roberts and coworkers were able to enhance the photocurrent response upon increasing device thickness.[27] Designing such a host-guest architecture requires careful alignment of singlet and triplet energy levels to enable exciton migration and eventual charge separation. Assigning triplet exciton ionization potentials is also required when designing devices to harness singlet exciton fission to increase the possible number of electrons per photon. Singlet fission, the process by which one singlet exciton can split into two triplet excitons, a form of multi-exciton generation, opens the possibility of single-junction power conversion efficiencies above the Shockley-Queisser limit.[28-34] Quantum efficiencies of above 100% have already been shown for acene-derivatives, although low V_{oc}'s limit the overall power conversion efficiency.[30]

The convention introduced in Figure 2-6 is well-suited to depict device architectures in which one must consider processes involving triplet and singlet excitons.

Additionally, this diagram allows one to integrate the ionization energy associated with charge-transfer (CT) states, a set of chemical species about which there has been much debate in the literature. Of particular interest is whether CT states ultimately limit the overall photocurrent generation efficiency of organic solar cells. On the one hand, a number of reports based on steady-state external quantum efficiency measurements suggest that CT states can contribute to photocurrent generation with relatively high yield, in some cases approaching that of neutral excitons.[35-41] However, time-resolved, pump-push photocurrent measurements suggest that the overall photocurrent generation efficiency is governed by kinetic competition between CT relaxation and CT dissociation.[42-44] In both cases, it can be advantageous to integrate this information into the energy landscape for system design.

2.4.3 *Methods for Determining Energy Levels*

Ground-state

Determining the values associated with IP and EA is achieved most directly with ultraviolet photoemission spectroscopy (UPS) and inverse photoemission spectroscopy (IPES), respectively. Briefly, in UPS a sample is irradiated with a photon of sufficiently high energy to eject an electron from the surface of the material. The difference between the energy of the incoming photon and the measured kinetic energy of the ejected electron is the energy required to remove the electron from the material, thus providing the material's IP.[45-46] Conversely, in IPES the sample is subjected to an electron beam and the resulting optical emission energy is measured, the difference in energy between the emitted light and the kinetic energy of the electron is the EA.[45, 47] While UPS and IPES are, in principle, direct probes of the IP and EA, respectively, these methods also have several

practical limitations. Films must be compatible with ultrahigh vacuum and stable under ultraviolet radiation.[48] Additionally, these techniques are both time-consuming and often prohibitively costly for routine measurements. Moreover, the nearly-ubiquitous sample degradation that can occur during IPES measurements makes data acquisition and analysis tractable for only a handful of the most highly specialized and skilled research groups.

In many cases, a more readily accessible experimental alternative for estimating these energy levels is to pair electrochemical measurements with optical absorption and emission spectroscopy.[48-49] This approach uses the respective linear correlations between reduction and oxidation potentials from cyclic voltammetry (CV) measurements with EA and IP values obtained from UPS and IPES. The linear relationship between these energies is shown in Figure 2-7. CV measurements can be taken of materials dissolved in solution or deposited on a conductive film to more closely reflect the solid-state properties.[20] In short, the electrochemical cell consists of working, counter, and reference electrodes immersed in a solvent containing an electrolyte and reference solute. The material of interest is either dissolved in solution or deposited on the working electrode. The applied electrode potential is varied at the working electrode, relative to the reference electrode, and the resulting current that flows between the working and counter electrodes is measured. At a given potential, the compound of interest will be either oxidized or reduced, typically resulting in an exponential increase in electrochemical current signal. In the case when the analyte is dissolved in solutions, the current magnitude diminishes once all nearby-molecules have been reduced or oxidized. At such potentials, the rate of the electron transfer process becomes diffusion-limited, and the current signal exhibits a characteristic peak. If the process is reversible, the thermodynamic half-wave anodic potential is the numerical average in potentials of, for example, the oxidation peak and the corresponding reduction peak for the process

of reducing the oxidized form of the analyte back to the neutral state. Equal and opposite current values for the corresponding oxidation and reduction peaks are characteristic of a reversible electrochemical process. In such cases the measured potential is representative of the thermodynamic potential for the redox couple of interest. The potential corresponding to the +1 oxidation state and -1 reduction state can be correlated with the IP and EA, respectively. In the event that one encounters a quasi-reversible or non-reversible redox couple exhibiting disparate peak amplitudes, or no electrochemical return wave is observed, a significant overpotential must often be applied to drive the electrochemical process. In this case the irreversible nature of the redox couple obscures the thermodynamic potential and one must proceed with great caution.

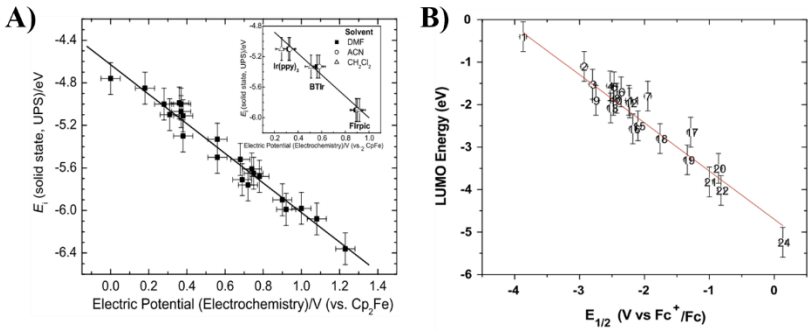

Figure 2-7 Estimating EA and IP energies

A) The linear relationship between reduction potential, corresponding to the IP, determined via UPS and the electrochemical oxidation potential for several organic molecules and oligomers. Adapted with permission from Reference 40. Copyright 2005 Elsevier B.V. B) Linear relationship between LUMO energy, or EA, determined by IPES and the electrochemical reduction potential. Adapted with permission from Reference 41. Copyright 2009 Elsevier B.V.

D'Andrade and coworkers constructed the plot shown in Figure 2-7 to show the relationship between IP and the oxidation potential using several small-molecule and oligomeric organic electronic materials.[48] Similarly, the relationship between reduction potential and EA was investigated by Djurovich and coworkers, leading to the linear relationship shown in Figure 2-7.[49]

By linear regression, one obtains Equations 1 and 2 for the lines of best fit that correlate the measured redox potentials to IP and EA values, respectively.

$$E_{IP} = -(1.4 \pm 0.1) \times \left(qV_{CV_{ox}}\right) - (4.6 \pm 0.08)eV \quad (1)$$

$$E_{EA} = -(1.19 \pm 0.08) \times \left(qV_{CV_{red}}\right) - (4.78 \pm 0.17)eV \quad (2)$$

In Equations 1 and 2, the terms E_{IP} and E_{EA} represent the IP and EA energies in eV as determined by UPS and IPES respectively, $V_{CV_{ox}}$ and $V_{CV_{red}}$ are the oxidation and reduction potentials relative to Fc/Fc^{+} (+0.40 V vs SHE) respectively, and q is the charge of an electron. Using these equations one can approximate the ground-state IP and EA using CV techniques.

Polarization energies should also be considered when discussing IP and EA levels. Polarization energy is defined as the difference in IP or EA in the gas phase versus in the solid state and arises from electronic and nuclear polarization of nearby molecules. Particularly, for conjugated organic systems, these values can range from 0.1 to 2 eV. Extensive computational work has been carried out by Brédas and coworkers to clarify the effects of morphological packing in the bulk and at interfaces on polarization energies.[50-52] These polarization effects are important when considering the different techniques for determining these energy levels. One should be particularly cautious when extrapolating solution-phase CV measurements to solid state applications. Even in thin-film measurements, it is important to consider the effect of varying morphology and interfacing the material with vacuum or solution.[50, 52]

Excited-state Energy Levels

As previously mentioned, it is necessary to use excited-state energy levels to accurately estimate the driving force that is available for photoinduced charge-transfer. Similar to ground-state levels, excited-state values can be determined using different techniques with unique advantages and disadvantages. Time-resolved two-photon photoemission spectroscopy (TR-2PPE) most directly

measures IP*.[53-55] In this technique, the sample is excited using an IR-Vis pump beam, the induced photoexcited-states are then probed using a UV pulse at a controlled time delay to eject an electron from the excited material. This provides complementary information to UPS, but now of the excited-state. Additionally, it can be carried out in a time-resolved manner. While 2PPE is uniquely capable of measuring the IP* value for various excited-states, it is a highly-specialized technique which is presently accessible to only a handful of research groups in the world. It is also worth noting that no corresponding technique exists at this time for measuring EA*.[18] Alternatively, one can use the singlet exciton energy, E_g^{opt}, to approximate IP* and EA* from the ground-state IP and EA using equations 3 and 4.[56] The singlet exciton energy can be estimated from the spectral intersection of the peak-area-normalized ground-state absorption and photoluminescence spectra, as shown in Figure 2-8. The value of this intersection point is also referred to as the E_{00} transition energy.

$$EA^*_{(M*\rightarrow M^-)} = EA_{(M\rightarrow M^-)} - E_g^{opt} \quad (3)$$

$$IP^*_{(M*\rightarrow M^+)} = IP_{(M\rightarrow M^+)} + E_g^{opt} \quad (4)$$

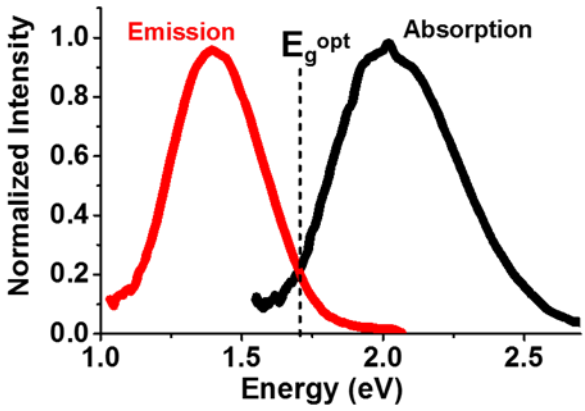

Figure 2-8. Determining the excited-state energy

Thin-film ground-state absorption (black) and photoluminescence (red) spectra are used to determine the exciton energy for thin films of organic semiconductors. The intersection of these curves represents E_{00} transition, or E_g^{opt}, which accounts for the excitonic binding energy.

2.5 REFERENCES

1. Turro, N. J.; Ramamurthy, V.; Scaiano, J. C., *Principles of Molecular Photochemistry: An Introduction.* University Science Books Sausalito, California, 2009.
2. Beer, Bestimmung der Absorption des rothen Lichts in farbigen Flüssigkeiten. *Annalen der Physik* **1852,** *162* (5), 78-88.
3. Viswanath, G.; Kasha, M., Confirmation of the Anomalous Fluorescence of Azulene. *J. Phys. Chem.* **1956,** *24* (3), 574-577.
4. Brown, P. J.; Sirringhaus, H.; Harrison, M.; Shkunov, M.; Friend, R. H., Optical spectroscopy of field-induced charge in self-organized high mobility poly(3-hexylthiophene). *Phys. Rev. B* **2001,** *63* (12), 11.
5. Chin, X. Y.; Yin, J.; Wang, Z.; Caironi, M.; Soci, C., Mapping polarons in polymer FETs by charge modulation microscopy in the mid-infrared. *Scientific Reports* **2014,** *4*, 3626.
6. Xu, H.; Xiao, T.; Li, J.; Mai, J.; Lu, X.; Zhao, N., In Situ Probing of the Charge Transport Process at the Polymer/Fullerene Heterojunction Interface. *J. Phys. Chem. C* **2015,** *119* (45), 25598-25605.
7. Spano, F. C., The Spectral Signatures of Frenkel Polarons in H- and J-Aggregates. *Acc. Chem. Res.* **2010,** *43* (3), 429-439.
8. Snellenburg, J. J.; Laptenok, S. P.; Seger, R.; Mullen, K. M.; Stokkum, I. H. M. v., Glotaran: A Java-Based Graphical User Interface for the R Package TIMP. *J. Stat. Softw.* **2012,** *49* (3), 22.
9. Schlenker, C. W.; Thompson, M. E., Current Challenges in Organic Photovoltaic Solar Energy Conversion. In *Unimolecular and Supramolecular Electronics I: Chemistry and Physics Meet at Metal-Molecule Interfaces*, Metzger, R. M., Ed. Springer Berlin Heidelberg: Berlin, Heidelberg, 2012; pp 175-212.
10. Robertson, N., Organic Photovoltaics. Mechanisms, Materials and Devices. Edited by Sam-Shajing Sun and Niyazi Serdar Sariciftci. *Angew. Chem. Int. Ed.* **2006,** *45* (44), 7321-7321.
11. Walker, B.; Liu, J.; Kim, C.; Welch, G. C.; Park, J. K.; Lin, J.; Zalar, P.; Proctor, C. M.; Seo, J. H.; Bazan, G. C.; Nguyen, T.-Q., Optimization of energy levels by molecular design: evaluation of bis-diketopyrrolopyrrole molecular donor materials for bulk heterojunction solar cells. *Energy Environ. Sci.* **2013,** *6* (3), 952.
12. Gong, X.; Tong, M.; Brunetti, F. G.; Seo, J.; Sun, Y.; Moses, D.; Wudl, F.; Heeger, A. J., Bulk Heterojunction Solar Cells with Large Open-Circuit Voltage: Electron Transfer with Small Donor-Acceptor Energy Offset (Adv. Mater. 20/2011). *Adv. Mater.* **2011,** *23* (20), 2271-2271.
13. He, Y.; Chen, C.; Richard, E.; Dou, L.; Wu, Y.; Li, G.; Yang, Y., Novel fullerene acceptors: synthesis and application in low band gap polymer solar cells. *J. Mater. Chem.* **2012,** *22* (26), 13391-13394.
14. Bredas, J.-L., Mind the gap! *Materials Horizons* **2014,** *1* (1), 17-19.
15. Mathieu, H.; Lefebvre, P.; Christol, P., Simple analytical method for calculating exciton binding energies in semiconductor quantum wells. *Phys. Rev. B* **1992,** *46* (7), 4092-4101.
16. Blossey, D. F., Wannier Exciton in an Electric Field. I. Optical Absorption by Bound and Continuum States. *Phys. Rev. B* **1970,** *2* (10), 3976-3990.
17. Blossey, D. F., Wannier Exciton in an Electric Field. II. Electroabsorption in Direct-Band-Gap Solids. *Phys. Rev. B* **1971,** *3* (4), 1382-1391.

18. Zhu, X. Y., How to Draw Energy Level Diagrams in Excitonic Solar Cells. *J. Phys. Chem. Lett.* **2014,** *5* (13), 2283-2288.
19. Hill, I. G.; Kahn, A.; Soos, Z. G.; Pascal, J. R. A., Charge-separation energy in films of π-conjugated organic molecules. *Chem. Phys. Lett.* **2000,** *327* (3–4), 181-188.
20. Bard, A. J.; Faulkner, L. R., *Electrochemical Methods: Fundamentals and Applications*. Wiley: 2000.
21. Delcamp, J. H.; Yella, A.; Nazeeruddin, M. K.; Gratzel, M., Modulating dyeE(S+/S*) with efficient heterocyclic nitrogen containing acceptors for DSCs. *Chem. Commun.* **2012,** *48* (17), 2295-2297.
22. Hagfeldt, A.; Grätzel, M., Molecular Photovoltaics. *Acc. Chem. Res.* **2000,** *33* (5), 269-277.
23. Lee, S. K.; Zu, Y.; Herrmann, A.; Geerts, Y.; Müllen, K.; Bard, A. J., Electrochemistry, Spectroscopy and Electrogenerated Chemiluminescence of Perylene, Terrylene, and Quaterrylene Diimides in Aprotic Solution. *J. Am. Chem. Soc.* **1999,** *121* (14), 3513-3520.
24. Tachibana, Y.; Moser, J. E.; Grätzel, M.; Klug, D. R.; Durrant, J. R., Subpicosecond Interfacial Charge Separation in Dye-Sensitized Nanocrystalline Titanium Dioxide Films. *J. Phys. Chem.* **1996,** *100* (51), 20056-20062.
25. Benson-Smith, J. J.; Ohkita, H.; Cook, S.; Durrant, J. R.; Bradley, D. D. C.; Nelson, J., Charge separation and fullerene triplet formation in blend films of polyfluorene polymers with [6,6]-phenyl C61 butyric acid methyl ester. *Dalton Transactions* **2009,** (45), 10000-10005.
26. Kroeze, J. E.; Savenije, T. J.; Warman, J. M., Efficient Charge Separation in a Smooth-TiO2/Palladium-Porphyrin Bilayer via Long-Distance Triplet-State Diffusion. *Adv. Mater.* **2002,** *14* (23), 1760-1763.
27. Roberts, S. T.; Schlenker, C. W.; Barlier, V.; McAnally, R. E.; Zhang, Y.; Mastron, J. N.; Thompson, M. E.; Bradforth, S. E., Observation of Triplet Exciton Formation in a Platinum-Sensitized Organic Photovoltaic Device. *J. Phys. Chem. Lett.* **2011,** *2* (2), 48-54.
28. Burdett, J. J.; Müller, A. M.; Gosztola, D.; Bardeen, C. J., Excited state dynamics in solid and monomeric tetracene: The roles of superradiance and exciton fission. *J. Phys. Chem.* **2010,** *133* (14), 144506.
29. Chan, W.-L.; Tritsch, J. R.; Zhu, X. Y., Harvesting Singlet Fission for Solar Energy Conversion: One- versus Two-Electron Transfer from the Quantum Mechanical Superposition. *J. Am. Chem. Soc.* **2012,** *134* (44), 18295-18302.
30. Congreve, D. N.; Lee, J.; Thompson, N. J.; Hontz, E.; Yost, S. R.; Reusswig, P. D.; Bahlke, M. E.; Reineke, S.; Van Voorhis, T.; Baldo, M. A., External Quantum Efficiency Above 100% in a Singlet-Exciton-Fission–Based Organic Photovoltaic Cell. *Science* **2013,** *340* (6130), 334-337.
31. Lee, J.; Jadhav, P.; Reusswig, P. D.; Yost, S. R.; Thompson, N. J.; Congreve, D. N.; Hontz, E.; Van Voorhis, T.; Baldo, M. A., Singlet Exciton Fission Photovoltaics. *Acc. Chem. Res.* **2013,** *46* (6), 1300-1311.
32. Roberts, S. T.; McAnally, R. E.; Mastron, J. N.; Webber, D. H.; Whited, M. T.; Brutchey, R. L.; Thompson, M. E.; Bradforth, S. E., Efficient Singlet Fission Discovered in a Disordered Acene Film. *J. Am. Chem. Soc.* **2012,** *134* (14), 6388-6400.
33. Yost, S. R.; Lee, J.; Wilson, M. W. B.; Wu, T.; McMahon, D. P.; Parkhurst, R. R.; Thompson, N. J.; Congreve, D. N.; Rao, A.; Johnson, K.; Sfeir, M. Y.; Bawendi, M. G.; Swager, T. M.; Friend, R. H.; Baldo, M. A.; Van Voorhis, T., A transferable model for singlet-fission kinetics. *Nat Chem* **2014,** *6* (6), 492-497.

34. Zimmerman, P. M.; Musgrave, C. B.; Head-Gordon, M., A Correlated Electron View of Singlet Fission. *Acc. Chem. Res.* **2013,** *46* (6), 1339-1347.
35. Lee, J.; Vandewal, K.; Yost, S. R.; Bahlke, M. E.; Goris, L.; Baldo, M. A.; Manca, J. V.; Voorhis, T. V., Charge Transfer State Versus Hot Exciton Dissociation in Polymer−Fullerene Blended Solar Cells. *J. Am. Chem. Soc.* **2010,** *132* (34), 11878-11880.
36. Deotare, P. B.; Chang, W.; Hontz, E.; Congreve, D. N.; Shi, L.; Reusswig, P. D.; Modtland, B.; Bahlke, M. E.; Lee, C. K.; Willard, A. P.; Bulovic, V.; Van Voorhis, T.; Baldo, M. A., Nanoscale transport of charge-transfer states in organic donor-acceptor blends. *Nat Mater* **2015,** *14* (11), 1130-1134.
37. Chang, W.; Congreve, D. N.; Hontz, E.; Bahlke, M. E.; McMahon, D. P.; Reineke, S.; Wu, T. C.; Bulović, V.; Van Voorhis, T.; Baldo, M. A., Spin-dependent charge transfer state design rules in organic photovoltaics. *Nat. Comm* **2015,** *6*.
38. Vandewal, K.; Albrecht, S.; Hoke, E. T.; Graham, K. R.; Widmer, J.; Douglas, J. D.; Schubert, M.; Mateker, W. R.; Bloking, J. T.; Burkhard, G. F.; Sellinger, A.; Fréchet, J. M. J.; Amassian, A.; Riede, M. K.; McGehee, M. D.; Neher, D.; Salleo, A., Efficient charge generation by relaxed charge-transfer states at organic interfaces. *Nat Mater* **2014,** *13* (1), 63-68.
39. Vandewal, K.; Gadisa, A.; Oosterbaan, W. D.; Bertho, S.; Banishoeib, F.; Van Severen, I.; Lutsen, L.; Cleij, T. J.; Vanderzande, D.; Manca, J. V., The Relation Between Open-Circuit Voltage and the Onset of Photocurrent Generation by Charge-Transfer Absorption in Polymer : Fullerene Bulk Heterojunction Solar Cells. *Adv. Funct. Mater.* **2008,** *18* (14), 2064-2070.
40. Vandewal, K.; Himmelberger, S.; Salleo, A., Structural Factors That Affect the Performance of Organic Bulk Heterojunction Solar Cells. *Macromolecules* **2013,** *46* (16), 6379-6387.
41. Albrecht, S.; Vandewal, K.; Tumbleston, J. R.; Fischer, F. S.; Douglas, J. D.; Fréchet, J. M.; Ludwigs, S.; Ade, H.; Salleo, A.; Neher, D., On the efficiency of charge transfer state splitting in polymer: fullerene solar cells. *Adv. Mater.* **2014,** *26* (16), 2533-2539.
42. Gélinas, S.; Paré-Labrosse, O.; Brosseau, C.-N.; Albert-Seifried, S.; McNeill, C. R.; Kirov, K. R.; Howard, I. A.; Leonelli, R.; Friend, R. H.; Silva, C., The Binding Energy of Charge-Transfer Excitons Localized at Polymeric Semiconductor Heterojunctions. *J. Phys. Chem. C* **2011,** *115* (14), 7114-7119.
43. Bakulin, A. A.; Rao, A.; Pavelyev, V. G.; van Loosdrecht, P. H.; Pshenichnikov, M. S.; Niedzialek, D.; Cornil, J.; Beljonne, D.; Friend, R. H., The role of driving energy and delocalized states for charge separation in organic semiconductors. *Science* **2012,** *335* (6074), 1340-1344.
44. Bakulin, A. A.; Dimitrov, S. D.; Rao, A.; Chow, P. C. Y.; Nielsen, C. B.; Schroeder, B. C.; McCulloch, I.; Bakker, H. J.; Durrant, J. R.; Friend, R. H., Charge-Transfer State Dynamics Following Hole and Electron Transfer in Organic Photovoltaic Devices. *J. Phys. Chem. Lett.* **2013,** *4* (1), 209-215.
45. Cahen, D.; Kahn, A., Electron Energetics at Surfaces and Interfaces: Concepts and Experiments. *Adv. Mater.* **2003,** *15* (4), 271-277.
46. Ishii, H.; Sugiyama, K.; Ito, E.; Seki, K., Energy Level Alignment and Interfacial Electronic Structures at Organic/Metal and Organic/Organic Interfaces. *Adv. Mater.* **1999,** *11* (8), 605-625.
47. Seki, K.; Kanai, K., Development of Experimental Methods for Determining the Electronic Structure of Organic Materials. *Mol. Cryst. Liq. Cryst.* **2006,** *455* (1), 145-181.

48. Dandrade, B.; Datta, S.; Forrest, S.; Djurovich, P.; Polikarpov, E.; Thompson, M., Relationship between the ionization and oxidation potentials of molecular organic semiconductors. *Org. Electron.* **2005,** *6* (1), 11-20.
49. Djurovich, P. I.; Mayo, E. I.; Forrest, S. R.; Thompson, M. E., Measurement of the lowest unoccupied molecular orbital energies of molecular organic semiconductors. *Org. Electron.* **2009,** *10* (3), 515-520.
50. Ryno, S. M.; Fu, Y.-T.; Risko, C.; Brédas, J.-L., Polarization Energies at Organic–Organic Interfaces: Impact on the Charge Separation Barrier at Donor–Acceptor Interfaces in Organic Solar Cells. *ACS Applied Materials & Interfaces* **2016,** *8* (24), 15524-15534.
51. Ryno, S. M.; Risko, C.; Brédas, J.-L., Impact of Molecular Packing on Electronic Polarization in Organic Crystals: The Case of Pentacene vs TIPS-Pentacene. *J. Am. Chem. Soc.* **2014,** *136* (17), 6421-6427.
52. Ryno, S. M.; Risko, C.; Brédas, J.-L., Impact of Molecular Orientation and Packing Density on Electronic Polarization in the Bulk and at Surfaces of Organic Semiconductors. *ACS Applied Materials & Interfaces* **2016,** *8* (22), 14053-14062.
53. Dutton, G.; Quinn, D. P.; Lindstrom, C. D.; Zhu, X. Y., Exciton dynamics at molecule-metal interfaces: C60/Au(111). *Phys. Rev. B* **2005,** *72* (4), 045441.
54. Muntwiler, M.; Yang, Q.; Tisdale, W. A.; Zhu, X. Y., Coulomb Barrier for Charge Separation at an Organic Semiconductor Interface. *Phys. Rev. Lett.* **2008,** *101* (19), 196403.
55. Zhu, X. Y., Photoemission from excitons in organic semiconductors. *J. Electron. Spectrosc. Relat. Phenom.* **2015,** *204, Part A*, 75-79.
56. Ren, G.; Schlenker, C. W.; Ahmed, E.; Subramaniyan, S.; Olthof, S.; Kahn, A.; Ginger, D. S.; Jenekhe, S. A., Photoinduced Hole Transfer Becomes Suppressed with Diminished Driving Force in Polymer-Fullerene Solar Cells While Electron Transfer Remains Active. *Adv. Funct. Mater.* **2013,** *23* (10), 1238-1249.

Chapter 3. Synthesis and Characterization of Heptazine Derivatives

This chapter will cover the synthesis procedures used for making a heptazine derivative studied throughout this work and an overview of the photophysical characterization. These general synthesis and characterization procedures are currently being used to in our lab to also make and study other derivatives; this work remains ongoing. The end of the chapter will discuss the unusual singlet-triplet inversion found in heptazine along with implications of this unique photophysical property.

3.1 Synthesis of Tri-Anisole Heptazine (TAHz)

Synthesis of bulk carbon nitride: Urea (10 g) was heated in a porcelain crucible (20 mL) using a potter's kiln at 500 °C for 3 h, with a ramp rate of 30 °C per hour under ambient atmosphere. The light yellow product was ground thoroughly with a mortar and pestle before use.

Synthesis of potassium cyamelurate: 4.5 g of bulk carbon nitride was refluxed in 150 mL of 3.0 M KOH for 6 h. The solution was filtered over a glass frit while still warm and then put in the fridge to cool and recrystallize. The resulting white crystals were filtered over a glass frit and washed with cold (-10 °C) ethanol. CNMR in D_2O showed two sharp peaks at 168 and 158 ppm respectively. Adapted from reference 1.[1]

Synthesis of cyameluric chloride:

* Safety note: $POCl_3$ and PCl_5 react with water exothermically to produce HCl gas and H_3PO_4. Keep these reagents in a ventilated chemical fume hood at all times and quench carefully.

A volume of 35 mL of $POCl_3$ was added to a flame-dried 100 mL round-bottom flask with a stir bar. 4.6 g of PCl_5 was added and allowed to stir for ~5 minutes. 2.0 g of 2 was added and refluxed

under N_2 at 110°C for 6 hrs. Reaction was removed from heat and let cool. $POCl_3$ was removed under reduced pressure using a distillation set-up in the hood, and the 100 mL round bottom used to catch the distilled $POCl_3$ was placed in an ice water bath. $POCl_3$ was moved to a large beaker and quenched with sodium bicarbonate. Meanwhile, the remaining product and PCl_5 was lowered into an ice water bath, and 50 mL of ice cold water was added dropwise and stirred for 5 minutes. This is to quench the remaining PCl_5, however in the presence of water and heat the product will hydrolyze to an undesired side-product, so the flask was kept on ice. The product was filtered using vacuum filtration onto a cold fine glass frit or PVDF filter and washed with cold water. Resulting product was transferred to a flame-dried vial and dried in a vacuum oven at 100°C for a few hours. FT-IR was used to qualitatively assess the extent of hydrolysis resulting in terminal hydroxyls. If significant intensity was observed at 3,000 cm^{-1} by FTIR, then the product was reintroduced to the chlorination conditions. If the FTIR indicated negligible hydroxyl content, then the product was stored in a desiccator in the freezer.

Synthesis of 2,5,8-tris(4-methoxyphenyl)-1,3,4,6,7,9,9b-heptaazaphenalene (TAHz): 10 mL of anisole was purged in a flame-dried 50 mL round bottom flask. 4.0 g of $AlCl_3$ was added to the flask and allowed to stir for a few minutes at 60°C. 1 g of cyameluric chloride was added slowly over 30 minutes. The reaction mixture was stirred at 60°C under nitrogen and turned a deep red. After 5 hours the flask was removed from heat, and 25 mL DI H_2O was added. This was returned to heat and allowed to stir until the color changed to yellow and the large chunks had dissolved. The resulting bright yellow powder was filtered and washed with water. The product was purified by recrystallizing in hot DMSO (~3 mg/mL). First, about 200 mg of product was added to an Erlenmeyer flask and kept warm using a heat gun. The solution turned transparent after several minutes of heating. Any undissolved material was filtered out using a fine glass frit (this is to

remove oligomeric species). The resulting filtrate was reheated to completely dissolve the product again and moved to an oil bath at 50°C. The temperature was turned down slowly over the course of a day and the product was filtered the next day. Adapted from reference 1.[1]

Scheme 3-1 TAHz synthesis

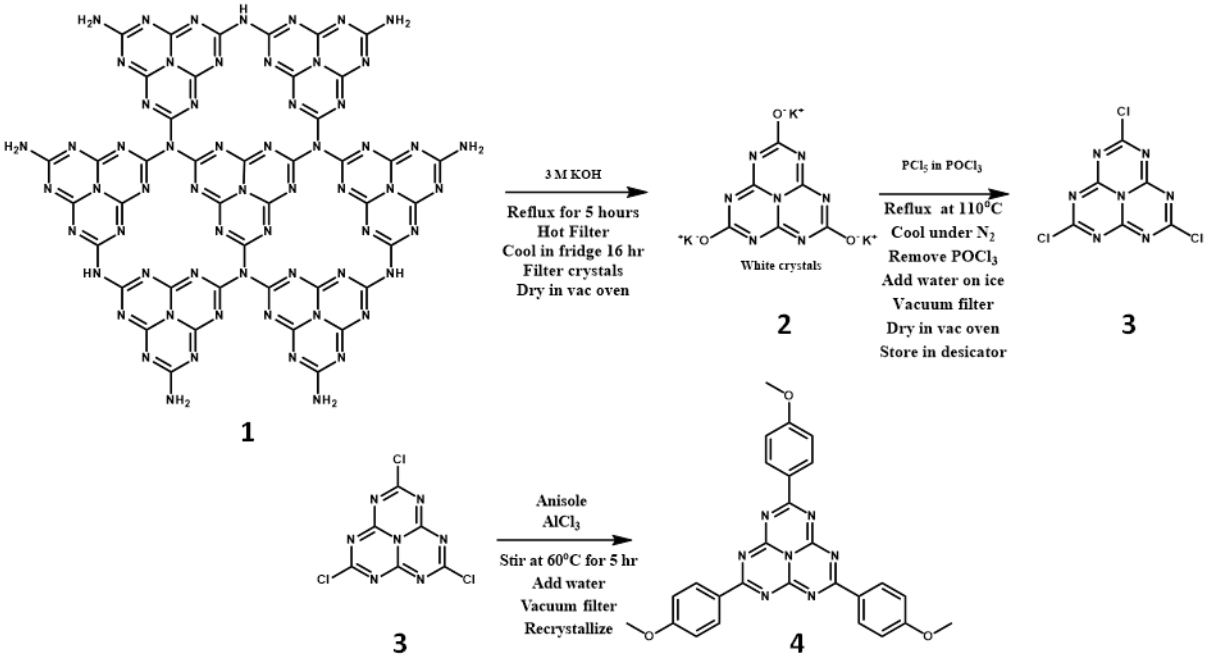

3.2 CHARACTERIZING TAHZ STRUCTURE

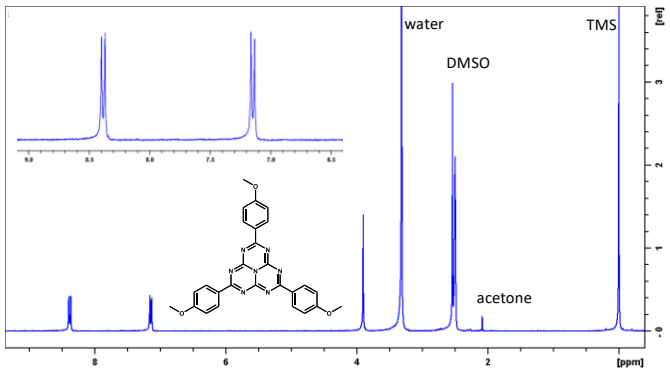

Figure 3-1. TAHz HNMR

[1]HNMR for TAHz taken in d6-DMSO. Peaks at 3.3, 2.5, 2.1 and 0.0 ppm correspond to water, DMSO (solvent), acetone, and TMS respectively. Singlet at 3.90 ppm corresponds to methyl

hydrogens, doublets at 7.14 and 8.38 correspond to aromatic hydrogens, and gives relative integration of 9:6:6, respectively. Inset shows the aromatic peaks with clear doublet splitting.

[1]HNMR: TAHz is dissolved in deuterated DMSO (d6) via vigorous heating. Figure 3-1 shows the three characteristic peaks of TAHz in the [1]HNMR: two doublets in the aromatic region and one singlet at 3.90 ppm corresponding to the methyl groups. Note that crude TAHz shows small peaks near these due to, presumably, singly or doubly substituted heptazines.

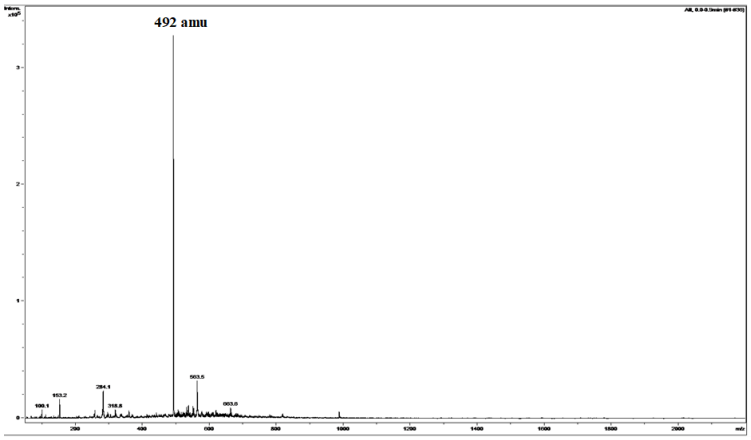

Figure 3-2. TAHz ESI

Electrospray ionization mass spectrum for TAHz dissolved in a 1:1 ratio of toluene:methanol. Peak centered at 492.5 amu (TAHz + 1). Peaks near baseline were observed in initial blank run and correspond to contaminants on the column.

Electrospray ionization mass spectrometry (ESI): Due to the limited solubility of TAHz, solution-phase [13]CNMR is not possible. Instead, to confirm that the major product is indeed the tri-substituted, we use ESI mass spectrometry. Because TAHz is not soluble in traditional ESI solvents, TAHz is first dissolved in toluene then mixed 50:50 with methanol with a drop of acetic acid. Figure 3-2 clearly shows the desired 492 amu (TAHz+ H^+) peak as the tallest feature. While this does not exclude other species from being present, in conjunction with [1]HNMR, it is reasonable to assume TAHz is present and is reasonably pure; ESI would likely show easily ionizable molecules, such as unfunctionalized heptazine cores and [1]HNMR would show impurities

with protons. It is important to note TAHz appears to degrade in the presence of light and methanol, resulting in a 600 amu peak. This peak corresponds to TAHz (491 amu) + anisole (108 amu) + H^+ (1 amu). Oddly enough we see the same phenomenon when instead of anisole, we use Friedel crafts to install a tolyl- or phenyl-group (expected mass + aromatic group + proton). I have not yet figured out what is happening to cause this.

3.3 Understanding the Excited State Landscape of TAHz

At first glance, or months of glances, the photophysics of TAHz seem incredibly strange: a large shift between peak absorption and emission (800 meV), high photoluminescent quantum yield (>50%), and long luminescent lifetime (~300 ns) that is invariant to the presence of oxygen. This section walks through how we made sense of these observations. The 800 meV shift between peak absorption and emission of TAHz, Figure 3-3C, is attributed to internal conversion to a weakly emitting state. The gaussian fits to the emission (Figure 3-4A) and low energy absorption (Figure 3-4B) are shown, and the intersection of the normalized spectra is taken to be the E_{00} transition, or singlet energy.

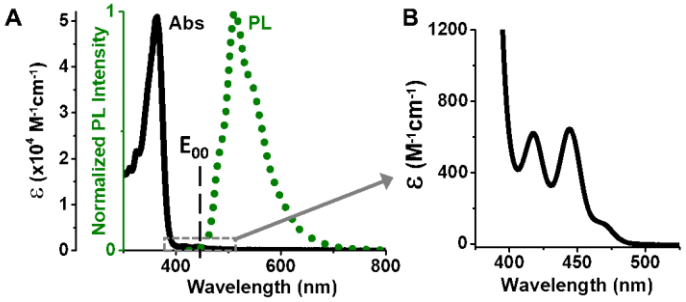

Figure 3-3. TAHz absorption and emission

A) TAHz optical extinction spectrum (solid, λ_{max}=365 nm) and PL spectrum (dotted, λ_{max}=505 nm) for a 33 μM TAHz solution in toluene. B) Extinction spectrum of weakly-allowed features at lower energy attributed to weakly allowed mixed $n\pi^*/\pi\pi^*$ states.

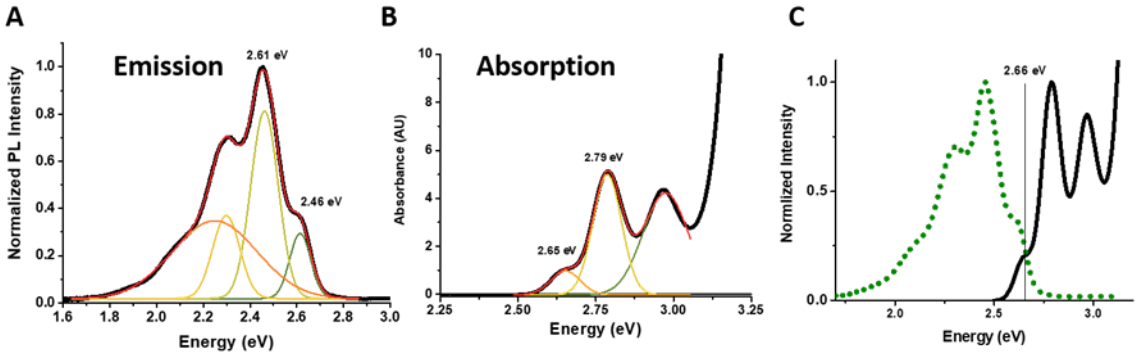

Figure 3-4. Determining the S_1 energy

A) Gaussian fits to TAHz PL in toluene showing the high energy vibronic features roughly 150 meV apart. B) Gaussian fits to TAHz in toluene showing the low energy features are split by roughly 140 meV. C) Normalized absorption and emission spectra assuming the low energy shoulder of the absorption is vibronic and not a separate transition.

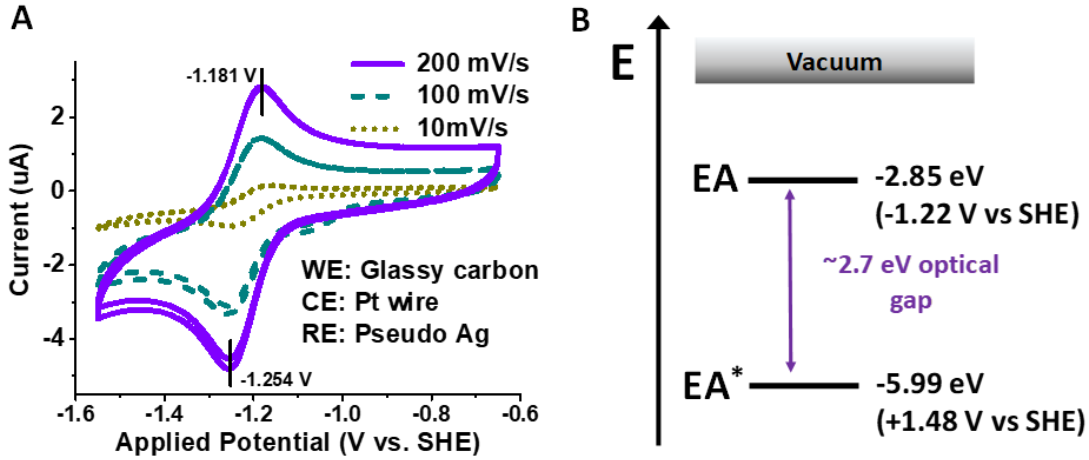

Figure 3-5. TAHz electrochemistry

A) Cathodic cyclic voltammogram of 475 μM TAHz in THF with 250 mM $TABPF_6$ as the supporting electrolyte. The reversible reduction allows us to calculate the E_{red} to be -1.22 V vs SHE. This allows us to calculate the electron affinity (EA) and excited state electron affinity (EA*) shown in B.

Given this S_1 energy, we used electrochemistry to understand where these levels sit on an energy scale relative to vacuum. Cyclic voltammograms of TAHz in THF taken inside an argon glovebox are shown in Figure 3-5A. The 73 mV peak separation suggests this reduction is reversible. From

this reduction CV we can estimate the electron affinity (EA), which corresponds to the LUMO, to be -2.85 eV relative to vacuum.[2] Using the singlet energy, we can estimate the excited state electron affinity (EA*) to be -5.99 eV relative to vacuum. This energy landscape is depicted in Figure 3-5B. The EA* represented the driving force for one-electron water oxidation of the photoexcited TAHz molecule.

To verify this assignment, we explored other plausible origins, including emission from an aggregate or triplet state. Since TAHz is a planar aromatic molecule and has minimal solubility, we first explored the possibility of aggregation. To determine if the low energy absorption peak was due to aggregate absorption, UV-vis measurements were taken over a range of concentrations shown in Figure 3-6A, and the linearity of the absorption with respect to concentration suggests this is not due to aggregation. Additionally, as the concentration was decreased by an order of magnitude, the PL spectral shape did not change, nor was a new emission peak at higher energies observed, Figure 3-6B.

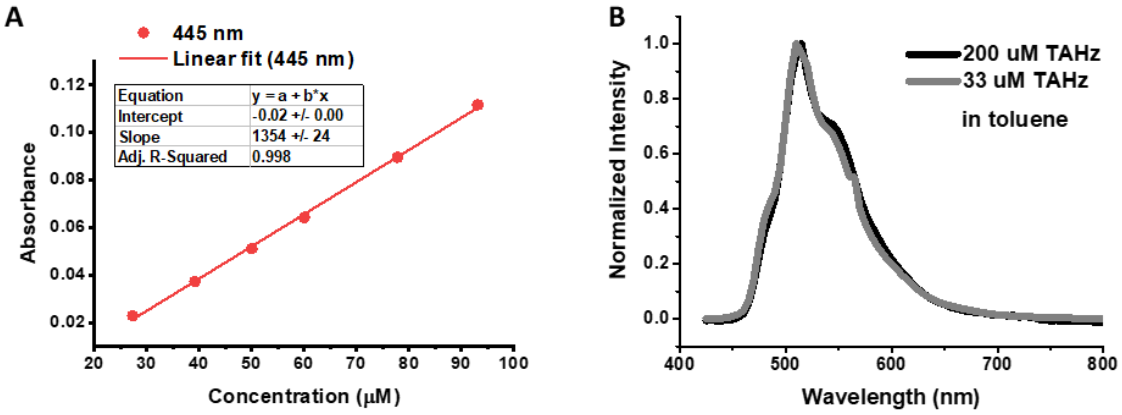

Figure 3-6. Concentration dependent absorption and emission

A) Plot of absorbance at 445 nm versus concentration of TAHz in toluene showing a linear relationship suggesting this absorption peak is not due to aggregation. B) Steady-state PL spectra for TAHz in toluene in at 200 μM (black) and 33 μM (grey) concentrations showing no significant spectral change.

Furthermore, temperature-dependent UV-vis were taken from 25-80°C shown in Figure 3-7A, and no significant change in intensity was observed for the low energy peak, except for a broadening of the main absorption. If this were aggregate emission, we would expect the intensity to drop dramatically upon increasing temperature. We do observe a decrease in PL intensity upon heating to 80°C, but this is likely due to increased rate of non-radiative decay rather than a decrease in aggregation, shown in Figure 3-7B.

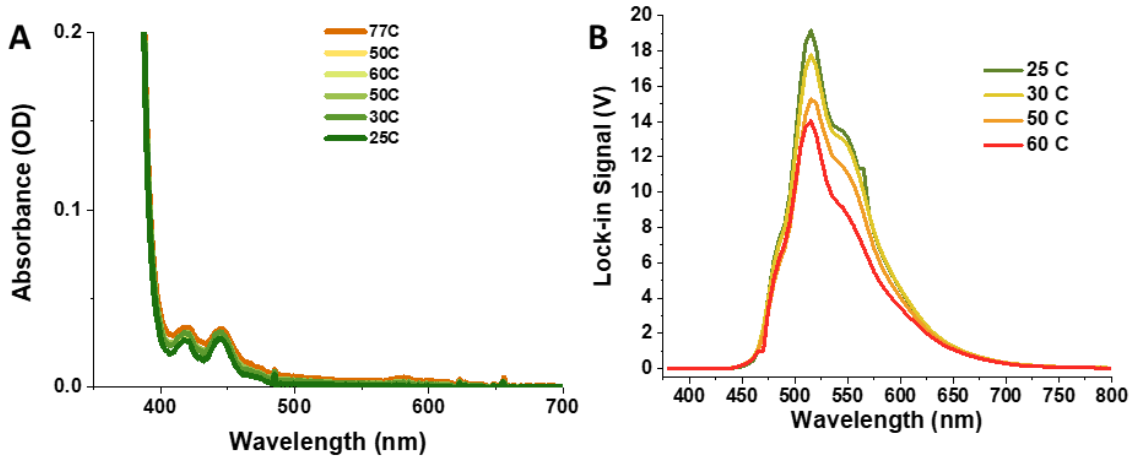

Figure 3-7. Temperature dependent absorption and emission

Temperature dependent absorption (A) and emission (B) of 33 μM TAHz in toluene. Aside from a slight broadening and increase in absorption with increasing temperature, little change is observed. We would expect a significant increase in absorption with increasing temperature if the absorption was due to aggregation. PL intensities decreased significantly with increasing temperature. This is expected as non-radiative decay rates increase with increasing thermal energy. However, no new higher energy emission was observed.

Computational Studies: The ground-state equilibrium geometries of TAHz and the reference molecule heptazine were determined with the second-order Møller-Plesset (MP2) method. Vertical electronic excitation energies and oscillator strengths were computed with the second-order algebraic-diagrammatic-construction (ADC(2)) method, which is a computationally efficient single-reference propagator method.[3] The correlation-consistent split-valence double-ζ basis set

with polarization functions on all atoms (cc-pVDZ)[4] was employed in these calculations. The MP2 and ADC(2) calculations were carried out with the TURBOMOLE program package,[5] making use of the resolution-of-the-identity (RI) approximation[6] for the evaluation of the electron-electron repulsion integrals.

The vertical excitation energies and oscillator strengths of the lowest four excited singlet states of the isolated heptazine molecule are given in Table 3-1. The excitation spectrum in the energy range of interest consists of a low-lying $^1\pi\pi^*$ excited state at 2.57 eV ($^1A_1'$), two $^1n\pi^*$ excited states near 3.8 eV, one of which is degenerate ($^1A_2''$, $^1E''$), and the second $^1\pi\pi^*$ excited state at 4.43 eV which is degenerate ($^1E'$). While the low-lying $^1\pi\pi^*$ excited state ($^1A'$) is dark in absorption, the second $^1\pi\pi^*$ excited state ($^1E'$) carries a large oscillator strength (0.54). The $^1n\pi^*$ states are dark. It is noteworthy that the lowest three excited electronic states of the heptazine chromophore are dark. However, the nominally forbidden S_0-S_1, S_0-S_2, and S_0-S_3 transitions can borrow intensity from the strongly allowed S_0-S_4 transition *via* vibronic coupling.

Table 3-1. Vertical transitions of Hz

State	Energy	*f*
$^1A_1'$ ($\pi\pi^*$)	2.57	0.000
$^1A_2''$ ($n\pi^*$)	3.76	0.000
$^1E''$ ($n\pi^*$)	3.84	0.000
$^1E'$ ($\pi\pi^*$)	4.43	0.536

Symmetry labels refer to D_{3h} point group

Table 3-2. Vertical transitions of TAHz

State	Energy	*f*
^1A ($\pi\pi^*$)	2.62	0.0
^1E ($\pi\pi^*$)	3.62	2.378
^1A ($n\pi^*$)	3.66	0.0
^1E ($n\pi^*$)	3.79	0.0

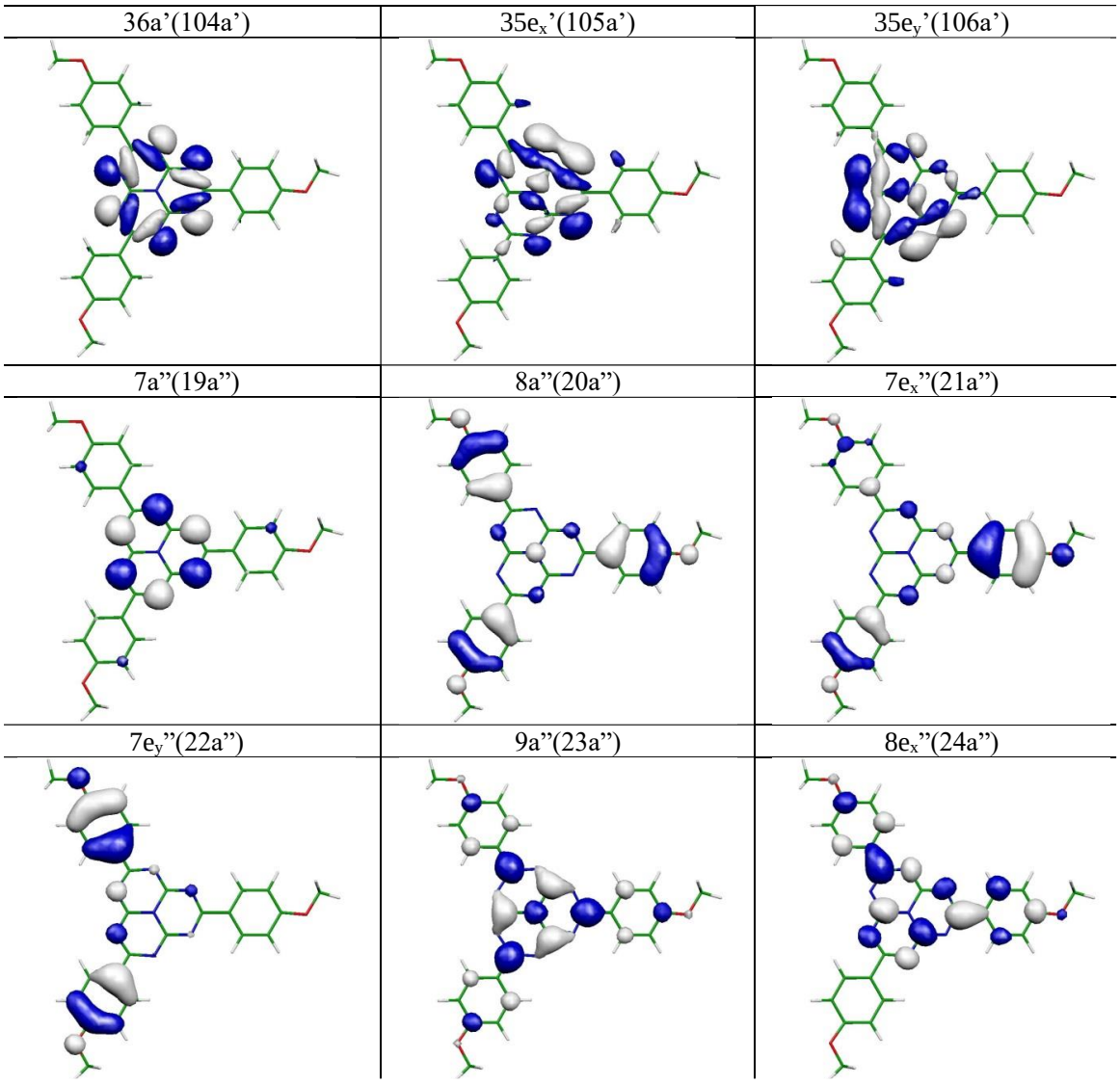

Figure 3-8. Hartree-Fock molecular orbitals of TAHz.

Hartree-Fock molecular orbitals involved in the excitation of the lowest excited electronic singlet states of TAHz. The orbitals 104a' – 106a' (first row) are n-orbitals; the orbitals 19a" – 22a" are occupied π-orbitals; the orbitals 23a", 24a" are unoccupied π-orbitals.

The calculated vertical excitation energies and oscillator strengths of the lowest four excited singlet states of TAHz are given in Table 3-2. The highest occupied and lowest unoccupied molecular orbitals involved in the excitation of these states are displayed in Figure 3-8. These orbitals allow the correlation of the excitation spectrum of TAHz with the excitation spectrum of

heptazine. Remarkably, the excitation energy of the lowest $^1\pi\pi^*$ state of TAHz (2.62 eV) is nearly identical with that of heptazine (2.57 eV). Indeed, the character of this state is a nearly pure 19a" → 23a" excitation, that is, a $\pi \rightarrow \pi^*$ excitation localized the heptazine core of TAHz, see Figure 3-8. The excitation energy of the second $^1\pi\pi^*$ state of TAHz, on the other hand, is lower than the excitation energy of the corresponding state of heptazine by about 0.8 eV (see Table 3-1 and Table 3-2). This excited state consists mainly of excitations from the substituent-centered π-orbitals 20a", 21a" to the π*-orbital of heptazine (23a"), see Figure 3-8. This state therefore has intramolecular charge-transfer character (from the substituents towards the center). It also has excitonic character, as shown by the drastically increased oscillator strength (*f* = 2.38) compared to heptazine. The nπ* states are excitations from the three n-orbitals of the heptazine core to the π* orbital of the heptazine core. Their energies therefore are rather similar to those of heptazine. In TAHz, the ^{1}nπ* states are nearly degenerate with the second $^1\pi\pi^*$ state. ADC(2) predicts the ^{1}nπ* states slightly above the bright second excited singlet state (^{1}E') (see Table 3-2), while the ^{1}nπ* states of TAHz have been observed to be slightly below the bright $^1\pi\pi^*$ state in toluene (Figure 4-1B). This deviation from experiment is within the expected accuracy of the excitation energies calculated with the ADC(2) method, which is estimated as 0.3 eV.[3]

An unusual feature of the excitation spectrum of TAHz is the large (for a molecule of this size) energy gap of about 1.0 eV between the S_1 state and the next higher excited singlet states. By the so-called energy-gap law, this feature reduces the rate of internal conversion from the S_n states to the S_1 state and thus favors fluorescence from the S_n states (in violation of Kasha's rule).

Unfortunately, we were not able to compute the vertical excitation energies of the hydrogen-bonded complex of TAHz with one or several water molecules. The loss of symmetry and the need of a more extended basis set render these computations unfeasible with the computational

resources which are available to us. Therefore, the proton-coupled electron transfer *via* the water-to-TAHz charge-transfer state has to be discussed by analogy to the available results for the photochemistry of the triazine-H_2O and heptazine-H_2O complexes.[7-8]

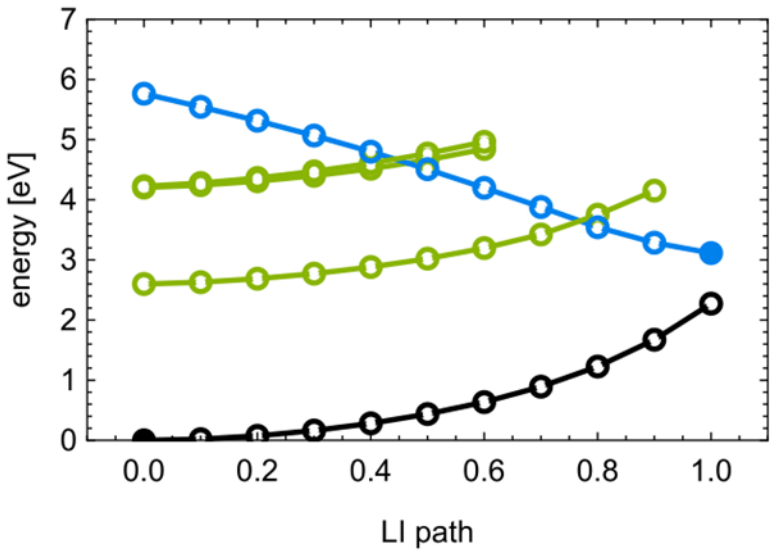

Figure 3-9. Energy profiles of the Hz-water complex.

Energy profiles of the lowest $^1\pi\pi^*$ state and the second $^1\pi\pi^*$ state (green) of the heptazine-water complex along the linearly interpolated (LI) proton-transfer reaction path between the ground-state equilibrium geometry of the complex (left, full black circle) and the optimized geometry of the charge-transfer state at R_{OH} = 1.2 Å (right, full blue circle). The water-to-heptazine charge-transfer state (blue) is stabilized by the transfer of the proton and crosses the energies of the two $^1\pi\pi^*$ states (green). An upper bound of 0.4 eV is estimated for the barrier resulting from the crossing of the charge-transfer state with the higher $^1\pi\pi^*$ state. The degeneracy of the second $^1\pi\pi^*$ state is slightly lifted by the hydrogen-bonded water molecule. For clarity, the $^1n\pi^*$ states located in between the two $^1\pi\pi^*$ states are not shown. Adapted from Reference 8.

A computational result for the heptazine-H_2O complex which is of immediate interest for the interpretation of the present results for TAHz in water is shown in Figure 3-9. An approximate (not fully optimized) reaction path from the ground-state equilibrium geometry of the hydrogen-bonded heptazine-H_2O complex to the relaxed geometry of the lowest charge-transfer state (from H_2O to heptazine) of $^1p_z\pi^*$ character, where p_z denotes the p orbital of H_2O perpendicular to the molecular plane and π^* is the LUMO of heptazine, was constructed by linear interpolation in

Cartesian coordinates. Along this reaction path, the energy profiles of the dim $^1\pi\pi^*$ state and the bright $^1\pi\pi^*$ state (green) are crossed by the energy profile of the reactive charge-transfer state (blue). The curve crossings in Figure 3-9are actually multi-dimensional conical intersections of the adiabatic potential-energy surfaces. The crossing of the upper (bright) $^1\pi\pi^*$ state with the charge-transfer state occurs approximately 0.4 eV above the vertical excitation energy of the former. The energy of this crossing is an upper limit to the actual height of the reaction barrier for excited-state proton transfer from water to heptazine. By this intermolecular reaction, the fluorescence of the bright $^1\pi\pi^*$ state is quenched.

3.4 Singlet-Triplet Inversion in Heptazine

It is textbook knowledge that the lowest triplet excited state (T_1) is located below the lowest singlet excited state (S_1) in closed-shell organic molecules, an example of Hund's multiplicity rule.[9-10] This rule is taken into account in the well-known Jablonski diagram which predicts that the S_1 state can be depopulated by spin−orbit-induced intersystem crossing (ISC) to the lower-lying triplet states. For excited states with the same orbital composition, the S_1/T_1 energy gap is determined by the exchange integral, which in general is large in organic chromophores at their ground-state equilibrium geometry and stabilizes the T_1 state relative to the S_1 state. In extended conjugated systems, the energy of the T_1 state can be lower than the energy of the S_1 state by an electron volt or more.[11] According to current knowledge, there exist few, if any, stable aromatic molecules which violate Hund's multiplicity rule for their S_1 and T_1 states. Koseki et al. found a violation of Hund's multiplicity rule for the nonalternant hydrocarbons propalene, pentalene, and heptalene with Pariser−Parr−Pople (PPP) configuration interaction (CI) calculations when the

structures were constrained to have high (D_{2h}) symmetry.[12] However, the S_1/T_1 inversion disappears at the relaxed (C_{2h}) symmetry of these systems.

It has been noted that the exchange integral can become very small when the highest occupied molecular orbital (HOMO) and the lowest unoccupied molecular orbital (LUMO) are spatially nonoverlapping. In such cases, near degeneracy of the S_1 and T_1 states can be expected. This applies, in particular, for charge-transfer (CT) excited states in extended systems[13-16] and for biradicals.[17-18] Nearly degenerate S_1 and T_1 states are favorable for organic optoelectronics, because so-called thermally activated delayed fluorescence may lead to a significant enhancement of the quantum efficiency of organic light-emitting diodes (OLEDs).[19-20] This discovery motivated the synthesis of a large variety of supramolecular systems with low-lying CT states with nonoverlapping HOMOs and LUMOs.[21-22]

In collaboration with the Domcke and Sobolewski groups, we have both computational and experimental evidence for the inversion of the S_1 and T_1 states for a comparatively simple and compact heptazine (1,3,4,6,7,9,9b-heptaazaphenalene or tri-s-triazine) molecule ($C_6N_7H_3$). In heptazine (Hz), the S_1/T_1 near degeneracy arises from the peculiar and rigid nuclear geometry as well as from a specific and unusual structure of the HOMO and the LUMO. The HOMO is exclusively located on the six peripheral nitrogen atoms of Hz, whereas the LUMO is exclusively located on the six carbon atoms and the central nitrogen atom. The HOMO−LUMO excitation therefore is an "internal" CT excitation in this chromophore, which results in a near-zero exchange integral. As discussed below, the stabilization of the S_1 state by spin polarization[12, 23] leads to S_1/T_1 inversion. The elimination of the ISC deactivation channel of the S_1 state of Hz by S_1/T_1 inversion has obvious implications for two large and active research areas: organic optoelectronics[19, 22] and water-oxidation photocatalysis.[24-26] While Hz-derived materials were occasionally tested for

OLEDs and received vast attention as photocatalysts for hydrogen evolution by water splitting, the potential of S_1/T_1 inversion in the Hz chromophore has not been recognized so far and therefore has not been systematically exploited in either research area.

3.4.1 *Computational Results*

Method. The ground-state equilibrium geometries of Hz and several derivatives of Hz were optimized with the second-order Møller−Plesset (MP2) method. The structures are planar and exhibit D_{3h} symmetry. The vertical excitation energies of the singlet and triplet excited states were computed with four wave-function-based electronic-structure methods and with time-dependent density functional theory (TDDFT). We employed a single-reference propagator method (second-order algebraic diagrammatic construction (ADC(2)),[26] two single-reference coupled-cluster methods (approximate second-order coupled cluster (CC2)[27] and equation-of-motion singles-and-doubles coupled cluster (EOM-CCSD)[28]), and a multiconfiguration self-consistent field multireference perturbation method (CASSCF/ CASPT2).[29] The active space for the CASSCF calculations for Hz consisted of 12 electrons in 12 orbitals, five occupied and five unoccupied π orbitals as well as the highest occupied n orbital and the lowest unoccupied σ orbital. Because the S_1 and T_1 states are nearly pure HOMO (π) to LUMO (π*) excitations, their energies are not sensitive to the choice of the active space. The TDDFT calculations were performed with five widely used exchange−correlation functionals, the three parameter Becke, Lee, Yang, Parr functional (B3LYP),[30-31] the Perdew−Burke−Ernzerhof functional (PBE0),[32] the Minnesota 06 functional (M06-2X),[33] and two range-separated functionals, CAM-B3LYP[34] and ωB97XD,[35] which are specifically designed to describe CT states. The equilibrium geometries of the S_1 and T_1

excited states were optimized with the ADC(2) method, and adiabatic (minimum-to-minimum) excitation energies were calculated.

To characterize the excited-state potential-energy (PE) surfaces in the vicinity of the Franck−Condon (FC) region, linearly interpolated scans in Cartesian coordinates between the S_0, S_1, and T_1 minima were computed. Dunning's correlation-consistent double-ζ basis set (ccpVDZ)[36] was used for all electronic-structure calculations. Calculations for Hz with the triple-ζ basis set (cc-pVTZ) and with the augmented double-ζ basis set (aug-cc-pVDZ) confirmed that the S_1 and T_1 excitation energies are insensitive to extensions of the double-ζ basis set. The MP2, ADC(2), and CC2 calculations were performed with the TURBOMOLE program package.[5] For the EOM-CCSD calculations the QChem program[37] was used. The MOLPRO package32 was used for the CASSCF/CASPT2 calculations. The DFT and TDDFT calculations were performed with either TURBOMOLE or QChem.

Results. The vertical singlet and triplet excitation energies of the two lowest ππ* and the two lowest nπ* states of Hz calculated with the ADC(2) method are given in Table 3-3. In the singlet manifold, the Hz chromophore exhibits a low-lying (2.57 eV) ππ* state of $^1A_2'$ symmetry (S_1), followed by two nπ* states of $^1A_1''$ and $^1E''$ symmetry, respectively (S_2, S_3). The second ππ* state of E′ symmetry (S_4) is located at 4.43 eV excitation energy at the ADC(2) level. While the S_1−S_0 transition is dipole-forbidden in D_{3h} symmetry, the second ππ* state carries significant oscillator strength. In polymeric carbon nitride (melon), the S_1 state is weakly allowed due to vibronic intensity borrowing from higher allowed states as well as slight out-of-plane distortions of the Hz frame. The S_1 absorption can be seen as a faint tail extending to longer wavelengths (≈600 nm). The S_4(ππ*) state gives rise to the pronounced absorption threshold of melon near 400 nm.15 In the triplet manifold, the low-lying $^3A_2'$ state at 2.85 eV (T_1) is followed by the $^3E'$ state (T_2) at 3.67

eV, which is almost 0.8 eV lower in energy than the corresponding singlet state ($_1E'$ (S_4)). The next two states are the nondegenerate $^3A_1''$ state (T_3) and the degenerate $^3E''$ state (T_4); see Table 3-3. No experimental data on the excitation energies of the triplet states of Hz are available. Remarkably, the energy of the S_1 state is below the energy of the T_1 state in Hz. The S_1/T_1 vertical energy gap is defined as $\Delta_{ST} = E_{S1} - E_{T1}$. For Hz, $\Delta_{ST} = -0.28$ eV. For the two $n\pi^*$ states (S_2/T_3 and S_3/T_2), the energies of the singlet and triplet states of the same spatial symmetry are almost degenerate, with the singlet energies being slightly higher than the corresponding triplet energies; see Table 3-3.

Table 3-3. Vertical excitation energies of the lowest four singlet and triplet states of Hz.

Symmetry	Singlet	Triplet
A_2'	2.569	2.851
A_1''	3.758	3.755
E''	3.845	3.819
E'	4.430	3.667

Calculated with ADC(2) method with the cc-pVDZ basis set. The geometry was optimized at the MP2/cc-pVDZ level.

The inverted ordering of the S_1 and T_1 states ($\Delta_{ST} < 0$) in Hz and in derivatives of Hz is the main focus so we will concentrate on the lowest singlet and triplet states in what follows. Both states are nearly pure HOMO−LUMO excitations (the weight of the HOMO− LUMO configuration is 96.4% for S_1, 98.4% for T_1 at the ADC(2) level). The highest occupied and the lowest unoccupied Hartree−Fock orbitals of Hz are displayed in Figure 3-10. It can be seen that the HOMO is exclusively localized on the peripheral nitrogen atoms, while the LUMO is exclusively localized on the carbon atoms and on the central nitrogen atom. As a result of this pattern, the spatial overlap

of HOMO and LUMO is essentially zero. The HOMO−LUMO transition therefore can be considered as an intramolecular CT transition: one electronic charge is transferred from the peripheral nitrogen atoms to the carbon atoms and the central nitrogen atom. Due to D_{3h} symmetry, the electric dipole moments of the ground state and the nondegenerate excited states are zero. A similar effect of short-range charge transfer has also been reported for boron-centered azatriangulene molecules, which exhibit a small but positive singlet−triplet gap and are promising candidates for OLEDs.[38] The lack of spatial overlap of HOMO and LUMO has two consequences: (i) the S_1−S_0 transition dipole moment is unusually small, and (ii) the exchange integral, which is primarily responsible for the singlet−triplet energy gap, is very small, resulting in a near degeneracy of S_1 and T_1 states. In this situation, spin polarization, which stabilizes the singlet state relative to the triplet state,[12, 23] becomes relevant and leads to the inversion of the S_1 and T_1 states; see below.

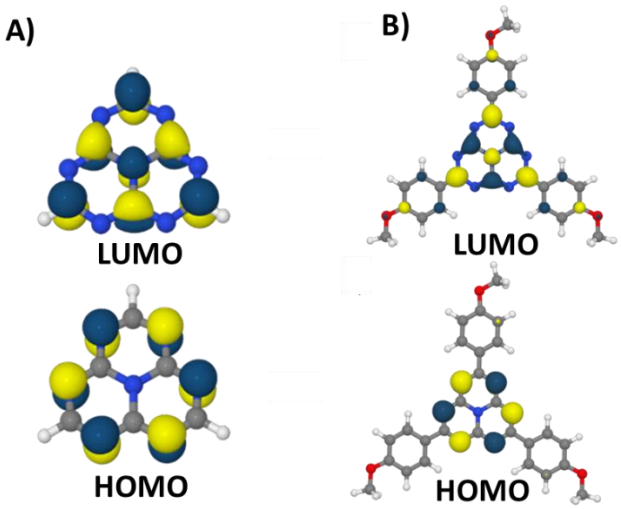

Figure 3-10. HOMO and LUMO orbitals of Hz and TAHz

Highest occupied (HOMO) and lowest unoccupied (LUMO) Hartree-Fock molecular orbitals of Hz.

To confirm the origin of the S_1/T_1 inversion in Hz predicted by ADC(2), we computed the vertical S_1 and T_1 excitation energies with the CC2, EOM-CCSD, and CASSCF/CASPT2 methods. The close agreement of the four ab initio wave function methods based on different approximation schemes for electron correlation reveals that the S_1/T_1 inversion in Hz is not the result of intricate electron correlation effects. This confirms the splitting results from the unusually small exchange and spin polarization.[23] In the restricted orbital picture, spin polarization in the singlet state is reflected by a slightly higher weight of doubly excited configurations (and correspondingly a lower weight of the HOMO−LUMO configuration) in the singlet wave function than in the triplet wave function.[12] This effect is robustly reproduced by all wavefunction-based methods. Interestingly, TDDFT fails to recover these effects. With all five functionals, TDDFT predicts a positive Δ_{ST} of about 0.20 eV. TDDFT therefore cannot be recommended as a computational method for large-scale screening studies for OLED materials.[39] However, the correct (negative) Δ_{ST} of Hz can be obtained by calculating the S_1 and T_1 excitation energies with unrestricted Kohn−Sham DFT, taking advantage of the fact that the $^1A_2'$ and $^3A_2'$ states are the lowest states of their respective symmetries.[40]

The equilibrium geometries of the S_1 and T_1 excited states of Hz were optimized with the ADC(2) method. The adiabatic (minimum-to-minimum) excitation energies of the S_1 and T_1 states are 2.488 and 2.777 eV, respectively. The vibrational stabilization energy therefore is 0.081 eV in the S_1 state and 0.074 eV in the T_1 state. These unusually small vibrational stabilization energies reflect the rigidity of the fused ring structure of Hz. The exceptionally weak electron-vibration coupling in the S_1 and T_1 states is favorable for solar energy harvesting with the Hz chromophore. Additionally, the computed linearly interpolated scans between the ground-state equilibrium geometry and the S_1 and T_1 equilibrium geometries, show essentially parallel energy profiles of

the S_1 and T_1 states. These findings tentatively indicate that the rate of ISC from the T_1 state to the S_1 state of Hz is comparatively small.

With the ADC(2) method, we computed the vertical excitation energies of three derivatives of Hz: trichloroheptazine (TClHz), tricyanoheptazine (TCNHz), and TAHz. For all three derivatives, the HOMO and the LUMO are exclusively localized on the Hz frame and the S_1 and T_1 states are nearly pure HOMO−LUMO transitions in all three derivatives. Correspondingly, the S_1 and T_1 excitation energies of the three derivatives are close to those of Hz, despite the varying electron withdrawing or donating character of the substituents.

3.4.2 *Experimental Results*

One could initially regard the unusually long decay time of the TAHz emission, with τ on the order of 300 ns,[41] as indicating that a long-lived triplet state contributes to the PL lifetime in some manner, for example, by phosphorescence or reverse intersystem crossing and thermally activated delayed fluorescence (TADF). Indeed, depending on the measurement conditions, the phosphorescence lifetime of the ubiquitous triplet material, ruthenium(II) tris-bipyridine $[Ru(bpy)_3]^{2+}$, has been well documented to be on the order of 500−900 ns.[42] We measured the time-dependent PL decay of TAHz in toluene on the microsecond time scale to investigate whether the presence of molecular oxygen, a known triplet quencher, has any influence on the TAHz excited state decay dynamics. The resulting luminescence lifetime data shown in Figure 3-11A demonstrate that we observe only monoexponential decay over two decades in intensity, with no discernible influence on the lifetime from molecular oxygen and no perceptible biphasic character that would imply a contribution from a delayed fluorescence component. The fact that we observe negligible dependence of the emission lifetime on the presence of molecular oxygen, which would quantitatively quench any molecular triplet state T_1 with an energy of >1.0 eV on this time scale,

renders the possibility unlikely that TADF plays any role in extending the PL decay time in TAHz. Interestingly, as Figure 3-11A also demonstrates, the emission lifetime is virtually independent of the presence of external heavy atom sources, such as ethyl iodide (EtI), that are commonly used to sensitize intersystem crossing to populate the T_1 state. The PL quantum yield (PLQY) also exhibits no dependence on the presence of EtI. The fact that introducing an external heavy atom to enhance the intersystem crossing rate constant does not quench the singlet PLQY or lifetime is consistent with the absence of a lower-lying triplet state that would otherwise act as a nonradiative energy sink.

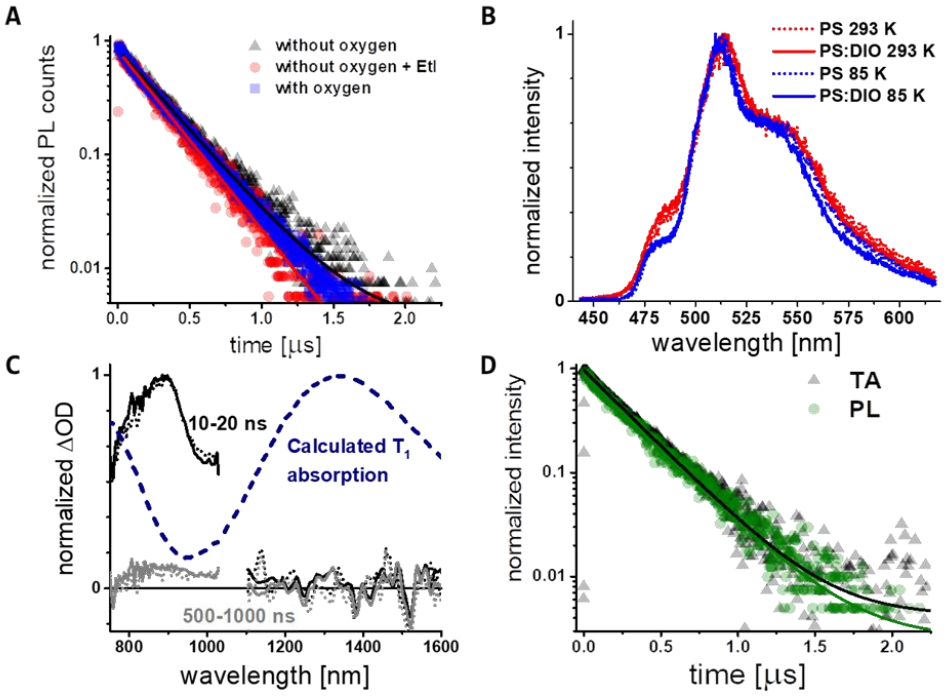

Figure 3-11. The absence of triplets in TAHz PL and TA.

A) Emission lifetimes of TAHz in toluene show very little dependence on the presence of oxygen or a heavy atom. Comparing emissions with (blue) and without oxygen (black), we do not see any evidence of thermally activated delayed florescence. B) The emission spectra of TAHz in toluene with (solid) and without (dotted) a heavy atom present in a polystyrene matrix at 298 K (red) and 80 K (blue) do not show evidence of phosphorescence. C) Transient absorption data with (dotted) and without (solid) a heavy atom present at early (black) and long (grey) timescales shows no significant difference. Notably, we see no long-lived signal in the NIR region where a strong triplet absorption transition is predicted by the calculations (dashed line). D) Decay kinetics of the

photoluminescence (green circles) matches the decay of the prominent spectral feature at 900 nm seen in transient absorption measurements (black triangles), suggesting that we only see the S_1 absorption feature in our TA measurements.

The kinetics data in Figure 3-11A do not provide any spectral information that could report on the possible role of phosphorescence from the T_1 state. To discern whether phosphorescence contributes to the overall TAHz PL signal, we present in Figure 3-11B time-averaged low-temperature PL spectra for TAHz with and without diiodooctane (DIO) as an external heavy atom source. We have previously employed this method in our laboratory to detect extremely weak phosphorescence signatures from organic chromophores that do not exhibit measurable steady-state triplet emission in the absence of an external heavy atom.[43] Nevertheless, in the case of TAHz, the PL spectra that we collect with and without the presence of an external heavy atom are virtually indistinguishable. We observe no evidence for phosphorescence from TAHz, even affixed in an inert polystyrene matrix at low temperatures in the presence of a heavy atom. Therefore, the lack of quenching with EtI in Figure 3-11A cannot be explained by increased phosphorescence.

While our PL measurements indicate that the emission properties of TAHz do not involve a low-lying triplet state, the strong fluorescence signal may mask any contribution from a triplet-associated emission component. Therefore, in order to more clearly reveal how the predicted S_1/T_1 energy inversion manifests in the excited-state dynamics of TAHz, we turned to microsecond transient absorption (TA) measurements. Figure 3-11C shows TA spectra of TAHz in toluene with and without oxygen present at both early and late times. We computed the $S_1 \rightarrow S_n$ and $T_1 \rightarrow T_n$ excitation energies and oscillator strengths with the ADC(2) method to guide our spectroscopic investigation. Looking in the region of the theoretically predicted T_1 absorption, we do not see any measurable induced absorption signal for either sample in Figure 3-11C, while the S_1 absorption near 900 nm is clearly observed. Moreover, Figure 3-11D shows that the decay of the

TA signal overlays with the fluorescence decay. The essentially identical kinetic data for the TA feature and the fluorescence suggest that this feature is attributable solely to the singlet excited state absorption.

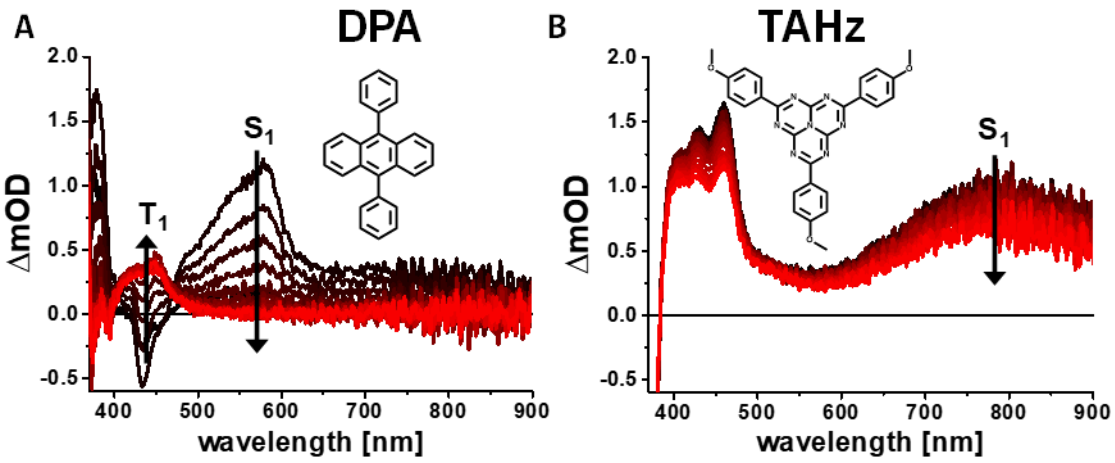

Figure 3-12. DPA and TAHz TA comparison.

Transient absorption spectral traces from 2-100 ns (black to red) for chromophores DPA (A) and TAHz (B) in 1:1 toluene:Br-octane solutions. We observe a clear isosbestic behavior in the case for DPA the singlet absorption at 550 nm is converted to the lower-lying triplet with a characteristic absorption at 450 nm. However, in the case of TAHz, we only see the decrease across the spectral region. The TAHz PL decay matches the decay of the large feature at 800 nm. This suggests that there is no lower-lying triplet for the heavy atom-enhanced intersystem crossing to be formed from the long-lived singlet excited state.

As a means of benchmarking the peculiar photophysical behavior that TAHz exhibits as a result of its inverted S_1/T_1 energy landscape, we compare the excited-state dynamics of TAHz against an archetypal organic fluorophore in the presence of an external heavy atom. We chose diphenyl anthracene (DPA) as a model organic fluorophore due to its well-documented near-unity PLQY, implying that very few triplets are readily formed in DPA under illumination. In the presence of bromooctane, the evolution of the DPA TA signal in Figure 3-12A is markedly different from the spectral evolution that TAHz exhibits in Figure 3-12B. Figure 3-12A shows the transient absorption traces of DPA in a toluene:bromooctane solution ranging from 2 to 100 ns. We observe a clear isosbestic point near 465 nm as the DPA S_1 state relaxes by ISC to the lower energy T_1

state. The DPA S_1 induced absorption signature at 560 nm dominates the DPA TA spectrum at 2 ns in black, but undergoes complete decay by 100 ns, as shown in the red trace. The concomitant rise of the T_1-T_n absorption signal at 450 nm results from the DPA singlets being converted into DPA triplets. Conversely, in Figure 3-12B, TAHz exhibits no clear signs of interconversion among excited states. Instead, we observe only a decrease in the signal amplitude over this spectral range. We do not observe growth of a new state which would accompany conversion to the triplet manifold. The decay kinetics at 450 and 800 nm overlap with the PL decay, suggesting that these features are attributable to the TAHz S_1 absorption. We do not see any long-lived signal intensity near 800 or 1400 nm (see Figure 3-13), as predicted by theory, which would also suggest that we do not see long-lived triplet formation.

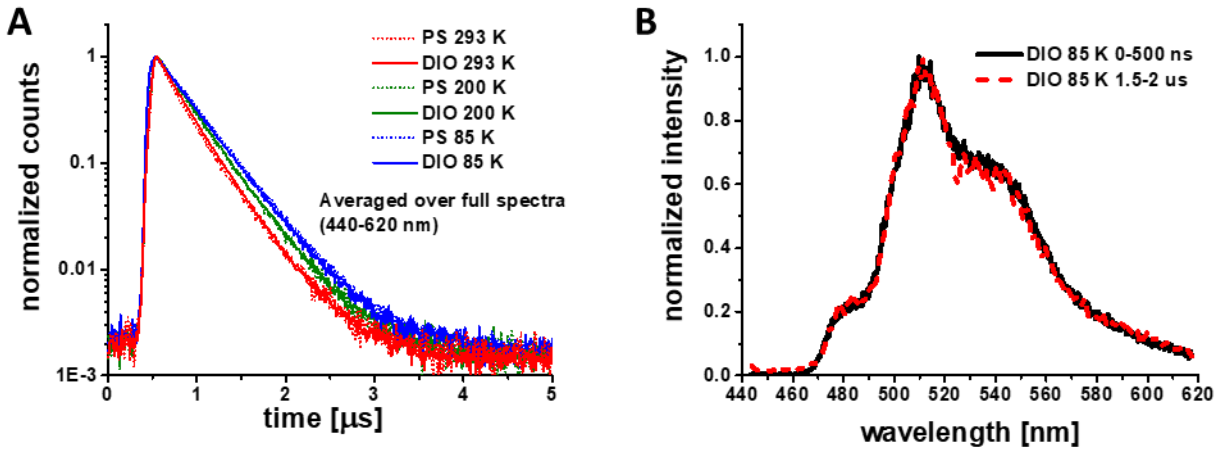

Figure 3-13. Temperature dependent TAHz TR-PL.

A) Kinetic traces of TAHz PL in polystyrene films as described in the main text. The PL lifetime increases slightly as the sample is cooled, 293 K (red), 200K (green), and 85 K (blue), but there is no kinetic difference between samples with (solid) or without diiodooctane (DIO) (dotted). The temperature-dependent kinetics data are inconsistent with thermally activated delayed florescence, since they distinctly exhibit monoexponential decay dynamics, with no indication of a second, longer-lived, kinetic component that would reflect the lifetime of a lower energy triplet excited state. We also observe slightly shorter lifetimes rather than longer lifetimes at warmer temperatures, which is also inconsistent with TADF. B) We see no spectral difference between the emission at early (solid black) or late times (dashed red) of TAHz in the presence of DIO at 85 K, where we would most expect to see phosphorescence.

3.5 REFERENCES

1. Ke, Y.; Collins, D. J.; Sun, D.; Zhou, H.-C., (10,3)-a Noninterpenetrated Network Built from a Piedfort Ligand Pair. *Inorg. Chem.* **2006,** *45* (5), 1897-1899.
2. Djurovich, P. I.; Mayo, E. I.; Forrest, S. R.; Thompson, M. E., Measurement of the lowest unoccupied molecular orbital energies of molecular organic semiconductors. *Org. Electron.* **2009,** *10* (3), 515-520.
3. Trofimov, A. B.; Schirmer, J., An Efficient Polarization Propagator Approach to Valence Electron Excitation Spectra. *Journal of Physics B: Atomic, Molecular and Optical Physics* **1995,** *28* (12), 2299.
4. Jr., T. H. D., Gaussian basis sets for use in correlated molecular calculations. I. The atoms boron through neon and hydrogen. *J. Phys. Chem.* **1989,** *90* (2), 1007-1023.
5. TURBOMOLE *A development of University of Karlsruhe and Forschungszentrum Karlsruhe GmbH, 1989-2007*, TURBOMOLE GmbH since 2007.
6. Hättig, C.; Weigend, F., CC2 excitation energy calculations on large molecules using the resolution of the identity approximation. *J. Phys. Chem.* **2000,** *113* (13), 5154-5161.
7. Ehrmaier, J.; Janicki, M. J.; Sobolewski, A. L.; Domcke, W., Mechanism of photocatalytic water splitting with triazine-based carbon nitrides: insights from ab initio calculations for the triazine-water complex. *Phys. Chem. Chem. Phys.* **2018,** *20* (21), 14420-14430.
8. Ehrmaier, J.; Karsili, T. N. V.; Sobolewski, A. L.; Domcke, W., Mechanism of Photocatalytic Water Splitting with Graphitic Carbon Nitride: Photochemistry of the Heptazine–Water Complex. *J. Phys. Chem. A* **2017,** *121* (25), 4754-4764.
9. Miessler, G. L.; Tarr, D. A., *Inorganic Chemistry*. 4th Edition ed.; 2011.
10. Turro, N. J.; Ramamurthy, V.; Scaiano, J. C., *Principles of Molecular Photochemistry: An Introduction*. University Science Books Sausalito, California, 2009.
11. Birks, J. B., *Photophysics of Aromatic Molecules*. 1970.
12. Koseki, S.; Nakajima, T.; Toyota, A., Violation of Hund's multiplicity rule in the electronically excited states of conjugated hydrocarbons. *Can. J. Chem.* **1985,** *63* (7), 1572-1579.
13. Segal, M.; Singh, M.; Rivoire, K.; Difley, S.; Van Voorhis, T.; Baldo, M. A., Extrafluorescent electroluminescence in organic light-emitting devices. *Nat. Mater.* **2007,** *6* (5), 374-378.
14. Difley, S.; Beljonne, D.; Van Voorhis, T., On the Singlet−Triplet Splitting of Geminate Electron−Hole Pairs in Organic Semiconductors. *J. Am. Chem. Soc.* **2008,** *130* (11), 3420-3427.
15. Zhang, C.-R.; Sears, J. S.; Yang, B.; Aziz, S. G.; Coropceanu, V.; Brédas, J.-L., Theoretical Study of the Local and Charge-Transfer Excitations in Model Complexes of Pentacene-C60 Using Tuned Range-Separated Hybrid Functionals. *J. Chem. Theory Comput.* **2014,** *10* (6), 2379-2388.
16. Bittner, E. R.; Lankevich, V.; Gélinas, S.; Rao, A.; Ginger, D. A.; Friend, R. H., How disorder controls the kinetics of triplet charge recombination in semiconducting organic polymer photovoltaics. *Phys. Chem. Chem. Phys.* **2014,** *16* (38), 20321-20328.
17. De Kanter, F. J. J.; Kaptein, R., CIDNP and triplet-state reactivity of biradicals. *J. Am. Chem. Soc.* **1982,** *104* (18), 4759-4766.
18. Doubleday, C.; Turro, N. J.; Wang, J. F., Dynamics of flexible triplet biradicals. *Acc. Chem. Res.* **1989,** *22* (6), 199-205.

19. Uoyama, H.; Goushi, K.; Shizu, K.; Nomura, H.; Adachi, C., Highly efficient organic light-emitting diodes from delayed fluorescence. *Nature* **2012,** *492* (7428), 234-238.
20. Goushi, K.; Yoshida, K.; Sato, K.; Adachi, C., Organic light-emitting diodes employing efficient reverse intersystem crossing for triplet-to-singlet state conversion. *Nat. Photon.* **2012,** *6*, 253.
21. Tao, Y.; Yuan, K.; Chen, T.; Xu, P.; Li, H.; Chen, R.; Zheng, C.; Zhang, L.; Huang, W., Thermally Activated Delayed Fluorescence Materials Towards the Breakthrough of Organoelectronics. *Adv. Mater.* **2014,** *26* (47), 7931-7958.
22. Jou, J.-H.; Kumar, S.; Agrawal, A.; Li, T.-H.; Sahoo, S., Approaches for fabricating high efficiency organic light emitting diodes. *J. Mat. Chem. C* **2015,** *3* (13), 2974-3002.
23. Kollmar, H.; Staemmler, V., Violation of Hund's rule by spin polarization in molecules. *Theor. Chim. Acta* **1978,** *48* (3), 223-239.
24. Wang, X.; Maeda, K.; Thomas, A.; Takanabe, K.; Xin, G.; Carlsson, J. M.; Domen, K.; Antonietti, M., A Metal-Free Polymeric Photocatalyst for Hydrogen Production from Water Under Visible Light. *Nat. Mater.* **2008,** *8*, 76.
25. Ong, W. J.; Tan, L. L.; Ng, Y. H.; Yong, S. T.; Chai, S. P., Graphitic Carbon Nitride (g-C3N4)-Based Photocatalysts for Artificial Photosynthesis and Environmental Remediation: Are We a Step Closer To Achieving Sustainability? *Chem. Rev.* **2016,** *116* (12), 7159-329.
26. Wen, J. Q.; Xie, J.; Chen, X. B.; Li, X., A Review on g-C3N4-based Photocatalysts. *Appl. Surf. Sci.* **2017,** *391*, 72-123.
27. Christiansen, O.; Koch, H.; Jørgensen, P., The second-order approximate coupled cluster singles and doubles model CC2. *Chem. Phys. Lett.* **1995,** *243* (5), 409-418.
28. Stanton, J. F.; Bartlett, R. J., The equation of motion coupled-cluster method. A systematic biorthogonal approach to molecular excitation energies, transition probabilities, and excited state properties. *J. Phys. Chem.* **1993,** *98* (9), 7029-7039.
29. Andersson, K.; Malmqvist, P. Å.; Roos, B. O., Second-order perturbation theory with a complete active space self-consistent field reference function. *J. Phys. Chem.* **1992,** *96* (2), 1218-1226.
30. Becke, A. D., Density-functional thermochemistry. III. The role of exact exchange. *J. Phys. Chem.* **1993,** *98* (7), 5648-5652.
31. Lee, C.; Yang, W.; Parr, R. G., Development of the Colle-Salvetti correlation-energy formula into a functional of the electron density. *Phys. Rev. B* **1988,** *37* (2), 785-789.
32. Perdew, J. P.; Ernzerhof, M.; Burke, K., Rationale for mixing exact exchange with density functional approximations. *J. Phys. Chem.* **1996,** *105* (22), 9982-9985.
33. Zhao, Y.; Truhlar, D. G., The M06 suite of density functionals for main group thermochemistry, thermochemical kinetics, noncovalent interactions, excited states, and transition elements: two new functionals and systematic testing of four M06-class functionals and 12 other functionals. *Theor. Chem. Acc.* **2008,** *120* (1), 215-241.
34. Yanai, T.; Tew, D. P.; Handy, N. C., A new hybrid exchange–correlation functional using the Coulomb-attenuating method (CAM-B3LYP). *Chem. Phys. Lett.* **2004,** *393* (1), 51-57.
35. Chai, J.-D.; Head-Gordon, M., Systematic optimization of long-range corrected hybrid density functionals. *J. Phys. Chem.* **2008,** *128* (8), 084106.
36. Dunning Jr, T. H., Gaussian basis sets for use in correlated molecular calculations. I. The atoms boron through neon and hydrogen. *J. Chem. Phys.* **1989,** *90*, 1007.
37. Shao, Y.; Gan, Z.; Epifanovsky, E.; Gilbert, A. T. B.; Wormit, M.; Kussmann, J.; Lange, A. W.; Behn, A.; Deng, J.; Feng, X.; Ghosh, D.; Goldey, M.; Horn, P. R.; Jacobson, L. D.;

Kaliman, I.; Khaliullin, R. Z.; Kuś, T.; Landau, A.; Liu, J.; Proynov, E. I.; Rhee, Y. M.; Richard, R. M.; Rohrdanz, M. A.; Steele, R. P.; Sundstrom, E. J.; Woodcock, H. L.; Zimmerman, P. M.; Zuev, D.; Albrecht, B.; Alguire, E.; Austin, B.; Beran, G. J. O.; Bernard, Y. A.; Berquist, E.; Brandhorst, K.; Bravaya, K. B.; Brown, S. T.; Casanova, D.; Chang, C.-M.; Chen, Y.; Chien, S. H.; Closser, K. D.; Crittenden, D. L.; Diedenhofen, M.; DiStasio, R. A.; Do, H.; Dutoi, A. D.; Edgar, R. G.; Fatehi, S.; Fusti-Molnar, L.; Ghysels, A.; Golubeva-Zadorozhnaya, A.; Gomes, J.; Hanson-Heine, M. W. D.; Harbach, P. H. P.; Hauser, A. W.; Hohenstein, E. G.; Holden, Z. C.; Jagau, T.-C.; Ji, H.; Kaduk, B.; Khistyaev, K.; Kim, J.; Kim, J.; King, R. A.; Klunzinger, P.; Kosenkov, D.; Kowalczyk, T.; Krauter, C. M.; Lao, K. U.; Laurent, A. D.; Lawler, K. V.; Levchenko, S. V.; Lin, C. Y.; Liu, F.; Livshits, E.; Lochan, R. C.; Luenser, A.; Manohar, P.; Manzer, S. F.; Mao, S.-P.; Mardirossian, N.; Marenich, A. V.; Maurer, S. A.; Mayhall, N. J.; Neuscamman, E.; Oana, C. M.; Olivares-Amaya, R.; O'Neill, D. P.; Parkhill, J. A.; Perrine, T. M.; Peverati, R.; Prociuk, A.; Rehn, D. R.; Rosta, E.; Russ, N. J.; Sharada, S. M.; Sharma, S.; Small, D. W.; Sodt, A.; Stein, T.; Stück, D.; Su, Y.-C.; Thom, A. J. W.; Tsuchimochi, T.; Vanovschi, V.; Vogt, L.; Vydrov, O.; Wang, T.; Watson, M. A.; Wenzel, J.; White, A.; Williams, C. F.; Yang, J.; Yeganeh, S.; Yost, S. R.; You, Z.-Q.; Zhang, I. Y.; Zhang, X.; Zhao, Y.; Brooks, B. R.; Chan, G. K. L.; Chipman, D. M.; Cramer, C. J.; Goddard, W. A.; Gordon, M. S.; Hehre, W. J.; Klamt, A.; Schaefer, H. F.; Schmidt, M. W.; Sherrill, C. D.; Truhlar, D. G.; Warshel, A.; Xu, X.; Aspuru-Guzik, A.; Baer, R.; Bell, A. T.; Besley, N. A.; Chai, J.-D.; Dreuw, A.; Dunietz, B. D.; Furlani, T. R.; Gwaltney, S. R.; Hsu, C.-P.; Jung, Y.; Kong, J.; Lambrecht, D. S.; Liang, W.; Ochsenfeld, C.; Rassolov, V. A.; Slipchenko, L. V.; Subotnik, J. E.; Van Voorhis, T.; Herbert, J. M.; Krylov, A. I.; Gill, P. M. W.; Head-Gordon, M., Advances in molecular quantum chemistry contained in the Q-Chem 4 program package. *Mol. Phys.* **2015,** *113* (2), 184-215.

38. Pershin, A.; Hall, D.; Lemaur, V.; Sancho-Garcia, J.-C.; Muccioli, L.; Zysman-Colman, E.; Beljonne, D.; Olivier, Y., Highly emissive excitons with reduced exchange energy in thermally activated delayed fluorescent molecules. *Nat. Comm* **2019,** *10* (1), 597.

39. Gómez-Bombarelli, R.; Aguilera-Iparraguirre, J.; Hirzel, T. D.; Duvenaud, D.; Maclaurin, D.; Blood-Forsythe, M. A.; Chae, H. S.; Einzinger, M.; Ha, D.-G.; Wu, T.; Markopoulos, G.; Jeon, S.; Kang, H.; Miyazaki, H.; Numata, M.; Kim, S.; Huang, W.; Hong, S. I.; Baldo, M.; Adams, R. P.; Aspuru-Guzik, A., Design of efficient molecular organic light-emitting diodes by a high-throughput virtual screening and experimental approach. *Nat. Mater.* **2016,** *15* (10), 1120-1127.

40. Ehrmaier, J.; Rabe, E. J.; Pristash, S. R.; Corp, K. L.; Schlenker, C. W.; Sobolewski, A. L.; Domcke, W., Singlet–Triplet Inversion in Heptazine and in Polymeric Carbon Nitrides. *J. Phys. Chem. A* **2019,** *123* (38), 8099-8108.

41. Rabe, E. J.; Corp, K. L.; Sobolewski, A. L.; Domcke, W.; Schlenker, C. W., Proton-Coupled Electron Transfer from Water to a Model Heptazine-Based Molecular Photocatalyst. *J. Phys. Chem. Lett.* **2018,** *9* (21), 6257-6261.

42. Caspar, J. V.; Meyer, T. J., Photochemistry of tris(2,2'-bipyridine)ruthenium(2+) ion (Ru(bpy)32+). Solvent effects. *J. Am. Chem. Soc.* **1983,** *105* (17), 5583-5590.

43. Sulas, D. B.; Rabe, E. J.; Schlenker, C. W., Kinetic Competition between Charge Separation and Triplet Formation in Small-Molecule Photovoltaic Blends. *J. Phys. Chem. C* **2017,** *121* (48), 26667-26676.

Chapter 4. Proton-Coupled Electron Transfer from Water to a Model Heptazine-Based Molecular Photocatalyst

4.1 SUMMARY

To gain mechanistic understanding of heptazine-based photochemistry, we synthesized and studied 2,5,8-tris(4-methoxyphenyl)-1,3,4,6,7,9,9b-heptaazaphenalene (TAHz), a model molecular photocatalyst chemically related to carbon nitride. Based on time-resolved photoluminescence (TR-PL) spectroscopy, we kinetically reveal a new feature that emerges in aqueous dispersions of TAHz. Using global target analysis, we spectrally and kinetically resolve the new emission feature to be blueshifted from the steady state luminescence, and observe a fast decay component exhibiting a kinetic isotope effect (KIE) of 2.9 in H_2O versus D_2O, not observed in the steady-state PL. From ab initio electronic-structure calculations, we attribute this new PL peak to the fluorescence of an upper excited state of mixed $n\pi^*/\pi\pi^*$ character. In water, the KIE suggests the excited state is quenched by proton-coupled electron transfer, liberating hydroxyl radicals that we detect using terephthalic acid. Our findings are consistent with recent theoretical predictions that heptazine-based photocatalysts can participate in proton-coupled electron transfer with H_2O.

4.2 INTRODUCTION

Proton-coupled electron transfer (PCET) reactions are scientifically and technologically relevant for characterizing and controlling energy conversion and storage processes.[1-5] The majority of inter-molecular PCET literature to date focuses on metal-containing complexes,[1-3, 6] with fewer

examples of all-organic heterocyclic aromatics,[7-9] despite their photophysical properties being extensively studied over the past century.[10-14] Historically, researchers have heavily debated the nature of the excited state responsible for the photochemical reactivity of heteroaromatics.[10, 15-19] Recent computational studies suggest inter-molecular excitations involving photon-initiated electron transfer from H-bonded water to aza-aromatics facilitate H-atom abstraction to form neutral radicals.[8, 20-21] These studies highlight the importance of photochemical pathways beyond strictly local excited $n\pi^*$ and $\pi\pi^*$ states. Since PCET from H_2O to a chromophore could lead to photocatalytic water splitting, it is compelling to spectroscopically reexamine the photochemistry of aza-aromatics.

In the field of photocatalytic hydrogen evolution, the heptazine unit has received significant attention due to immense interest in poly(heptazine imides), commonly termed carbon nitride or g-C_3N_4.[22-27] Readily synthesized from cheap and earth-abundant precursors, these materials have emerged as archetypal organic photocatalysts capable of evolving H_2 from water.[24] Numerous studies catalog gains in H_2 production from g-C_3N_4 by altering surface area,[28-29] adding defects,[30-31] and tuning aromatic groups.[32] However, the fundamental mechanism of photocatalytic activity remains largely enigmatic. The inherent structural ambiguity of g-C_3N_4 introduces numerous possible catalytic sites and reactive states. It is, therefore, attractive to examine model molecular systems with well-defined structures to gain mechanistic understanding.[20, 25, 30, 33-35] While the organic light emitting diode community has studied the energy landscape relevant to the emission of aryl-substituted heptazine molecules,[36-37] far less is understood about the photophysics preceding hydrogen evolution using heptazine-based molecules. A recent computational study by Ehrmaier et al. suggests photoexcited hydrogen abstraction from water via a molecular PCET

process can occur in hydrogen-bonded heptazine-water complexes.[20] However, to the best of our knowledge, there has been no spectroscopic verification of those predictions prior to this report.

Inspired by recent reports of photocatalysis from heptazine-based small molecules,[30, 34] we have synthesized tri-anisole heptazine (TAHz) via a Friedel-Crafts reaction (Scheme 3-1 TAHz synthesis) adapted from literature.[38] We selected TAHz for its high photoluminescence quantum yields (PLQY) (Φ_f = 0.69) in non-polar aromatic solvents and long PL lifetimes. These characteristics allow us to perform time-resolved emission quenching studies not possible with common g-C_3N_4 samples, where bulk luminescence is strongly quenched.[25]

Herein, we present luminescence spectra of a higher-lying excited state of TAHz which can serve as reactive intermediate in the photoinduced hydrogen transfer from water to the heptazine core. Our computational results show the electronic excitation spectrum of isolated TAHz consists of a low-lying dipole-forbidden $S_0 \rightarrow S_1(\pi\pi^*)$ transition, two dark $S_0 \rightarrow S_{2,3}(n\pi^*)$ transitions and one exceptionally bright $S_0 \rightarrow S_4(\pi\pi^*)$ transition (*cf.* Chapter 3.3). In toluene, the bright $\pi\pi^*$ state relaxes nonradiatively via intermediate $n\pi^*$ states to the lowest $\pi\pi^*$ state, from which all luminescence occurs. However, in water, the $n\pi^*$ states are up-shifted and the $\pi\pi^*$ state (or quasi-degenerate mixed $n\pi^*/\pi\pi^*$ states) can fluoresce at early times. Scheme 4-1 summarizes the photochemical reaction pathway of a photoexcited TAHz-H_2O complex from this upper excited state. Isotope-dependent luminescence quenching of TAHz in water and $^{\bullet}$OH detection are consistent with PCET from water to TAHz.

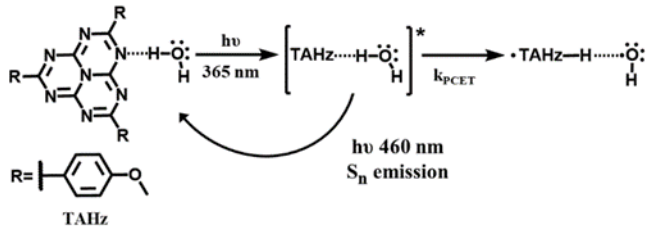

Scheme 4-1 Proposed Photochemical Mechanism

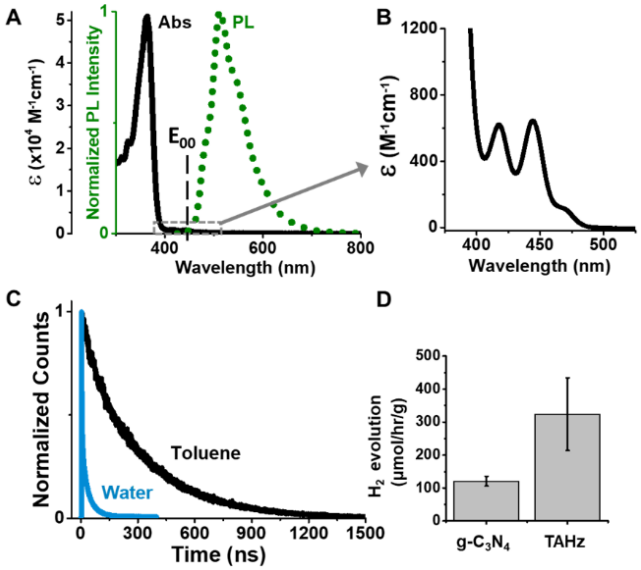

Figure 4-1. TAHz absorption, emission, and hydrogen production.

A) TAHz optical extinction spectrum (solid, λ_{max}=365 nm) and PL spectrum (dotted, λ_{max}=505 nm) for a 33 μM toluene solution. B) Extinction spectrum of weakly-allowed features below the absorption band of the bright ππ* state. C) Time-correlated single photon counting PL traces of TAHz in toluene (black) and water (blue) show dynamic PL quenching of TAHz in water. D) Hydrogen evolution rate for 3 mg TAHz, 15 mL H_2O, 1.5 mL triethanolamine and 2 wt% Pt under 5 mW/cm^2 365 nm LED illumination. H_2 activity of bulk g-C_3N_4 under identical conditions included for reference.

We characterized TAHz in toluene, a non-polar, aprotic solvent to determine the energy landscape of the isolated chromophore. Figure 4-1A shows strong absorption at 365 nm and emission centered at 510 nm. Additionally, we observe lower energy peaks with molar absorptivities (ε) of a few hundred $M^{-1}cm^{-1}$. The nominally dark nπ* states can borrow intensity from the nearby bright ππ* state through vibronic coupling. Assuming luminescence occurs from the lowest weakly allowed (dim) singlet ππ* state, we estimate the $S_1 \rightarrow S_0$ singlet transition energy (E_{00}) to be 2.7 eV (Figure 3-4),[39] consistent with calculations (Table 3-2). The low oscillator strength of this transition leads to a long monoexponential PL lifetime in toluene ($\tau_{f\,tol}$=287 ns), shown in Figure 4-1C. From these measurements in toluene and ab initio electronic-structure

calculations, we propose the energies of the locally excited states in Figure 4-2. While this long lifetime could suggest triplet character, we find it unlikely based on negligible lifetime variation with and without oxygen or at cryogenic temperatures (Figure 3-11).

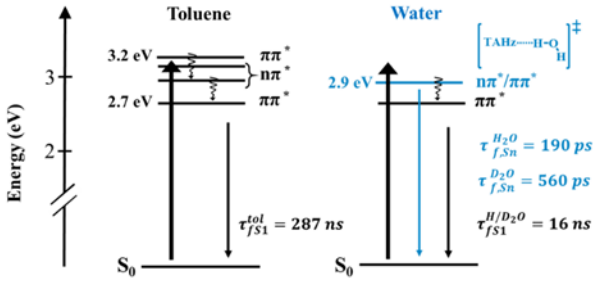

Figure 4-2 Jablonski diagram in toluene and water.

Jablonski diagram depicting bright high-lying absorption, fast internal conversion and monoexponential S_1 PL lifetime ($\tau_{f,S1}^{tol}$=287 ns) in toluene. In H_2O and D_2O (3.2 μg/mL), we observe dynamic S_1 PL quenching ($\tau_{f,S1}^{H/D2O}$=16 ns) and an additional high-energy PL signal attributed to mixed nπ*/ππ* states. The sub-ns S_n decay components determined by global target analysis for TAHz in H_2O ($\tau^{H}_{f,Sn}$=190 ps) and D_2O ($\tau^{D}_{f,Sn}$=560 ps) exhibit a kinetic isotope effect of KIE =2.9. S_1 decay dynamics show negligible isotopic dependence.

Jablonski diagram depicting bright high-lying absorption, fast internal conversion and monoexponential S_1 PL lifetime ($\tau_{f,S1}^{tol}$=287 ns) in toluene. In H_2O and D_2O (3.2 μg/mL), we observe dynamic S_1 PL quenching ($\tau_{f,S1}^{H/D2O}$=16 ns) and an additional high-energy PL signal attributed to mixed nπ*/ππ* states. The sub-ns S_n decay components determined by global target analysis for TAHz in H_2O ($\tau^{H}_{f,Sn}$=190 ps) and D_2O ($\tau^{D}_{f,Sn}$=560 ps) exhibit a kinetic isotope effect of KIE =2.9. S_1 decay dynamics show negligible isotopic dependence.

In Table 4-1, we tabulate radiative (k_R) and nonradiative (k_{NR}) rate constants for TAHz in various media. As expected for a photocatalyst, the PLQY ($\Phi_f=k_R/[k_R+k_{NR}]$) and lifetime ($\tau_f=1/[k_R+k_{NR}]$) of TAHz are strongly quenched in water, with k_{NR} roughly two orders of magnitude faster compared to toluene. We present photophysical parameters in DMSO and at higher mass loadings

in water as reference points for minor effects due to variations in relative permittivity (ε_r) and aggregation (*cf.* Chapter 3.3). Considering the catalytic activity (Figure 4-1D), we propose a significant fraction of excited states are quenched via photochemical processes in water.

Table 4-1. Photophysical Parameters of TAHz

Solvent	ε_r	Φ_f	τ_f (ns)	k_R ($\times 10^6$ s^{-1})	k_{NR} ($\times 10^6$ s^{-1})
Toluene*	2.7	0.69	286.9 ± 0.4	2.413 ± 0.003	1.084 ± 0.002
DMSO*	48	0.25	70.9 ± 0.9	3.42 ± 0.1	10.3 ± 0.4
Water 0.1 mg/mL	80	0.13	36.8 ± 0.35‡	3.5 ± 0.3	24 ± 2
Water supernatant	80	0.065	9.63 ± 0.06‡	2.9 ± 1	100 ± 36

*33 μM concentrations ‡Average Lifetime

While steady state TAHz PL spectra in toluene and water are nearly indistinguishable (Figure A-0-3), time-resolved PL (TR-PL) spectra in Figure 4-3 reveal a different story on picosecond (ps) to nanosecond (ns) timescales. Figure 4-3A shows the spectral traces at early times for TAHz in water vs. toluene. Though spectrally similar at low energies, TAHz emission in water exhibits a new feature at 460 nm. The kinetic traces in Figure 4-3B for high and low energy emission are distinct for TAHz in water, but not in toluene, suggesting an emissive higher-lying, presumably singlet, state exists in water.

We apply global target analysis to kinetically resolve overlapping emission features. We model total PL intensity $\Theta(t,\lambda)$ at time t and wavelength λ as a sum of concentration-weighted spectral components such that, $\Theta(t,\lambda)=\Sigma c_i(t)\sigma_i(\lambda)$, where $c_i(t)$ and $\sigma_i(\lambda)$, respectively, correspond to the time-dependent concentration and wavelength-dependent species-associated emission spectrum (SAES) of the i^{th} emissive species.[40] Global target analysis yields two kinetically resolvable emission features, one at higher energy attributed to a mixed S_n state and one to S_1. The SAES for S_n and S_1 are shown in Figure 4-3C. From this S_n SAES, we estimate its energy to be 2.9 eV

(Figure A-0-8). The expected blueshift of the nπ* transitions and the redshift of the ππ* states in water would move the nπ* states closer to the bright state and farther from the low-lying S_1 state. We see these expected shifts in absorption measurements of TAHz with phenol (Figure A-0-10). This mixing can explain the lack of emission from the bright ππ* state in toluene and the appearance in water, as the wavefunctions strongly mix allowing the nπ* states to "light up."

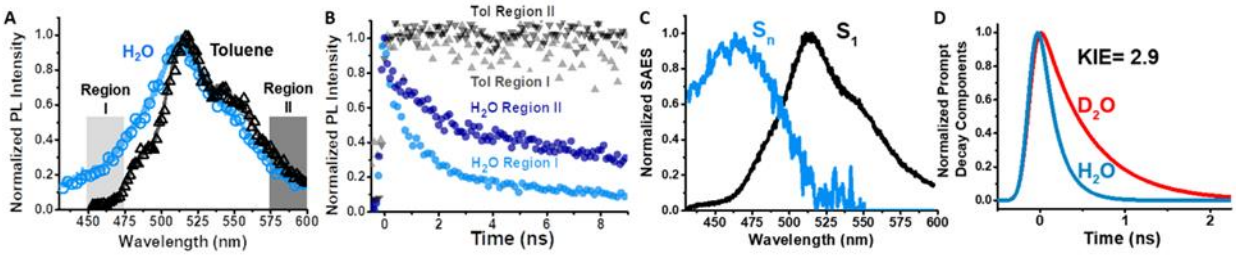

Figure 4-3. TR-PL spectra of TAHz in water and toluene.

A) In water (blue), the TR-PL spectra averaged over the first 500 ps exhibit a new PL feature in Region I compared to toluene (black). Solid lines represent global fits to the data (symbols). B) Kinetic data traces are shown for water (circles) and toluene (triangles). Kinetics from Region I and II are shown in light and dark colors respectively. TAHz in toluene decays monoexponentially with a constant rate across the emission spectrum. TAHz in water shows disparate decay rates in Regions I and II, suggesting two kinetically distinct emissive states exist. C) Species-associated emission spectra (SAES) from global target analysis of the TAHz:H_2O data in 3A show the fast S_n emission (blue) and the slow S_1 emission (black). D) The prompt decay components of the S_n emission extracted from global target analysis for TAHz in D_2O (red) and H_2O (blue). The KIE = 2.9 is consistent with dynamic quenching of the S_n emission due to PCET.

We apply a parallel decay model to analyze the emission from the S_n and S_1 states in water. For the S_n SAES, we recover a prompt and a delayed *c(t)* component. To confirm the assignment of the S_n emission and to understand the two decay components, we performed a kinetic isotope study comparing PL decay rates in H_2O versus D_2O. As shown in Scheme 4-1, one conceivable decay pathway for the S_n state includes a photochemical transformation wherein electron density is transferred from a hydrogen-bonded water molecule to the heptazine core, and the proton of water moves along the hydrogen bonding axis towards TAHz, forming a neutral •TAHz-H/HO• state with biradical character (Scheme 4-1). A luminescent excited state quenched by PCET should exhibit

an isotope-dependent emission lifetime, in H_2O versus D_2O.[2, 41-42] Consistent with this mechanism, in Figure 4-3D we see a kinetic isotope effect (KIE) of 2.9 for the prompt *c(t)* decay component of S_n SAES in H_2O ($\tau^{H}_{f,Sn}$=190 ps) and D_2O ($\tau^{D}_{f,Sn}$=560 ps). The second *c(t)* component of S_n SAES shows minimal isotopic dependence (KIE=1.3), and its origin is still unclear. Possible explanations could involve exciton-exciton annihilation, or back H-atom transfer to reform water and photoexcited TAHz. The S_1 emission shows no significant KIE (Figure A-0-12), but exhibits three *c(t)* components, which we attribute to heterogeneity introduced by aggregation in water (*cf.* Figure A-0-2).

We propose the fluorescence quenching of the mixed nπ* /ππ* state of TAHz in water is analogous to the hydrogen-bonded heptazine-water complex, previously studied with computational methods.[20] Those results revealed that the potential-energy surfaces on the locally excited states of heptazine cross that of the lowest charge-transfer state (from H_2O to heptazine) along the reaction path for proton transfer (Figure 3-9). While the precise energetic location of the corresponding charge-transfer state in the TAHz-H_2O complex is not known, the energy could be drastically lowered by the proton transfer from water to TAHz, resulting in low-lying curve crossings with the locally excited states, as illustrated in Figure 3-9.

To monitor •OH formation (Scheme 4-1), we also employed radical detection using terephthalic acid (Figure A-0-13). Terephthalic acid is a well-known •OH scavenger which is non-luminescent until reacting with •OH to form 2-hydroxyterephthalic acid which exhibits characteristic

luminescence at 430 nm.[43-44] We observe a linear increase in 2-hydroxyterephthalate PL with illumination time, indicating TAHz in H_2O photochemically liberates $^{\bullet}OH$

4.3 CONCLUSIONS

Herein we present a heptazine-based small molecule photocatalyst with emission from a low-lying dim S_1 state that is dramatically quenched in water. TR-PL spectra of TAHz in water reveal a new high-energy luminescence feature with a significantly shorter lifetime and KIE = 2.9. We attribute the isotope-dependent quenching to PCET from a hydrogen-bonded water molecule to TAHz. This significant finding is consistent with predictions that molecular excitations lead to H_2 production in aza-aromatic photocatalysts.[8, 20-21] Further mechanistic studies are underway in our laboratory to determine if PCET occurs via a stepwise or a concerted pathway, to explore possible photochemistry of the triplet manifold, and to understand the role of PCET in heptazine-based photocatalysis. Interesting questions remain concerning the fate of the resulting heptazinyl and $^{\bullet}OH$, which is of possible interest for full water splitting.

4.4 EXPERIMENTAL METHODS

Materials.

Reagents. Urea, potassium hydroxide, phosphorous oxychloride, phosphorous pentachloride, phenol, and terephthalic acid were all purchased from Sigma Aldrich. Anisole (99%) was purchased from Alfa Aesar. Aluminum chloride was purchased from Fischer Scientific. D_2O

(99%) was purchased from Cambridge Isotopic Laboratories. All reagents were used without further purification.

Characterization.

NMR. Solution-phase ^{1}HNMR was taken on a Bruker AV-300 instrument using a PABBI: X [1H] probe. TAHz was dissolved in d6-DMSO at ~100 μM concentration.

Electrospray ionization. Mass spectra were obtained using a Bruker Esquire LC ion trap. TAHz was dissolved in toluene at a 200 μM concentration, then 1 mL of TAHz toluene solution was added to 1 mL methanol, shaken, and injected onto the inlet column.

Sample Preparation. The supernatant water sample for photophysical rate constants was prepared by sonicating 0.1 mg/mL suspension of TAHz in water for half an hour followed by centrifuging for 5 minutes at 6,000 rpm.

Samples made for aqueous TR-PL kinetic isotope dependence were made to minimize any possible changes in lifetime due to different mass loadings. To achieve this, a 0.1 mg/mL suspension in D_2O was prepared, purged with nitrogen, and stirred in the dark (covered in aluminum foil) for 48 h. 100 μL of this suspension was placed into 3.0 mL of either H_2O or D_2O, resulting in 3.2 μg/mL mass loading, was purged and stirred in the dark for another 48 h before measuring. The H_2O sample from this experiment was used in Figure 3 of the main text.

Samples in mixtures of DMSO and water were prepared using 100 μL of the aforementioned TAHz suspension in D_2O for consistency, but instead added to 3 mL of pre-mixed solutions of 1:14 and 1:5 DMSO:H_2O. The 1:14 solution was 2.8 mL H_2O and 200 μL DMSO, and the 1:5

solution was 2.5 mL H_2O and 500 μL DMSO. These solutions were not stirred in the dark for an additional day, but instead measured within a few hours.

Steady-State Optical Characterization. Ground-state absorption spectra were collected with a Cary5000 UV−vis−NIR spectrometer. Steady-state photoluminescence (PL) was acquired on a home-built spectrometer using amplitude-modulated excitation and phase sensitive detection. Samples were irradiated with a modulated (200 Hz) 365-nm LED (5.2 mW/cm^2).

Time-Correlated Single-Photon Counting (TCSPC). Unless otherwise stated, TCSPC PL lifetimes were measured using a PicoQuant FluoTime 100 with a 375 nm laser diode excitation. Lifetimes measured out to 2 μs were triggered using an external function generator at 500 kHz.

Photoluminescence Quantum Yields. PLQY's were measured on a Hamamatsu external quantum efficiency measurement system (C9920-12). All PLQY's reported were excited with 365 nm light and the PL was integrated from 440 to 800 nm.

Photocatalytic Activity. Hydrogen evolution was measured with an SRI GC (8610 C) equipped with a thermal conductivity detector and a 6-ft MS-13X column, using argon as the carrier gas. Samples were prepared with 3.0 mg TAHz or carbon nitride suspensions in DI water with 10% (v/v) triethanolamine as a sacrificial hole acceptor and chloroplatinic acid (2% by weight photo-deposited Pt loading). Samples were illuminated with four 365-nm LEDs (5 mW/cm^2) for 24 h while stirring at 1150 rpm. The hydrogen generation rate is normalized to the length of time the sample was illuminated as well as the total mass of the catalyst in the system.

Time-Resolved Photoluminescence (TR-PL) Spectra. TR-PL spectra were collected using a Hamamatsu streak camera (C10910) with a slow-sweep unit (M10913-01) in photon counting mode. Samples were irradiated with 50 fs pulses at 365 nm and 1 kHz pump from a Coherent/Light

Conversion OPerA solo optical parametric amplifier (OPA). Pump fluences were $2.7x10^{13}$ photons cm^{-3} unless otherwise stated.

Laser Beam Characterization. The pump beam profile was characterized at the sample position using the BC106N-VIS CCD Camera Beam Profiler purchased from Thorlabs. Spatial beam images and spot size calculations were obtained from Thorlabs' standard beam profiler software package. Average power was measured using the Coherent FieldMate laser power meter equipped with the OP-2 VIS high sensitivity sensor purchased from Edmond Optics.

Terephthalic Acid Radical Detection. A suspension of 25 μg/mL TAHz in a 3.0 mM NaOH aqueous solution with 15 mM terephthalic acid was irradiated with a modulated (200 Hz) 365 nm LED (5.2 mW/cm^2). Steady-state photoluminescence (PL) measurements were acquired over time on a home-built spectrometer using amplitude-modulated excitation and phase sensitive detection. PL measurements were taken with and without terephthalic acid to subtract any baseline from TAHz emission.

4.5 REFERENCES

1. Concepcion, J. J.; Brennaman, M. K.; Deyton, J. R.; Lebedeva, N. V.; Forbes, M. D. E.; Papanikolas, J. M.; Meyer, T. J., Excited-State Quenching by Proton-Coupled Electron Transfer. *J. Am. Chem. Soc.* **2007,** *129* (22), 6968-6969.
2. Lennox, J. C.; Kurtz, D. A.; Huang, T.; Dempsey, J. L., Excited-State Proton-Coupled Electron Transfer: Different Avenues for Promoting Proton/Electron Movement with Solar Photons. *ACS Enery Lett.* **2017,** *2* (5), 1246-1256.
3. Weinberg, D. R.; Gagliardi, C. J.; Hull, J. F.; Murphy, C. F.; Kent, C. A.; Westlake, B. C.; Paul, A.; Ess, D. H.; McCafferty, D. G.; Meyer, T. J., Proton-Coupled Electron Transfer. *Chem. Rev.* **2012,** *112* (7), 4016-4093.
4. Gagliardi, C. J.; Vannucci, A. K.; Concepcion, J. J.; Chen, Z.; Meyer, T. J., The role of proton coupled electron transfer in water oxidation. *Energy Environ. Sci.* **2012,** *5* (7), 7704-7717.
5. Oliver, T. A. A.; Zhang, Y.; Roy, A.; Ashfold, M. N. R.; Bradforth, S. E., Exploring Autoionization and Photoinduced Proton-Coupled Electron Transfer Pathways of Phenol in Aqueous Solution. *J. Phys. Chem. Lett.* **2015,** *6* (20), 4159-4164.
6. Damrauer, N. H.; Hodgkiss, J. M.; Rosenthal, J.; Nocera, D. G., Observation of Proton-Coupled Electron Transfer by Transient Absorption Spectroscopy in a Hydrogen-Bonded, Porphyrin Donor−Acceptor Assembly. *J. Phys. Chem. B* **2004,** *108* (20), 6315-6321.

7. Eisenhart, T. T.; Dempsey, J. L., Photo-induced Proton-Coupled Electron Transfer Reactions of Acridine Orange: Comprehensive Spectral and Kinetics Analysis. *J. Am. Chem. Soc.* **2014,** *136* (35), 12221-12224.
8. Liu, X.; Karsili, T. N.; Sobolewski, A. L.; Domcke, W., Photocatalytic Water Splitting with the Acridine Chromophore: A Computational Study. *J. Phys. Chem. B* **2015,** *119* (33), 10664-72.
9. Reimers, J. R.; Cai, Z.-L., Hydrogen Bonding and Reactivity of Water to Azines in Their S1 (n,pi*) Electronic Excited States in the Gas Phase and in Solution. *Phys. Chem. Chem. Phys.* **2012,** *14* (25), 8791-8802.
10. Whitten, D. G.; Lee, Y. J., Photochemistry of Aza Aromatics. Identification of the Reactive Intermediate in the Photoreduction of Acridine. *J. Am. Chem. Soc.* **1971,** *93* (4), 961-966.
11. Peon, J.; Tan, X.; Hoerner, J. D.; Xia, C.; Luk, Y. F.; Kohler, B., Excited State Dynamics of Methyl Viologen. Ultrafast Photoreduction in Methanol and Fluorescence in Acetonitrile. *J. Phys. Chem. A* **2001,** *105* (24), 5768-5777.
12. Stermitz, F. R.; Wei, C. C.; O'Donnell, C. M., Photochemistry of n-Heterocycles. V. Photochemistry of Quinoline and Some Substituted Quinoline Derivatives. *J. Am. Chem. Soc.* **1970,** *92* (9), 2745-2752.
13. Pearson, R. M.; Lim, C.-H.; McCarthy, B. G.; Musgrave, C. B.; Miyake, G. M., Organocatalyzed Atom Transfer Radical Polymerization Using N-Aryl Phenoxazines as Photoredox Catalysts. *J. Am. Chem. Soc.* **2016,** *138* (35), 11399-11407.
14. Theriot, J. C.; Lim, C. H.; Yang, H.; Ryan, M. D.; Musgrave, C. B.; Miyake, G. M., Organocatalyzed Atom Transfer Radical Polymerization Driven by Visible Light. *Science* **2016,** *352* (6289), 1082-6.
15. Chen, Y.; Wang, B.; Lin, S.; Zhang, Y.; Wang, X., Activation of n → π* Transitions in Two-Dimensional Conjugated Polymers for Visible Light Photocatalysis. *J. Phys. Chem. C* **2014,** *118* (51), 29981-29989.
16. Kellmann, A.; Dubois, J. T., Photoreactive State of Acridine in Solution. *J. Chem. Phys.* **1965,** *42* (7), 2518-2522.
17. Kikuchi, K.; Kasama, K.; Kanemoto, A.; Ujiie, K.; Kikubun, H., Reaction and deactivation of excited acridine in ethanol. *J. Phys. Chem.* **1985,** *89* (5), 868-871.
18. Koizumi, M.; Ikeda, Y.; Iwaoka, T., Reactive State of Acridine in the Photoreduction in Alcohols. *J. Phys. Chem.* **1968,** *48* (4), 1869-1870.
19. Wilkinson, F.; Dubois, J. T., Reactive State in the Photoreduction of Acridine in Ethanol. *J. Phys. Chem.* **1968,** *48* (6), 2651-2654.
20. Ehrmaier, J.; Karsili, T. N. V.; Sobolewski, A. L.; Domcke, W., Mechanism of Photocatalytic Water Splitting with Graphitic Carbon Nitride: Photochemistry of the Heptazine–Water Complex. *J. Phys. Chem. A* **2017,** *121* (25), 4754-4764.
21. Ehrmaier, J.; Janicki, M. J.; Sobolewski, A. L.; Domcke, W., Mechanism of photocatalytic water splitting with triazine-based carbon nitrides: insights from ab initio calculations for the triazine-water complex. *Phys. Chem. Chem. Phys.* **2018,** *20* (21), 14420-14430.
22. Lotsch, B. V.; Döblinger, M.; Sehnert, J.; Seyfarth, L.; Senker, J.; Oeckler, O.; Schnick, W., Unmasking Melon by a Complementary Approach Employing Electron Diffraction, Solid-State NMR Spectroscopy, and Theoretical Calculations—Structural Characterization of a Carbon Nitride Polymer. *Chem. Eur. J.* **2007,** *13* (17), 4969-4980.

23. Teter, D. M.; Hemley, R. J., Low-Compressibility Carbon Nitrides. *Science* **1996,** *271* (5245), 53-55.
24. Ong, W.-J.; Tan, L.-L.; Ng, Y. H.; Yong, S.-T.; Chai, S.-P., Graphitic Carbon Nitride (g-C3N4)-Based Photocatalysts for Artificial Photosynthesis and Environmental Remediation: Are We a Step Closer To Achieving Sustainability? *Chem. Rev.* **2016,** *116* (12), 7159-7329.
25. Corp, K. L.; Schlenker, C. W., Ultrafast Spectroscopy Reveals Electron-Transfer Cascade That Improves Hydrogen Evolution with Carbon Nitride Photocatalysts. *J. Am. Chem. Soc.* **2017,** *139* (23), 7904-7912.
26. Wang, X.; Maeda, K.; Thomas, A.; Takanabe, K.; Xin, G.; Carlsson, J. M.; Domen, K.; Antonietti, M., A Metal-Free Polymeric Photocatalyst for Hydrogen Production from Water Under Visible Light. *Nat. Mater.* **2008,** *8*, 76.
27. Liu, J.; Zhang, Y.; Lu, L.; Wu, G.; Chen, W., Self-regenerated solar-driven photocatalytic water-splitting by urea derived graphitic carbon nitride with platinum nanoparticles. *Chem. Commun.* **2012,** *48* (70), 8826-8828.
28. Niu, P.; Zhang, L.; Liu, G.; Cheng, H.-M., Graphene-Like Carbon Nitride Nanosheets for Improved Photocatalytic Activities. *Adv. Funct. Mater.* **2012,** *22* (22), 4763-4770.
29. Sun, J.; Zhang, J.; Zhang, M.; Antonietti, M.; Fu, X.; Wang, X., Bioinspired hollow semiconductor nanospheres as photosynthetic nanoparticles. *Nat. Comm* **2012,** *3*, 1139.
30. Lau, V. W.-h.; Moudrakovski, I.; Botari, T.; Weinberger, S.; Mesch, M. B.; Duppel, V.; Senker, J.; Blum, V.; Lotsch, B. V., Rational Design of Carbon Nitride Photocatalysts by Identification of Cyanamide Defects as Catalytically Relevant Sites. *Nat. Comm* **2016,** *7*, 12165.
31. Wang, W.; Yu, J. C.; Shen, Z.; Chan, D. K. L.; Gu, T., g-C3N4 quantum dots: direct synthesis, upconversion properties and photocatalytic application. *Chem. Commun.* **2014,** *50* (70), 10148-10150.
32. Chu, S.; Wang, Y.; Guo, Y.; Feng, J.; Wang, C.; Luo, W.; Fan, X.; Zou, Z., Band Structure Engineering of Carbon Nitride: In Search of a Polymer Photocatalyst with High Photooxidation Property. *ACS Catal.* **2013,** *3* (5), 912-919.
33. Ilic, S.; Zoric, M. R.; Kadel, U. P.; Huang, Y.; Glusac, K. D., Metal-Free Motifs for Solar Fuel Applications. *Annu. Rev. Phys. Chem.* **2017,** *68* (1), 305-331.
34. Lau, V. W.-h.; Mesch, M. B.; Duppel, V.; Blum, V.; Senker, J.; Lotsch, B. V., Low-Molecular-Weight Carbon Nitrides for Solar Hydrogen Evolution. *J. Am. Chem. Soc.* **2015,** *137* (3), 1064-1072.
35. Jing, W.; Ruiyu, L.; Rong, L.; Anchi, Y., Photophysics and Photocatalysis of Melem: A Spectroscopic Reinvestigation. *Chem. Asian J.* **2018,** *13* (8), 1060-1066.
36. Li, J.; Nakagawa, T.; MacDonald, J.; Zhang, Q.; Nomura, H.; Miyazaki, H.; Adachi, C., Highly Efficient Organic Light-Emitting Diode Based on a Hidden Thermally Activated Delayed Fluorescence Channel in a Heptazine Derivative. *Adv. Mater.* **2013,** *25* (24), 3319-3323.
37. Li, J.; Nomura, H.; Miyazaki, H.; Adachi, C., Highly efficient exciplex organic light-emitting diodes incorporating a heptazine derivative as an electron acceptor. *Chem. Commun.* **2014,** *50* (46), 6174-6176.
38. Ke, Y.; Collins, D. J.; Sun, D.; Zhou, H.-C., (10,3)-a Noninterpenetrated Network Built from a Piedfort Ligand Pair. *Inorg. Chem.* **2006,** *45* (5), 1897-1899.
39. Rabe, E. J.; Schlenker, C. W., Excited State Energies Drive Charge Transfer in Organic Semiconductors. In *World Scientific Handbook of Organic Optoelectronic Devices*, Thompson, C. B., Ed. World Scientific Publishing Co Pte Ltd: 2018; Vol. Organic Photovoltaics (OPV's).

40. Snellenburg, J. J.; Laptenok, S. P.; Seger, R.; Mullen, K. M.; van Stokkum, I. H. M., Glotaran: A Java-Based Graphical User Interface for the R Package TIMP. *J. Stat. Softw.* **2012,** *49* (3), 1-22.
41. Bronner, C.; Wenger, O. S., Kinetic Isotope Effects in Reductive Excited-State Quenching of Ru(2,2′-bipyrazine)32+ by Phenols. *J. Phys. Chem. Lett.* **2012,** *3* (1), 70-74.
42. Zhang, W.; Burgess, I. J., Kinetic isotope effects in proton coupled electron transfer. *J. Electroanal. Chem.* **2012,** *668*, 66-72.
43. Morawski, O.; Izdebska, K.; Karpiuk, E.; Suchocki, A.; Zhydachevskyy, Y.; Sobolewski, A. L., Titanyl Phthalocyanine as a Water Photooxidation Agent. *J. Phys. Chem. C* **2015,** *119* (25), 14085-14093.
44. Arunkumar, N.; Vijayaraghavan, R., Enhanced photocatalytic activity of nanocrystalline N-doped ZnSb2O6: role of N doping, cation ordering, particle size and crystallinity. *RSC Advances* **2014,** *4* (110), 65223-65231.

Chapter 5. Barrierless Heptazine-Driven Excited-State Proton-Coupled Electron Transfer: Implications for Controlling Photochemistry of Carbon Nitrides and Aza-Arenes

Reprinted (adapted) with permission from J. Phys. Chem. C.
DOI: 10.1021/acs.jpcc.9b08842

5.1 INTRODUCTION

Concerted motion of protons and electrons is critical for a variety of chemical transformations relevant for applications spanning energy storage[1] to municipal wastewater treatment.[2] Recently, there has been mounting world-wide interest in deploying molecular and polymeric organic constructs as photoredox catalysts to drive these transformations using photons.[3-5] In order to utilize solar energy in such processes, it is desirable to understand what molecular properties control the efficiency of inter-molecular excited-state proton-coupled electron transfer (ES-PCET) reactions. The majority of inter-molecular ES-PCET literature to date focuses on metal-containing complexes,[6-9] with fewer examples of all-organic chromophores,[10-12] despite their photophysical properties being extensively studied over the past century.[3-4, 13-15] Precious metal-containing catalysts have become promising candidates, in part, due to their long-lived excited state lifetimes ranging from hundreds of nanoseconds to microseconds.[16] However, identifying earth-abundant alternatives continues to be a compelling challenge to overcome. We have elected to examine all-organic materials with long excited-state lifetimes and good photostability. Recently, the nitrogen-rich heptazine (Hz) unit has garnered increased attention for applications in photocatalytic hydrogen production.[5, 17-19] The mechanism of molecular Hz driving ES-PCET has been studied computationally,[20-22] and our group reported the first experimental evidence for this processes resulting in neutral radical species.[23] This Hz-based chromophore exhibits a singlet lifetime of

roughly 300 ns, the same order of magnitude as $[Ru(bpy)_3]^{2+}$, a compound which is ubiquitous in the study of photochemical transformations.[16, 24] Interestingly, this 300 ns lifetime is significantly longer than first row transition metal complexes[25] as well as traditional strongly-absorbing organic chromophores, which typically have lifetimes of no more than tens of nanoseconds.[26] Additionally, we previously reported computational and experimental evidence that Hz derivatives can exhibit an extremely unusual inversion of the energies of their lowest singlet and triplet excited states.[27] This peculiar violation of Hund's multiplicity rule stands in contrast to virtually all other classes of known organic compounds. With the lowest lying excited state being a singlet rather than a triplet, the sensitization of singlet oxygen appears to become an inaccessible decay pathway for Hz-based chromophores. Those results imply that Hz molecules should enjoy unique photostability in the presence of oxygen. This is important because typical organic photocatalysts achieve the long excited-state lifetimes necessary to outlast slow diffusive processes by accessing the triplet manifold through efficient intersystem crossing. Unfortunately, relying on triplet molecular photoexcitations relegates the use of such chromophores to anaerobic environments in order to avoid destroying the photocatalyst by sensitizing highly reactive singlet oxygen.

Herein, we provide further mechanistic insights into inter-molecular ES-PCET using 2,5,8-tris(4-methoxyphenyl)-1,3,4,6,7,9,9b-heptaazaphenalene (TAHz) with a series of phenol (PhOH) derivatives as proton and electron donors, shown in Figure 5-1. By altering the functional group on PhOH, we monitor the effect of redox potential and hydrogen-bonding on the mechanism of the resulting photochemical reaction.[28-32] In particular, we consider the energy of the intermolecular charge transfer (CT) states that form in these complexes and the corresponding excited state reaction barrier heights. For each PhOH, we determine a quenching rate constant (k_Q)

of excited TAHz, an association constant (K_A), and a kinetic isotope effect (KIE) of excited-state deactivation with R-PhOH versus R-PhOD.

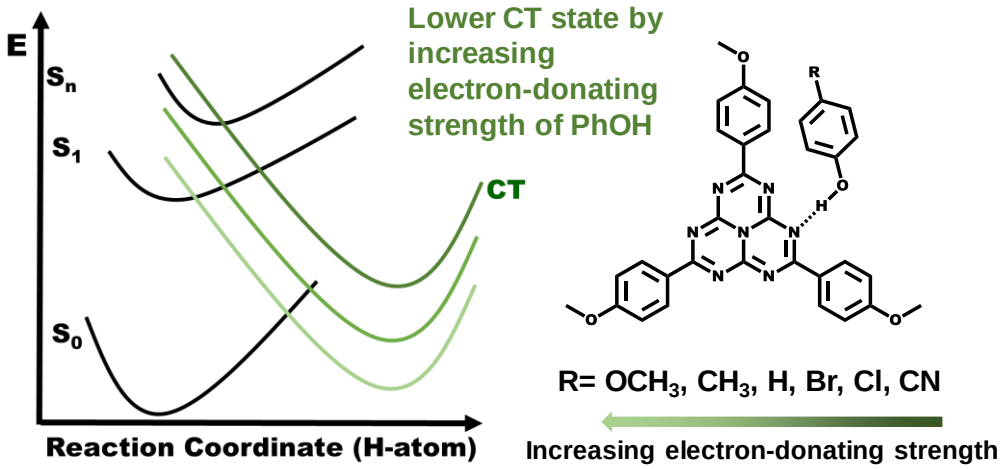

Figure 5-1. A cartoon depicting the proposed excited-state landscape.
This is depicting the landscape along the H-atom transfer coordinate from phenol (PhOH) to TAHz. As proposed previously, there exists a charge transfer (CT) state in which an electron has moved from the oxygen atom of PhOH to the heptazine core and which can drive proton motion after the CT has occurred. Previous studies with TAHz and water suggest that the CT state was accessible from the S_n states. We believe the energy curve of the CT state can be lowered by adding electron-donating groups on the H-atom donor. In this study we do this by using the series of R-PhOH derivatives shown.

As the electron-donating strength of the para-substituent, R, on R-PhOH is increased, we observe an increase in quenching rate constant accompanied by a decrease in KIE. Using *ab initio* quantum chemical calculations to examine the energy landscape for the interaction of the Hz core with the same series of PhOHs, we observe the same trend, wherein the transition state barrier for the photoinduced reaction decreases until the photon-driven reaction becomes completely barrierless for the most electron-donating PhOH. By using time-resolved photoluminescence measurements and global analysis, we can separately monitor hydrogen-bonded and free TAHz emission. Correspondingly, we observe no evidence for emission from hydrogen-bound complexes in the

case of OCH_3-PhOH, consistent with barrierless excited-state reactivity. This photochemical reactivity information provides new insight that synthetic chemists and materials scientists can deploy to outline new molecular design strategies targeting Hz-based photocatalysis.

5.2 Results and Discussion

5.2.1 *Association Constants for Hydrogen-Bonding*

We observe evidence of hydrogen bonding in the ground-state absorption spectra of TAHz with and without PhOH present, as shown in Figure 5-2A. Upon hydrogen-bonding, we see a redshift in the bright $\pi \rightarrow \pi^*$ transition, labeled "Peak 1." At lower energies, we observe a blueshift of the weakly allowed transitions with $n \rightarrow \pi^*$ character, labeled "Peak 2." Figure 5-2B shows the magnitude of the peak shift as a function of the pKa of the PhOH derivative. PhOHs with electron-donating substituents, such as CH_3-PhOH and OCH_3-PhOH, show only small shifts whereas CN-PhOH displays a significantly larger shift at 50 mM PhOH concentrations. This suggests that the hydrogen bonding strength is not equal across the series of PhOH derivatives. The calculations (see Section 5.2.4) indeed show that the length of the hydrogen bond between the OH group of PhOH and the acceptor N-atom of Hz (R_{NH}) is 1.937 Å in the Hz-PhOH complex. R_{NH} increases to 1.943 Å for the strongest electron donating substituent (OCH_3) and decreases to 1.904 Å for the strongest electron withdrawing substituent (CN), see

Table 5-1. As is well known, the length of the hydrogen bond is a proxy for the strength (binding energy) of the latter. In order to quantify these differences from the experimental side, we determined the association constant between TAHz and each of the six PhOH derivatives. We employed the method previously used by the Hammarström group to fit the saturation behavior of the changing ground state absorption as a function of PhOH concentration.[33-34] Figure 5-2C shows

the change in absorption spectra for TAHz with increasing PhOH concentrations. Figure 5-2D plots the change in optical density as a function of PhOH concentration, showing a clear saturation behavior. Fitting this data to the following equation allows us to extract a K_A value for TAHz-PhOH in the ground state.

$$\frac{\Delta A}{l} = \Delta\varepsilon_{380}\left(\frac{[TAHz]_0 + [PhOH]_0 + K_A^{-1}}{2}\right)\begin{matrix}(+)\\(-)\end{matrix}\sqrt{\left(\frac{[TAHz]_0+[PhOH]_0+K_A^{-1}}{2}\right)^2 - [TAHz]_0[PhOH]_0} \quad (1)$$

Here ΔA is the change in absorption at a given wavelength, l is the path length of the cuvette, $\Delta\varepsilon_{380}$ is the difference in molar absorptivity at 380 nm between the bound TAHz-PhOH complex and free TAHz chromophore, $[TAHz]_0$ and $[PhOH]_0$ are the initial concentrations of TAHz and PhOH, respectively.

We have estimated the K_A values for the six PhOH derivatives with TAHz in Table 5-1 (see Appendix B for fits). As expected, we see an increased K_A for PhOHs with electron-withdrawing substituents with the largest being for CN-PhOH. Notably, there is a very small difference between the K_A values for PhOH, CH_3-PhOH, and OCH_3-PhOH despite there being a significant difference between the oxidation potentials of these PhOHs. The computed ground-state hydrogen bond lengths follow the same trend.

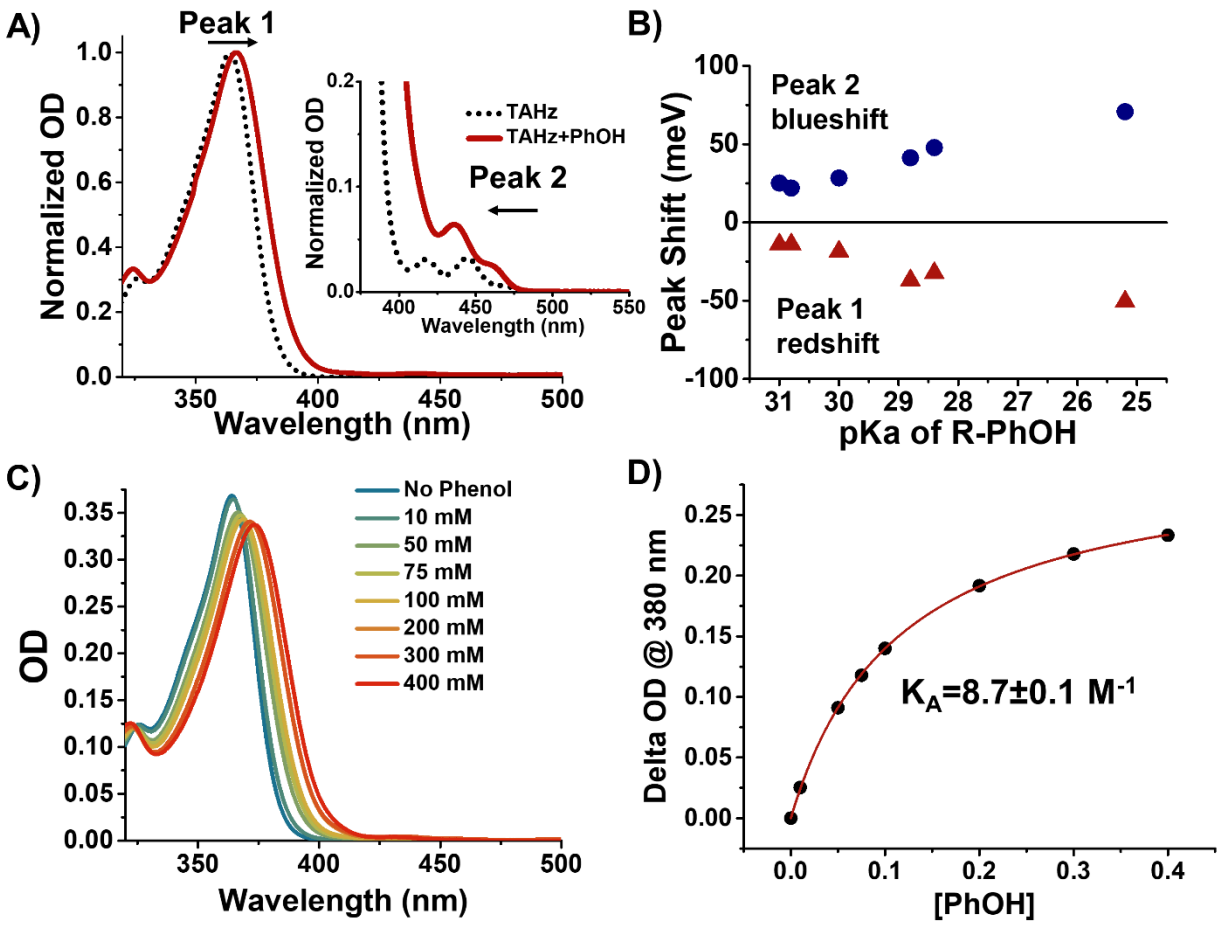

Figure 5-2. Ground state absorption shifting as a function of phenol concentration.
A) The addition of phenol (PhOH) changes the ground state absorption of TAHz in toluene, suggesting hydrogen-bonding. A distinct redshift of the main absorption can be seen from TAHz in toluene without PhOH present (black dotted line) upon the addition of 100 mM PhOH (solid red line). The weakly allowed transitions at lower energies, on the other hand, show a blueshift upon addition of PhOH, shown in the inset. B) The peak shifts of TAHz absorption with 100 mM of R-PhOH as a function of the PhOH's pKa (in DMSO) shows a largely linear trend. This suggests that different PhOHs have different hydrogen bonding strengths with TAHz. C) Absorption traces at different PhOH concentrations shows a saturation behavior towards the absorption of the TAHz-PhOH complex. D) Fit of ΔOD at 380 nm to determine K_A for TAHz and PhOH to be 8.7 M^{-1}.

5.2.2 *Quenching Constants for PhOH Derivatives*

To monitor the quenching rate of the TAHz S_1 state with varying PhOH derivatives, we performed Stern-Volmer quenching analysis using both PL intensity and lifetime quenching data, shown in Figure 5-3A and Figure 5-3B, respectively. Table 5-1 shows all the k_Q values for the six

different PhOHs (see Appendix B) and calculated KIE values for the S_1 lifetime with R-PhOH/D. As expected, increasingly anodic oxidation potentials of the R-PhOH lead to smaller k_Q values, suggesting a kinetic barrier has been introduced along the photochemical reaction pathway. This is confirmed by the increasing KIE values with decreasing k_Q, suggesting proton motion must couple to electron motion for the reaction to proceed, most likely by a tunneling mechanism.

The calculated k_Q values from the two methods (intensity and lifetime) are close for PhOH, but the intensity quenching shows a slightly greater rate constant. We attribute this to the fact that intensity analysis can reflect both static and dynamic quenching, whereas lifetime analysis only captures the rate of dynamic quenching. We note that for PhOH derivatives with low K_A values and low oxidation potentials, we see a greater difference between the k_Q values we obtain from lifetime measurements compared with intensity measurements. One explanation could be, in this case, that complex formation is the rate determining step as opposed to ES-PCET. Whereas in the case of CN-PhOH, K_A is large but the driving force for electron transfer is low, so the rate of ES-PCET is rate determining. In this case, the intensity and lifetime quenching are the same as they both report on the rate of ES-PCET.

It is worth noting that we observe a two-component PL lifetime in the presence of PhOH, in contrast to the monoexponential decay of TAHz in neat toluene. We attribute the fast decay to the emission of hydrogen-bound complexes, as has been observed for coumarin complexes previously.[28]

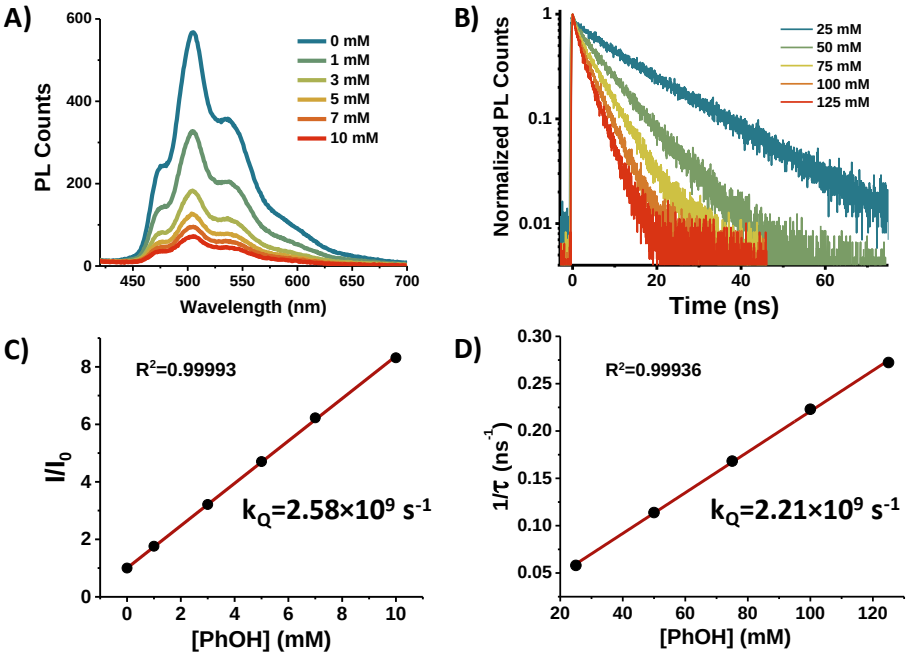

Figure 5-3. TAHz photoluminescence quenching as a function of phenol concentration.
A) Photoluminescence (PL) intensity quenching of TAHz shows significant static quenching with increasing concentrations of phenol (PhOH). B) PL lifetimes of TAHz with increasing concentrations of PhOH show dynamic quenching. Stern-Volmer analysis shows a straight line for both the (C) PL intensity quenching and (D) luminescence lifetime, fit after 5 ns.

Table 5-1. Comparison of key parameters determining hydrogen bonding and ES-PCET in complexes of TAHz or Hz with phenol (PhOH) derivatives.

R	E_0 ($RPhOH^+$/ RPhOH)†	pK_a PhOH§	k_Q (x10^9 s^{-1}) TCSPC	k_Q (x10^9 s^{-1}) PLQY	K_A (M^{-1})	S_1 KIE*	R_{NH} (Å)♦	$\Delta E^‡$ (eV)♦
CN	2.03	13.2	0.556	0.532	~87.4	1.9	1.904	0.369
Cl	1.88	16.75	2.78	2.80	17.2	1.4	1.924	0.169
Br	1.86	16.36	2.73	3.06	19.1	1.4	1.923	0.177
H	1.88	18.0	2.21	2.58	8.7	1.5	1.937	0.167
CH_3	1.79	18.9	4.21	5.14	8.9	1.2	1.940	0.093
OCH_3	1.68	19.1	4.26	5.23	8.9	1.1	1.943	----

† Versus SHE in ACN (±0.1 V)[31, 35]
§ In DMSO[32]
* All R-PhOH concentrations 50 mM
♦ From *ab initio* calculations, see Section 5.2.4

5.2.3 *Time-Resolved Photoluminescence*

Using time-resolved photoluminescence spectra in tandem with global analysis, we analyzed the nature of the fast PL decay component mentioned above. Figure 5-4A shows the PL spectral traces of TAHz in a 100 mM PhOH solution at early (500 ps) and late (5 – 7 ns) times. Though the spectral difference is small, the increased intensity near 475 nm at early times does not appear for TAHz in neat toluene (Figure B-0-14). Figure 5-4B clearly shows different decay rates in the spectral range 450 – 475 nm in contrast to 500 – 525 nm, indicating that at least two separate luminescent species are present.

To kinetically resolve these overlapping emission features, we apply global target analysis. We model total PL intensity $\Theta(t,\lambda)$ at time t and wavelength λ as a sum of concentration-weighted spectral components such that $\Theta(t,\lambda)=\Sigma c_i(t)\sigma_i(\lambda)$, where $c_i(t)$ and $\sigma_i(\lambda)$, respectively, correspond to the time-dependent concentration and wavelength-dependent species-associated emission spectrum (SAES) of the i^{th} emissive species.[36] Global target analysis yields two kinetically resolvable emission features, shown in Figure 4c. The spectral trace at higher energies decays at a significantly faster rate, on the order of hundreds of picoseconds. We attribute this emission spectrum to that of a hydrogen-bonded TAHz-PhOH complex. The blueshift in emission corresponds to the blueshift of the low-lying and weakly-allowed transitions that appear in the absorption spectra in Figure 5-2A. Considering the $n\pi^*$ character of these low energy transitions, we would expect to see a blueshift for the emission of this state. It is also interesting to note that the vibronic structure is more pronounced for the fast component than for the slow component, although the peak spacings appear similar.

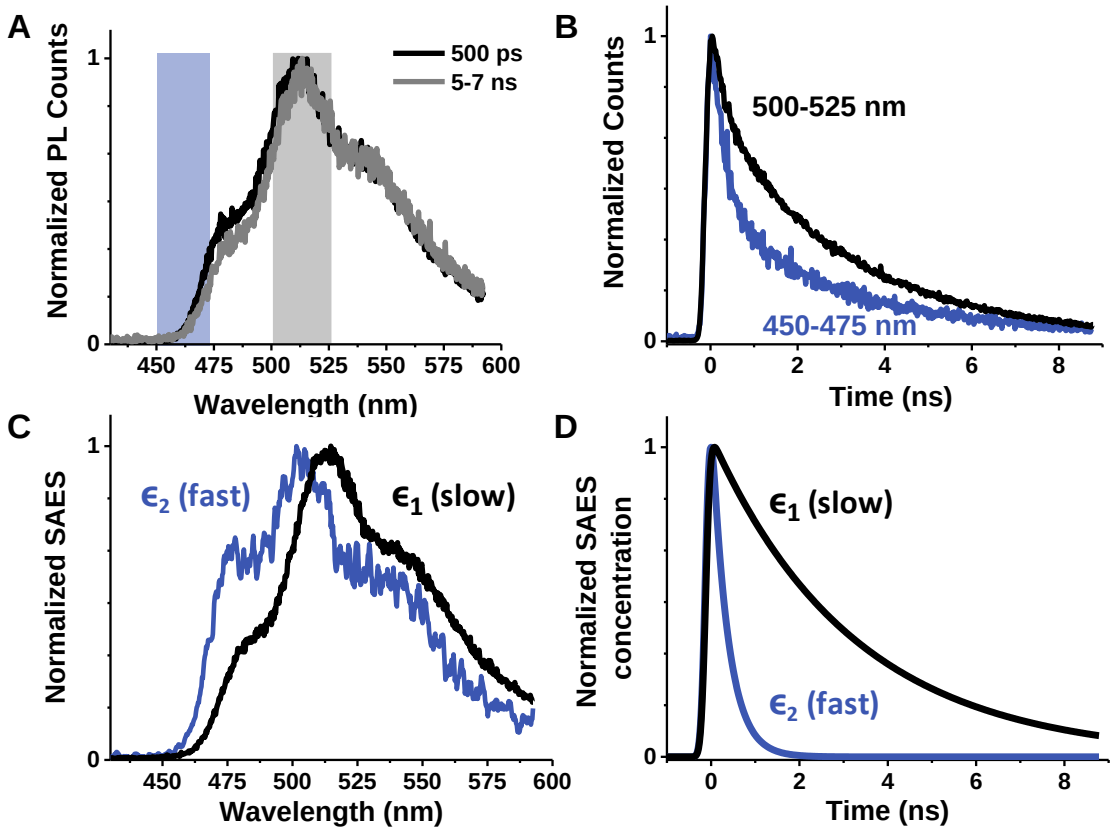

Figure 5-4. Time-resolved photoluminescence (TR-PL) measurements of TAHz with phenol. A) Spectral traces averaged over the first 500 ps (black) and 5 to 7 ns (gray) show a small spectral change. B) The kinetic decay traces averaged from 450-475 nm (blue) and 500-525 nm (black) suggest at least two kinetically distinct luminescent species. C) and D) Global target analysis of the TR-PL data shows two species associated emission spectra (SAES). Emission attributed to the S_1 state, labeled ϵ_1 (black), is the emission shape seen in steady-state measurements and has a lifetime of 3.23 ns. The second SAES, labeled ϵ_2 (blue), is seen at higher energies and decays notably faster than ϵ_1 with a lifetime of 0.36 ns. All experiments shown were done with 50 µM TAHz with 100 mM phenol.

To probe whether this state is associated with hydrogen bonding between TAHz and PhOH, we monitor the relative amplitude of the emission signal for this high energy species as a function of PhOH concentration. While Figure 5-5B shows that the spectral shape does not change for either species, Figure 5-5C reveals the relative intensity of the high energy features increases with increasing concentrations of PhOH. This intensity/concentration correlation strongly suggests that the high energy emission results from a hydrogen-bonded TAHz-PhOH complex. This distinction

between hydrogen bonded and free TAHz emission allows us to monitor the two populations separately for the different PhOH derivatives. We observe and kinetically resolve high energy emission spectra for all PhOHs that we have examined, with the exception of OCH_3-PhOH, for which this emission feature is absent on our experimental timescale (more discussion in Appendix B). We attribute this absence to barrierless reactivity from the S_1 state (vide infra). Such barrierless reactivity for OCH_3-PhOH would be consistent with this derivative possessing the lowest anodic oxidation potential and exhibiting no significant KIE. In the photoexcited TAHz and OCH_3-PhOH complex, the rate of reaction far outcompetes the rate of fluorescence. Therefore, the only emission we observe is from unbonded TAHz chromophores. The quenching rate of this free TAHz then becomes diffusion limited for the chromophore and OCH_3-PhOH in the solution.

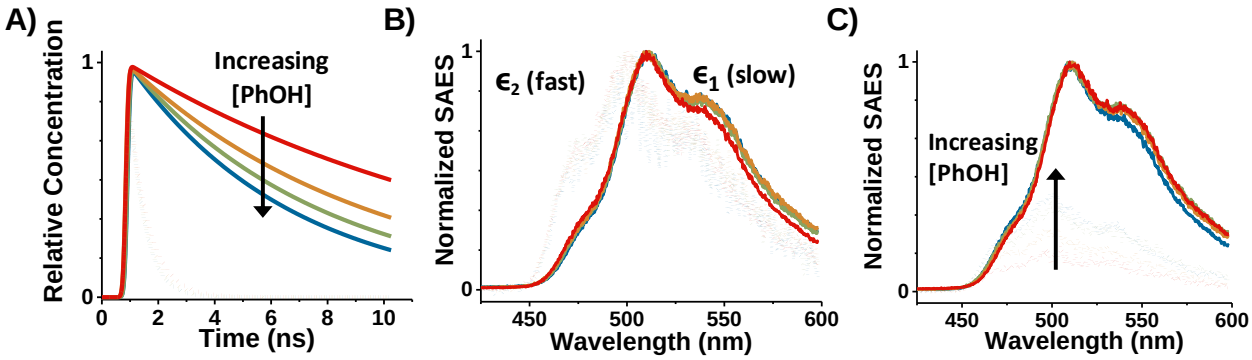

Figure 5-5. Phenol concentration-dependent TR-PL suggesting that the high energy emission is from a hydrogen-bonded complex.
A) Kinetic decay rates of bonded TAHz S_1 (solid) hydrogen-bonded TAHz-PhOH (dotted) with different PhOH concentrations: 25 mM (red), 50 mM (orange), 75 mM (green), and 100 mM (blue). B) Normalized SAES showing spectral shape isn't changing significantly. C) High energy emission grows in with [PhOH] relative to low-energy emission.

5.2.4 *Computational Studies of Hz-PhOH Complexes and Their Potential Energy Surfaces*

The ground-state equilibrium geometries of the hydrogen-bonded complexes of Hz with PhOH and derivatives thereof were determined with the second-order Møller-Plesset (MP2) method. Vertical electronic excitation energies and excited state potential energy surfaces were computed with the second-order algebraic-diagrammatic-construction (ADC(2)) method.[37] ADC(2) is a wave-function based single-reference propagator method which provides, in contrast to time-dependent density functional theory (TDDFT) with various functionals, an accurate and balanced description of locally excited (LE) states and CT states, which is essential for the determination of reliable *ab initio* potential energy surfaces for ES-PCET reactions. The complex of TAHz with PhOH is too big for wave-function based excited state *ab initio* calculations. All *ab initio* calculations were therefore performed for complexes of the Hz core of TAHz with PhOH and its derivatives.

The most relevant nuclear coordinates for PCET processes are the H-atom transfer coordinate (chosen here as the OH bond length R_{OH} of the hydrogen-bonded PhOH molecule) and the distance R_{ON} between the oxygen atom of PhOH and the H-atom accepting nitrogen atom of Hz. For fixed R_{OH} and R_{ON}, the energy of the lowest excited singlet state was minimized with respect to all other nuclear coordinates of the complex. This procedure yields a two-dimensional (2D) relaxed potential energy surface for the PCET reaction. The saddle point (transition state) on this 2D relaxed surface was located and used as the starting guess for a full optimization of the transition state with the ADC(2) method. Analysis of the eigenvalues of the Hessian confirmed that there was only a single imaginary frequency, implying a first-order saddle point. The difference between

the energy of the transition state and the energy minimum of the S_1 state in the Frank Condon (FC) zone defines the reaction barrier $\Delta E^{\ddagger}$. The reaction barriers are listed in Table 5-1.

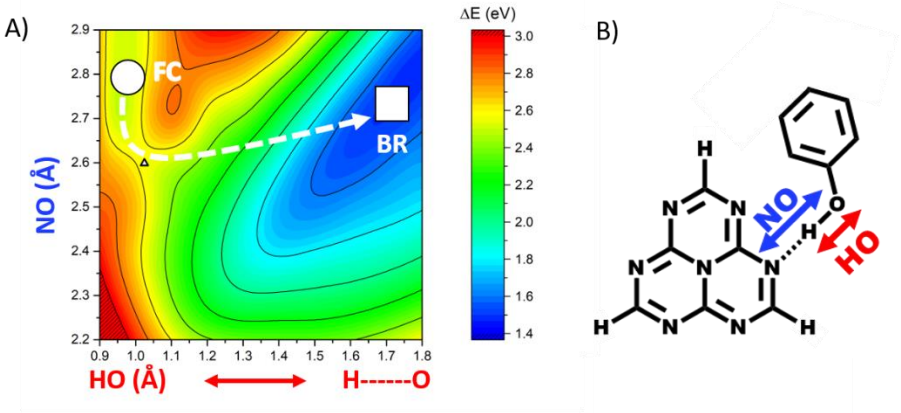

Figure 5-6. 2D potential energy surface of the S_1 excited state of the Hz-PhOH complex. The reaction coordinates are the OH bond length of PhOH and the distance between the O-atom of PhOH and N-atom of Hz, see (B). The circle designates the energy minimum of the locally excited (LE) state in the Frank Condon (FC) region. The square indicates the equilibrium geometry of the HzH···PhO biradical (BR) formed by H-atom transfer. A saddle point (marked by the triangle) separates the two energy minima.

Figure 5-6A shows the two-dimensional relaxed S_1 potential energy surface of the Hz-PhOH complex. For small OH distances, the H-atom is covalently bonded to the oxygen atom of PhOH and forms a hydrogen bond with a peripheral nitrogen atom of Hz. For large OH distances, on the other hand, the H-atom is covalently bonded to the nitrogen atom of Hz (forming the heptazinyl (HzH) radical) and is hydrogen bonded with the phenoxy (PhO) radical. The 2D relaxed energy surface clearly exhibits two minima. The minimum for small OH distances is the energy minimum of the LE state in the FC region (indicated by the white circle in Figure 5-6A). The second minimum at large OH distances (indicated by the white square in Figure 5-6A) represents the HzH-PhO biradical. For the ES-PCET transfer to occur, the photoexcited complex must overcome the barrier separating the two minima, which is indicated by the triangle in Figure 5-6A. At the saddle point, the wave function of the S_1 state changes from a $\pi\pi^*$ state of LE character to a $\pi\pi^*$ state of

CT character. For the Hz-PhOH complex, the energy of the saddle point is 2.68 eV above the energy minimum of the S_0 state and the barrier height is 0.167 eV.

Figure 5-7 shows the 2D relaxed S_1 energy surfaces of the Hz-CN-PhOH (A) and Hz-OCH_3-PhOH (B) complexes. These are the systems with the highest (Hz-CN-PhOH) and lowest (Hz-OCH_3-PhOH) barrier for the ES-PCET reaction. For CN-PhOH-Hz, the energy of the transition state is 2.89 eV above the S_0 energy minimum and the height of the barrier of the PCET reaction is 0.369 eV. The comparatively high barrier is a consequence of the electron-withdrawing character of the cyano (CN) group of the Hz-CN-PhOH complex, which leads to a blue shift of the CT state compared to the Hz-PhOH complex (E_{CT}^{GS} = 3.86 eV, see Table B-0-1 in Appendix B). The methoxy (OCH_3) group of the OCH_3-PhOH complex (Figure 5-7B), on the other hand, is a relatively strong electron-donating group which causes a substantial red shift of the CT state (E_{CT}^{GS} = 2.80 eV, see Table B-0-1 in Appendix B). The vertical excitation energies of the CT states of Hz-CN-PhOH and Hz-OCH_3-PhOH differ by the amazing amount of more than 1.0 eV. For Hz-OCH_3-PhOH, the red shift of the CT state is large enough to eliminate the barrier on the S_1 potential energy surface, see Figure 5-7B. The theoretically predicted barrierless ES-PCET reaction matches the experimental observations for OCH_3-PhOH: no observable fast PL component attributable to a hydrogen-bonded complex and no significant KIE.

Additional *ab initio* data (vertical excitation energies of the LE and CT states and vibrational stabilization energies of the LE state) are collected in Table B-0-1 in Appendix B. The molecular structures of the transition states of the six Hz-R-PhOH complexes are displayed in Figure B-0-22 in Appendix B. The lengths of the OH···N hydrogen bonds at the transition state are specified in this figure. While the vertical excitation energies of the S_1 states, E_1^{GS}, and the minimum-to-minimum excitation energies of the LE states, E_1^{min}, differ by merely 0.02 eV, the energies of the

transition state, E_1^{TS}, vary substantially for the substituents R on PhOH, resulting in a significant variation of the barrier height $\Delta E^{\ddagger}$. The stronger the electron-donating character of the substituent, the lower the barrier. Importantly, the barrier height $\Delta E^{\ddagger}$ and the vertical excitation energy of the CT state, E_{CT}^{GS}, are strongly correlated. While the latter decreases by about 1.0 eV from the CN substituent to the OCH_3 substituent, the barrier height changes by 0.37 eV. These findings imply that the vertical excitation energy of the CT state can be used as a proxy for the relative barrier height in future *ab initio* screening studies of carbon nitride photocatalysts.

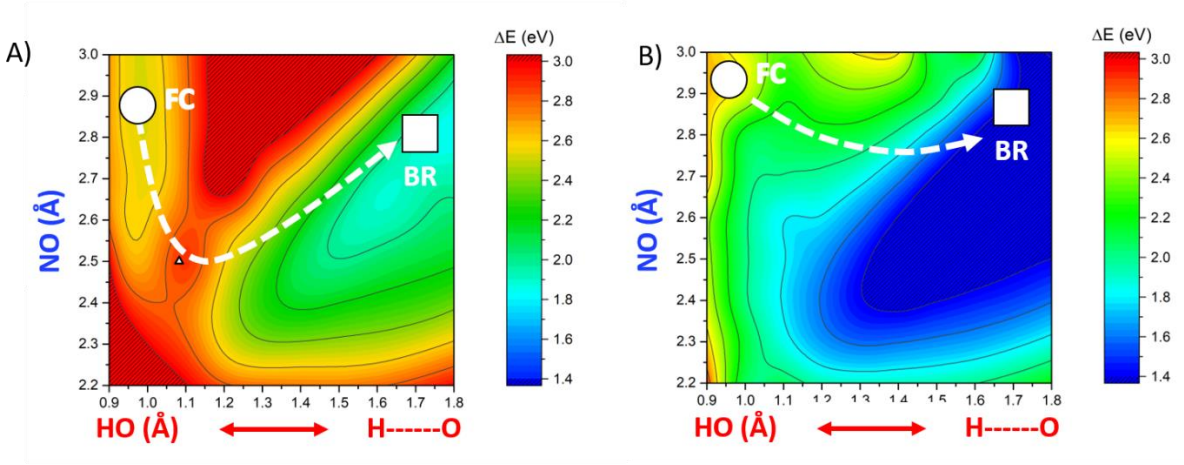

Figure 5-7. 2D potential energy surface of the S_1 excited state of the CN-PhOH-Hz complex. (A) and the heptazine-methoxyphenol (B) complexes computed at the ADC(2) level. See caption ofFigure 5-6 for the definition of the reaction coordinates. The heptazine-methoxyphenol complex (B) exhibits a barrierless S1 potential energy surface.

5.2.5 *Implications for Molecular Design*

While the limited solubility of TAHz restricts our ability to reliably estimate pK_a and ΔG_{PCET} values, we can readily infer that proton motion must play a significant role in the photochemical reactivity of TAHz since the excited state reduction potential of the free chromophore is 1.48V vs SHE. Comparing the potentials for the isolated half reactions, this reduction potential would be insufficient to drive oxidation of any of the PhOHs in the series that we have studied here.

Fortunately, we can glean critical insight by examining *ab initio* computational results for the barrier height $\Delta E^{\ddagger}$ of the ES-PCET reaction from PhOH to the Hz core. The computed $\Delta E^{\ddagger}$ values exhibit a reasonable correlation with the rate constants for excited state quenching plotted in Figure 5-8. We observe that the greater the degree of electron-donating character of the substituent on the PhOH, the lower the value of $\Delta E^{\ddagger}$, and the faster the excited-state quenching. This trend suggests that chemically inverting this effect by appending strongly electron-withdrawing moieties to the heptazine core, could significantly increase the rate constant for the ES-PCET reaction of a hydrogen-bonded Hz-water complex. However, it is interesting to note that for PhOH derivatives with similar oxidation potentials, Cl-PhOH, PhOH, and Br-PhOH, the effect of hydrogen bonding is evident. The PhOHs with lower pKa's have larger K_A values, stronger hydrogen bonds and greater quenching rate constants. Achieving efficient intermolecular ES-PCET in hydrogen-bonded aza-arene-water complexes could lay the groundwork to kick off a variety of future applications with the potential to utilize compelling reactions with these photogenerated hydroxyl and heptazinyl radical species, including hydrogen production, CO_2 reduction, and municipal waste-water decontamination.

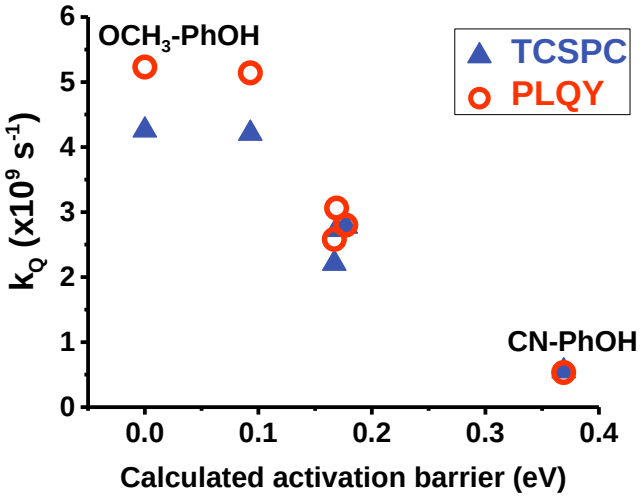

Figure 5-8. Correlation between the calculated activation barrier and the excited-state quenching rate constants.

Quenching rate constants were determined by PLQY (red open circles) and TCSPC (blue triangles). Overall, we see a significant increase in the excited-state quenching rate as the phenol substituent becomes more electron-donating. We see a greater difference between the two methods as the calculated activation barrier decreases, indicating that the rate of ES-PCET is limited by diffusion and complex formation.

5.3 CONCLUSIONS

We hypothesized that the rate of ES-PCET of heptazine chromophores and hydroxylic compounds could be controlled by tuning the excited state barrier height for H-atom abstraction. We have proposed that this tunability could be achieved by adding electron-donating groups to the hydroxylic compound (Figure 5-1). We present a combined experimental and theoretical study to assess the validity of such a design strategy by adding electron-donating groups to PhOH, acting as a model hydroxylic species. In support of our hypothesis, we observe increased quenching rate constants for PhOH derivatives with more electron-donating substituents. The ES-PCET reactivity is found to be governed by the barrier height $\Delta E^{\ddagger}$ on the potential energy surface of the long-lived S_1 state of the TAHz-PhOH complex, which in turn scales with the vertical excitation energy of the Hz-to-PhOH CT state. In the case of the most electron-donating PhOH, OCH_3-PhOH, we computationally predict and experimentally verify that the excited state H-atom transfer reaction becomes barrierless in the S_1 excited state of the hydrogen-bonded complex. This increased reactivity does not come at a significant cost of hydrogen-bonding as the K_A for TAHz-OCH_3-PhOH and TAHz-PhOH are essentially the same.

It is common practice in photocatalytic hydrogen evolution experiments, for example with g-C_3N_4 photocatalysts, to use sacrificial electron donors such as triethanolamine (TEOA), triethylamine (TEA), or methanol.[5] While TEOA and TEA are the most widely employed sacrificial electron donors in this context, a systematic investigation of the mechanistic role of

different sacrificial electron donors apparently has not been performed. Herein, we presented a systematic and theory-supported analysis of the ES-PCET reactivity for the TAHz photocatalyst with substituted PhOHs as sacrificial electron donors. The oxidation potentials E_0 of the electron donors vary from 1.40 eV (CN-PhOH) to 1.05 eV (OCH_3-PhOH) (Table 5-1). The *ab initio* computed reaction barriers vary from 0.369 eV for CN-PhOH to zero (no barrier) for OCH_3-PhOH, following closely the trend of the oxidation potentials. While it is comparatively easy to photo-oxidize sacrificial electron donors with low oxidation potentials, the challenge consists in the efficient photo-oxidation of water molecules with visible light. Rather than lowering the oxidation potential of the solvent, the reduction potential of the photocatalyst should be increased such that hydrogen-bonded water molecules can be oxidized in a barrierless and therefore efficient ES-PCET reaction. We conjecture that this can be achieved with Hz-based photocatalysts by adding strong electron withdrawing groups to the Hz core. Synthetic efforts guided by *ab initio* electronic structure-calculations are currently underway in our laboratories to experimentally develop this scenario. Interesting questions remain regarding the nature of the proton-transfer mechanism (tunneling vs. barrier-crossing) and the fate of the radicals that are produced.

5.4 Experimental Methods

Reagents. Urea, potassium hydroxide, phosphorous oxychloride, phosphorous pentachloride, phenol, and deuterated methanol (MeOD) were all purchased from Sigma Aldrich. Anisole (99%) was purchased from Alfa Aesar. Aluminum chloride was purchased from Fischer Scientific. 4-

methoxyphenol, 4-bromophenol, p-cresol, 4-chlorophenol, and 4-hydroxybenzonitrile were all purchased from TCI. All reagents were used without further purification.

Sample Preparation. TAHz was dissolved in toluene (100 μM) and stirred overnight before measurements were preformed to ensure minimal aggregation effects and accurate concentrations were prepared. Samples were kept in the dark until measurements were performed.

Ground State Absorption. Ground-state absorption spectra were collected with a Cary5000 UV−vis−NIR spectrometer. Within each R-PhOH series, the same TAHz stock solution was used to ensure consistent TAHz concentration with the varying phenol concentrations.

Time-Correlated Single-Photon Counting (TCSPC). Unless otherwise stated, TCSPC PL lifetimes were measured using a PicoQuant FluoTime 100 with a 375 nm laser diode excitation. Lifetimes measured out to 2 μs were triggered using an external function generator at 500 kHz.

Photoluminescence Quantum Yields. PLQY's were measured on a Hamamatsu external quantum efficiency measurement system (C9920-12). All PLQY's reported were excited with 365 nm light and the PL was integrated from 440 to 800 nm.

Time-Resolved Photoluminescence (TR-PL) Spectra. TR-PL spectra were collected using a Hamamatsu streak camera (C10910) with a slow-sweep unit (M10913-01) in photon counting mode. Samples were irradiated with 50 fs pulses at 365 nm and 1 kHz pump from a Coherent/Light Conversion OPerA solo optical parametric amplifier (OPA). Pump fluences were 2.7×10^{13} photons cm^{-3} unless otherwise stated.

Synthesis.

Graphitic carbon nitride: Briefly, urea (10 g) was heated in a porcelain crucible (20 mL) using a potter's kiln at 500 °C for 3 h, with a ramp rate of 30 °C per hour under ambient atmosphere.

The light-yellow product was ground thoroughly with a mortar and pestle prior to use in further reactions.

Potassium cyamelurate: 4.5 g of graphitic carbon nitride was refluxed in KOH (3.0 M, 150 mL) for 6 h. The solution was hot filtered over a glass frit and then cooled for recrystallization. The resulting white crystals were filtered and washed with cold ethanol.

Cyameluric chloride: Phosphorous oxychloride (35 mL) was added to a flame-dried round-bottom flask with a stir bar. Phosphorous pentachloride (4.6 g) was added and allowed to stir for 5 minutes. Potassium cyamelurate (2.0 g) was added and the suspension was refluxed under N_2 at 110°C for 6 hrs. $POCl_3$ was removed under reduced pressure using a distillation set-up in the fume hood. The remaining solution was put on ice and ice water (50 mL) was added dropwise while stirring. The product was vacuum filtered and washed with ice-cold water. The resulting product was dried under vacuum for a few hours and stored in a desiccator. Safety note: $POCl_3$ and PCl_5 react with water exothermically to produce HCl gas and H_3PO_4. Always keep these reagents in a ventilated chemical fume hood and quench slowly with sodium bicarbonate.

2,5,8-tris(4-methoxyphenyl)-1,3,4,6,7,9,9b-heptaazaphenalene (TAHz): Anisole (10 mL) was purged with nitrogen for at least 15 minutes. Aluminum chloride (4.0 g) was added to the flask and allowed to stir for a few minutes at 60°C. Cyameluric chloride (1.0 g) was added slowly over 30 minutes. The reaction mixture was stirred at 60°C under nitrogen for 5 hours. Deionized water (25 mL) was added and the solution was stirred until the color changed to yellow and the large chunks dissolved. The resulting bright yellow powder was filtered and washed with ice cold water.

The product was purified by slowly recrystallizing in hot DMSO. Characterization of TAHz is shown in our previous manuscript.[23]

Deuterating phenols were done according to literature precedent.[38] Briefly, 0.5 g of each phenol was dissolved in deuterated methanol (MeOD) in a dried round bottom flask and stirred for 1 hour. Methanol was removed under vacuum and the procedure was repeated a second time to give the deuterated phenol. The product was confirmed by ^{1}H-NMR to be >80% deuterated.

5.5 REFERENCES

1. Mora, S. J.; Odella, E.; Moore, G. F.; Gust, D.; Moore, T. A.; Moore, A. L., Proton-Coupled Electron Transfer in Artificial Photosynthetic Systems. *Acc. Chem. Res.* **2018,** *51* (2), 445-453.
2. Wang, J. L.; Xu, L. J., Advanced Oxidation Processes for Wastewater Treatment: Formation of Hydroxyl Radical and Application. *Crit. Rev. Env. Sci. Technol.* **2012,** *42* (3), 251-325.
3. Pearson, R. M.; Lim, C.-H.; McCarthy, B. G.; Musgrave, C. B.; Miyake, G. M., Organocatalyzed Atom Transfer Radical Polymerization Using N-Aryl Phenoxazines as Photoredox Catalysts. *J. Am. Chem. Soc.* **2016,** *138* (35), 11399-11407.
4. Theriot, J. C.; Lim, C. H.; Yang, H.; Ryan, M. D.; Musgrave, C. B.; Miyake, G. M., Organocatalyzed Atom Transfer Radical Polymerization Driven by Visible Light. *Science* **2016,** *352* (6289), 1082-6.
5. Ong, W.-J.; Tan, L.-L.; Ng, Y. H.; Yong, S.-T.; Chai, S.-P., Graphitic Carbon Nitride (g-C3N4)-Based Photocatalysts for Artificial Photosynthesis and Environmental Remediation: Are We a Step Closer To Achieving Sustainability? *Chem. Rev.* **2016,** *116* (12), 7159-7329.
6. Concepcion, J. J.; Brennaman, M. K.; Deyton, J. R.; Lebedeva, N. V.; Forbes, M. D. E.; Papanikolas, J. M.; Meyer, T. J., Excited-State Quenching by Proton-Coupled Electron Transfer. *J. Am. Chem. Soc.* **2007,** *129* (22), 6968-6969.
7. Weinberg, D. R.; Gagliardi, C. J.; Hull, J. F.; Murphy, C. F.; Kent, C. A.; Westlake, B. C.; Paul, A.; Ess, D. H.; McCafferty, D. G.; Meyer, T. J., Proton-Coupled Electron Transfer. *Chem. Rev.* **2012,** *112* (7), 4016-4093.
8. Lennox, J. C.; Kurtz, D. A.; Huang, T.; Dempsey, J. L., Excited-State Proton-Coupled Electron Transfer: Different Avenues for Promoting Proton/Electron Movement with Solar Photons. *ACS Enery Lett.* **2017,** *2* (5), 1246-1256.
9. Damrauer, N. H.; Hodgkiss, J. M.; Rosenthal, J.; Nocera, D. G., Observation of Proton-Coupled Electron Transfer by Transient Absorption Spectroscopy in a Hydrogen-Bonded, Porphyrin Donor−Acceptor Assembly. *J. Phys. Chem. B* **2004,** *108* (20), 6315-6321.
10. Eisenhart, T. T.; Dempsey, J. L., Photo-induced Proton-Coupled Electron Transfer Reactions of Acridine Orange: Comprehensive Spectral and Kinetics Analysis. *J. Am. Chem. Soc.* **2014,** *136* (35), 12221-12224.

11. Liu, X.; Karsili, T. N.; Sobolewski, A. L.; Domcke, W., Photocatalytic Water Splitting with the Acridine Chromophore: A Computational Study. *J. Phys. Chem. B* **2015,** *119* (33), 10664-72.
12. Reimers, J. R.; Cai, Z.-L., Hydrogen Bonding and Reactivity of Water to Azines in Their S1 (n,pi*) Electronic Excited States in the Gas Phase and in Solution. *Phys. Chem. Chem. Phys.* **2012,** *14* (25), 8791-8802.
13. Whitten, D. G.; Lee, Y. J., Photochemistry of aza aromatics. Identification of the reactive intermediate in the photoreduction of acridine. *J. Am. Chem. Soc.* **1971,** *93* (4), 961-966.
14. Peon, J.; Tan, X.; Hoerner, J. D.; Xia, C.; Luk, Y. F.; Kohler, B., Excited State Dynamics of Methyl Viologen. Ultrafast Photoreduction in Methanol and Fluorescence in Acetonitrile. *J. Phys. Chem. A* **2001,** *105* (24), 5768-5777.
15. Stermitz, F. R.; Wei, C. C.; O'Donnell, C. M., Photochemistry of n-Heterocycles. V. Photochemistry of Quinoline and Some Substituted Quinoline Derivatives. *J. Am. Chem. Soc.* **1970,** *92* (9), 2745-2752.
16. Arias-Rotondo, D. M.; McCusker, J. K., The Photophysics of Photoredox Catalysis: A Roadmap for Catalyst Design. *Chem. Soc. Rev.* **2016,** *45* (21), 5803-5820.
17. Corp, K. L.; Schlenker, C. W., Ultrafast Spectroscopy Reveals Electron-Transfer Cascade That Improves Hydrogen Evolution with Carbon Nitride Photocatalysts. *J. Am. Chem. Soc.* **2017,** *139* (23), 7904-7912.
18. Zhang, G.; Lin, L.; Li, G.; Zhang, Y.; Savateev, A.; Zafeiratos, S.; Wang, X.; Antonietti, M., Ionothermal Synthesis of Triazine–Heptazine-Based Copolymers with Apparent Quantum Yields of 60 % at 420 nm for Solar Hydrogen Production from "Sea Water". *Angew. Chem. Int. Ed.* **2018,** *57* (30), 9372-9376.
19. Wang, X.; Maeda, K.; Thomas, A.; Takanabe, K.; Xin, G.; Carlsson, J. M.; Domen, K.; Antonietti, M., A Metal-Free Polymeric Photocatalyst for Hydrogen Production from Water Under Visible Light. *Nat. Mater.* **2008,** *8*, 76.
20. Ullah, N.; Chen, S.; Zhao, Y.; Zhang, R., Photoinduced Water–Heptazine Electron-Driven Proton Transfer: Perspective for Water Splitting with g-C3N4. *J. Phys. Chem. Lett.* **2019,** *10* (15), 4310-4316.
21. Domcke, W.; Ehrmaier, J.; Sobolewski, A. L., Solar Energy Harvesting with Carbon Nitrides and N-Heterocyclic Frameworks: Do We Understand the Mechanism? *Chem. Photo. Chem.* **2019,** *3* (1), 10-23.
22. Ehrmaier, J.; Karsili, T. N. V.; Sobolewski, A. L.; Domcke, W., Mechanism of Photocatalytic Water Splitting with Graphitic Carbon Nitride: Photochemistry of the Heptazine–Water Complex. *J. Phys. Chem. A* **2017,** *121* (25), 4754-4764.
23. Rabe, E. J.; Corp, K. L.; Sobolewski, A. L.; Domcke, W.; Schlenker, C. W., Proton-Coupled Electron Transfer from Water to a Model Heptazine-Based Molecular Photocatalyst. *J. Phys. Chem. Lett.* **2018,** *9* (21), 6257-6261.
24. Caspar, J. V.; Meyer, T. J., Photochemistry of tris(2,2'-bipyridine)ruthenium(2+) ion (Ru(bpy)32+). Solvent effects. *J. Am. Chem. Soc.* **1983,** *105* (17), 5583-5590.
25. McCusker, J. K., Electronic Structure in the Transition Metal Block and Its Implications for Light Harvesting. *Science* **2019,** *363* (6426), 484-488.
26. Turro, N. J.; Ramamurthy, V.; Scaiano, J. C., *Principles of Molecular Photochemistry: An Introduction*. University Science Books Sausalito, California, 2009.

27. Ehrmaier, J.; Rabe, E. J.; Pristash, S. R.; Corp, K. L.; Schlenker, C. W.; Sobolewski, A. L.; Domcke, W., Singlet-Triplet Inversion in Heptazine and in Polymeric Carbon Nitrides. *The journal of physical chemistry. A* **2019,** *123* (38), 8099-8108.
28. Barman, N.; Singha, D.; Sahu, K., Fluorescence Quenching of Hydrogen-Bonded Coumarin 102-Phenol Complex: Effect of Excited-State Hydrogen Bonding Strength. *J. Phys. Chem. A* **2013,** *117* (19), 3945-3953.
29. Hossen, T.; Sahu, K., New Insights on Hydrogen-Bond-Induced Fluorescence Quenching Mechanism of C102–Phenol Complex via Proton Coupled Electron Transfer. *J. Phys. Chem. A* **2018,** *122* (9), 2394-2400.
30. Bronner, C.; Wenger, O. S., Proton-Coupled Electron Transfer between 4-Cyanophenol and Photoexcited Rhenium(I) Complexes with Different Protonatable Sites. *Inorg. Chem.* **2012,** *51* (15), 8275-8283.
31. Bronner, C.; Wenger, O. S., Kinetic Isotope Effects in Reductive Excited-State Quenching of Ru(2,2′-bipyrazine)32+ by Phenols. *J. Phys. Chem. Lett.* **2012,** *3* (1), 70-74.
32. Warren, J. J.; Tronic, T. A.; Mayer, J. M., Thermochemistry of Proton-Coupled Electron Transfer Reagents and its Implications. *Chem. Rev.* **2010,** *110* (12), 6961-7001.
33. Dongare, P.; Bonn, A. G.; Maji, S.; Hammarström, L., Analysis of Hydrogen-Bonding Effects on Excited-State Proton-Coupled Electron Transfer from a Series of Phenols to a Re(I) Polypyridyl Complex. *The Journal of Physical Chemistry C* **2017,** *121* (23), 12569-12576.
34. Petersson, J.; Hammarström, L., Ultrafast Electron Transfer Dynamics in a Series of Porphyrin/Viologen Complexes: Involvement of Electronically Excited Radical Pair Products. *J. Phys. Chem. B* **2015,** *119* (24), 7531-7540.
35. Yamaji, M.; Oshima, J.; Hidaka, M., Verification of the electron/proton coupled mechanism for phenolic H-atom transfer using a triplet π,π∗ carbonyl. *Chem. Phys. Lett.* **2009,** *475* (4-6), 235-239.
36. Snellenburg, J. J.; Laptenok, S. P.; Seger, R.; Mullen, K. M.; van Stokkum, I. H. M., Glotaran: A Java-Based Graphical User Interface for the R Package TIMP. *J. Stat. Softw.* **2012,** *49* (3), 1-22.
37. Schirmer, J., Beyond the random-phase approximation: A new approximation scheme for the polarization propagator. *Phys. Rev. A* **1982,** *26* (5), 2395-2416.
38. Bronner, C.; Wenger, O. S., Kinetic Isotope Effects in Reductive Excited-State Quenching of Ru(2,2′-bipyrazine)32+ by Phenols. *J. Phys. Chem. Lett.* **2012,** *3* (1), 70-74.

Chapter 6. Intermolecular hydrogen bonding tunes vibronic coupling in heptazine complexes

6.1 SUMMARY

To better understand how hydrogen-bonding influences the excited-state landscapes of aza-aromatic materials, we studied hydrogen-bonded complexes of 2,5,8-tris(4-methoxyphenyl)-1,3,4,6,7,9,9b-heptaazaphenalene (TAHz), a molecular photocatalyst related to graphitic carbon nitride, with a variety of phenol derivatives (R-PhOH's). By varying the electron-withdrawing character of the para-substituent on the phenol, we can modulate the strength of the hydrogen bond. Using time-resolved photoluminescence, we extract a spectral component associated with the R-PhOH-TAHz hydrogen-bonded complex. Surprisingly, we noticed a striking change in the relative amplitude of vibronic peaks in the TAHz-centered emission as a function of R-group on phenol. To gain a physical understanding of these spectral changes, we employed a displaced-oscillator model of molecular emission to fit these spectra. This fit assumes two vibrational modes are dominantly coupled to the emissive electronic transition and extracts their frequencies and relative nuclear displacements (related to Huang-Rhys factor). With the aid of quantum chemical calculations, we found heptazine ring breathing and ring puckering modes are likely responsible for the observed vibronic progression, and both modes indicate decreasing molecular distortion in the excited-state with increasing hydrogen-bond strength. This finding offers new insight into intermolecular excited-state hydrogen-bonding, which is a crucial step towards controlling excited-state proton-coupled electron transfer and proton-transfer reactions.

6.2 INTRODUCTION

Excited-state proton transfer and proton-coupled electron transfer (ES-PCET) reactions are ubiquitous in biological and chemical transformations such as photosynthesis and

photopolymerization.[1-4] For these reactions, understanding the interplay between electronic and vibrational motions within a hydrogen-bonded complex is critical.[5-6] Yet, studying hydrogen-bonding, especially in the excited state, is complicated given the short lifetimes, dynamic reorganizations, and numerous photochemical branching pathways of these complexes.[7-10] This has led to ambiguity in even simple quantities such as the excited-state hydrogen-bonding association constants, as the calculation requires deconvoluting the rate of excited-state hydrogen-bond formation and excited-state reactivity.[11] The picture becomes further complicated by the presence of multiple hydrogen-bonding sites for many heteroaromatic materials and the hydrogen-bonding networks created by high concentrations of hydrogen-bond donors.[10, 12] These complications must be considered in order to understand and control the reactivity of intermolecular complexes, and generally map how the excited-state landscape is influenced by hydrogen-bond formation.

Past work considering intermolecular ES-PCET reactions has demonstrated that the hydrogen-bond coordinate can largely predict excited state reactivity by calculating the energy of a charge transfer state along that hydrogen-bond coordinate.[13-15] In this framework, we generally assume changing the quencher (hydrogen-bond donor) alters only the energy and position of the charge transfer state, which ultimately determines reaction rates. It is relatively rare to consider the chromophore's intrinsic molecular vibrations as a significant contributor to intermolecular PCET, despite the need for coordination of nuclear and electronic motion across a hydrogen bond.[5] However, there has been a great deal of work to understand the interconnectedness of molecular vibrations and proton transfer in the context of intramolecular hydrogen-bonding, particularly with the aid of ultrafast IR spectroscopy.[16-17] This work has shown how O-H stretching frequencies can couple to lower frequency molecular vibrations of a chromophore, which is somewhat intuitive

since all the atoms are covalently linked. It is currently an open question as to what extent this insight extends to intermolecular chemical reactions and whether it is possible to manipulate reaction dynamics or pathways by vibrational excitation.

If achievable, this kind of reaction control would be extremely useful in the context of poly(heptazine imides), commonly termed carbon nitride, which has become a model organic material for driving a host of intermolecular photochemical reactions[18-22] Yet fundamental photophysical studies aimed at understanding the ground and excited-state hydrogen bonding of these materials are currently rare, owing to the structural ambiguity in this nitrogen-rich material.[23-24] To gain insight into the heptazine hydrogen-bonding, integral to several carbon nitride catalyzed reactions, we have chosen a model heptazine-based chromophore (TAHz), previously used to study the heptazine-driven ES-PCET reaction.[15, 25-26] In those previous studies, we found the quenching rate constant of TAHz with different phenols generally followed the driving force for electron transfer.[15] However, when comparing H-PhOH and Cl-PhOH, which have the same oxidation potential, we observed a faster quenching rate constant for Cl-PhOH. Barman and coworkers observed a similar effect with coumarin and attributed this to hydrogen-bonding.[9] In this study, we explore how hydrogen-bonding influences the excited-state energy landscape and reactivity using time-resolved photoluminescence spectroscopy (TR-PL) together with a displaced-oscillator model of molecular emission and quantum chemical calculations. We use TR-PL to extract emission spectra from hydrogen-bonded complexes of heptazine using global analysis.[15] As we change the Hammett parameter of the phenol derivative, we notice a surprising change in the vibronic progression of emission from the hydrogen-bonded complexes. Analysis of the spectral lineshape provides insight beyond the strength of the hydrogen-bond and allows us to understand how hydrogen bonding influences molecular distortions between the ground and

excited states. Modeling the vibronic excitations as a pair of displaced harmonic oscillators captures the spectral shape of emission from these hydrogen-bonded complexes and allows us to extract both a high and low frequency mode that are significantly coupled to the S_1 transition.[27] From this analysis, we quantify how the displacement along representative nuclear coordinates change as a function of the R-group on the hydrogen-bonded phenol. Using quantum chemical calculations, we further visualize representative vibrational modes to build a more holistic picture of how molecular distortions can affect ES-PCET and ES-PT reactivity.

6.3 Results and Discussion

6.3.1 *Varying the Phenol to Increase Hydrogen Bond Strength*

Substituted phenols are ubiquitous in systematic studies on PT and PCET reactions.[2, 28-29] Phenols are often considered to act as "functionalized water," wherein we can change the oxidation potential and pKa of the hydroxyl group by changing a functional group on the phenyl ring. However, these two properties are often intertwined; adding an electron withdrawing group to the phenol will likely increase its oxidation potential and decrease its pKa. Previously, we focused on the quenching rate constant as a function of oxidation potential for heptazine-phenol systems.[15] In this study, we are interested in exploring the hydrogen-bonded complexes formed and understanding how the energy landscape is perturbed by changing the electronic nature of the R-group. To quantify the electron-withdrawing strength of the R-group, we will use the calculated Hammett parameter for each substituent in the para-position, values shown in Table 6-1.[30] These well-accepted parameters allow us to quantitatively rank a wide range of phenols as we explore their hydrogen-bonded complexes formed with TAHz, shown in Figure 6-1A.

To study the strength of ground-state hydrogen-bonded complexes, it is common to use ground state absorption spectroscopy to monitor the free versus bound populations as a function of the

concentration of the H-bond donor.[11-12, 31] The absorption spectrum of TAHz, and other heptazine derivatives, comprises a series of closely spaced electronic transitions with varying oscillator strengths and is discussed in detail elsewhere.[15, 25-26, 32] Briefly, the strong peak seen at 365 nm in Figure 6-1B is attributed to a bright intramolecular charge transfer $\pi\pi^*$ transition and the lowest-lying transition shown in the inset of Figure 6-1B is attributed to the symmetry-forbidden $S_1(\pi\pi^*)$ state. To study how the strength of hydrogen-bonding affects these electronic transitions, we can compare the absorption spectrum of TAHz in the presence of different R-PhOH's. When the same concentration of each phenol is present with TAHz in toluene, we observe variations in the magnitude of peak shifts in Figure 6-1B. We observe that larger shifts correlate with larger Hammett parameters. As expected, this suggests that higher association constants, indicating stronger hydrogen bonds, are seen for more electron-withdrawing R groups on the phenol species. This is supported by quantum chemical calculations of the H-bond length for each TAHz-R-PhOH complex listed in Table 6-1 and previous K_A estimates.[15].

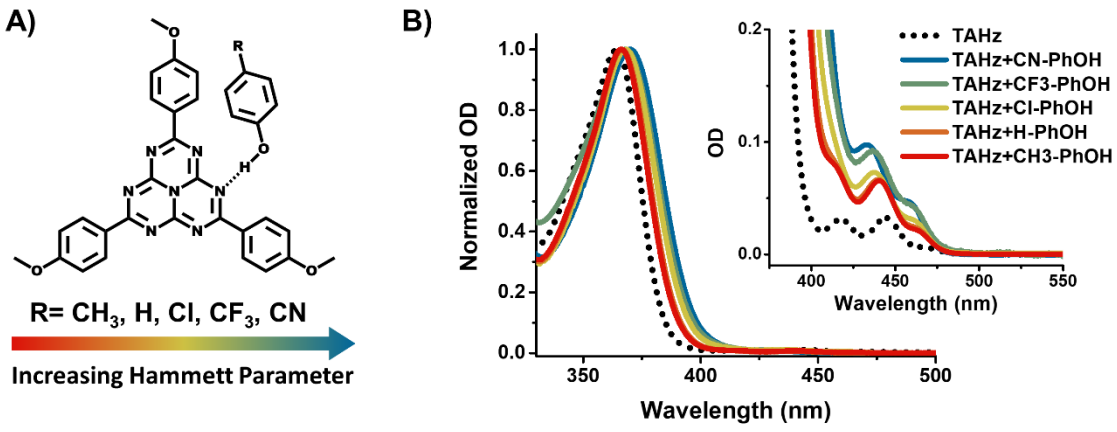

Figure 6-1. Phenol system and absorption profiles

A) Para-substituted phenols serve as a model system for understanding how changing electronegativity, quantified by the Hammett parameter, changes the hydrogen-bond strength with heptazine. B) The effect of increasing Hammett parameter can be seen in the ground state

absorption of TAHz in toluene. The bright $\pi\pi^*$ transition redshifts with increasing Hammett parameter. The lower-energy and weaker transitions (inset) appear to show the opposite effect: they blueshift and begin to overlap with the tail of the bright transition. All phenol concentrations were 50 mM.

Previously, we analyzed TAHz-R-PhOH complexes assuming only conversion from unbound TAHz to TAHz-PhOH and estimated K_A's accordingly.[15] However, heptazine-based materials, and TAHz specifically, are capable of forming multiple hydrogen bonds due to the numerous heteroatoms. Multiple hydrogen bonds can complicate the analysis as different hydrogen-bonded complexes can have different spectral features. This is evident in the absence of a clear isosbestic point upon increasing the hydrogen-bond donor concentration. The spectral shape does not converge to that of a hydrogen-bonded complex; therefore, it requires deconvolution to extract the absorption spectra associated with different hydrogen-bonded complexes from concentration-dependent absorption data. Using the framework laid out by Demeter and co-workers, we are able to model the concentration-dependent absorption spectra assuming TAHz undergoes two distinct hydrogen-bonding events with two association constants.[12] Under this assumption we can model the total absorption at wavelength λ as the sum of three component spectra $A_\lambda = \epsilon_{T\lambda}[T] + \epsilon_{TX\lambda}[TX] + \epsilon_{TX_2\lambda}[TX_2]$, where $\epsilon_{T\lambda}$, $\epsilon_{TX\lambda}$, $\epsilon_{TX_2\lambda}$ are the molar extinction coefficients of TAHz (T), a 1:1 complex of TAHz-PhOH (TX), and a 1:2 complex of TAHz-$(PhOH)_2$ (TX_2). We can express [TX] and [TX_2] in terms of concentration of phenol and the two association constants (K_1 and K_2), described in detail in Appendix C. By performing a least squares fit to the absorption vs [PhOH] curves iteratively for each wavelength, we are able to extract the parameters $\epsilon_{TX\lambda}$, $\epsilon_{TX_2\lambda}$, K_1, and K_2. While TAHz could form more than two hydrogen bonds, the data appears to be fit well by accounting for only two distinct spectral shapes, see Figure C-0-1.

Figure 6-2B compares the molar absorptivity spectrum of TAHz compared to the extracted spectra for TAHz-PhOH and TAHz-$(PhOH)_2$. However, despite being able to extract the

absorption spectra for the TAHz-PhOH and TAHz-$(PhOH)_2$ complexes shown in Figure 6-2B, the red-shifting of the bright $\pi\pi^*$ state and the blue-shifting of the S_1 state obscures the vibronic progression for these hydrogen-bonded complexes. So, while we would ideally compare vibronic structure in both the absorption and emission spectra, we must instead rely on TR-PL measurements where we can kinetically resolve individual emission components. Additionally, using the two extracted K_A values, we can estimate the relative amounts of each complex at the time of excitation for a given phenol concentration and chose our conditions accordingly.

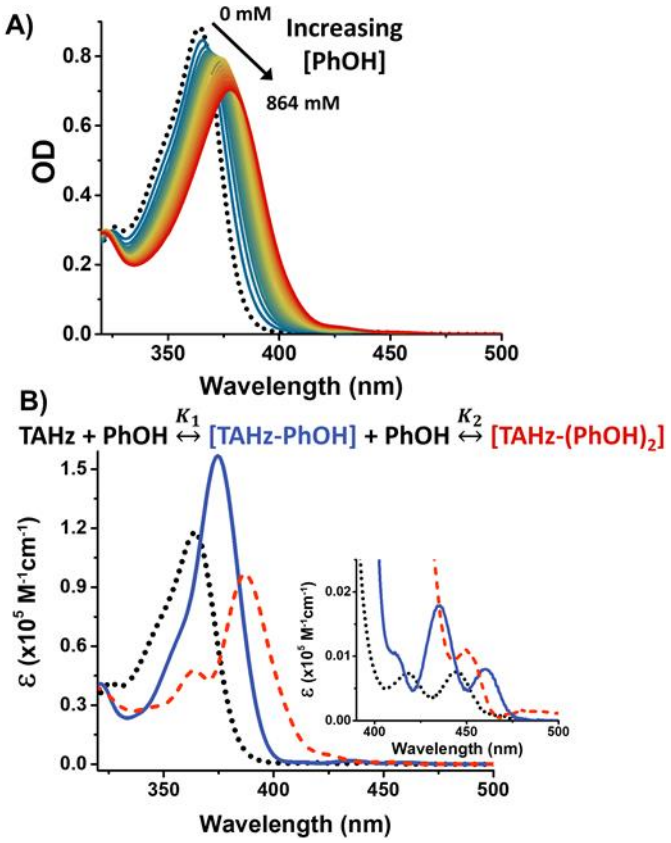

Figure 6-2. Two-component association model

A) Ground-state absorption spectra of TAHz in neat toluene (dotted back line) and upon increasing PhOH concentrations ranging from 30-860 mM (blue to red). The lack of a clear isosbestic point suggested there are more than two absorbing species, this could be due to the existence of a second hydrogen-bonded complexation. The measurement was taken by sequential additions of a 3 M PhOH stock solution and the resulting spectra were corrected for changing TAHz concentration.

B) The data fit well to a double-complexation model and using an iterative least squares method, we were able to extract the individual components. The extracted traces for unbound (black dotted), singly bound (blue solid), and doubly-bound (dashed red) show a red-shift of the bright transition and blue-shift of the weak transitions.

6.3.2 *Time-Resolved Photoluminescence*

In the absence of a hydrogen-bonding donor, the TAHz emission exhibits a monoexponential decay (Figure C-0-2). When a hydrogen-bond donor, such as phenol, is present then we observe two kinetically distinct components. Keeping in mind the possibility of a 1:2 complex, we chose a low concentration of phenol (100 mM) in order to focus our study on the 1:1 complex. From the K_A values extracted above, we can calculation the concentration, prior to laser excitation, of each population, free TAHz, 1:1 complex, and 1:2 complex, to be 4.3 μM, 2.8 μM, and 0.4 μM respectively. These results indicate that in our emission measurements we are primarily monitoring emission from the free and 1:1 complex. Indeed, using time-resolved photoluminescence (TR-PL) and global analysis, we extract only two distinct spectral components, described in detail previously.[15] Briefly, temporally- and spectrally-resolved photoluminescence data are collected using a streak camera for solutions of TAHz in the presence of 100 mM phenol. These three-dimensional datasets are analyzed using global analysis, which allows us to kinetically resolve overlapping spectral features.[33] We model the time- and wavelength-dependent PL intensity $\Theta(t,\lambda)$ at time t and wavelength λ as a sum of concentration-weighted spectral components such that $\Theta(t,\lambda)=\Sigma_i c_i(t)\sigma_i(\lambda)$, where $c_i(t)$ and $\sigma_i(\lambda)$, respectively, correspond to the time- dependent concentration and wavelength-dependent species-associated emission spectrum (SAES) of the i^{th} emissive species.[34] Global analysis yields two kinetically resolvable emission features, shown in Figure 6-3A, with kinetics shown in Figure 6-3B. The spectral feature at higher energies

corresponds to the faster decay rate and is attributed to the TAHz-PhOH complex (see Appendix C).

When we compare the fast component emission spectra, shown in Figure 6-3C, we notice significant spectral changes across the phenol series, yet the slow component emission spectra, Figure 6-3D, remain nearly identical. Initially, we considered whether this effect could be due to an increase in the dielectric constant of the solution due to the increasingly polar phenol. However, the emission spectra of TAHz in toluene ($\varepsilon \sim 2.4$), appears identical to the spectral shape in half benzonitrile ($\varepsilon \sim 25.9$), shown in Figure C-0-4, despite an increase in solvent dielectric constant of more than an order of magnitude. Upon further inspection, it appears that the spacing between vibronic peaks remains more or less unchanged among all fast and slow component spectra, which suggests the vibronic progression in all spectra are likely reporting on the TAHz-centered vibrational modes with the same vibrational character. Rather, what is changing is the relative intensity of the peaks, or the Franck Condon progression. This redistribution of oscillator strength between the vibronic peaks suggests varying degrees of nuclear displacement in the excited state along a representative vibrational coordinate; less displacement is observed in complexes with higher Hammett parameters and more displacement is observed for lower Hammett parameters. Initially it was quite surprising to observe that a pendant group on phenol could influence the excited-state displacement of a local TAHz vibration. However, this somewhat unintuitive result highlights how the hydrogen bond can alter the broader excited-state landscape. A deeper understanding of this picture could provide opportunities for rationally designed hydrogen-bonding environments or controlling reactions by specifically exciting molecular vibrations on the

chromophore. In order to quantitatively analyze these spectral changes, in the next section we will turn to a displaced-oscillator model of molecular emission.

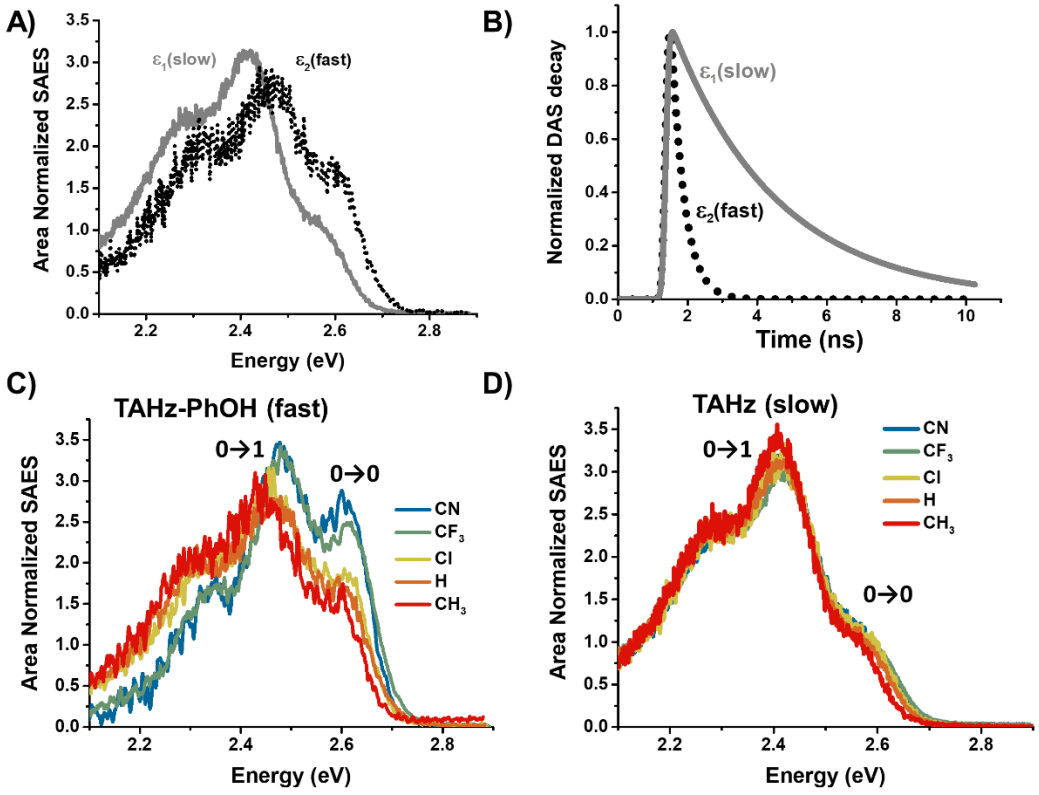

Figure 6-3. TR-PL spectral components of TAHz-PhOH emission

A) From the TR-PL data of TAHz in toluene with 100 mM PhOH, we are able extract, using global analysis, two distinct species-associated emissions spectra (SAES). These species decay at different rates, one with a faster rate (black dots) and with on a slower rate (grey solid). We attribute species decaying more slowly to unbound excited-state TAHz chromophores, whereas the fast component is attributed to an excited-state hydrogen-bound complex. C) We see a significant change in the spectral shape of the fast component depending on the R-group of the phenol: CN (blue), CF_3 (green), Cl (yellow), H (orange), CH_3 (red). D) We do not observe significant spectral differences in the low component.

6.3.3 *Modelling the Emission Lineshape*

The analysis of absorption and emission lineshapes has helped reveal the photophysics of organic molecules for decades.[35] For example, the vibronic structure observed in benzophenone

corresponds to the C=O stretching (~1700 cm^{-1}), which allows for the mixing of $\pi\pi^*$ character into the otherwise forbidden $n\pi^*$ transition. Today, there still exists a vast body of literature focused on understanding the vibronic coupling in optoelectronic materials to guide materials design for applications such as organic solar cells and light emitting dioides.[6, 36-39] It is common to quantify molecular distortion in the excited state by the Huang-Rhys factor (HR), which is a unitless measure of the electron-vibration coupling strength, and is also directly related to the relative displacement of the nuclear coordinate in the Franck-Condon picture.[36-37, 39] This is typically achieved by fitting Gaussian curves to the spectra and using their areas or peak heights to assume $HR = {I_{1\leftarrow 0}}/{I_{0\leftarrow 0}}$, where $I_{1\leftarrow 0}$ is the intensity of the transition from the 0^{th} vibrational state in the first electronic state to the 1^{st} vibrational state in the ground electronic state and $I_{0\leftarrow 0}$ is the intensity of the transition from the 0^{th} vibrational state in the first electronic state to the 0^{th} vibrational state in the ground electronic state. A large HR factor is calculated for spectra with small oscillator strength of the 0→0 and represents significant excited state displacement along a certain vibrational coordinate.

However, when Gaussians were fit to the spectral traces shown in Figure 6-3, the individual Gaussian curves were of varying widths and resulted in seemingly unphysical Huang-Rhys factors of over 4 (see Appendix C). Evidently, in our case, this approach does not adequately capture all relevant physics needed to describe the system. As such, we surmised that more than one vibrational mode could be coupled to the electronic transition and contributing to the observed spectra. Therefore, to best understand how changing the R-group on the phenol influences multiple modes of molecular distortion in the excited state, we implemented a model of vibronic emission to fit the spectra. Within the displaced-oscillator model, a chosen number of vibrational modes are represented by harmonic oscillators whose equilibrium position becomes displaced upon

excitation of the adiabatically-coupled electronic transition; for the interested reader, see Appendix C for the publicly available code.[27] By least-squares fitting this model (with two vibrational modes) to the data, we extract six physically meaningful parameters: the 0→0 transition energy (E_{00}), the frequency of each vibrational mode (ω_1 and ω_2), the displacement of each mode upon excitation in terms of unitless Huang-Rhys factors (HR_1 and HR_2), and a damping coefficient (γ) which broadens the individual vibronic peaks and is attributed to non-H-bond interactions with the solvent. In this context, the Huang-Rhys factor is directly related to the equilibrium displacement d_i of the electronic potential along the nuclear vibration coordinate. For the i^{th}vibrational mode, the Huang-Rhys factor is $HR_i = \frac{d_i^2 m_i \omega_i}{2 \hbar}$, where the displacement squared is rendered dimensionless by the oscillator effective mass m_i, the vibrational frequency ω_i, and the reduced Planck constant $\hbar$. While this factor was originally used in ionic crystals, it has since been applied more broadly and allows us to quantitatively compare molecular displacement upon emission.[40]

Figure 6-4 shows the area-normalized model fit to the fast component extracted from the TAHz-PhOH TR-PL dataset. With two vibrational modes, the model appears to fit the data well and does not significantly improve upon the addition of a third mode (both R^2 values are 0.965). The area-normalized contribution from each mode is shown in the top plot of Figure 6-4B. We extract two modes: a high frequency mode at 1070 cm^{-1} and a low frequency mode at 185 cm^{-1}. To gain physical insight into what vibrational modes these transitions represent, we turn to quantum chemical calculations in Section 6.3.4.

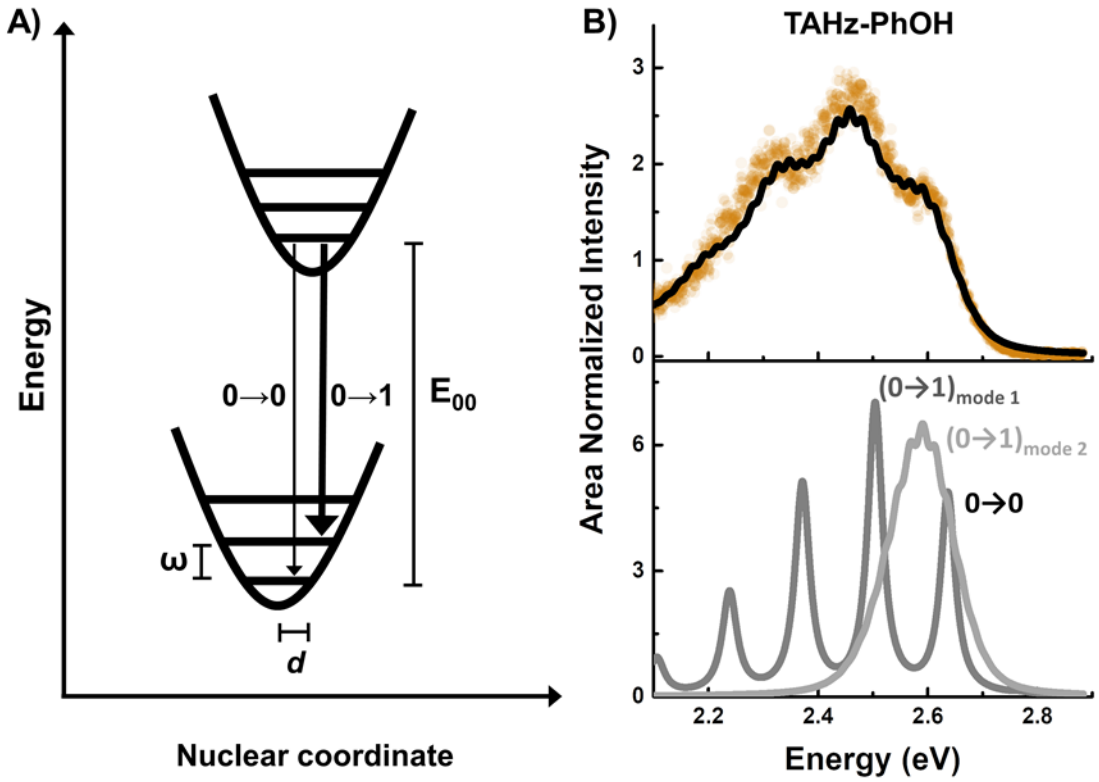

Figure 6-4. Quantum-optical emission model and fit

A) Pictorial representation of the model parameters for one vibrational mode adiabatically coupled to the emissive electronic transition. The harmonic wells represent the vibrational potential energy surfaces in the ground and first excited electronic state separated by energy E_{00}. Each well has a series of vibrational states spaced by energy ω. The displacement of the excited state potential equilibrium position relative to the ground state, *d*, represents the molecular distortion along that specific vibrational coordinate. This displacement gives rise to varying overlap between the 0^{th} vibrational state wave function in the electronic excited state and the vibrations in the electronic ground state well, resulting in varying probability of emission, shown by the 0→0 and 0→1 emission lines. B) The extracted TAHz-PhOH emission (orange dots) is fit well by the model (black line) assuming two vibrational modes are coupled to the electronic transition: one low frequency mode around 200 cm^{-1}, and one high frequency mode around 1050 cm^{-1}. The bottom plot shows the emission spectra from each of the two vibrational modes independently, with the low frequency mode in light grey and the high frequency mode in dark grey. Since both modes are coupled to the same electronic transition, the two-mode model fit (top panel) to the data is instead a convolution of the two component curves in the bottom panel.

Fitting the extracted fast-component spectra with this model allows us to quantify the displacement of each mode across the series of complexes for all R-groups of the phenols, Figure 6-3. The extracted frequencies and Huang-Rhys factors for each TAHz-R-PhOH complex are displayed in Table 6-1. Most notably, we see a clear trend of decreasing Huang-Rhys factor

(proportional to the displacement squared) with increasing electron-withdrawing effect for the high-frequency mode. The nearly linear correlation between the Huang-Rhys factor and Hammett parameter for the high frequency mode can be seen in Figure 6-5B. We also observe that the distortion decreases for the low-frequency mode with increasing Hammett parameter, see Appendix C. However, we acknowledge that thermal energy at room temperature is on the order of 200 cm^{-1}. Additionally, the covariance matrices returned by the least squares fits indicate moderate correlation between the damping coefficient and the low frequency mode parameters. This result may be expected, considering that the low frequency vibronic progression effectively broadens the more distinct high frequency peaks upon convolution of the independent mode emission spectra in Figure 6-4B. So despite needing the low frequency mode to accurately describe the spectra, we take some caution in interpreting the numerical quantities assigned to the low frequency mode.

It is interesting to recall that the spectral shape associated with non-hydrogen bonded species, both from the slow component and free TAHz emission spectrum, show a greater molecular displacement in the excited state than any of the fast-component spectra. Therefore, it appears that the hydrogen-bond serves to hinder molecular distortion of the heptazine chromophore in the excited state. Interestingly, neither the slow component nor the free TAHz spectral shapes could be fit well by the harmonic oscillator model, Figure C-0-12. By introducing anharmonicity to the model in the form of a Morse potential, we can obtain spectra that appear closer to the experimental data than possible with the harmonic assumption, but the parameter space quickly becomes unwieldy and more work is needed to fit those spectra, see Appendix C.

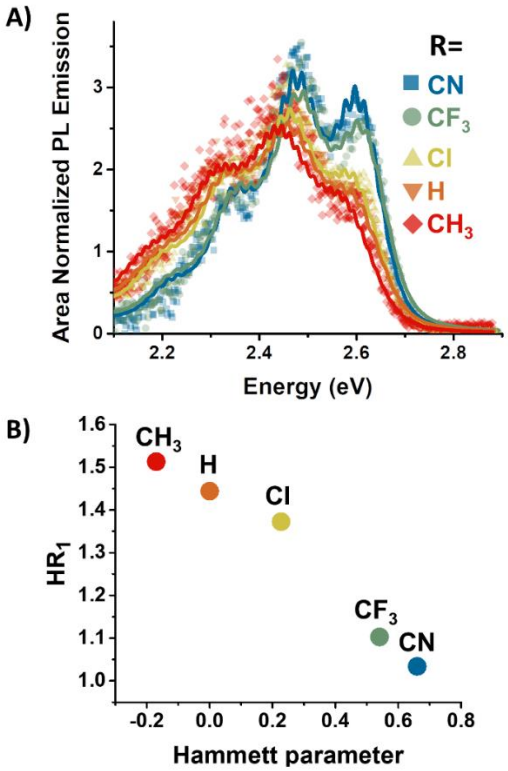

Figure 6-5. Comparing displacement across all TAHz-R-PhOH complexes

A) Data (dots) compared to model fit (solid lines) for all phenol derivatives. Fit for each spectrum are shown individually in Figure C-0-7-Figure C-0-11. B) The Huang-Rhys parameter for the high frequency mode as a function of Hammett parameter of the para substituent on phenol, values in Table 6-1. We observe greater molecular distortion corresponding to weaker hydrogen-bonds (lower Hammett parameters). From this data, we note that the stronger the hydrogen-bound the less distorted the molecule becomes in the excited state.

Table 6-1. Extracted parameters from displaced oscillator model for each vibrational mode

R	Hammett parameter (σ_p)[30]	Mode 1		Mode 2		Calculated H-bond length (Å)
		Frequency (cm^{-1})	HR_1*	Frequency (cm^{-1})	HR_2	
CH_3	-0.17	1068.92±0.04	1.513	128.043±0.004	3.6±0.9	1.940
H	0	1070.37±0.05	1.444	185.68±0.02	2.24±0.02	1.937
Cl	0.227	1061.96±0.04	1.372	159.12±0.01	2.36±0.02	1.924
CF_3	0.54	1057.08±0.05	1.103	179.92±0.04	1.77±0.02	1.910
CN	0.66	1035.49±0.02	1.034	156.800±0.004	1.924±0.007	1.904

*Uncertainty < $\pm 10^{-3}$

6.3.4 *Quantum Chemical Calculations*

To help visualize the molecular vibrations, we used density functional theory (DFT) and time-dependent density functional theory (TD-DFT), see Appendix C. Using the optimized ground state geometry of TAHz, we calculated the normal modes and FTIR spectrum shown in Figure 6-6A. The calculated spectrum shows surprisingly good agreement to the experimental FTIR of TAHz powder. There exist a number of vibrational transitions in the 1000-1200 cm^{-1} region that are generally attributable to heptazine ring breathing modes and C-N stretching.[41] An example of such a vibration is shown in Figure 6-6B, wherein the center nitrogen is displaced off axis within the heptazine plane, with two of the peripheral nitrogens within the heptazine ring being displaced outwardly in opposite directions. Figure C-0-15 shows other ring-breathing vibrations in the 1000-1200 cm^{-1} frequency range. It is conceivable that these ring-breathing modes could be strongly coupled to the electronic transition; the symmetry-forbidden $\pi\pi^*$ S_1 transition must couple to vibrations which break the symmetry of the heptazine ring. In light of these results, the vibrational distortion of the chromophore in the excited state appears to be influenced by the hydrogen-bonding interaction of the peripheral nitrogen to the phenol species. The modulation of the N-H hydrogen-bond distance could possibly even serve as a handle for reactivity. Preliminary results from DFT calculation of the TAHz - Cl-PhOH complex showed the N-H hydrogen-bond distance can be significantly modulated by heptazine ring-breathing vibrations (Figure 6-6C and Figure C-0-16 and Figure C-0-17), both at ground state and symmetry-forbidden $\pi\pi^*$ excited state optimized geometry.

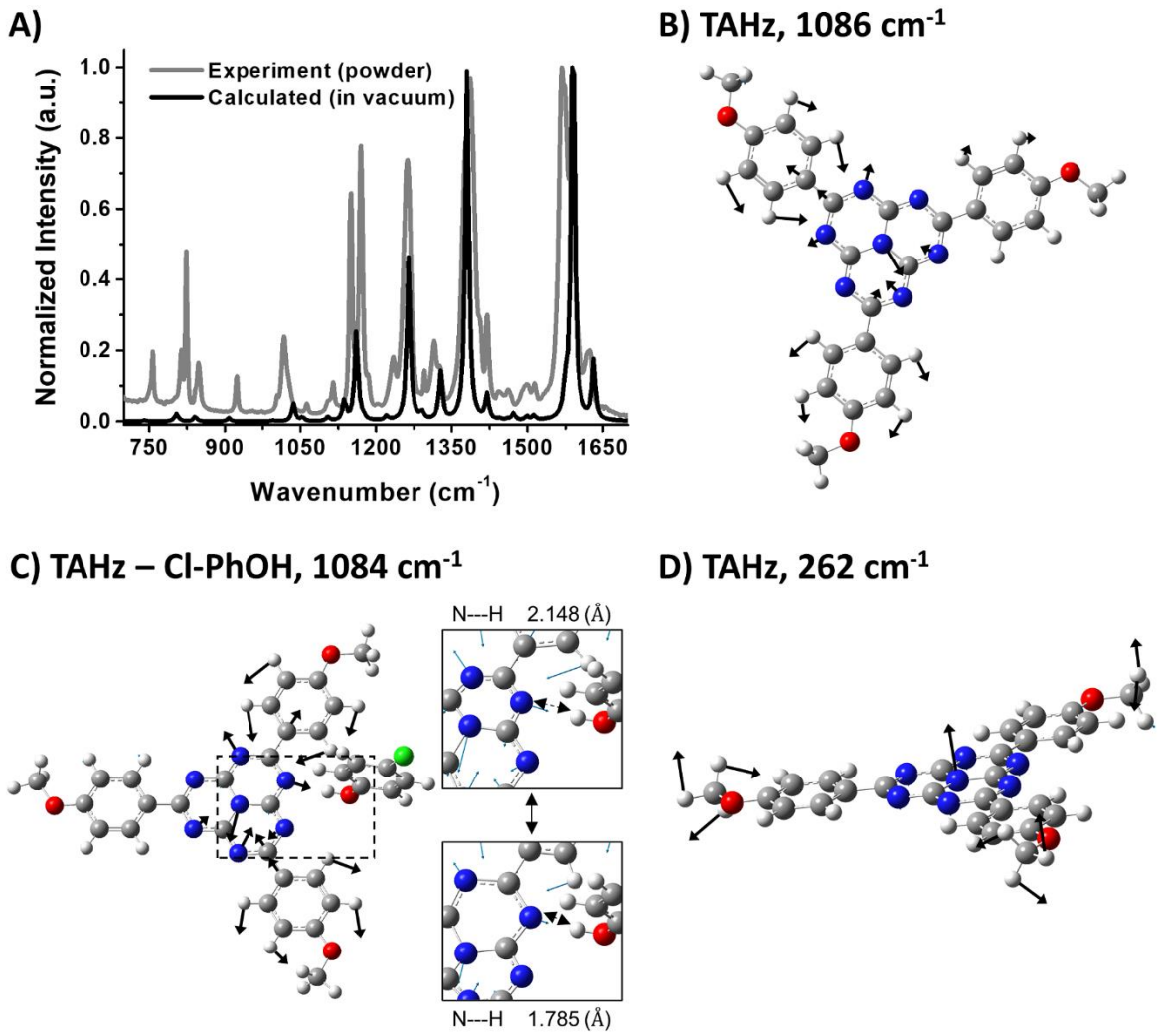

Figure 6-6 Calculated TAHz molecular vibrations

A) FTIR spectrum of TAHz powder (grey) compared to the calculated FTIR spectrum in vacuum (back). The range of transitions in the 1000-1600 cm^{-1} displayed in Table 1 range are generally attributed to heptazine ring breathing and C-N stretching modes. B) An example molecular vibration calculated to be at 1086 cm^{-1} is shown by the displacement vectors, see the Supporting Information for more images. The high frequency mode extracted from the PL spectral fit is attributed to one of these modes which is modulated by the nearby PhOH. C) An example heptazine ring-breathing vibration of TAHz – Cl-PhOH complex that modulate N-H hydrogen bonding distance significantly. D) A low frequency mode around 262 cm^{-1} corresponds to the ring-puckering, wherein the central nitrogen moves up out of plane, and the outer nitrogens move down, see Supporting Information for more images.

While the low frequency mode is outside the experimental window in Figure 6-6A, quantum chemical calculations for heptazine predict that the ring puckers out of plane in the excited state

and the inversion of this umbrella motion occurs in the 200-300 cm^{-1} range, shown in Figure 6-6 and Figure C-0-13. This puckering not only breaks the planarity of the heptazine chromophore, but also imparts a double-well character on the potential energy surface of the excited-state. It should be noted that the displaced-oscillator model of molecular emission does not allow for specific mode assignment beyond matching the resonance frequency. It is therefore possible that the vibrational modes predicted by the model more accurately represent a collection of modes closely spaced in energy. In this case the predicted Huang-Rhys parameter would be approximately the sum of those Huang-Rhys parameters from each contributing mode, and the predicted frequency would be a weighted average of contributing modes.[42] We expect that this, along with the correlation in predicted parameters with the damping coefficient (discussed above), is the likely cause of the numerical discrepancy between low-energy mode frequency predicted by the displaced-oscillator emission model and the quantum-chemical calculations.

6.4 CONCLUSIONS

Using a series of phenol derivatives, we modulate the electron-withdrawing nature of the hydrogen-bond donor and systematically study the hydrogen-bonding interactions with a heptazine chromophore. We observe stronger hydrogen bonds for larger Hammett parameters, as expected. By kinetically resolving and comparing individual PL spectral components for this series of hydrogen-bonded complexes, we see a trend of decreasing displacement of the S_1 and S_0 equilibrium geometries with increasing intermolecular hydrogen bond strength. By implementing a displaced-oscillator model to fit the PL spectral components, we extract the frequencies and displacements of two vibrational modes that are most strongly coupled to the S_1 electronic transition. We use this information to monitor how these coupling strengths are influenced by varying hydrogen-bond strength. From quantum chemical calculations, we further visualize

pertinent TAHz-centered molecular vibrations, which correspond to heptazine-ring breathing modes around 1100 cm^{-1} and umbrella-like modes involving an out-of-plane puckering of the central nitrogen atom near 200 cm^{-1}.

Altering the extent of distortion along each of these modes has interesting implications for ES-PCET and ES-PT reactions as they both modulate the position of the hydrogen-bonded nitrogen. As we previously showed, the out-of-plane puckering in the excited state breaks the symmetry of the heptazine core and increases the oscillator strength of transitions to higher-lying excited states, thus enabling further optical control of the photochemical reactivity of these complexes using ultrafast spectroscopy.[26]

Additionally, this new insight may help inform molecular design parameters to enable future advanced materials discovery for solar energy conversion and storage. Seeing how the stronger hydrogen-bonded complexes undergo less distortion of the heptazine ring in the excited state, it is interesting to return to the reactivity difference of H-PhOH and Cl-PhOH. Given the same driving force for electron transfer, it is possible that the excited state molecular distortion may have the effect of hindering the ES-PCET reaction. While adding electron-withdrawing groups to heptazine could increase the ES-PCET reactivity, we have found here that it is also important to consider tailoring the hydrogen-bonding environment. In particular, if one aims to increase ES-PCET with water, as in natural photosynthesis, our results suggest that tailored hydrogen bonding environments may provide a critical molecular design parameter moving forward. Work is ongoing in our lab to control both the oxidation potential and the hydrogen-bonding environment around the heptazine core through chemical functionalization of the chromophore. Additionally, we are working to implement an anharmonic extension to the displaced-oscillator model, which should be capable of fitting the unbound TAHz emission. We anticipate that this work will provide a more

comprehensive picture of the excited-state landscape and how it can be altered by hydrogen-bonding and chromophore design.

6.5 Materials and Methods

Reagents. Urea, potassium hydroxide, phosphorous oxychloride, phosphorous pentachloride, phenol, and 4-(trifluoromethyl)phenol were all purchased from Sigma Aldrich. Anisole (99%) was purchased from Alfa Aesar. Aluminum chloride was purchased from Fischer Scientific. P-cresol, 4-chlorophenol, and 4-hydroxybenzonitrile were all purchased from TCI. All reagents were used without further purification.

Synthesis. The full synthetic and characterization procedure of TAHz was the same as described in our previous publication in the Supporting Information.[25]

Sample Preparation. TAHz was dissolved in toluene (20 uM) and stirred overnight before measurements were preformed to ensure minimal aggregation effects and accurate concentrations were prepared. Samples were kept in the dark until measurements were performed.

Ground State Absorption. Ground-state absorption spectra were collected using a Cary5000 UV−vis−NIR spectrometer. Within each R-PhOH series, the same TAHz stock solution was used to ensure consistent TAHz concentration with the varying phenol derivatives. Each solution of the spectra shown in Figure 1 of the main text was 7.5 uM TAHz and 50 mM R-PhOH.

For the data collected in Figure 2 of the main text, the initial TAHz concentration was 7.5 uM in toluene. Using a 3 M PhOH stock solution in toluene, 10 uL of PhOH solution were added, stirred, and a spectrum was recorded. This process was repeated a total of 10 times. Then 20 uL aliquots were added, stirred, and recorded a total of ten times. The resulting 21(one with no PhOH and 20 with sequential additions) spectra were baseline corrected by subtracting the average OD from 495-500 nm. Each spectra was then multiplied by the fraction TAHz was diluted by (new total

volume/old volume). The PhOH concentration was calculated by accounting for the change in volume upon each addition.

Time-Resolved Photoluminescence (TR-PL) Spectra. TR-PL spectra were collected using a Hamamatsu streak camera (C10910) with a slow-sweep unit (M10913-01) in photon counting mode. Samples were irradiated with 50 fs pulses at 365 nm and 1 kHz pump from a Coherent/Light Conversion OPerA solo optical parametric amplifier (OPA). Pump fluences were approximately $2.7x10^{13}$ photons cm^{-3}. All samples for global analysis were prepared to be 50 μM TAHz and 100 mM R-PhOH with the exception of CN-PhOH which was 50 mM due to solubility restraints, however the spectral shape of the fast component was not found to be dependent on concentration of R-PhOH. For each R-PhOH, the solution was made and measured in duplicate. The resulting extracted duplicate spectra from global analysis were averaged together prior to fitting. No smoothing was performed on the data. Prior to fitting, the x-axis was converted to energy in eV. The y-axis was adjusted accordingly (Intensity/eV = (Intensity/nm)*(1240 nm*eV)/eV/eV), where Intensity/nm was the original y-axis value. The spectra were then area normalized.

Calculations. Density functional theory (DFT) and time-dependent DFT calculations were carried out with Gaussian16 (rev. C.01).[43] The Becke 3-Parameter Lee-Yang-Parr (B3LYP) functional and 6-31G(d,p) Pople basis set were used. We first optimized ground state geometry of TAHz molecule and calculate normal modes and IR spectrum. The scaling factor of vibrational wavenumber for comparison with experimental FTIR spectrum (Fig. 5) was 0.97. For excited state optimized geometry, TD-DFT optimization was performed at lowest Singlet excited state of TAHz (weakly allowed π-π* transition). DFT and TD-DFT calculation were facilitated through the use

of advanced computational, storage, and networking infrastructure provided by the Hyak supercomputer system and funded by the STF at the University of Washington.

6.6 REFERENCES

1. Tommos, C.; Babcock, G. T., Proton and hydrogen currents in photosynthetic water oxidation. *Biochem. Biophys. Acta* **2000,** *1458* (1), 199-219.
2. Warren, J. J.; Tronic, T. A.; Mayer, J. M., Thermochemistry of Proton-Coupled Electron Transfer Reagents and its Implications. *Chem. Rev.* **2010,** *110* (12), 6961-7001.
3. Crivello, J. V., The discovery and development of onium salt cationic photoinitiators. *J. Polym. Sci., Part A: Polym. Chem.* **1999,** *37* (23), 4241-4254.
4. Roy, S.; Ardo, S.; Furche, F., 5-Methoxyquinoline Photobasicity Is Mediated by Water Oxidation. *J. Phys. Chem. A* **2019,** *123* (31), 6645-6651.
5. Harshan, A. K.; Yu, T.; Soudackov, A. V.; Hammes-Schiffer, S., Dependence of Vibronic Coupling on Molecular Geometry and Environment: Bridging Hydrogen Atom Transfer and Electron–Proton Transfer. *J. Am. Chem. Soc.* **2015,** *137* (42), 13545-13555.
6. Hestand, N. J.; Spano, F. C., Expanded Theory of H- and J-Molecular Aggregates: The Effects of Vibronic Coupling and Intermolecular Charge Transfer. *Chem. Rev.* **2018,** *118* (15), 7069-7163.
7. Han, F.; Liu, W.; Zhu, L.; Wang, Y.; Fang, C., Initial hydrogen-bonding dynamics of photoexcited coumarin in solution with femtosecond stimulated Raman spectroscopy. *J. Mat. Chem. C* **2016,** *4* (14), 2954-2963.
8. Zhao, G.-J.; Han, K.-L., Early Time Hydrogen-Bonding Dynamics of Photoexcited Coumarin 102 in Hydrogen-Donating Solvents: Theoretical Study. *J. Phys. Chem. A* **2007,** *111* (13), 2469-2474.
9. Barman, N.; Singha, D.; Sahu, K., Fluorescence Quenching of Hydrogen-Bonded Coumarin 102-Phenol Complex: Effect of Excited-State Hydrogen Bonding Strength. *J. Phys. Chem. A* **2013,** *117* (19), 3945-3953.
10. Hunt, J. R.; Dawlaty, J. M., Kinetic Evidence for the Necessity of Two Proton Donor Molecules for Successful Excited State Proton Transfer by a Photobase. *J. Phys. Chem. A* **2019,** *123* (48), 10372-10380.
11. Dongare, P.; Bonn, A. G.; Maji, S.; Hammarström, L., Analysis of Hydrogen-Bonding Effects on Excited-State Proton-Coupled Electron Transfer from a Series of Phenols to a Re(I) Polypyridyl Complex. *J. Phys. Chem. C* **2017,** *121* (23), 12569-12576.
12. Demeter, A.; Ravasz, L.; Bérces, T., Influence of Hydrogen Bond Formation on the Photophysics of N-(2,6-Dimethylphenyl)-2,3-naphthalimide. *J. Phys. Chem. A* **2004,** *108* (19), 4357-4364.
13. Ehrmaier, J.; Karsili, T. N. V.; Sobolewski, A. L.; Domcke, W., Mechanism of Photocatalytic Water Splitting with Graphitic Carbon Nitride: Photochemistry of the Heptazine-Water Complex. *J. Phys. Chem. A* **2017,** *121* (25), 4754-4764.
14. Liu, X.; Karsili, T. N.; Sobolewski, A. L.; Domcke, W., Photocatalytic Water Splitting with the Acridine Chromophore: A Computational Study. *J. Phys. Chem. B* **2015,** *119* (33), 10664-72.

15. Rabe, E. J.; Corp, K. L.; Huang, X.; Ehrmaier, J.; Flores, R. G.; Estes, S. L.; Sobolewski, A. L.; Domcke, W.; Schlenker, C. W., Barrierless Heptazine-Driven Excited State Proton-Coupled Electron Transfer: Implications for Controlling Photochemistry of Carbon Nitrides and Aza-Arenes. *J. Phys. Chem. C* **2019,** *123* (49), 29580-29588.
16. Balasubramanian, M.; Reynolds, A.; Blair, T. J.; Khalil, M., Probing ultrafast vibrational dynamics of intramolecular hydrogen bonds with broadband infrared pump-probe spectroscopy. *Chem. Phys.* **2019,** *519*, 38-44.
17. Schriever, C.; Barbatti, M.; Stock, K.; Aquino, A. J. A.; Tunega, D.; Lochbrunner, S.; Riedle, E.; de Vivie-Riedle, R.; Lischka, H., The interplay of skeletal deformations and ultrafast excited-state intramolecular proton transfer: Experimental and theoretical investigation of 10-hydroxybenzo[h]quinoline. *Chem. Phys.* **2008,** *347* (1), 446-461.
18. Zhang, G.; Lin, L.; Li, G.; Zhang, Y.; Savateev, A.; Zafeiratos, S.; Wang, X.; Antonietti, M., Ionothermal Synthesis of Triazine–Heptazine-Based Copolymers with Apparent Quantum Yields of 60 % at 420 nm for Solar Hydrogen Production from "Sea Water". *Angew. Chem. Int. Ed.* **2018,** *57* (30), 9372-9376.
19. Lau Vincent, W. h.; Klose, D.; Kasap, H.; Podjaski, F.; Pignié, M. C.; Reisner, E.; Jeschke, G.; Lotsch Bettina, V., Dark Photocatalysis: Storage of Solar Energy in Carbon Nitride for Time-Delayed Hydrogen Generation. *Angew. Chem. Int. Ed.* **2016,** *56* (2), 510-514.
20. Markushyna, Y.; Lamagni, P.; Teutloff, C.; Catalano, J.; Lock, N.; Zhang, G.; Antonietti, M.; Savateev, A., Green radicals of potassium poly(heptazine imide) using light and benzylamine. *J. Mat. Chem. A* **2019,** *7* (43), 24771-24775.
21. Yan, S. C.; Li, Z. S.; Zou, Z. G., Photodegradation of Rhodamine B and Methyl Orange over Boron-Doped g-C3N4 under Visible Light Irradiation. *Langmuir* **2010,** *26* (6), 3894-3901.
22. Ong, W. J.; Tan, L. L.; Ng, Y. H.; Yong, S. T.; Chai, S. P., Graphitic Carbon Nitride (g-C3N4)-Based Photocatalysts for Artificial Photosynthesis and Environmental Remediation: Are We a Step Closer To Achieving Sustainability? *Chem. Rev.* **2016,** *116* (12), 7159-329.
23. Lau, V. W.; Moudrakovski, I.; Botari, T.; Weinberger, S.; Mesch, M. B.; Duppel, V.; Senker, J.; Blum, V.; Lotsch, B. V., Rational design of carbon nitride photocatalysts by identification of cyanamide defects as catalytically relevant sites. *Nat Commun* **2016,** *7*, 12165.
24. Ullah, N.; Chen, S.; Zhao, Y.; Zhang, R., Photoinduced Water–Heptazine Electron-Driven Proton Transfer: Perspective for Water Splitting with g-C3N4. *J. Phys. Chem. Lett.* **2019,** *10* (15), 4310-4316.
25. Rabe, E. J.; Corp, K. L.; Sobolewski, A. L.; Domcke, W.; Schlenker, C. W., Proton-Coupled Electron Transfer from Water to a Model Heptazine-Based Molecular Photocatalyst. *J. Phys. Chem. Lett.* **2018,** *9* (21), 6257-6261.
26. Corp, K. L.; Rabe, E. J.; Huang, X.; Ehrmaier, J.; Kaiser, M. E.; Sobolewski, A. L.; Domcke, W.; Schlenker, C. W., Control of Excited-State Proton-Coupled Electron Transfer by Ultrafast Pump-Push-Probe Spectroscopy in Heptazine-Phenol Complexes: Implications for Photochemical Water Oxidation. *J. Phys. Chem. C* **2020**.
27. Mukamel, S., *Principles of nonlinear optical spectroscopy*. Oxford University Press: 1995.
28. Bronner, C.; Wenger, O. S., Kinetic Isotope Effects in Reductive Excited-State Quenching of Ru(2,2′-bipyrazine)32+ by Phenols. *J. Phys. Chem. Lett.* **2012,** *3* (1), 70-74.
29. Bronner, C.; Wenger, O. S., Proton-Coupled Electron Transfer between 4-Cyanophenol and Photoexcited Rhenium(I) Complexes with Different Protonatable Sites. *Inorg. Chem.* **2012,** *51* (15), 8275-8283.

30. Hansch, C.; Leo, A.; Taft, R. W., A survey of Hammett substituent constants and resonance and field parameters. *Chem. Rev.* **1991,** *91* (2), 165-195.
31. Demeter, A.; Mile, V.; Bérces, T., Hydrogen Bond Formation between 4-(Dimethylamino)pyridine and Aliphatic Alcohols. *J. Phys. Chem. A* **2007,** *111* (37), 8942-8949.
32. Ehrmaier, J.; Rabe, E. J.; Pristash, S. R.; Corp, K. L.; Schlenker, C. W.; Sobolewski, A. L.; Domcke, W., Singlet–Triplet Inversion in Heptazine and in Polymeric Carbon Nitrides. *J. Phys. Chem. A* **2019,** *123* (38), 8099-8108.
33. Snellenburg, J. J.; Laptenok, S. P.; Seger, R.; Mullen, K. M.; Stokkum, I. H. M. v., Glotaran: A Java-Based Graphical User Interface for the R Package TIMP. *J. Stat. Softw.* **2012,** *49* (3), 22.
34. Snellenburg, J. J.; Laptenok, S. P.; Seger, R.; Mullen, K. M.; van Stokkum, I. H. M., Glotaran: A Java-Based Graphical User Interface for the R Package TIMP. *J. Stat. Softw.* **2012,** *49* (3), 1-22.
35. Turro, N. J.; Ramamurthy, V.; Scaiano, J. C., *Principles of Molecular Photochemistry: An Introduction.* University Science Books Sausalito, California, 2009.
36. Lim, S.-H.; Bjorklund, T. G.; Bardeen, C. J., Temperature-dependent exciton dynamics in poly(p-phenylene vinylene) measured by femtosecond transient spectroscopy. *Chem. Phys. Lett.* **2001,** *342* (5), 555-562.
37. Guha, S.; Rice, J. D.; Yau, Y. T.; Martin, C. M.; Chandrasekhar, M.; Chandrasekhar, H. R.; Guentner, R.; Scanduicci de Freitas, P.; Scherf, U., Temperature-dependent photoluminescence of organic semiconductors with varying backbone conformation. *Phys. Rev. B* **2003,** *67* (12), 125204.
38. Cho, Y.-J.; Kim, S.-Y.; Kim, J.-H.; Crandell, D. W.; Baik, M.-H.; Lee, J.; Kim, C. H.; Son, H.-J.; Han, W.-S.; Kang, S. O., Important role of ancillary ligand in the emission behaviours of blue-emitting heteroleptic Ir(iii) complexes. *J. Mat. Chem. C* **2017,** *5* (18), 4480-4487.
39. de Jong, M.; Seijo, L.; Meijerink, A.; Rabouw, F. T., Resolving the ambiguity in the relation between Stokes shift and Huang–Rhys parameter. *Phys. Chem. Chem. Phys.* **2015,** *17* (26), 16959-16969.
40. Huang, K.; Rhys, A.; Mott, N. F., Theory of light absorption and non-radiative transitions in F-centres. *Proc. R. Soc. Lond. A* **1950,** *204* (1078), 406-423.
41. Miller, T. S.; Jorge, A. B.; Suter, T. M.; Sella, A.; Corà, F.; McMillan, P. F., Carbon nitrides: synthesis and characterization of a new class of functional materials. *Phys. Chem. Chem. Phys.* **2017,** *19* (24), 15613-15638.
42. Mustroph, H.; Towns, A., Fine Structure in Electronic Spectra of Cyanine Dyes: Are Sub-Bands Largely Determined by a Dominant Vibration or a Collection of Singly Excited Vibrations? *ChemPhysChem* **2018,** *19* (9), 1016-1023.
43. Frisch, M. J.; Trucks, G. W.; Schlegel, H. B.; Scuseria, G. E.; Robb, M. A.; Cheeseman, J. R.; Scalmani, G.; Barone, V.; Petersson, G. A.; Nakatsuji, H.; Li, X.; Caricato, M.; Marenich, A. V.; Bloino, J.; Janesko, B. G.; Gomperts, R.; Mennucci, B.; Hratchian, H. P.; Ortiz, J. V.; Izmaylov, A. F.; Sonnenberg, J. L.; Williams; Ding, F.; Lipparini, F.; Egidi, F.; Goings, J.; Peng, B.; Petrone, A.; Henderson, T.; Ranasinghe, D.; Zakrzewski, V. G.; Gao, J.; Rega, N.; Zheng, G.; Liang, W.; Hada, M.; Ehara, M.; Toyota, K.; Fukuda, R.; Hasegawa, J.; Ishida, M.; Nakajima, T.; Honda, Y.; Kitao, O.; Nakai, H.; Vreven, T.; Throssell, K.; Montgomery Jr., J. A.; Peralta, J. E.; Ogliaro, F.; Bearpark, M. J.; Heyd, J. J.; Brothers, E. N.; Kudin, K. N.; Staroverov, V. N.; Keith, T. A.; Kobayashi, R.; Normand, J.; Raghavachari, K.; Rendell, A. P.; Burant, J. C.;

Iyengar, S. S.; Tomasi, J.; Cossi, M.; Millam, J. M.; Klene, M.; Adamo, C.; Cammi, R.; Ochterski, J. W.; Martin, R. L.; Morokuma, K.; Farkas, O.; Foresman, J. B.; Fox, D. J. *Gaussian 16 Rev. C.01*, Wallingford, CT, 2016.

Appendix A: Supplementary Information for Chapter 4

Determining values for photophysical properties in Table 1

The time-correlated single-photon counting (TCSPC) data for TAHz in toluene and DMSO were fit to single exponentials and the time constant was taken to be the lifetime in each solvent shown in Figure A-0-1. The fitting error for the time constant was the error presented in Table 4-1.

For both samples of TAHz in water (supernatant and 0.1 mg/mL) the TSCPC traces were fit to three exponentials (Figure A-0-2) and an average lifetime was calculated by Equation 1.

$$\langle\tau\rangle = \frac{A_1\tau_1+A_2\tau_2+A_3\tau_3}{A_1+A_1+A_1} \qquad (1)$$

Where A_i is the coefficient and τ_i is the lifetime of the i^{th} component. The error for these values was determined through error propagation for all coefficients and lifetimes.

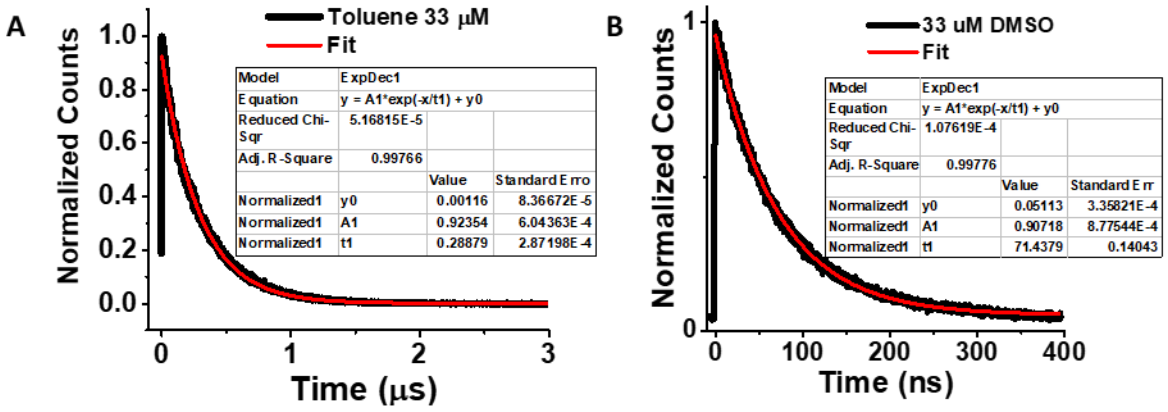

Figure A-0-1 TAHz PL kinetics in Toluene and DMSO.

TCSPC kinetic traces for 33 μM solutions of TAHz in toluene (A) and DMSO (B). Both traces were fit to single exponentials and errors for t_1 given by the fit were used as the error in Table 4-1.

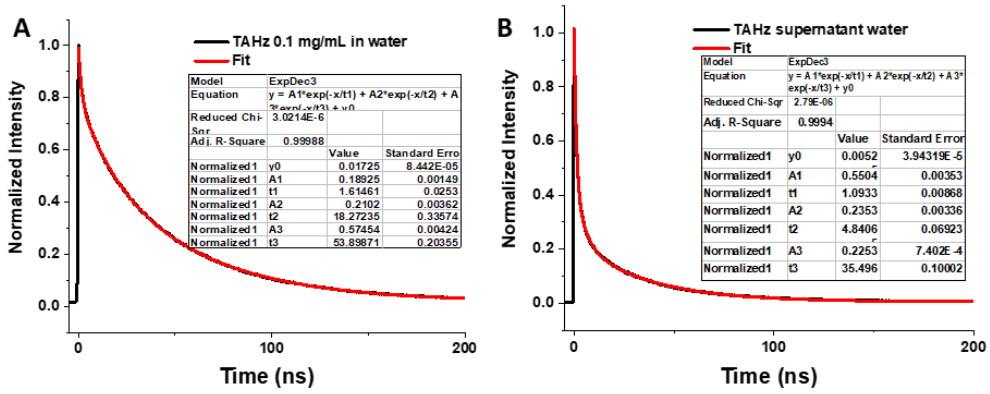

Figure A-0-2 TCSPC of TAHz in water.

A) TCSPC data for a supernatant of TAHz in water. The biexponential fit, shown in red was used to calculate average lifetime for Table 1. B) TCSPC data for 0.1 mg/mL mass loading suspension of TAHz in water. This curve was also fit to a biexponential and used to calculate the average lifetime. If the quenching was due to aggregation, the lifetime would not be longer in a higher mass loading sample with larger aggregates.

The PLQY error was assumed to be ±0.01 This is in part due to the inability of the instrument to measure below Φ=0.01 and accounting for the variation seen in PLQY values over several days, as temperature affects the PLQY of TAHz. Because the error was assumed to be a constant value, samples with lower PLQY had higher relative errors, resulting in the largest errors for k_R and k_{NR}.

As expected, k_R remains quite similar in all environments, whereas changes to k_{NR} are far more significant. Non-radiative decay increases with increasing dielectric constant, in the case of DMSO, however, the additional order of magnitude increase in water provides convincing evidence for an additional quenching process. Additionally, increasing the mass loading of TAHz in water decreases k_{NR}, indicating that aggregation is not responsible. In light of the catalytic

activity, we propose that a meaningful fraction of excited states is quenched through reaction with protons or hydrogen-bonded water molecules.

Understanding the TAHz TR-PL spectra in water

When considering how the energy landscape could be changing in water, it is interesting to note that the time averaged (steady state) PL spectra of toluene and water are very similar in Figure A-0-3. The following two assumptions can be made from this observation: 1) we do not observe long-lived aggregate emission (since TAHz in water shows visible aggregates) and 2) the low-lying dim S_1 is likely still accessible in water. We also see little change in the steady-state PL spectra of TAHz in solvents with a wide range of dielectric constants, Figure A-0-3. A small blueshift is observed for DMSO (ε=48), and some changes to the vibronic progression can be seen. However, the lack of significant redshifting suggests this emitting state is not an intramolecular charge transfer state.

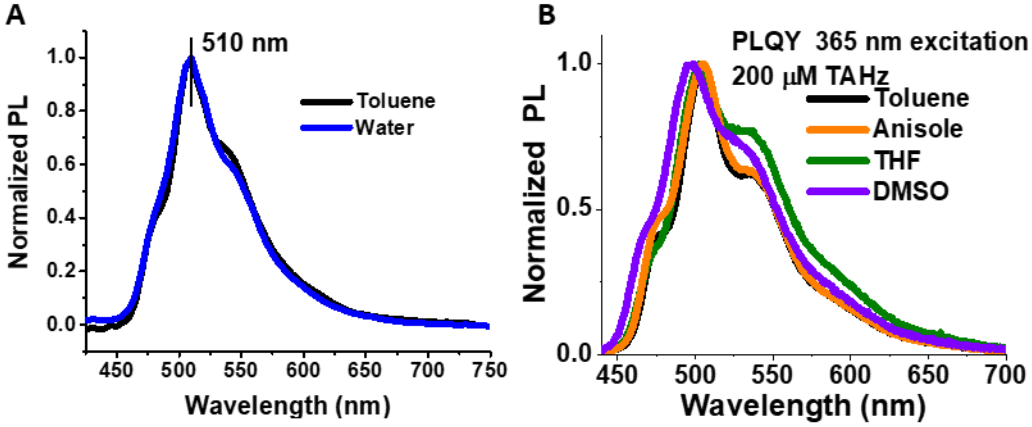

Figure A-0-3 TAHz PL in different solvents.

A) Steady-state PL spectra of TAHz in toluene (black) and water (blue) in 200 μM concentrations. The measurement was taken on a home-built spectrometer using lock-in amplification. B) PL spectra of TAHz in different solvents with a range of dielectric constants taken in the PLQY setup. DMSO showed a small blue-shift, but largely the only changes are in the vibronic structure. TAHz is reasonably soluble in these solvents.

As previously mentioned, higher TAHz mass loadings in water show longer lifetimes in TCSPC measurements. We attribute this to increased aggregate size with more chromophores unable to be quenched by water before emitting. Along these same lines, as we increase mass loading, the contribution from S_1 emission increases in the TR-PL spectra. Figure A-0-4 shows the TR-PL spectra averaged over the first two nanoseconds normalized to the peak emission for three different mass loadings. We can see a clear increase in the high energy emission with decreasing mass loading. This suggests the high energy emission is enhanced in smaller aggregates with increased interactions with water. We confirm this assumption by looking at the kinetic isotope effect at both high and low energies shown in Figure A-0-5. There is a distinct difference at high energy, and essentially no change at low energies. This provides strong evidence for the high energy emission to be from an S_n state in a hydrogen-bonded complex which can be quenched by PCET.

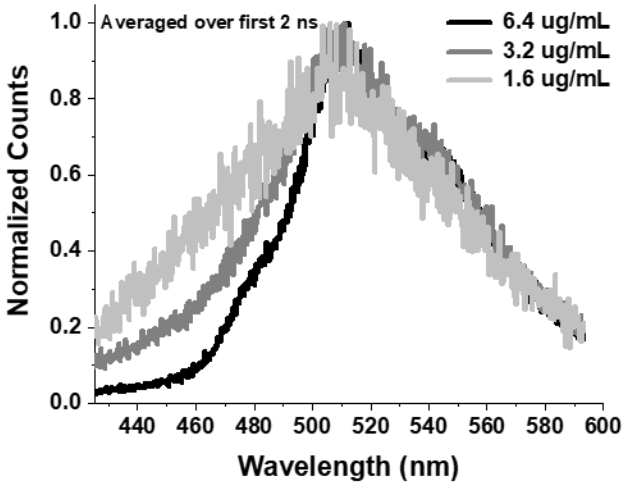

Figure A-0-4 TR-PL in water of different TAHz mass loadings.

TR-PL spectra of TAHz in water over the first two nanoseconds at increasing mass loadings upon 365 nm pulsed excitation. At lower mass loadings (light grey), the relative intensity of the high-energy emission feature is much larger than at higher mass loadings (black). This suggests that the high-energy emission is not from aggregates, but rather that aggregation suppresses this high energy emission. We attribute this suppression to a decrease in the number of sites for hydrogen bonding with water and propose that the S_1 emission at low energies is dominant for chromophores inside the aggregate.

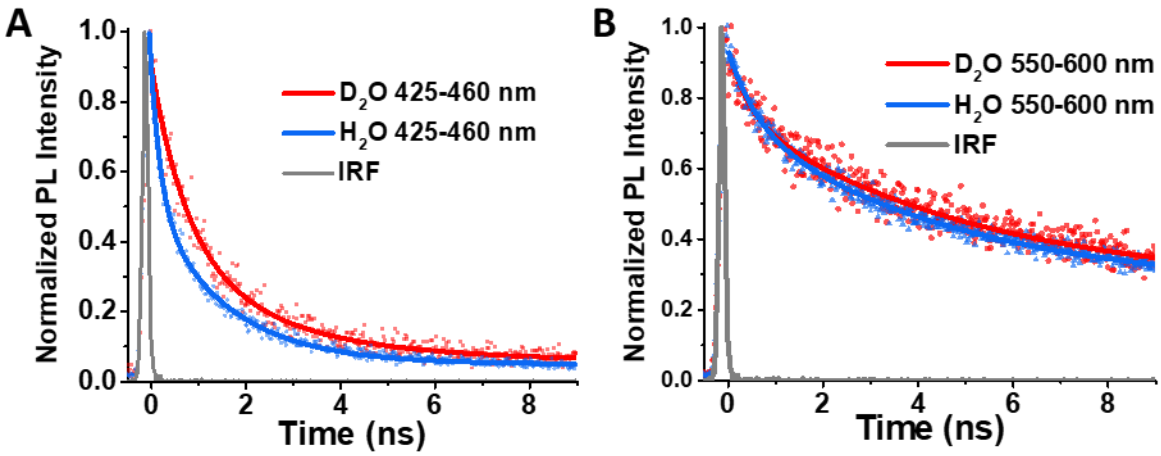

Figure A-0-5 Wavelength-dependent KIE.

A) Kinetic traces of higher energy emission in 3.2 μg/mL mass loadings of TAHz in H_2O (blue) and D_2O (red). At high energies there is a clear difference in the decay rates, resulting in a moderate kinetic isotope effect. B) Kinetics traces from the same datasets taken at low energy. At these wavelengths, S_1 emission dominates and we see essentially no isotopic dependence on the decay rate. This is consistent with our proposed mechanism, wherein only the S_n emission can be quenched by the motion of the proton.

Since our samples are illuminated in water without a sacrificial hole acceptor for TR-PL measurements, it is likely that photodegradation products are created. To investigate whether the high energy emission could be resulting from a photodegradation product, we performed TR-PL measurements of TAHz in water in the presence of a radical scavenger (DMSO),[1-2] and as a function of illumination time. If the high energy emission is from a photodegradation product formed by reacting with hydroxyl radicals, then adding a radical scavenger should decrease the intensity of the high energy emission. However, when we look at the high energy emission averaged over the first 500 ps of 1:14 and 1:5 DMSO:H_2O mixtures, we see that the high energy feature does not decrease with increasing DMSO, Figure A-0-6. In fact, we see an increase in

intensity which we attribute to DMSO further solubilizing TAHz and therefore breaking up the aggregates.

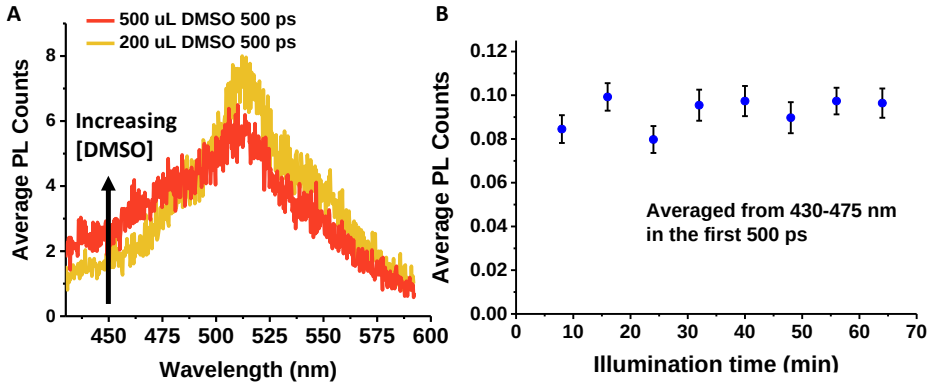

Figure A-0-6 Ruling out photochemical by-product emission.

A) Shows the TR-PL spectra of TAHz in water, averaged over the first 500 ps with 200 µL (yellow) and 500 µL (red) of DMSO in 2.8 mL and 2.5 mL of water, respectively. The total TAHz mass loading was 3.2 µg/mL. Adding increasing amounts of DMSO (a known radical scavenger) did not decrease the high-energy (S_n) emission as would be expected if this luminescence was the byproduct of a chemical reaction with photogenerated radicals. Instead, we see this peak increase in intensity and attribute this to increased solubility of TAHz chromophores with DMSO. Increasing the number of chromophores in contact with water increases the number of possible S_n emission states. B) Shows the average intensity of the S_n emission feature of TAHz in water (no DMSO) over the duration of the TR-PL experiment. There is no significant buildup of intensity over this time window, suggesting that the S_n emission feature does not likely arise from a photochemical byproduct created during the measurement. All samples were prepared in the dark.

Additionally, we looked at the TR-PL of TAHz in water over the duration of our measurement time (roughly an hour). Since the samples were prepared in the dark, the most significant light exposure should be during the PL measurement itself. Figure A-0-5shows the intensity in the high energy region (440-460 nm) averaged over the first 500 ps at 7-minute intervals. The signal is very weak and, thus, relatively noisy at each time slice, nevertheless, we saw no real increase in the signal intensity over the course of the hour measurement. Figure A-0-7 shows the lack of power dependence of the S_n emission kinetics ranging from 7.0×10^{12} photons/cm^2 to 1.7×10^{14}

photons/cm^2. Figure A-0-7B shows a representative beam profile for the TR-PL measurements used to calculate power densities.

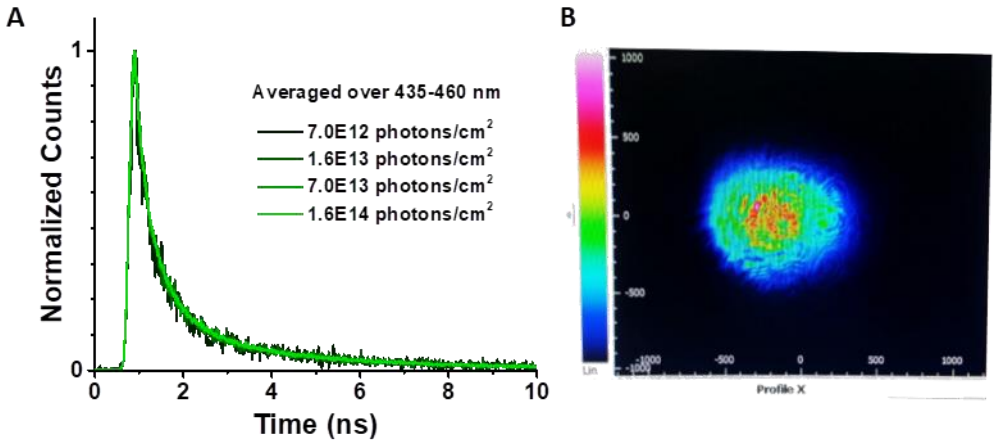

Figure A-0-7 TR-PL power dependence.

A) Kinetic traces of a 3.2 μg/mL mass loading of TAHz in water at increasing fluences highlighting the fluence independence in this range. B) Representative beam profile with an effective radius of ~400 μm. This was the beam radius used to calculate the fluences shown left.

To place the S_n energy level, Figure A-0-8 shows a Gaussian peak fit to the S_n associated spectrum extracted using global target analysis. To estimate the E_{00} transition, we find 10% of the peak max along the high energy side of emission, which in this case was extrapolated due to the window of collection being limited by Raman scattering from water centered around 420 nm (2.95 eV), Figure A-0-9. Acknowledging large potential error bars in this process, we place the S_n state

to be at 2.9 eV. We observe no distinct absorption feature associated with this transition, primarily due to optical scattering related to sample agglomeration.

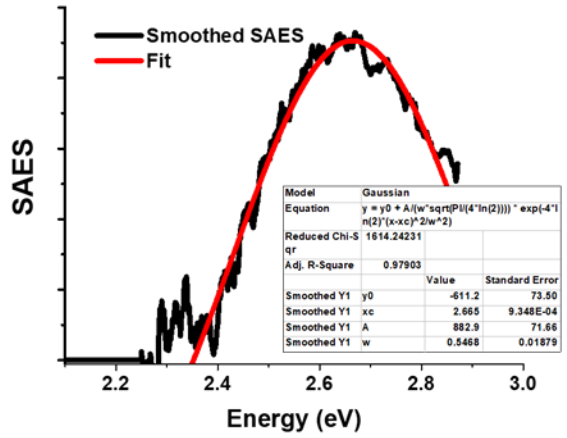

Figure A-0-8 Gaussian fit to Sn PL.

Species associated emission spectra (SAES) for the S_n emission of TAHz-H_2O extracted from global target analysis was smoothed by 10-point adjacent averaging and a Gaussian peak was fit to the data. From this Gaussian we can estimate the S_n energy level to be at 10% of the peak max on the high energy side.

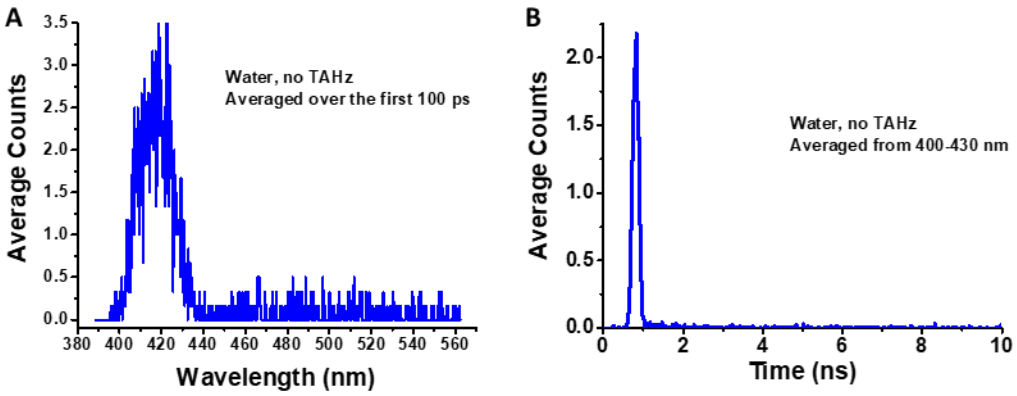

Figure A-0-9 Water Raman scattering.

A) Spectral shape of TR-PL measured for pure water after 365 nm illumination averaged over the first 500 ps. We can see that the Raman scattering feature from water has essentially zero amplitude at 435 nm and therefore, we use this as the cutoff for our analysis of the TR-PL spectra of TAHz in water. B) The kinetic trace averaged over 400-430 nm, showing the feature is indeed Raman scattering as it lives only within the IRF

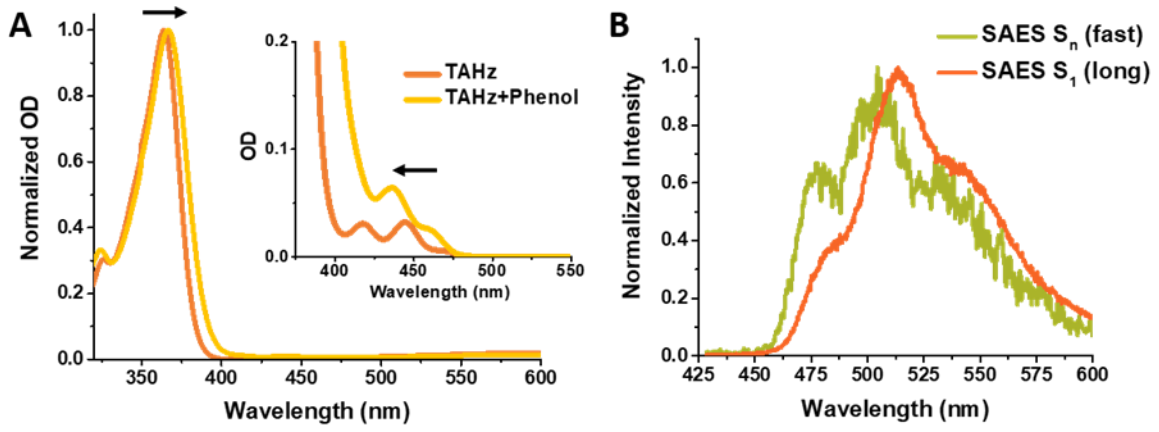

Figure A-0-10 TAHz-PhOH absorption and emission.

A) Normalized absorption spectra of 40 μM TAHz in toluene without phenol (orange) and with 100 mM phenol (yellow). Inset shows absorption spectra of 100 μM TAHz in toluene without phenol (orange) and with 100 mM phenol (yellow) at low energies. We see a blueshift of these peaks with addition of phenol and one becomes convoluted with the redshifted main absorption. This suggests these low-energy features are $n \rightarrow \pi^*$ in character. B) A TR-PL measurement of 40 μM TAHz in toluene with 100 mM phenol shows two distinct emission features, analogous to TAHz in water. The SAES of the S_n assigned feature decays with a lifetime of 494 ps, and the S_1 decays with a lifetime of 4.45 ns.

Additionally, we also studied TAHz with phenol (PhOH) as an electron and proton donor that is soluble in toluene. The solubility of TAHz in toluene allows for transmission measurements, and simpler analysis of decay kinetics. From the absorption measurements shown in Figure A-0-10, we can see a redshift of the main absorption peak, characteristic of $\pi \rightarrow \pi^*$ transitions. Looking at the low energy transitions, we see a blueshift, consistent with $n \rightarrow \pi^*$ transitions. We performed the analogous TR-PL experiment with TAHz:PhOH as with TAHz:H_2O. After 365 nm excitation, there were two kinetically distinct emissive states, extracted using global analysis shown in Figure A-0-10. This dataset was modelled with each component only having one exponential decay, which we attribute to the lack of aggregation. No other constraints were applied to the model. Once

again, blueshifted emission shows a fast decay with a lifetime of 494 ps, which we attribute to a higher-lying mixed $n\pi^*/\pi\pi^*$ state.

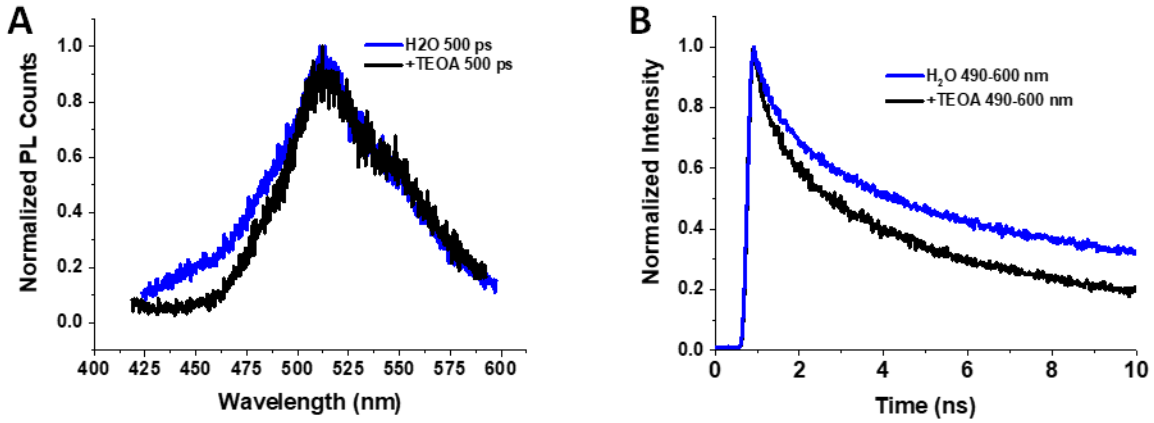

Figure A-0-11 TR-PL with TEOA.

A) TR-PL traces averaged over the first 500 ps for TAHz in water (blue) and TAHz in water plus 10% triethanolamine (TEOA) (black). The lack of high energy emission upon the addition of TEOA suggests that the high energy emission is outcompeted by addition of a strong electron donor. B) Kinetic traces of the S1 decay shows a faster initial decay of PL with added triethanolamine suggesting the electron transfer is significant quenching process. Remaining emission is likely from chromophores within aggregates.

Interestingly, when a strong electron donor is added, such as triethanolamine as shown in Figure A-0-11, the high energy emission is no longer present. This suggests that the high energy emission is outcompeted by fast electron transfer. We attribute a significant portion of the remaining emission to chromophores inside aggregates that cannot contact the triethanolamine and be quenched. However, the remaining S_1 emission could be due to a kinetic barrier to electron transfer.

Global target analysis and KIE discussion

We model the emission spectra of TAHz in water by global target analysis using the GloTarAn software package.[3] We take the total PL intensity $\Theta(t,\lambda)$ at time t and wavelength λ as a sum of concentration-weighted spectral components such that, $\Theta(t,\lambda) = \Sigma c_i(t)\sigma_i(\lambda)$, where $c_i(t)$ and $\sigma_i(\lambda)$,

respectively, correspond to time-dependent concentration and wavelength-dependent species-associated emission spectrum (SAES) of the i^{th} emissive species. Additionally, we use this fitting routine to determine the instrument response function (IRF) by fitting the rising edge to a Gaussian and deconvoluting it from the extracted $c_i(t)$ and $\sigma_i(\lambda)$.

From the TCSPC kinetic traces, shown in Figure A-0-2, we found the spectrally-averaged decay (primarily S_1 emission) fit best to three exponentials. We attribute this to the aggregation, mentioned in the previous section, causing inhomogeneity. Therefore, in our global target analysis model, we let our S_1 emission decay with three exponentials by creating three components where $\sigma_i(\lambda)$ was set to be equal (Equation 2). We did not constrain spectral shape in any way. Through an iterative process, we found that the S_n emission was best modelled with two decay components. The only constraint applied to this component was that the spectral intensity goes to zero at 550 nm. We justify this constraint by noting that we see no kinetic difference at energies lower than 550 nm upon isotopic substitution (Figure A-0-5), or spectral different from increasing mass loading (Figure A-0-4), or when comparing early-time and long-time slices (Figure A-0-12 A).

$$\psi_{Total}(t,\lambda) = \left(c_{Sn\_1}(t) + c_{Sn\_2}(t)\right)\epsilon_{Sn}(\lambda) + \left(c_{S1\_1}(t) + c_{S1\_2}(t) + c_{S1\_3}(t)\right)\epsilon_{S1}(\lambda) \quad (2)$$

We performed this analysis on TR-PL datasets taken in H_2O and D_2O and observed nearly identical SAES components shown in Figure A-0-12. This is expected, as one anticipates no spectral difference due to isotopic substitution. However, from the extracted concentration profiles shown in Figure A-0-12, we see that the prompt S_n decay component is significantly different between H_2O and D_2O. We attribute this decay pathway to be associated with quenching of the S_n through proton motion from water to TAHz. We would expect this to be dominant at early times in a hydrogen-bonded complex. We note that some of the H_2O S_n quenching is likely occurring

within the IRF, resulting in the prompt H_2O S_n concentration being at a lower relative amplitude compared to that of D_2O.

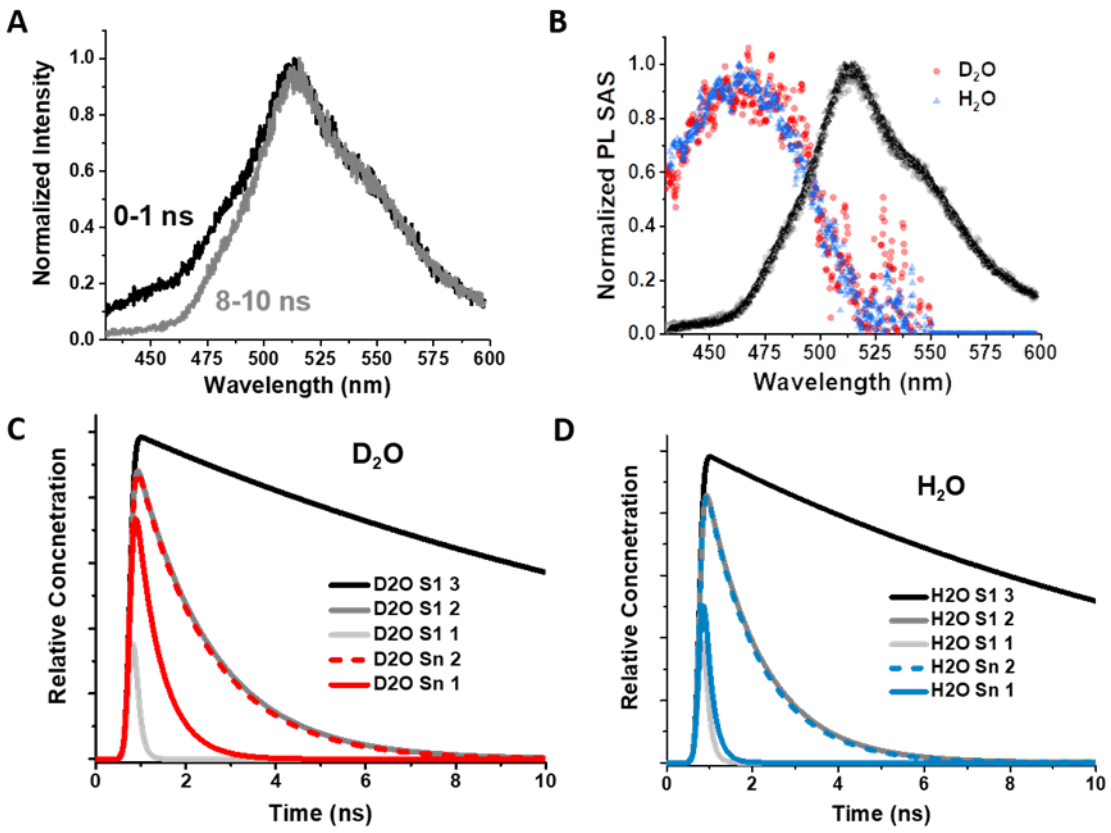

Figure A-0-12 TR-PL TAHz-water global target analysis.

A) TR-PL of TAHz in water at 6 μg/mL mass loading. When comparing the spectral shape over the first nanosecond (black) to that at later times (grey), we see a clear evolution in the high energy region. B) Species associated emission spectra (SAES) obtained through global analysis of the data shown in A and the equivalent dataset in D_2O. The spectral shapes pulled out for each H_2O (blue triangles) and D_2O (red circles), S_n emission spectra are very similar, as are the S_1 emission spectra shown in black and grey for H_2O and D_2O, respectively. However, there is a significant difference in the kinetics between TAHz in D_2O and H_2O shown in C and D, respectively. The prompt S_n decay components (labeled "S_n 1") are depicted in the solid red and blue lines for D_2O and H_2O, respectively. There is a clear difference in kinetics in those rates that we do not observe among any other components. We attribute this decay component to proton motion that quenches the S_n state on the picosecond and nanosecond timescale.

Radical Detection

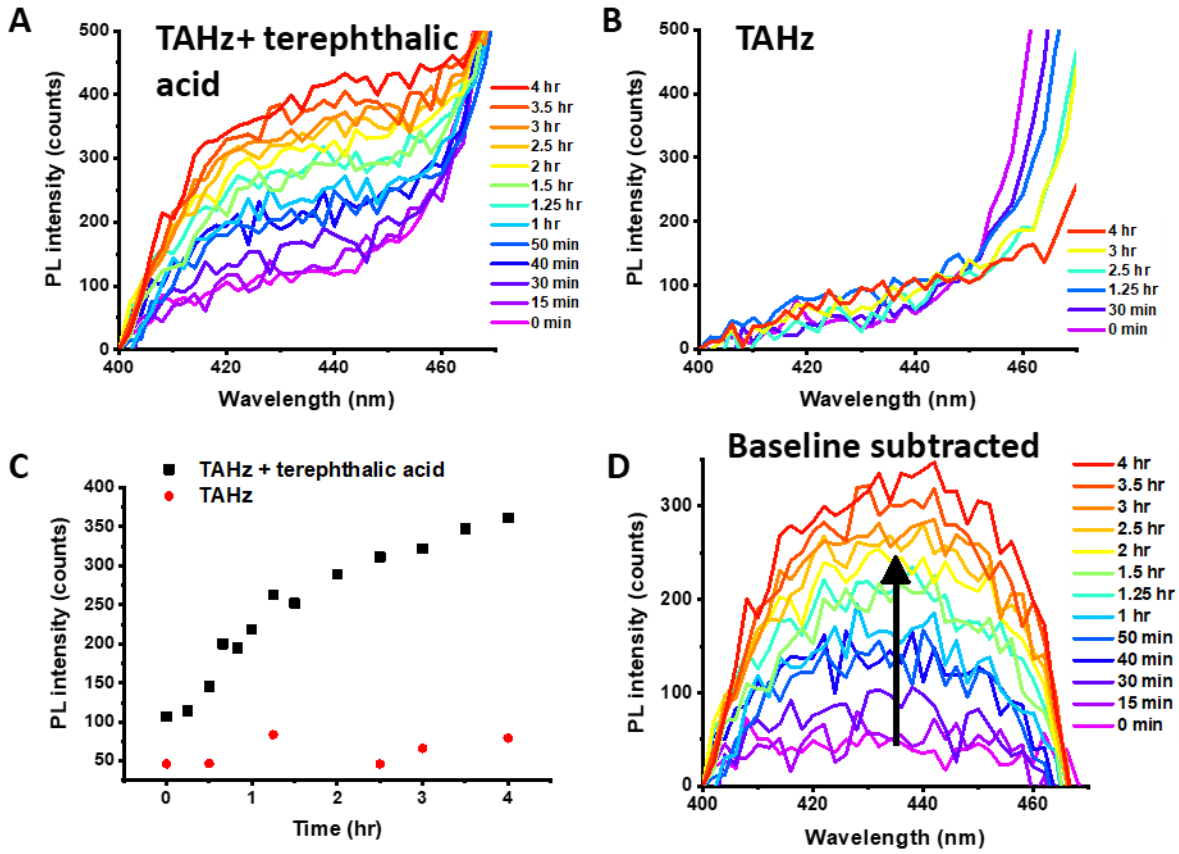

Figure A-0-13 Hydroxyl radical detection.

A) Raw PL spectra of terephthalic acid in a 3.0 mM aqueous solution of 25 μg/mL TAHz with increasing illumination time (purple to red). B) Shows PL spectra for 25 μg/mL mass loading of TAHz in a 3 mM NaOH aqueous solution without terephthalic acid. The spectra change negligibly over time with illumination. C) Plots the peak intensity averaged from 420-445 nm for just TAHz (red circles) and TAHz terephthalic acid (black squares). From this plot we can see an increase in hydroxyl radical with continued illumination. D) By subtracting an average PL spectrum from just TAHz (no terephthalic acid), we observe a distinct PL peak grow in at 435 nm, as expected for 2-hydroxyterephthalic acid.

To confirm that radicals are indeed forming as proposed in Scheme 1, we used terephthalic acid, a well-known radical scavenger that becomes luminescent upon reacting with hydroxyl radicals.[4] 2-hydroxyterephthalic acid also absorbs weakly at 365 nm, but emits ~430 nm, so we monitored the PL at 430 nm as a function of illumination time over 4 h, shown in Figure A-0-13. As TAHz becomes photoexcited and generates heptazinyl and hydroxyl radicals, the hydroxyl radicals are

scavenged by terephthalic acid to make 2-hydroxyterephthalic acid leading to increasing emission at 435 nm over time. Performing the same measurement without terephthalic acid shows that there is minimal background contribution from just TAHz emission as a function of illumination time. The slight change at 450-460 nm could be due to aggregates breaking up with illumination and stirring. We also looked for evidence of luminescence with only terephthalic acid in a 3 mM NaOH aqueous solution under the same illumination conditions but saw no PL at all.

REFERENCES

1. Eberhardt, M. K.; Colina, R., The reaction of OH radicals with dimethyl sulfoxide. A comparative study of Fenton's reagent and the radiolysis of aqueous dimethyl sulfoxide solutions. *J. Org. Chem.* **1988,** *53* (5), 1071-1074.
2. Rafat Husain, S.; Cillard, J.; Cillard, P., Hydroxyl radical scavenging activity of flavonoids. *Phytochemistry* **1987,** *26* (9), 2489-2491.
3. Snellenburg, J. J.; Laptenok, S. P.; Seger, R.; Mullen, K. M.; van Stokkum, I. H. M., Glotaran: A Java-Based Graphical User Interface for the R Package TIMP. *J. Stat. Softw.* **2012,** *49* (3), 1-22.
4. Morawski, O.; Izdebska, K.; Karpiuk, E.; Suchocki, A.; Zhydachevskyy, Y.; Sobolewski, A. L., Titanyl Phthalocyanine as a Water Photooxidation Agent. *J. Phys. Chem. C* **2015,** *119* (25), 14085-14093.

Appendix B: Supplementary Information for Chapter 5

K_A determination using ground state absorption

Ground state absorption was used to monitor the formation of TAHz-R-PhOH complexes prior to photoexcitation. To account for any changes to the baseline, each spectrum was averaged from 495-500 nm (where there is no TAHz absorption) and subtracted from the spectrum. We chose to plot the change in absorption at 380 nm because of the large change at that wavelength, resulting in the cleanest fit. Additionally, this is far away from any tail absorption of the phenols. Using the difference in absorption at 380 nm we calculated the association constant between TAHz and the series of phenols. In this fit both the change in molar absorptivity ($\Delta\varepsilon_{380}$) between free TAHz and the bound complex as well as the association constant (K_A) were parameters. In all cases the derived $\Delta\varepsilon_{380}$ was around 50,000 $M^{-1}cm^{-1}$.

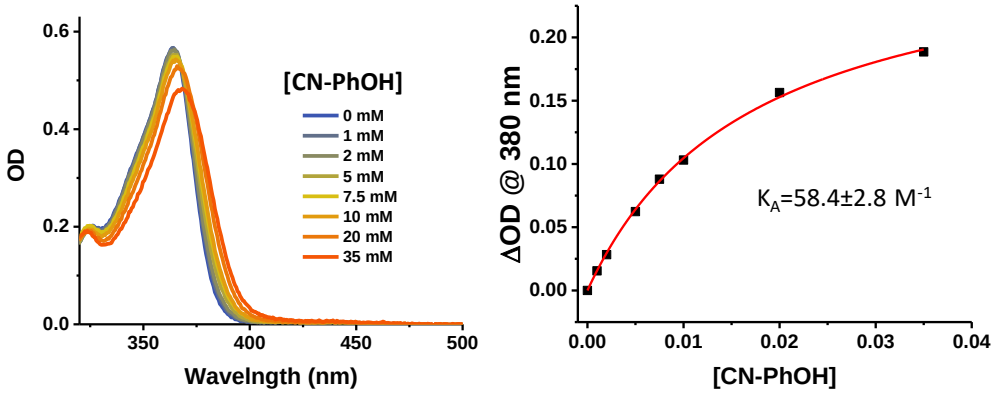

Figure B-0-1. Absorption of TAHz as a function of CN-PhOH concentration. Concentrations ranging from 0-35 mM (left). Fitting the difference in absorption at 380 nm versus the concentration of phenol gives a K_A= 58.4±2.8 M^{-1} (right).

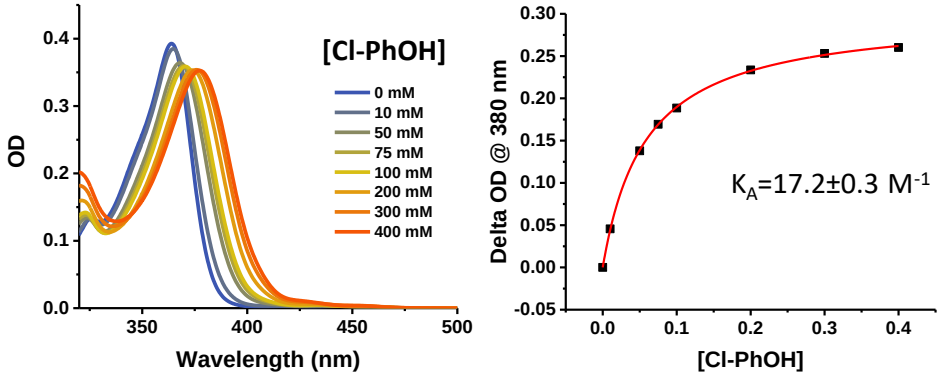

Figure B-0-2. Absorption of TAHz as a function of Cl-PhOH concentration. Concentrations ranging from 0-400 mM (left). Fitting the difference in absorption at 380 nm versus the concentration of phenol gives a K_A= 17.2±0.3 M^{-1} (right).

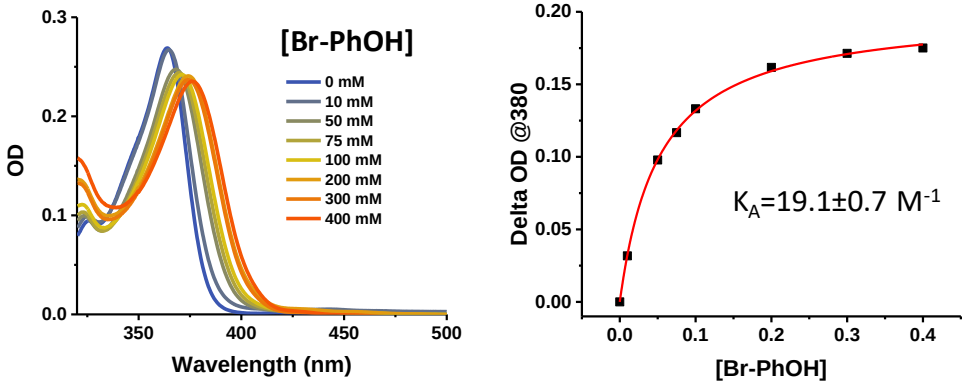

Figure B-0-3. Absorption of TAHz as a function of Br-PhOH concentration. Concentrations ranging from 0-400 mM (left). Fitting the difference in absorption at 380 nm versus the concentration of phenol gives a K_A= 19.1±0.7 M^{-1} (right).

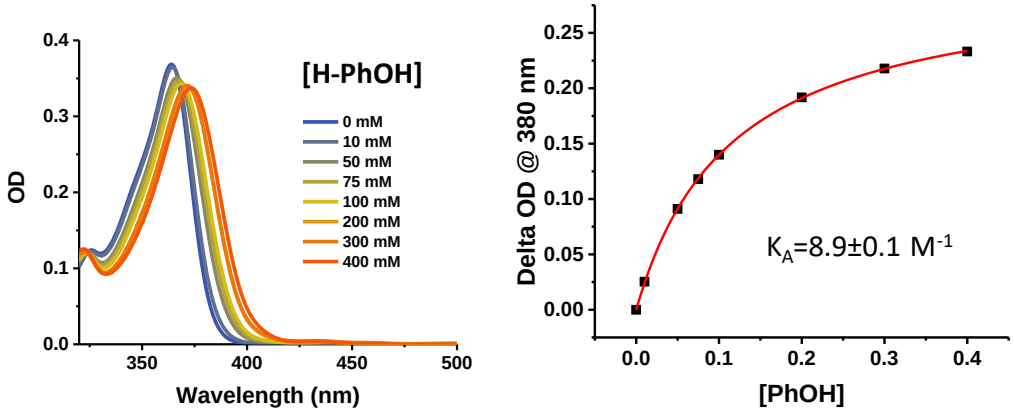

Figure B-0-4. Absorption of TAHz as a function of H-PhOH concentration. Concentrations ranging from 0-400 mM (left). Fitting the difference in absorption at 380 nm versus the concentration of phenol gives a K_A= 8.9±0.1 M^{-1} (right).

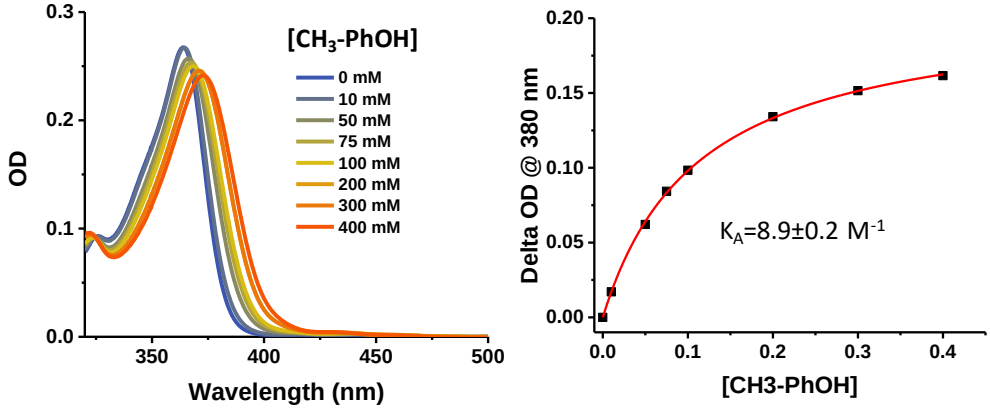

Figure B-0-5. Absorption of TAHz as a function of CH_3-PhOH concentration. Concentrations ranging from 0-400 mM (left). Fitting the difference in absorption at 380 nm versus the concentration of phenol gives a K_A= 8.9±0.2 M^{-1} (right).

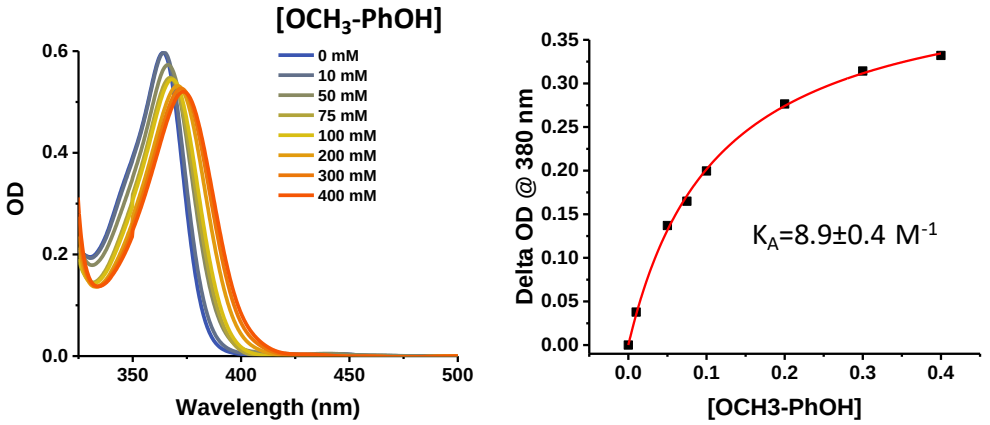

Figure B-0-6. Absorption of TAHz as a function of OCH_3-PhOH concentration. Concentrations ranging from 0-400 mM (left). Fitting the difference in absorption at 380 nm versus the concentration of phenol gives a K_A= 8.9±0.4 M^{-1} (right).

K_Q Determination via Lifetime Quenching

We took lifetime measurements of TAHz:R-PhOH systems in a range of concentrations using the TCSPC system mentioned above. We plotted the data according to $\frac{1}{\tau} = k_f + k_Q[Q]$, where τ is the florescence lifetime, k_f is the radiative rate constant, k_Q is the quenching rate constant, and [Q] is the concentration of phenol. In this case, the slope is quenching rate constant for each phenol

derivative. For CN-PhOH the concentration range was 2-10 mM and for all other phenols, the concentration range was 25- 125 mM. Due to residual pump light out to 5 ns, we fit all decay curves after this time period. This effectively cut out the fast lifetime component attributed to the hydrogen-bound complex. This only allows us to report on the quenching of free TAHz as a function of phenol concentration.

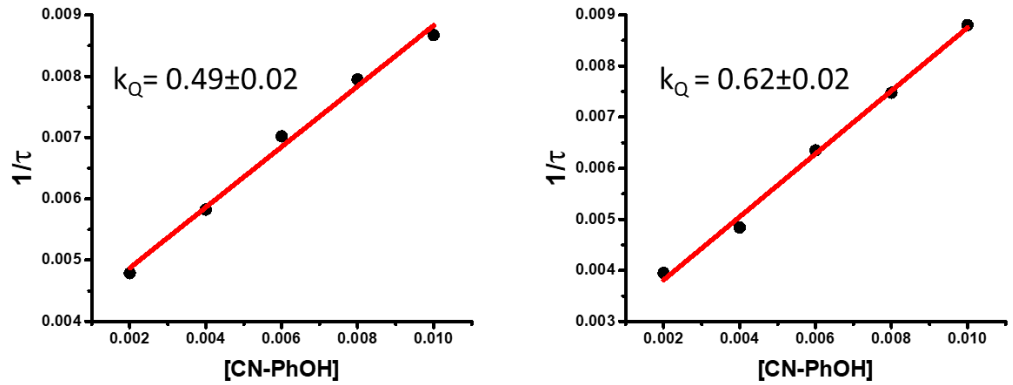

Figure B-0-7. Stern-Volmer quenching data for TAHz with CN-PhOH.
Gives an average k_Q=0.56 s^{-1}. The range of CN-PhOH concentrations was limited by the solubility of CN-PhOH in toluene.

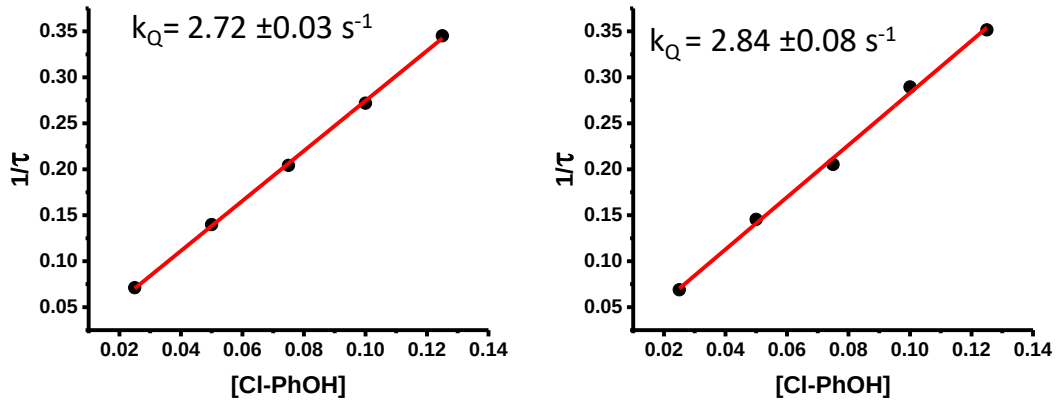

Figure B-0-8. Stern-Volmer quenching data for TAHz with Cl-PhOH.
Gives an average k_Q=2.78 s^{-1}.

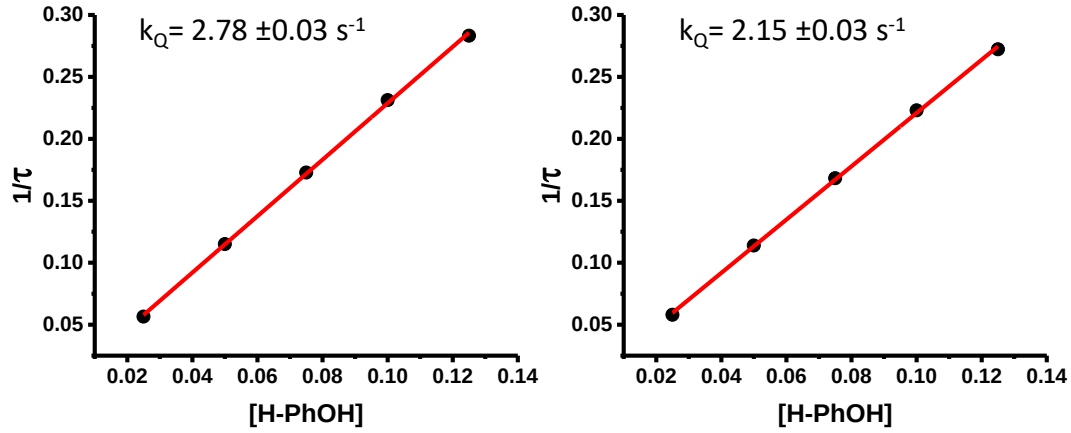

Figure B-0-9. Stern-Volmer quenching data for TAHz with H-PhOH.
Gives an average k_Q=2.21 s^{-1}.

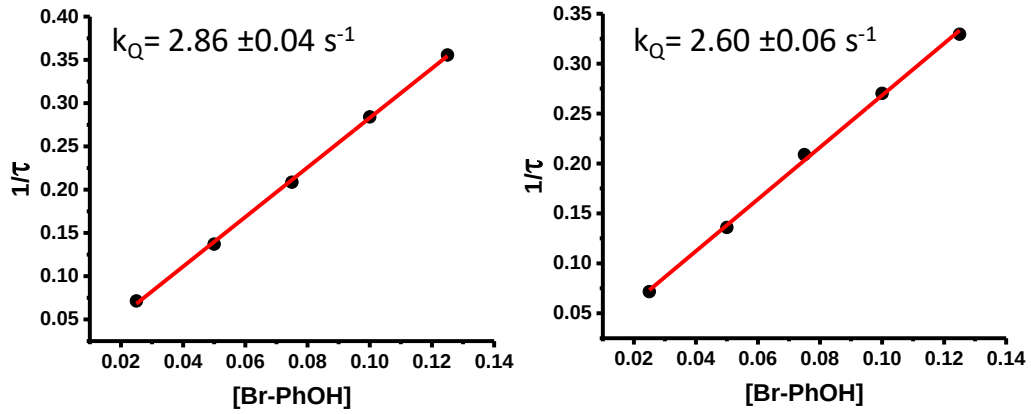

Figure B-0-10. Stern-Volmer quenching data for TAHz with Br-PhOH.
Gives an average k_Q=2.73 s^{-1}.

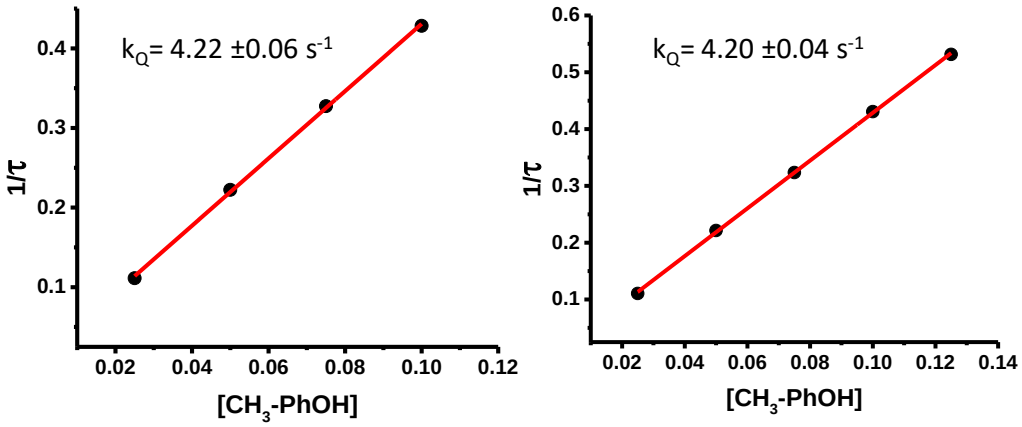

Figure B-0-11. Stern-Volmer quenching data for TAHz with CH_3-PhOH.
Gives an average k_Q=4.21 s^{-1}.

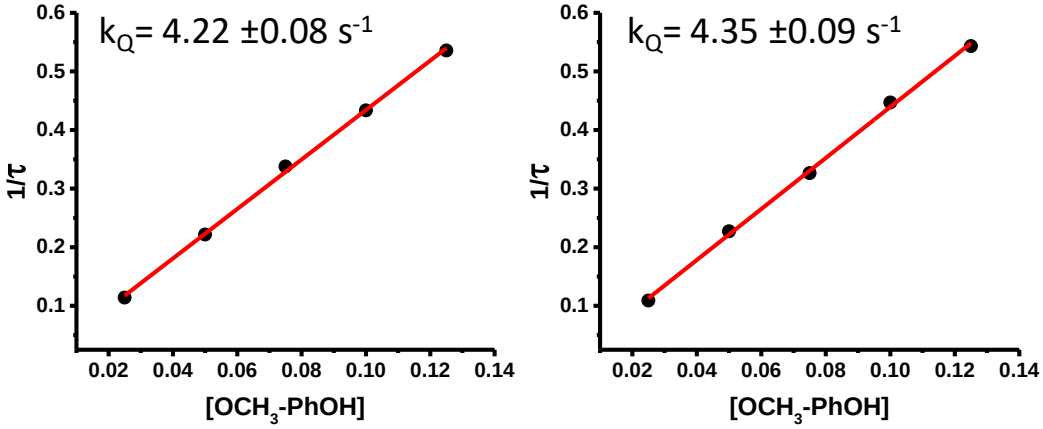

Figure B-0-12. Stern-Volmer quenching data for TAHz with OCH_3-PhOH.
Gives an average k_Q=4.26 s^{-1}.

Quenching Rate Constant Determination via Intensity Quenching

We took PLQY measurements of TAHz:R-PhOH systems in a range of concentrations (0-10 mM) to find the quenching constant and compare to the quenching constant found via lifetime quenching seen above. By plotting the ratio of the PLQY in the absence and presence of quencher

(I_0/I), we can find the quenching rate constant (k_Q) by using $\frac{I_0}{I} = 1 + \frac{k_Q}{k_f}[Q]$ and knowing the fluorescence rate constant of TAHz in toluene without quencher, 3.486x10^6 s^{-1}.[1]

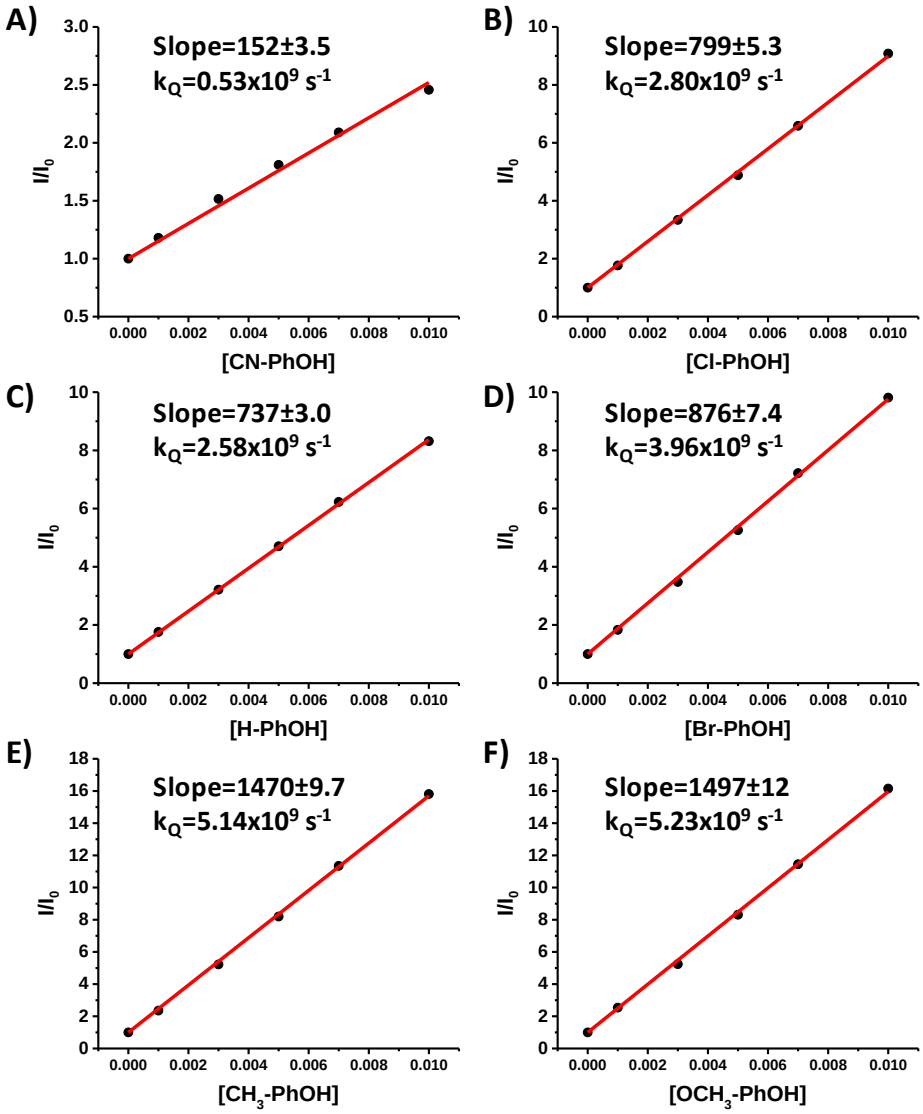

Figure B-0-13. Stern-Volmer quenching plots for TAHz.
A) CN-PhOH, B) CL-PhOH, C) H-PhOH, D) Br-PhOH, E) CH_3-PhOH, F) OCH_3-PhOH in toluene using PLQY values upon 365 nm excitation.

TR-PL of TAHz in Toluene

Without phenol present, the TAHz emission decays monoexponentially across the entire spectrum (Figure B-0-14). Therefore, we attribute the fast component of the PL spectrum of TAHz

and PhOH solutions to a hydrogen-bound TAHz-PhOH complex. We see this fast component with all phenol derivatives except OCH_3-PhOH (Figure B-0-20).

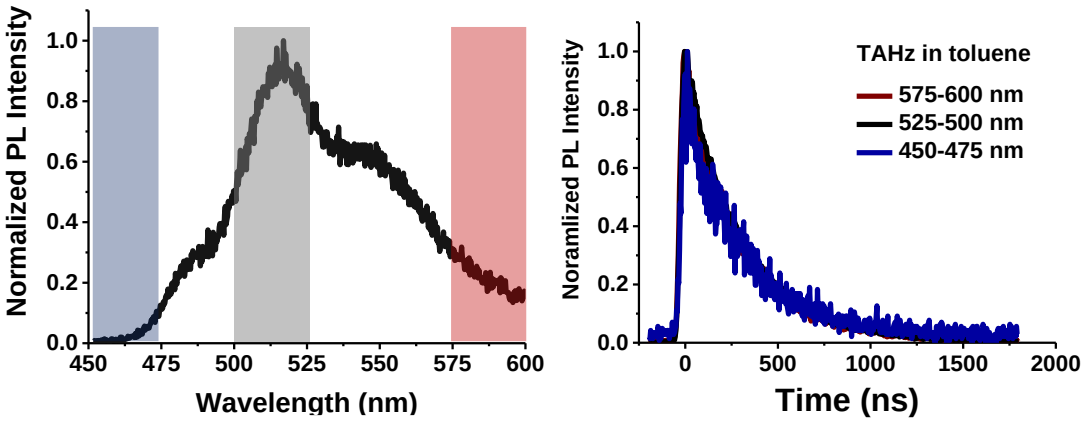

Figure B-0-14. The emission spectrum and decay of TAHz in toluene.
Without an abstractable hydrogen present the luminescence spectrum (left) shows a single exponential decay rate (right).

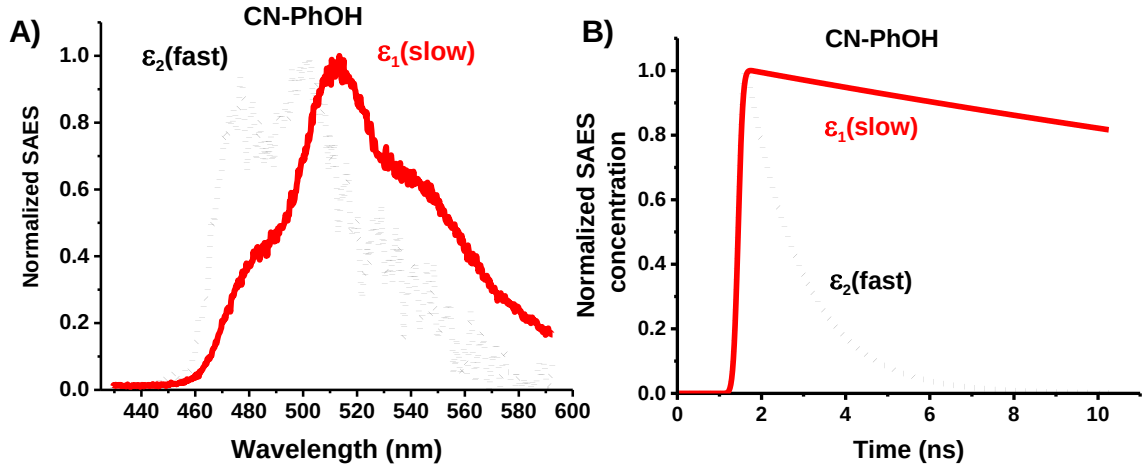

Figure B-0-15. Global target analysis of the TR-PL data of TAHz and 50 mM CN-PhOH.
It shows two species associated emission spectra (SAES) (A) and distinct kinetic decays (B). Emission attributed to the S_1 state, labeled ϵ_1 (red), is the emission shape seen in steady-state measurements. The second SAES, labeled ϵ_2 (dotted black), is seen at higher energies and decays notably faster than ϵ_1.

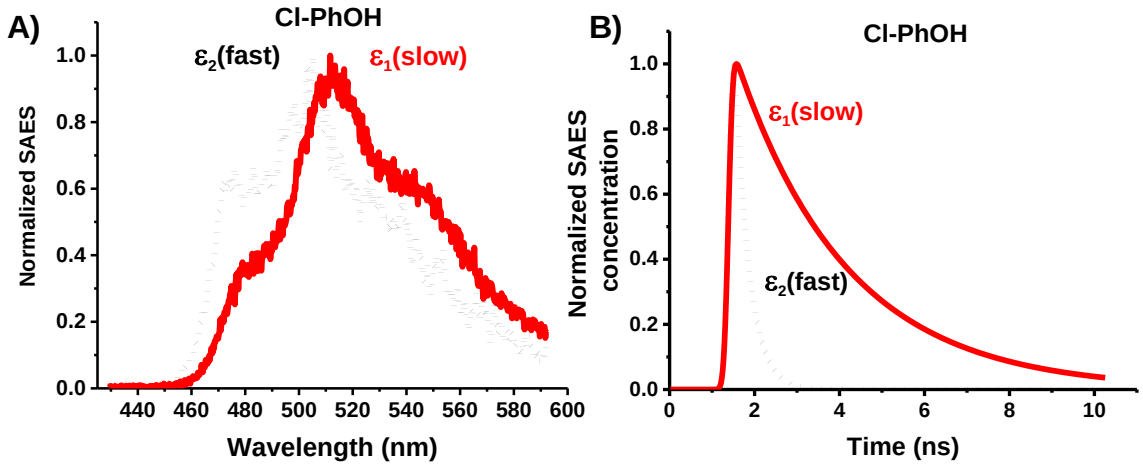

Figure B-0-16. Global target analysis of the TR-PL data of TAHz and 100 mM Cl-PhOH.
It shows two species associated emission spectra (SAES) (A) and distinct kinetic decays (B). Emission attributed to the S_1 state, labeled ϵ_1 (red), is the emission shape seen in steady-state measurements. The second SAES, labeled ϵ_2 (dotted black), is seen at higher energies and decays notably faster than ϵ_1.

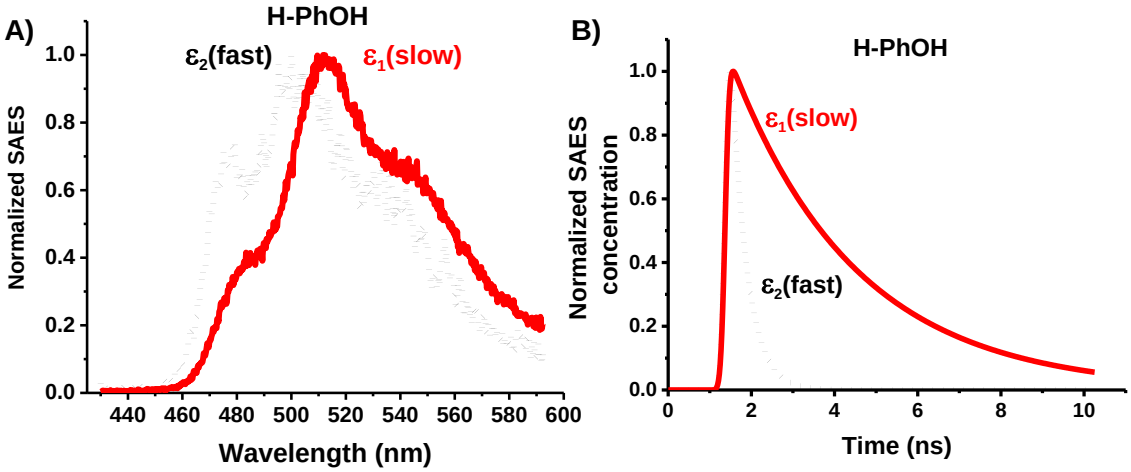

Figure B-0-17. Global target analysis of the TR-PL data of TAHz and 100 mM H-PhOH.
It shows two species associated emission spectra (SAES) (A) and distinct kinetic decays (B). Emission attributed to the S_1 state, labeled ϵ_1 (red), is the emission shape seen in steady-state measurements. The second SAES, labeled ϵ_2 (dotted black), is seen at higher energies and decays notably faster than ϵ_1.

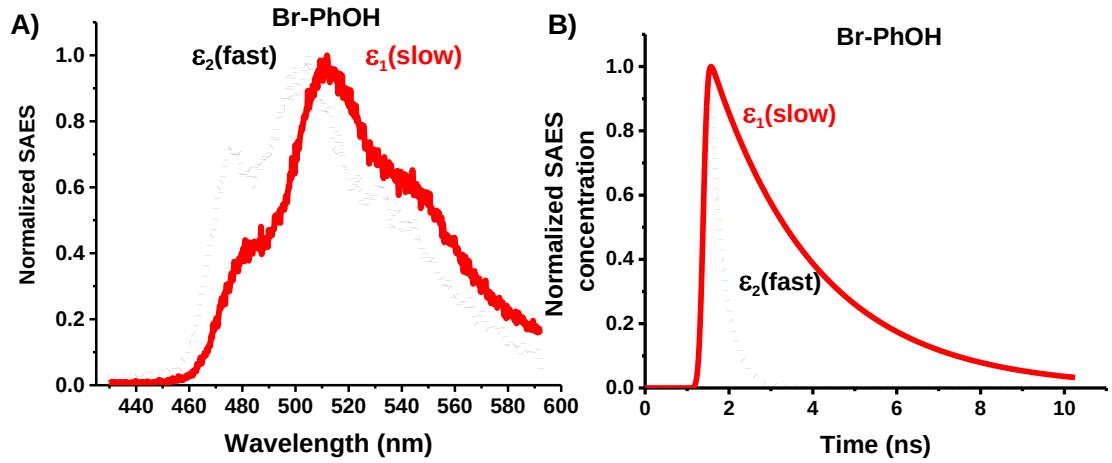

Figure B-0-18. Global target analysis of the TR-PL data of TAHz and 100 mM Br-PhOH.
It shows two species associated emission spectra (SAES) (A) and distinct kinetic decays (B). Emission attributed to the S_1 state, labeled ϵ_1 (red), is the emission shape seen in steady-state measurements. The second SAES, labeled ϵ_2 (dotted black), is seen at higher energies and decays notably faster than ϵ_1.

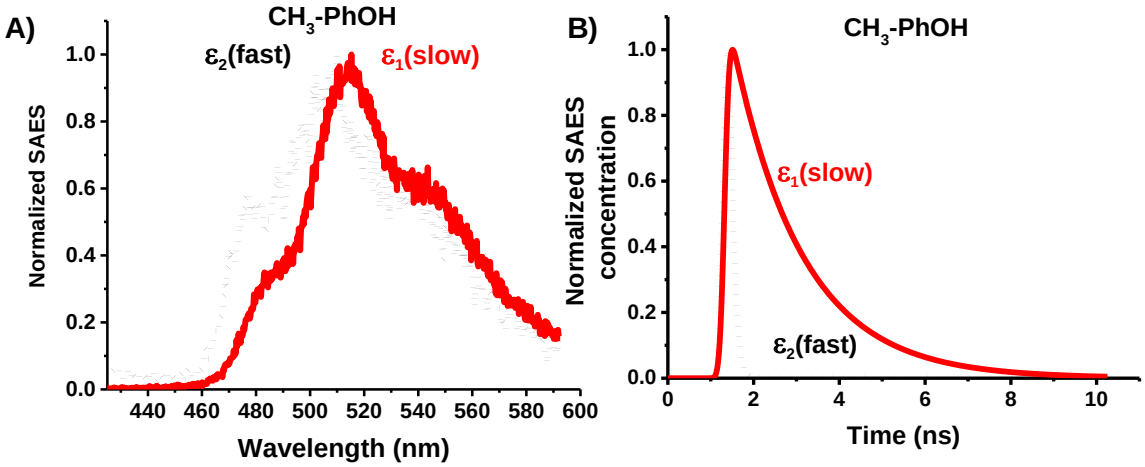

Figure B-0-19. Global target analysis of the TR-PL data of TAHz and 100 mM CH_3-PhOH.
It shows two species associated emission spectra (SAES) (A) and distinct kinetic decays (B). Emission attributed to the S_1 state, labeled ϵ_1 (red), is the emission shape seen in steady-state measurements. The second SAES, labeled ϵ_2 (dotted black), is seen at higher energies and decays notably faster than ϵ_1.

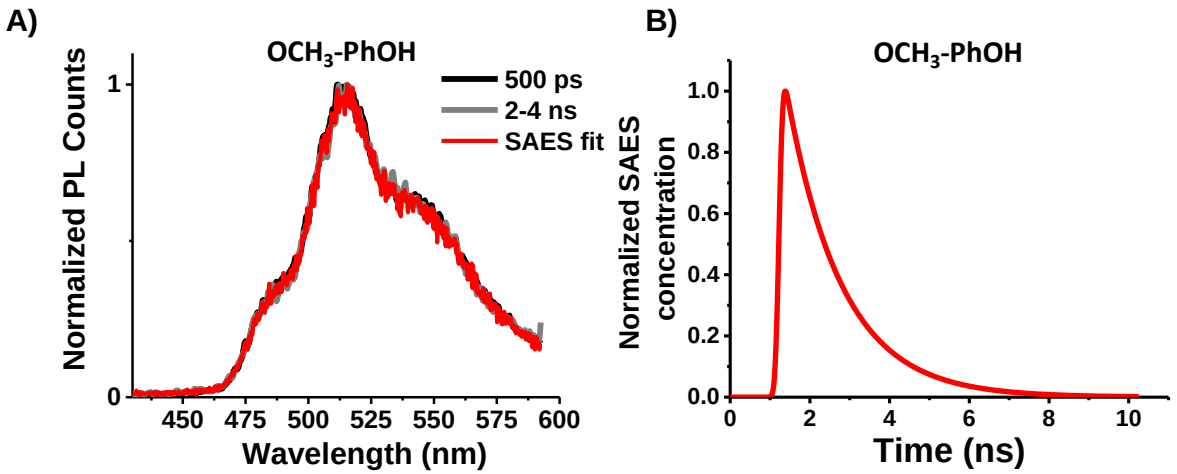

Figure B-0-20. The TR-PL of OCH_3-PhOH – a single component.
A) Normalized spectra of TAHz PL at 500 ps (black) and 2-4 ns (grey) show not spectral difference. The global analysis of the data showed the best fit with only one component, the spectrum of the species associated emission spectra (SAES) is shown in red. B) The kinetic decay of the SAES has a lifetime of 1.37 ns.

Electrochemistry

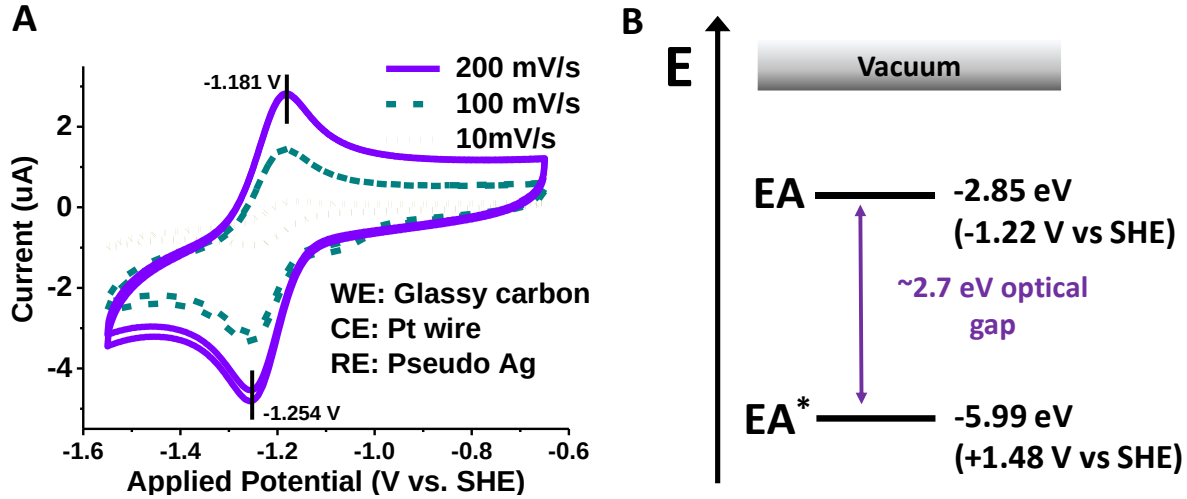

Figure B-0-21. Cyclic voltammogram of TAHz in THF.
A) Cathodic cyclic voltammogram of 475 μM TAHz in THF with 250 mM $TABPF_6$ as the supporting electrolyte. The reversible reduction allows us to calculate the E_{red} to be -1.22 V vs SHE. This allows us to calculate the electron affinity (EA) and excited state electron affinity (EA*) shown in B.

Cyclic voltammograms of TAHz in THF taken inside an argon glovebox are shown in Figure B-0-21. The 73 mV peak separation suggests this reduction is reversible. From this reduction CV we can estimate the electron affinity (EA), which corresponds to the LUMO, to be -2.85 eV relative

to vacuum.[2] Using the singlet energy, we can estimate the excited state electron affinity (EA*) to be -5.99 eV relative to vacuum. This energy landscape is depicted in Figure B-0-21 The EA* represented the driving force for one-electron reduction of the photoexcited TAHz molecule.

Computational Methods

The geometries of the heptazine with PhOH, CN-PhOH, Br-PhOH, Cl-PhOH, CH_3-PhOH and OCH_3-PhOH complexes were obtained by minimizing the energy of the electronic ground-state using second-order Møller-Plesset perturbation theory (MP2).[3] The equilibrium geometries of them were optimized in C_s symmetry to speed up convergence. Vertical excitation energies were evaluated at these geometries using the second-order algebraic diagrammatic construction scheme (ADC(2)).[4] MP2 and ADC(2) have been benchmarked in previous studies and have turned out to be reliable tools to describe H-atom transfer reactions from water to carbon-nitride chromophores.[5-6]

For the two-dimensional potential-energy surfaces, the OH- and ON-distances were kept fixed and all other degrees of freedom were relaxed in order to minimize the energy of the lowest excited-state of A′ symmetry. The C_s symmetry constraint has been applied for all calculations along the scans to be able to optimize the first excited state of A′ symmetry.

Minimum energy geometries of the S_1 states of the systems were obtained by relaxation of all degrees of freedom in order to minimize the energy of the S_1 state using the C_s symmetry constraint.

The saddle point geometries of the lowest excited-state of A′ symmetry are approached through structure optimization using the Trust Radius Image Minimization algorithm[7], which maximizes the energy along the only Hessian eigenvector with imaginary frequency while minimizing it along

all the other directions. This particular vector should describe the H-atom transfer from phenol (or its derivatives) to heptazine. The estimated geometry of the saddle point from the two-dimensional potential energy surface served as initial guess for the saddle point optimization. After the optimization a frequency calculation was performed to confirm that there is only one mode with an imaginary frequency at the saddle point geometry.

For all calculations Dunning's correlation-consistent double ξ basis set (cc-pVDZ)[8] has been used and the resolution-of-identity[9] approximation was applied. Calculations were performed with the Turbomole program package.[10]

Computational Results

Table B-0-1. Experimental data (for TAHz) and computational data (for Hz) for the hydrogen bonded complexes with the phenol derivatives, where R describes the substituent.
The energies of the first excited singlet state (S_1) at the ground-state equilibrium geometry (S_1^{GS}), at the equilibrium geometry (S_1^{min}), and at the geometry of the transition state of the ES-PCET reaction (S_1^{TS}) are given. S_{CT}^{GS} is the vertical excitation energy of the lowest charge-transfer state. ΔE^{min} is the vibrational stabilization energy of the S_1 state. $\Delta E^{‡}$ is the barrier height for the ES-PCET on the S_1 potential-energy surface calculated as the energy difference between the energy of the transition state and the energy minimum of the locally excited S_1 state.

Experimental Data				Computational Data (eV)					
R	E_0 ($RPhOH^+$/ RPhOH)	k_Q ($x10^9$ s^{-1}) PLQY	S_1 KIE	S_1^{GS}	S_{CT}^{GS}	S_1^{min}	ΔE^{min}	S_1^{TS}	$\Delta E^{‡}$
CN	2.03	0.532	1.9	2.61	3.86	2.52	0.085	2.89	0.369
Cl	1.88	2.80	1.4	2.60	3.45	2.52	0.083	2.69	0.169
Br	1.86	3.06	1.4	2.60	3.44	2.52	0.083	2.70	0.177
H	1.88	2.58	1.5	2.60	3.44	2.51	0.083	2.68	0.167
CH_3	1.79	5.14	1.2	2.60	3.23	2.51	0.082	2.61	0.093
OCH_3	1.68	5.23	1.1	2.59	2.80	2.51	0.081	----	----

The geometries at the saddle point of heptazine with phenol and its derivatives are shown in Figure B-0-22, except for heptazine with OCH_3-PhOH, as there is no barrier and saddle point along the ES-PCET. The structures are ordered according to their hydrogen bond length.

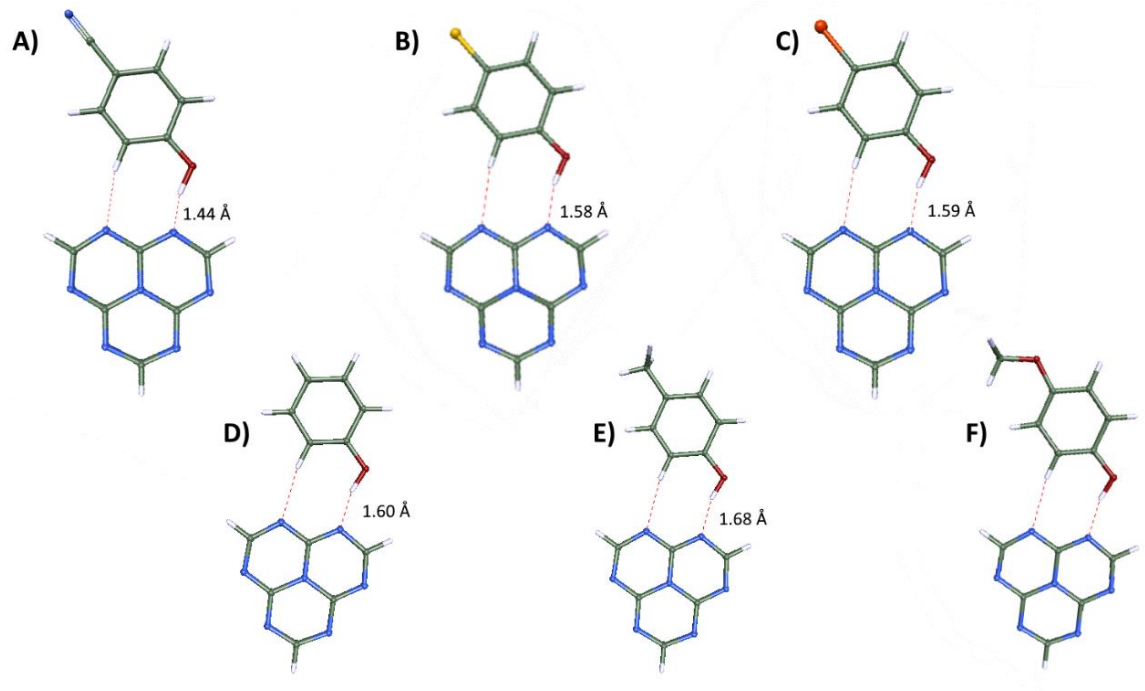

Figure B-0-22. Geometries of heptazine with A) CN-PhOH, B) Cl-PhOH, C) Br-PhOH, D) PhOH, E) CH_3-PhOH complexes at their transition state.
The geometry of heptazine with F) OCH_3-PhOH is an arbitrary structure between the FC point and the biradical state.

As optimization of the saddle points is a subtle task, the cartesian coordinates of the transition structures are given below for future benchmark calculations.

Heptazine with CN-PhOH:

C	2.2300760	-0.1260324	0.0000174
C	2.2186703	1.3014175	0.0000033
C	3.4540070	2.0159678	-0.0000115

C	4.6646841	1.3329382	-0.0000153
C	4.6655797	-0.0867014	-0.0000037
C	3.4473697	-0.8073914	0.0000134
O	1.1102537	2.0138420	-0.0000021
C	5.9179955	-0.7975145	-0.0000105
N	6.9515294	-1.3814581	-0.0000165
N	-1.1736144	0.9961279	0.0000169
C	-2.0876844	2.0225264	0.0000165
N	-3.4254300	1.9066063	0.0000076
C	-3.9273367	0.6680358	-0.0000010
N	-3.0361251	-0.4593672	0.0000008
C	-1.6419182	-0.2590085	0.0000101
N	-5.2464075	0.4426489	-0.0000108
C	-5.6425871	-0.8441613	-0.0000184
N	-4.8760309	-1.9685558	-0.0000172
C	-3.5590822	-1.7812680	-0.0000076
N	-0.8085020	-1.3075722	0.0000117
C	-1.3983079	-2.5315820	0.0000038
N	-2.7100661	-2.8252754	-0.0000057
H	-1.6622256	3.0313155	0.0000244
H	-6.7249568	-1.0115843	-0.0000268
H	-0.7126026	-3.3861185	0.0000057
H	3.4135492	3.1094777	-0.0000194
H	5.6146965	1.8756033	-0.0000274
H	3.4678433	-1.9015247	0.0000234
H	1.2792904	-0.6729761	0.0000315
H	0.1973327	1.4315844	0.0000072

Heptazine with Cl-PhOH:

C	3.9278357	1.5476083	0.0190938
C	2.5964686	1.0458386	0.0263108
C	1.5018287	1.9553608	-0.0217232
C	1.7440056	3.3292918	-0.0773288
C	3.0698595	3.8083290	-0.0861919
C	4.1664360	2.9180511	-0.0379357
O	2.4439508	-0.2729359	0.0793903
Cl	3.3628130	5.5142426	-0.1559581
N	0.0971589	-1.3587242	0.0752622
C	-1.1620603	-0.8971073	0.1284839
N	-2.2292070	-1.8243487	0.2263624
C	-1.9605675	-3.2142976	-0.0146609
N	-0.6939074	-3.6464823	-0.0649814
C	0.2684217	-2.7132800	0.0308302
N	-1.4066422	0.4180953	0.1204695
C	-2.7158536	0.7815606	0.1289987

N	-3.7946505	-0.0198823	0.0441063
C	-3.5629296	-1.3416886	0.0435611
N	-2.9842982	-4.0615444	-0.1542816
C	-4.2224452	-3.5220339	-0.1386480
N	-4.5649645	-2.2114521	-0.0942671
H	1.3074413	-3.0597282	0.0198841
H	-5.0542423	-4.2297484	-0.2208616
H	-2.9119065	1.8588365	0.1591130
H	4.7515454	0.8281815	0.0578408
H	5.1870083	3.3109952	-0.0451525
H	0.9115939	4.0379508	-0.1135978
H	0.4748125	1.5703829	-0.0091020
H	1.4524950	-0.5514719	0.0749836

Heptazine with Br-PhOH:

C	3.9335204	1.5424482	0.0001437
C	2.6016378	1.0423146	0.0002294
C	1.5082021	1.9542440	0.0000572
C	1.7512908	3.3295168	-0.0002426
C	3.0786915	3.8077553	-0.0003477
C	4.1747744	2.9138963	-0.0001409
O	2.4483562	-0.2772974	0.0004462
Br	3.3997614	5.6683855	-0.0007671
N	0.0946486	-1.3635378	0.0002546
C	-1.1622446	-0.8977604	0.0001589
N	-2.2314654	-1.8200351	-0.0003801
C	-1.9666951	-3.2269442	-0.0002541
N	-0.7016234	-3.6613174	-0.0001663
C	0.2626939	-2.7217680	-0.0000086
N	-1.4102110	0.4179536	0.0005525
C	-2.7204425	0.7780585	0.0004888
N	-3.8047288	-0.0232706	0.0002572
C	-3.5729374	-1.3454539	-0.0000687
N	-2.9976138	-4.0788839	-0.0003037
C	-4.2331844	-3.5340010	-0.0003408
N	-4.5788610	-2.2206972	-0.0001538
H	1.3011812	-3.0694736	-0.0000074
H	-5.0675845	-4.2433627	-0.0004563
H	-2.9165731	1.8557550	0.0007372
H	4.7564667	0.8209133	0.0002955
H	5.1978167	3.3006218	-0.0002121
H	0.9162146	4.0361045	-0.0003939
H	0.4805017	1.5705426	0.0001739
H	1.4584071	-0.5547074	0.0004490

Heptazine with PhOH:

C	1.1286021	-2.2374308	-0.0002474
C	-0.1700332	-2.8203391	0.0000657
C	-0.3143224	-4.2352230	0.0002561
C	0.8164897	-5.0509646	0.0000872
C	2.1055451	-4.4725596	-0.0002769
C	2.2519367	-3.0712447	-0.0004309
O	-1.2887446	-2.0972290	0.0000465
N	-1.2357627	0.5009980	0.0002413
C	-0.2720618	1.4329085	0.0005058
N	-0.6409764	2.7961418	0.0007939
C	-2.0233232	3.1664065	0.0001460
N	-2.9626872	2.2132679	-0.0001537
C	-2.5326956	0.9376523	-0.0000221
C	0.3673329	3.8001576	0.0002756
N	1.6595924	3.4366664	0.0002405
C	1.9128148	2.1124152	0.0004470
N	1.0207993	1.0867514	0.0004557
N	0.0136371	5.0857807	-0.0001741
C	-1.3197401	5.3426922	-0.0003552
N	-2.3458581	4.4637639	-0.0003140
H	2.9691275	1.8226052	0.0004575
H	-1.5985035	6.4017661	-0.0007892
H	-3.2954934	0.1518190	-0.0005202
H	1.2320194	-1.1459632	-0.0003525
H	3.2521441	-2.6260681	-0.0007216
H	2.9917347	-5.1152049	-0.0004539
H	0.7035785	-6.1397782	0.0002301
H	-1.3273702	-4.6491573	0.0005337
H	-1.0977816	-1.0906302	0.0000289

Heptazine with CH3-PhOH:

C	1.8772559	-0.2284492	-0.0000060
C	1.7223606	-1.6394014	-0.0000004
C	2.8740207	-2.4690413	0.0000298
C	4.1454649	-1.8986117	0.0000565
C	4.3177270	-0.4911198	0.0000528
C	3.1638519	0.3224606	0.0000197
O	0.5283238	-2.2450895	-0.0000150
C	5.7031992	0.1055202	0.0000862
N	-1.7264885	-0.8343502	-0.0001598
C	-2.0350670	0.4701705	-0.0002626
N	-3.3957455	0.8519782	-0.0005202
C	-4.4196429	-0.1438337	-0.0000297

N	-4.0825805	-1.4388206	0.0000650
C	-2.7638868	-1.7223676	-0.0001143
N	-1.0766353	1.4039970	-0.0001841
C	-1.4989945	2.6957832	-0.0001688
N	-2.7691177	3.1556942	-0.0000032
C	-3.7412400	2.2321955	-0.0000680
N	-5.7002411	0.2408159	0.0002661
C	-5.9319839	1.5736850	0.0002719
N	-5.0282938	2.5865154	0.0002249
H	-2.4820433	-2.7805274	-0.0001157
H	-6.9845343	1.8754426	0.0004359
H	-0.7098641	3.4550088	-0.0001938
H	0.9900810	0.4154575	-0.0000299
H	3.2768836	1.4127387	0.0000164
H	5.0282994	-2.5487082	0.0000815
H	2.7305184	-3.5541369	0.0000325
H	-0.2185091	-1.5697507	-0.0000541
H	6.2707608	-0.2195105	0.8891184
H	5.6653119	1.2057762	0.0000789
H	6.2708090	-0.2195210	-0.8889113

References

1. Rabe, E. J.; Corp, K. L.; Sobolewski, A. L.; Domcke, W.; Schlenker, C. W., Proton-Coupled Electron Transfer from Water to a Model Heptazine-Based Molecular Photocatalyst. *J. Phys. Chem. Lett.* **2018,** *9* (21), 6257-6261.
2. Djurovich, P. I.; Mayo, E. I.; Forrest, S. R.; Thompson, M. E., Measurement of the lowest unoccupied molecular orbital energies of molecular organic semiconductors. *Org. Electron.* **2009,** *10* (3), 515-520.
3. Møller, C.; Plesset, M. S., Note on an approximation treatment for many-electron systems. *Phys. Rev.* **1934,** *46* (7), 618.
4. Schirmer, J., Beyond the random-phase approximation: A new approximation scheme for the polarization propagator. *Phys. Rev. A* **1982,** *26* (5), 2395-2416.
5. Ehrmaier, J.; Janicki, M. J.; Sobolewski, A. L.; Domcke, W., Mechanism of photocatalytic water splitting with triazine-based carbon nitrides: insights from ab initio calculations for the triazine-water complex. *Phys. Chem. Chem. Phys.* **2018,** *20*, 14420-14430
6. Liu, X.; Sobolewski, A. L.; Borrelli, R.; Domcke, W., Computational investigation of the photoinduced homolytic dissociation of water in the pyridine–water complex. *Phys. Chem. Chem. Phys.* **2013,** *15* (16), 5957-5966.
7. Helgaker, T., Transition-state optimizations by trust-region image minimization. *Chem. Phys. Lett.* **1991,** *182* (5), 503-510.
8. Dunning Jr, T. H., Gaussian basis sets for use in correlated molecular calculations. I. The atoms boron through neon and hydrogen. *J. Chem. Phys.* **1989,** *90*, 1007.
9. Weigend, F.; Häser, M.; Patzelt, H.; Ahlrichs, R., RI-MP2: optimized auxiliary basis sets and demonstration of efficiency. *Chem. Phys. Lett.* **1998,** *294* (1-3), 143-152.
10. TURBOMOLE(V7.2), *a development of University of Karlsruhe and Forschungszentrum Karlsruhe GmbH, 1989–2007, TURBOMOLE GmbH, since 2007*.

Appendix C: Supplementary Information for Chapter 6

Two-Component K_A Model

The lack of isosbestic point seen in Figure 6-2 of the main text is a clear indication that the system is more complicated that conversion between free TAHz and a singly-bound TAHz chromophore. So while analyzing the data with the single-association model done previously[1] allows for a qualitative comparison of K_A values across the different phenol derivatives, it does not accurately represent the K_A values. Additionally, this means isolating an absorption spectrum for a specific complex cannot be obtained by simply saturating the solution with phenol. To attempt to extract a singly-bound absorption spectrum of the TAHz-PhOH complex, we used the method laid out by Demeter and coworkers to model the OD at a given wavelength (A_λ) as a function of PhOH concentration [X] given two association steps (K_1 and K_2) .[2-3]

At each wavelength, we perform a least squares fitting procedure to Equation 1.

$$A_\lambda = \epsilon_{T\lambda}[T] + \epsilon_{TX\lambda}[TX] + \epsilon_{TX_2\lambda}[TX_2] \quad (1)$$

Where the concentration of unbound TAHz (T), singly-bound TAHz-PhOH complex (TX) and the doubly-bound TAHz-$(PhOH)_2$ (TX_2) are defined by Equations 2-4.

$$[T] = [T]_0 - [TX] - [TX_2] \quad (2)$$

$$[TX] = \frac{K_1[T]_0[X]}{1+K_1[X]+K_1K_2[X]^2} \quad (3)$$

$$[TX_2] = \frac{K_1K_2[T]_0[X]^2}{1+K_1[X]+K_1K_2[X]^2} \quad (4)$$

To implement the model and to iterate the fit routine through at all wavelengths, we wrote a python script that is publicly available on GitHub (https://github.com/theomnipanda/double_association_constant). This code can be applied to

other systems, however, it is important to note that it does not currently account for the absorption of the H-bond donor. In our case, only TAHz absorbed in the region of interest, so we did not include any contribution from PhOH, although this could be easily be added.

While TAHz certainly has more than 2 hydrogen-bonding sites, it appears this model is sufficient to capture the trends in the data. Figure C-0-1 shows four different representative fits at 365, 380, 400, and 450 nm. All data traces appear to be fit well by the model and do not appear to require a 3rd association constant.

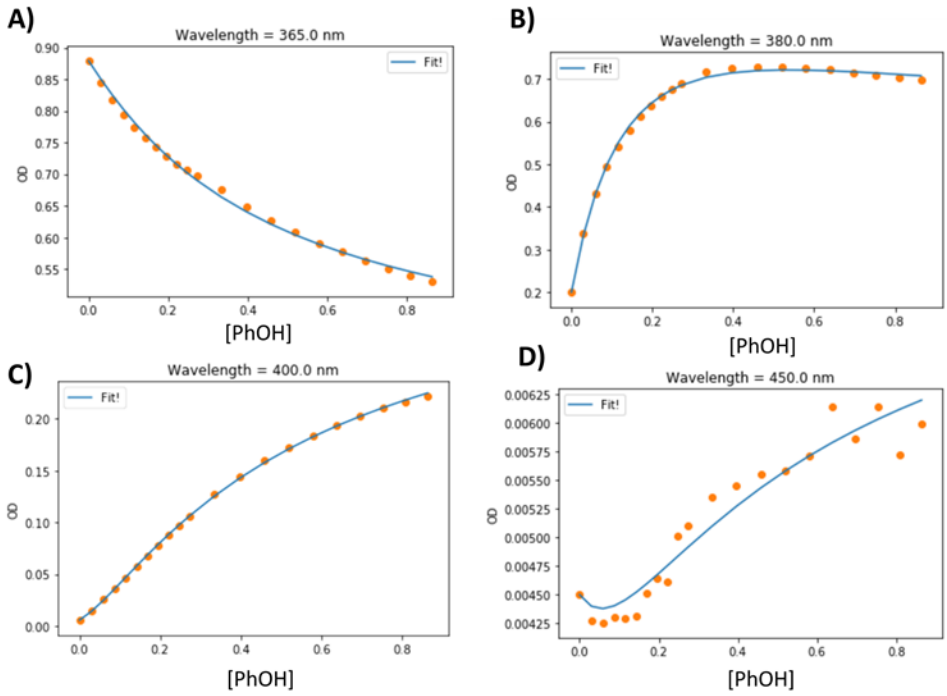

Figure C-0-1. Two-component fit compared to data

Measured optical densities (orange dots) compared to the model fit (blue lines) at A) 365 nm, B) 380 nm, C) 400 nm and D 450 nm. We observe a good fit to the data over a large range of wavelengths. Note that the data at 450 nm is on the order of mOD, so while the signal is near the detection limit, the model fits the trend well.

Time Resolved Photoluminescence

In the absence of a hydrogen-bond donor, the photoluminescence of TAHz shows only one component. Figure C-0-2 shows the spectral and kinetic traces from TR-PL of TAHz in toluene suggest there is only one luminescing species which decays with a lifetime of roughly 300 ns.

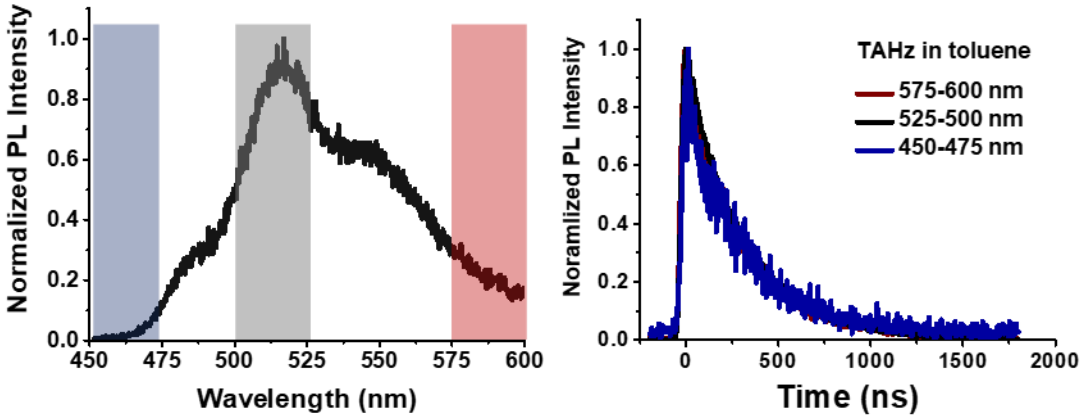

Figure C-0-2. TAHz in Toluene TR-PL

The emission of TAHz in toluene, without an abstractable hydrogen present, shows only one decay rate (right) across the PL spectrum (left).

When PhOH is present with TAHz in toluene, we observe a clear second component with a faster decay rate, shown in Figure 6-3. We attribute this new fast component to the emission from a hydrogen-bonded TAHz-PhOH complex. To support this assignment, Figure C-0-3 shows the relative growth of the high-energy fast component relative to the slow component upon increasing concentration of PhOH. Additionally, we cannot attribute this change in spectral shape to a change

in local dielectric constant, since the spectral of shape of TAHz emission in toluene and a 50:50 mixture of toluene and benzonitrile look nearly identical, as shown in Figure C-0-4.

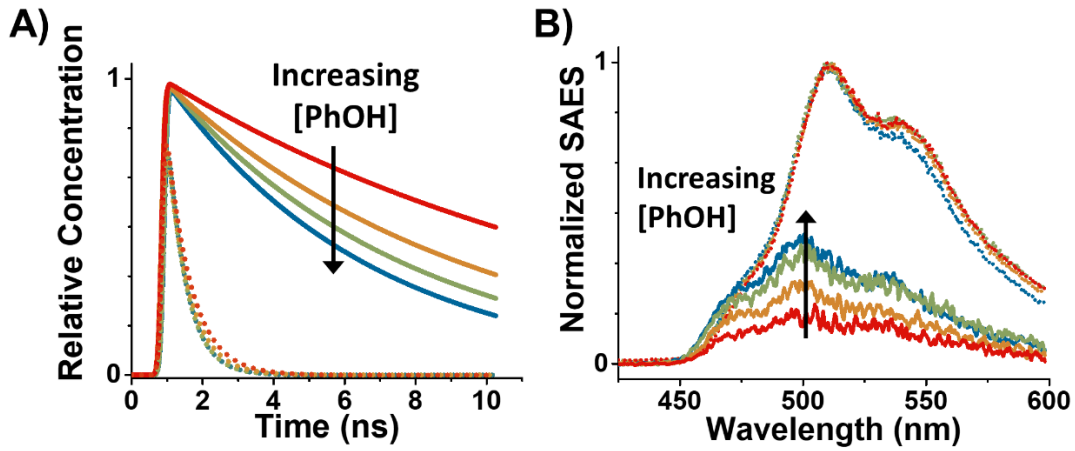

Figure C-0-3. TR-PL with increasing [PhOH]

Phenol (PhOH) concentration-dependent TR-PL suggesting that the high energy emission is from a hydrogen-bonded complex. A) Kinetic decay rates of bonded TAHz S_1 (solid) hydrogen-bonded TAHz-PhOH (dotted) with different PhOH concentrations: 25 mM (red), 50 mM (orange), 75 mM (green), and 100 mM (blue). B) High energy emission grows in with increasing [PhOH] relative to low-energy emission.

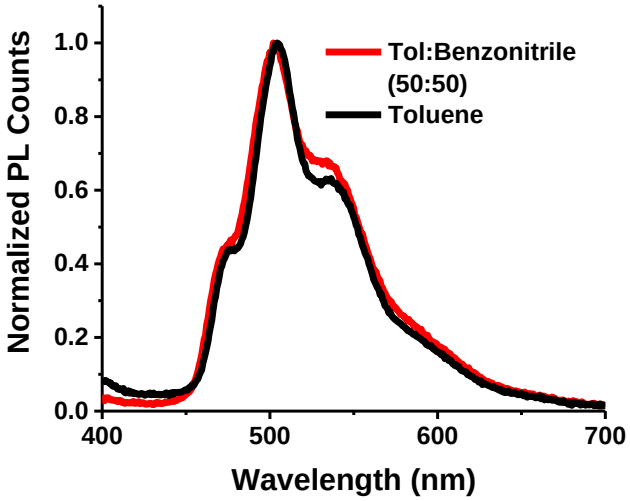

Figure C-0-4. Effect of dielectric constant of PL shape

The emission spectra of TAHz in toluene (black) and a 50:50 mixture of toluene and benzonitrile (red) show no meaningful spectral difference. This suggests the dielectric constant of the solvent

likely does not play a meaningful role in the change in spectral shape with varying phenol derivatives.

Spectral Modeling

Given the striking difference in spectral shape of the fast component spectra with different phenols, we wanted a way to quantify these changes. Initially, we fit Gaussian distributions to the distinct peaks/shoulders and compared across all TAHz-R-PhOH emission lineshapes. This was useful in picking out the spacing between vibronic peaks. We noticed that both the fast and slow components have similar spacing, which suggests that both transitions are coupled to a local TAHz molecular vibration (Figure C-0-5) but showed different relative intensities of those peaks. To quantify the extent of excited-state displacement for each complex, we attempted to estimate the Huang-Rhys factor by taking the ratio of the 0-0 and 0-1 individual Gaussian peaks. However, this resulted in Huang-Rhys factors as high as 5 for CH_3-PhOH-TAHz and 3 for PhOH-TAHz. This seemingly unphysical value along with the non-Poisson distribution of the individual Gaussian intensities, we turned to a quantum-optical model of the fluorescence lineshape to ensure we were extracting physically-relevant information. Indeed, when we attempted to fit the same spectrum with the model containing a single vibration (the assumption when fitting a series of Gaussians), the lineshape was not captured (Figure C-0-6).

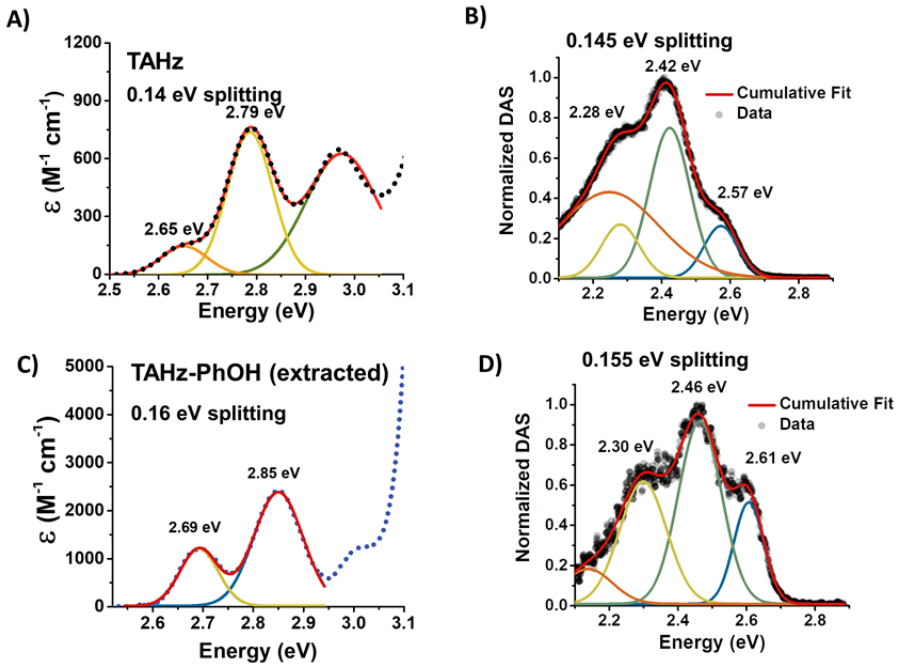

Figure C-0-5. Gaussian fits to absorption and emission spectra

Using a series of Gaussians, we can estimate the peak splitting of the vibronic progression for the free TAHz absorption (A) and emission (B) and the hydrogen-bonded TAHz-PhOH absorption (C) and emission (D). By looking at the difference in peak positions, all spectra have roughly the same spacing of ~0.15 eV. This suggests that all these transitions are coupled to a similar molecular vibrational mode of the TAHz chromophore.

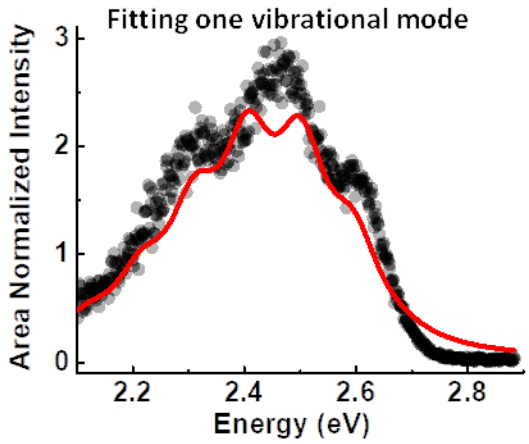

Figure C-0-6. One-vibrational mode fit to data

Using the harmonic quantum optical model to fit the area-normalized extracted TAHz-PhOH data (black dots), with only one vibrational mode, the fit (solid red line) does not capture the lineshape.

The resulting model and fitting procedure is publicly available on GitHub and can be found here (https://github.com/ejanerabe16/modeling_TAHz_emission).

For each dataset, the temperature parameter was set to 294 K, as that was the measured temperature in the lab during each experiment, though small changes in temperature (290K-298K) did not appear to dramatically change the resulting lineshape. In general, it is worth noting that the fit result is sensitive to initial guesses as there appears to be many local minima caused by the similar qualitative effect of increasing the intrinsic linewidth and the displacement of low mode. For all the following fits (Figure C-0-7 through Figure C-0-11), a range of physically relevant initial guesses were tried, and the ones returning the lowest R^2 value were used and listed in the figure captions. The errors listed with the fit results were taken from the diagonal elements of the covariance matrix of the fit parameters.

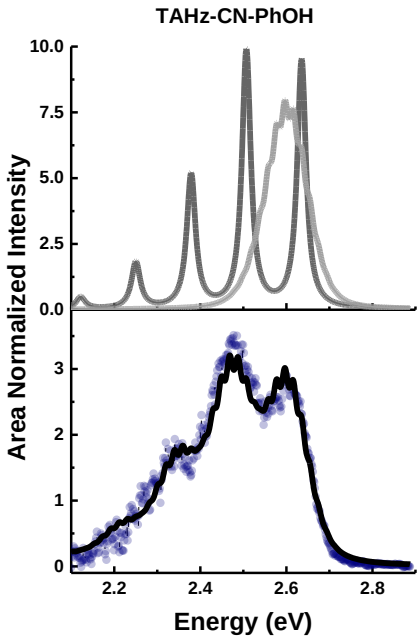

Figure C-0-7. CN-PhOH-TAHz model fit

Fitting the extracted CN-PhOH-TAHz emission data (blue dots) with the two-component harmonic model (black solid line on bottom plot). The initial guesses were: E_{00}= 2.63, ω_1= 0.13, d_1=1.4, ω_2= 0.02, d_2=1.3, γ=0.01. The fit results were: E_{00}= 2.63549±0.00005 eV, ω_1= 0.12839±0.000003 eV, d_1=1.4378±0.0003, ω_2=0.019441±0.000005 eV, d_2=1.961±0.003, γ=0.01233±0.00002 eV.

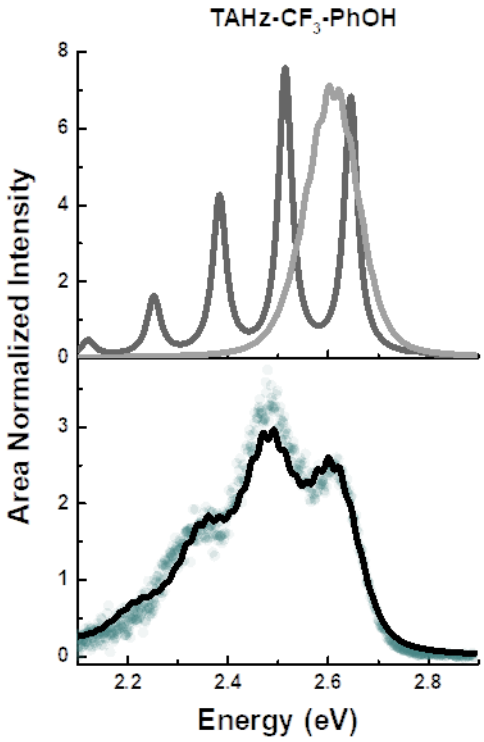

Figure C-0-8. CF3-PhOH-TAHz model fit

Fitting the extracted CF_3-PhOH-TAHz emission data (blue dots) with the two-component harmonic model (black solid line on bottom plot). The initial guesses were: E_{00}= 2.63, ω_1= 0.13, d_1=1.4, ω_2= 0.02, d_2=1.5, γ=0.015. The fit results were: E_{00}= 2.64521±0.00002 eV, ω_1= 0.13106±0.000007 eV, d_1=1.6567±0.0006, ω_2=0.02231±0.000005 eV, d_2=1.88±0.01, γ=0.01622±0.0001 eV.

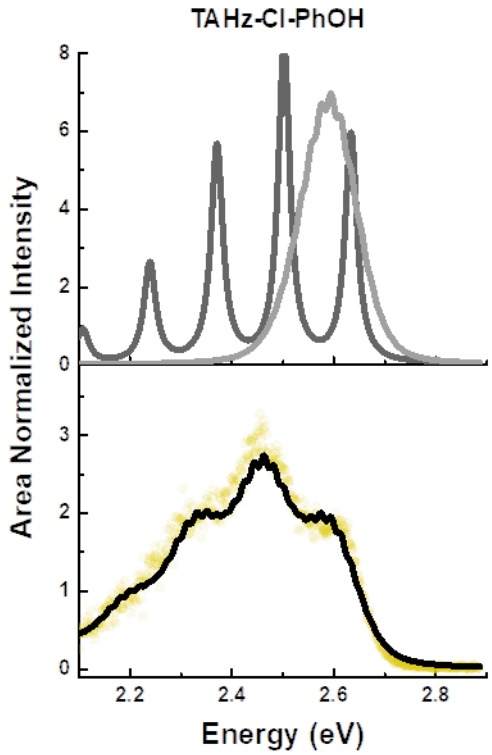

Figure C-0-9. Cl-PhOH-TAHz model fit

Fitting the extracted Cl-PhOH-TAHz emission data (blue dots) with the two-component harmonic model (black solid line on bottom plot). The initial guesses were: E_{00}= 2.63, ω_1= 0.13, d_1=1.4, ω_2= 0.02, d_2=2, γ=0.015. The fit results were: E_{00}= 2.63999±0.00002 eV, ω_1= 0.13167±0.000005 eV, d_1=1.6567±0.0005, ω_2=0.01973±0.000002 eV, d_2=2.17±0.009, γ=0.01418±0.0003 eV.

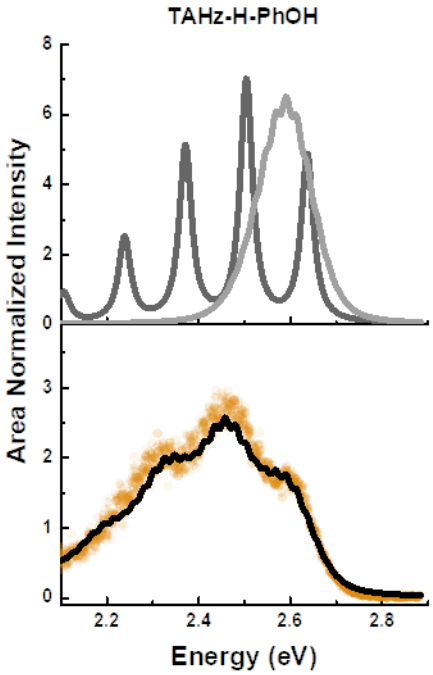

Figure C-0-10. PhOH-TAHz model fit

Fitting the extracted H-PhOH-TAHz emission data (blue dots) with the two-component harmonic model (black solid line on bottom plot). The initial guesses were: E_{00}= 2.62, ω_1= 0.13, d_1=1.8, ω_2= 0.02, d_2=2, γ=0.015. The fit results were: E_{00}= 2.63683±0.00003 eV, ω_1= 0.13271±0.000007 eV, d_1=1.6994±0.0008, ω_2=0.02302±0.000003 eV, d_2=2.11±0.01, γ=0.01626±0.0003 eV.

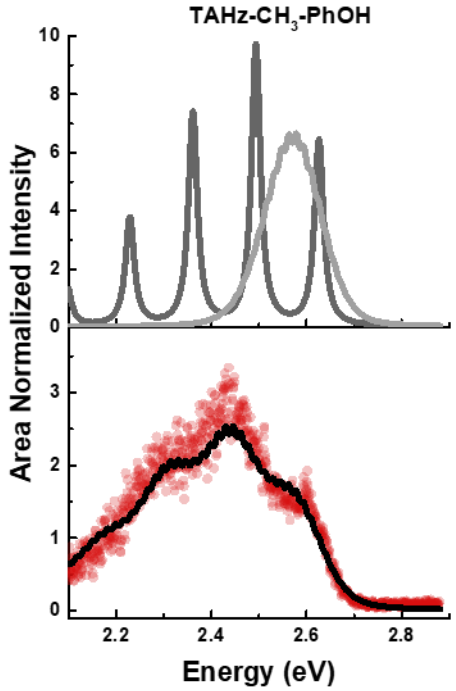

Figure C-0-11. CH3-PhOH-TAHz model fit

Fitting the extracted CH_3-PhOH-TAHz emission data (blue dots) with the two-component harmonic model (black solid line on bottom plot). The initial guesses were: E_{00}= 2.62, ω_1= 0.13, d_1=1.8, ω_2= 0.02, d_2=2, γ=0.015. The fit results with the corresponding errors from the fit routine were: E_{00}= 2.62307±0.00001 eV, ω_1= 0.132529±0.000005 eV, d_1=1.7395±0.0007, ω_2= 0.0158754 ±0.0000005 eV, d_2=2.67±0.01, γ=0.0113357±0.00001 eV.

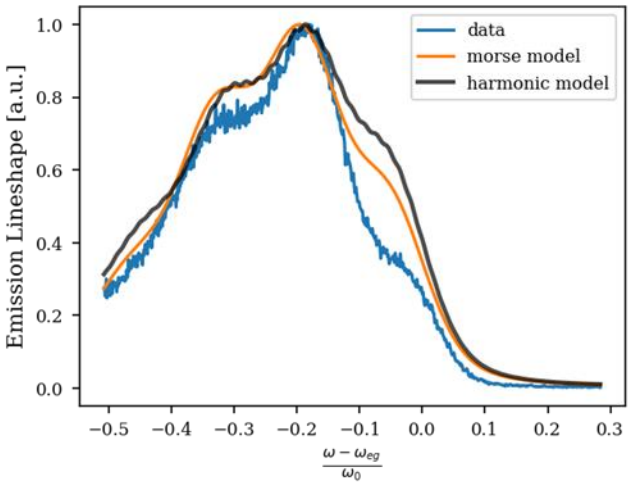

Figure C-0-12. Adding anharmonicity to slow component spectra

Fitting the extracted slow component of the TAHz-PhOH spectrum (blue line) is not well-described by the harmonic model (black line). Adding anharmonicity (orange line) to the high frequency mode improves the fit. However, the fit routine is complicated by frequently diverging

and requiring a specific number of cumulant terms. This fitting routine is in progress but has not yielded a satisfactory result yet.

Electronic Structure Calculations

In order to visualize what molecular vibrations are coupled to the electronic transition observed by the luminescence spectra, we used DFT and TD-DFT. Figure C-0-13 shows the different optimized geometries of TAHz in the ground and first excited state. We observe a clear distortion to the planarity of the ring. This supports the assignment of the ~200 cm^{-1} mode extracted from the emission model to be due to ring puckering motions shown in Figure C-0-14. The high frequency mode likely corresponds to a heptazine ring-breathing mode, of which there are many transitions in the 1000-1200 cm^{-1} range, shown in Figure C-0-15.

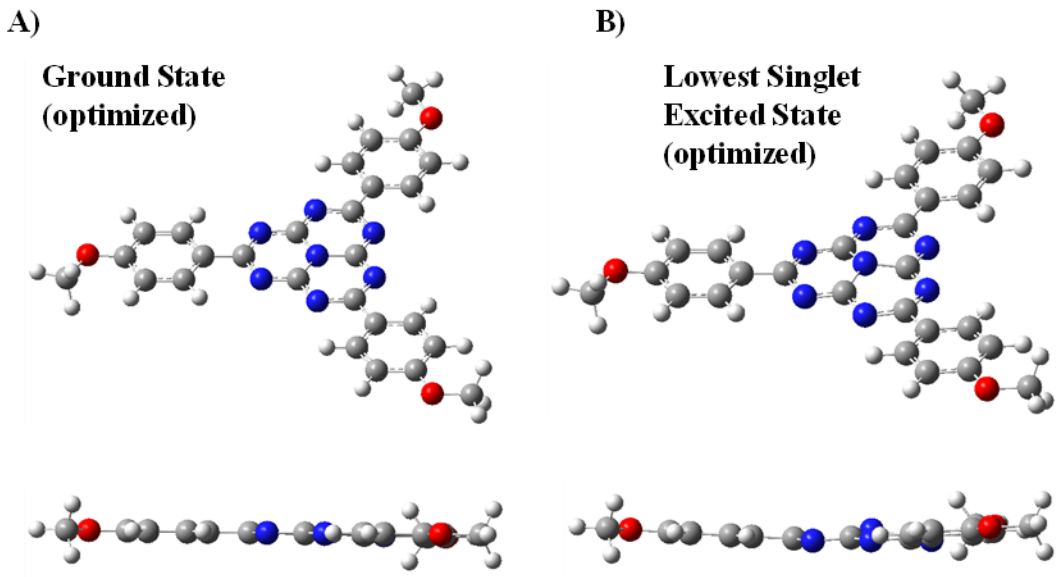

Figure C-0-13. Optimized geometry of TAHz in ground and excited state

A) Optimized ground state geometry of TAHz is planar. B) The optimized geometry of the first excited state. The most striking difference is the breaking of planarity by the umbrella motion of the central nitrogen.

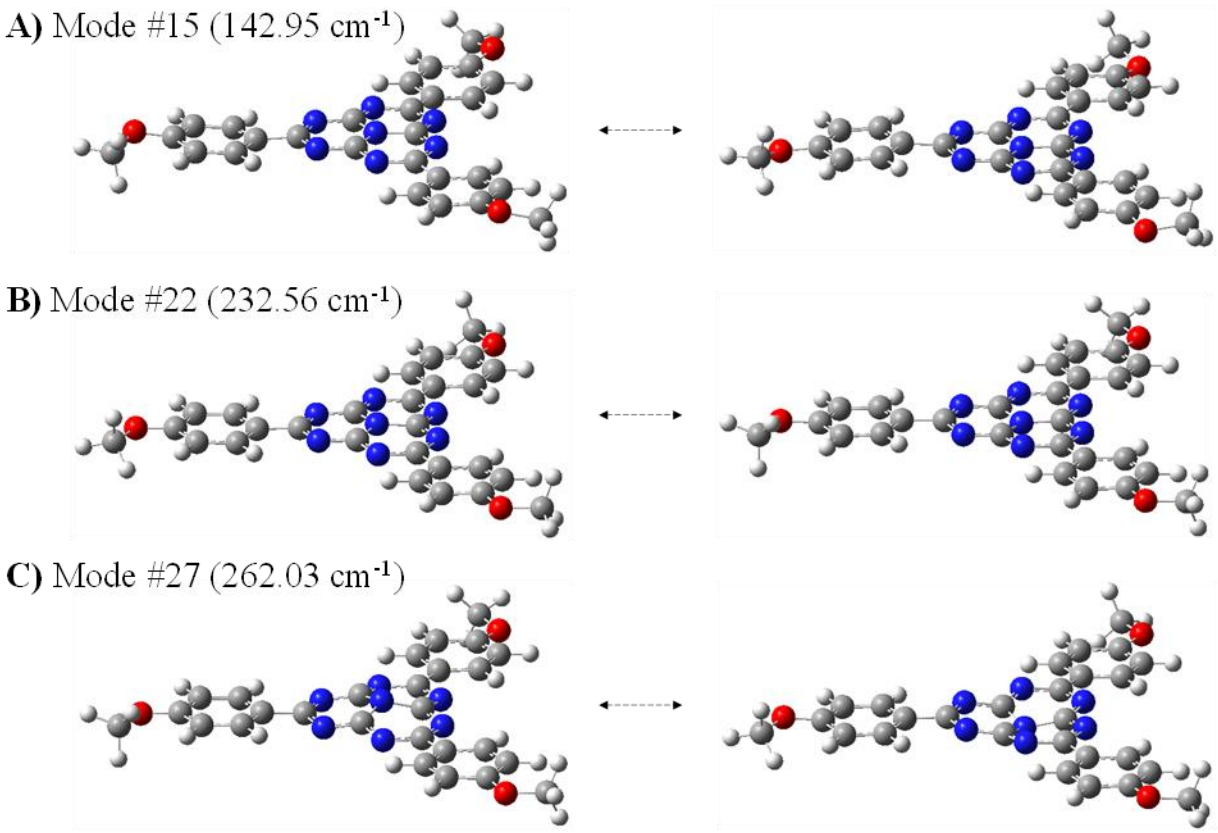

Figure C-0-14. Ring-puckering modes

Three representative ring-puckering vibration modes of TAHz calculated at ground state optimized geometry (wavenumbers are raw values from calculation).

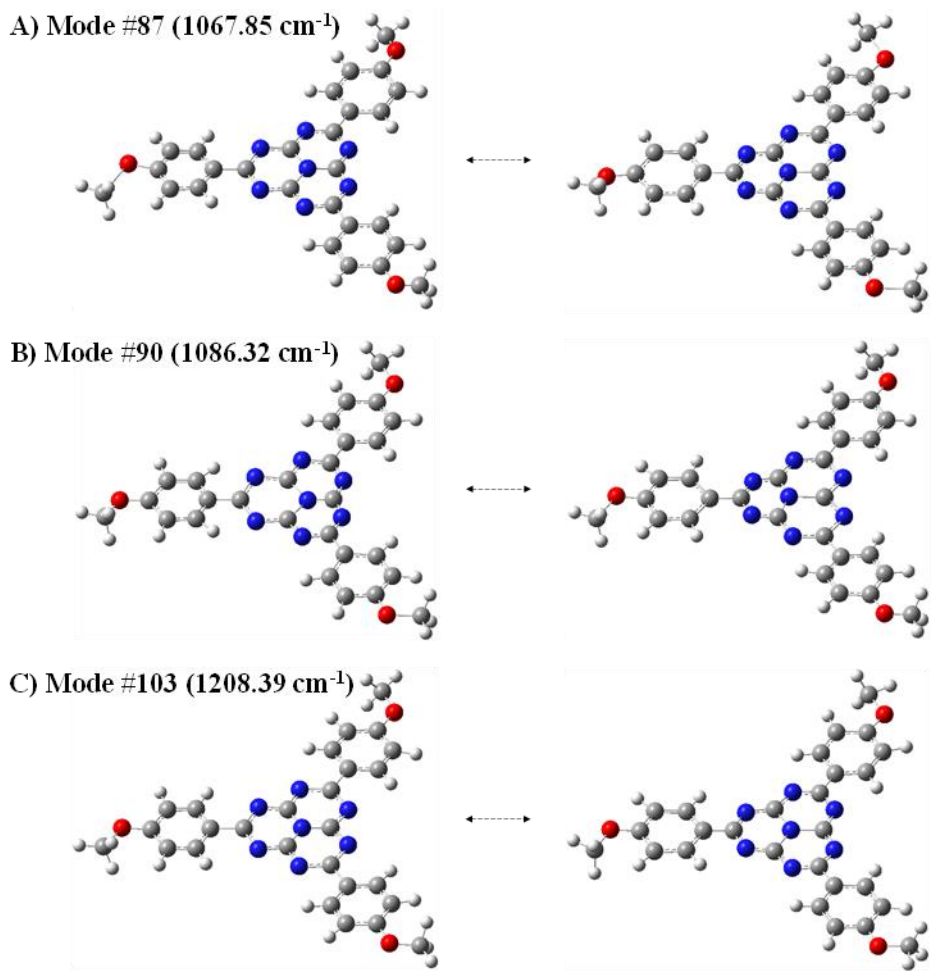

Figure C-0-15. Heptazine-ring breathing modes

Three representative ring-breathing vibration modes of TAHz calculated at ground state optimized geometry (wavenumbers are raw values from calculation).

(a) Mode #112 (Ground state optimized, 1083.87 cm^{-1})

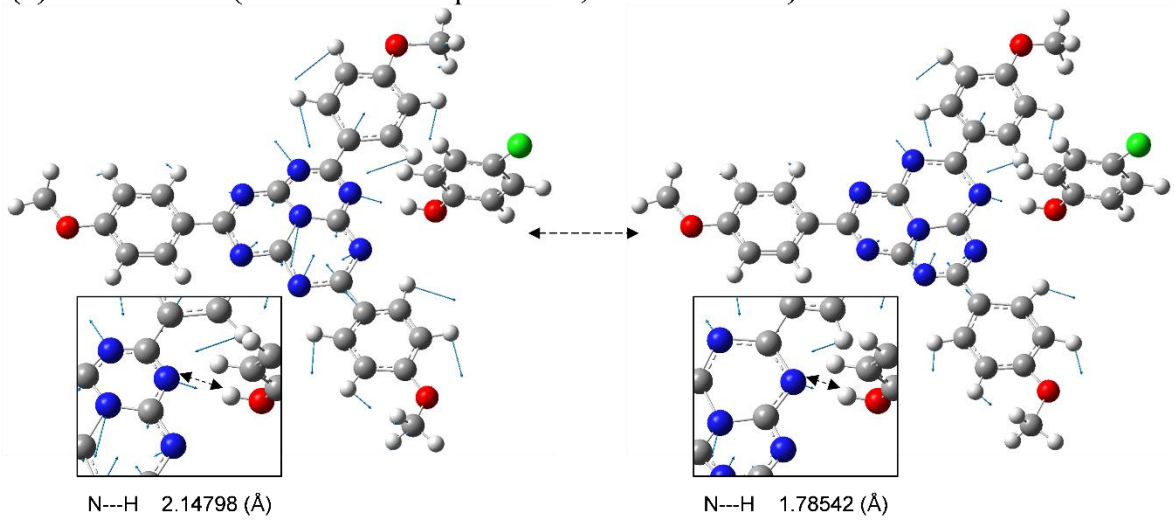

(b) Mode #113 (Ground state optimized, 1088.35 cm^{-1})

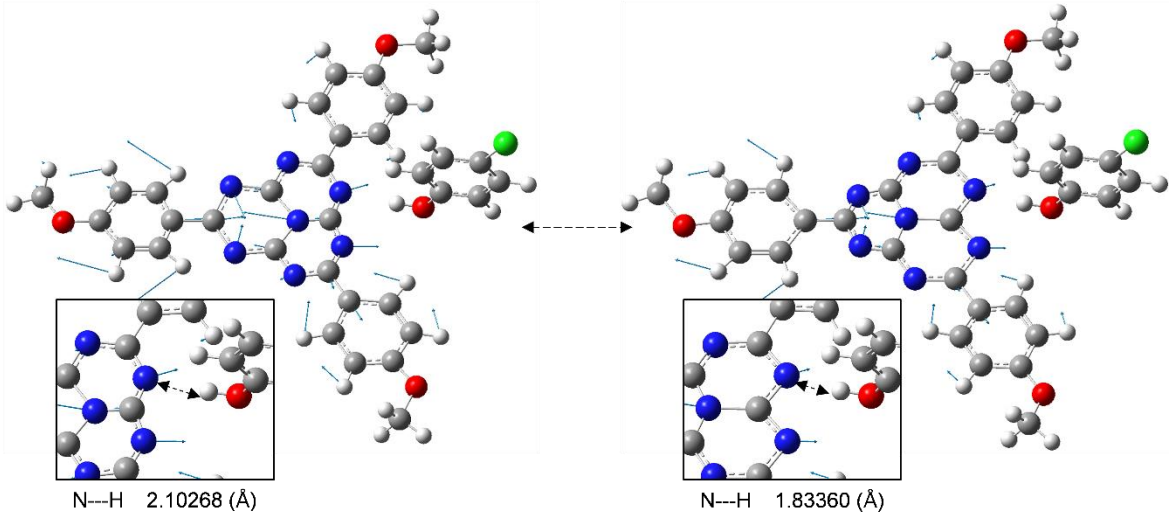

Figure C-0-16 Ground state Cl-PhOH-TAHz molecular vibrations

Two representative ring-breathing vibration modes of TAHz – Cl-PhOH complex calculated at ground state optimized geometry (wavenumbers are raw values from calculation).

(a) Mode #114 (symmetry-forbidden ππ* state optimized, 1068.95 cm^{-1})

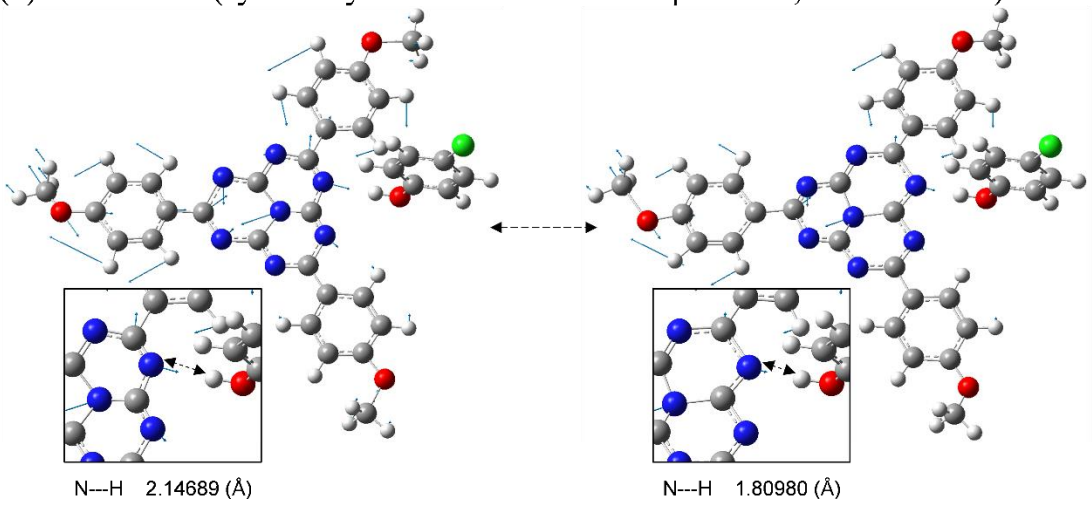

(b) Mode #110 (symmetry-forbidden ππ* state optimized, 1055.82 cm^{-1})

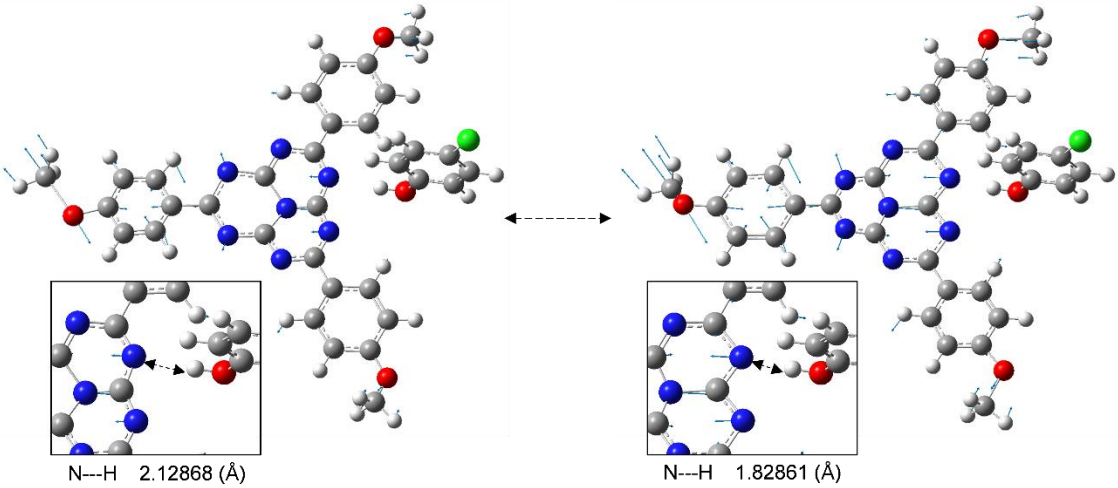

Figure C-0-17 Excited state Cl-PhOH-TAHz molecular vibrations

Two representative ring-breathing vibration modes of TAHz – Cl-PhOH complex calculated at excited state (symmetry-forbidden ππ*) optimized geometry (wavenumbers are raw values from calculation).

Table C-0-1 Ground state optimized geometry of TAHz (Cartesian coordinates in Angstroms)

Atom	X	Y	Z
C	1.84637600	-1.89122200	-0.00010100
C	-0.38030000	-1.35409700	-0.00011200
C	1.36255100	0.34769400	-0.00001200
C	-0.98264700	1.00620400	0.00000400
C	-2.56115800	-0.65358400	-0.00004800
C	0.71442600	2.54462200	0.00003700

N	-0.60534900	2.28238200	0.00004200
N	1.70502000	1.63282200	0.00002400
N	-0.00014300	-0.00006400	-0.00004700
N	2.27910900	-0.61713000	-0.00001200
N	0.56144400	-2.29323600	-0.00015600
N	-1.67415100	-1.66542700	-0.00013100
N	-2.26683200	0.66020900	0.00002700
C	1.11174100	3.95990100	0.00002400
C	2.46737400	4.32085300	0.00000400
C	0.13922400	4.97996400	0.00002800
C	2.85517500	5.65683500	-0.00001000
H	3.21377000	3.53494100	-0.00000100
C	0.51378700	6.31133900	0.00001500
H	-0.90779400	4.70037900	0.00004200
C	1.87569000	6.66146600	-0.00000100
H	3.90937100	5.90552400	-0.00003400
H	-0.22369400	7.10681500	0.00002000
C	2.87349400	-2.94285000	-0.00005700
C	2.50854200	-4.29742300	-0.00007600
C	4.24308200	-2.61038400	0.00000700
C	3.47184600	-5.30106300	-0.00003300
H	1.45477800	-4.55110200	-0.00012600
C	5.20900300	-3.60024100	0.00005000
H	4.52424800	-1.56379100	0.00001800
C	4.83154800	-4.95482500	0.00003500
H	3.16034900	-6.33843700	-0.00006200
H	6.26659400	-3.35907100	0.00010000
C	-3.98547900	-1.01717500	-0.00003100
C	-4.97593300	-0.02368000	0.00004700
C	-4.38254500	-2.36945700	-0.00009200
C	-6.32680600	-0.35588900	0.00006800
H	-4.66855100	1.01568500	0.00008900
C	-5.72280500	-2.71083600	-0.00007400
H	-3.61686300	-3.13636400	-0.00014800
C	-6.70701600	-1.70650100	0.00001000
H	-7.06933800	0.43268200	0.00012500
H	-6.04290900	-3.74727000	-0.00012100
O	2.13870500	7.99417900	-0.00001300
O	-7.99267100	-2.14512400	0.00002300
O	5.85440500	-5.84871900	0.00008000
C	3.49511500	8.42070200	0.00002000
H	4.02652100	8.07280400	-0.89408700
H	3.46544100	9.51083500	0.00003300
H	4.02648600	8.07278200	0.89413900
C	5.54593600	-7.23675000	0.00015700
H	4.97907400	-7.52320100	-0.89397000

H	6.50499500	-7.75586200	0.00025200
H	4.97896300	-7.52307800	0.89425100
C	-9.04022600	-1.18366900	0.00014400
H	-9.00461300	-0.54946800	-0.89393100
H	-9.96949300	-1.75439800	0.00016400
H	-9.00450900	-0.54957900	0.89429300

Table C-0-2 Lowest singlet excited state optimized geometry of TAHz

Atom	X	Y	Z
C	0.69415300	2.56954700	-0.14828500
C	-0.98981300	0.99328300	-0.12806700
C	1.35509800	0.36000700	-0.12845700
C	-0.36582600	-1.35424200	-0.12770600
C	-2.57286400	-0.68386500	-0.14796300
C	1.87817800	-1.88647600	-0.14890000
N	0.57878800	-2.27730200	-0.22897100
N	2.27398900	-0.58885600	-0.23067400
N	-0.00012900	-0.00030300	0.12422000
N	1.68215300	1.63961000	-0.22963800
N	-0.62754600	2.26356300	-0.22998900
N	-2.26149700	0.63675300	-0.22915900
N	-1.64710200	-1.67558200	-0.22936900
C	2.90517200	-2.91749900	-0.07035200
C	4.26805900	-2.57452300	-0.02790400
C	2.55558500	-4.28504100	-0.02075500
C	5.25442800	-3.55113200	0.06147500
H	4.54533300	-1.52741300	-0.06897300
C	3.53034000	-5.26161300	0.06833300
H	1.50763000	-4.55940400	-0.05654700
C	4.88986100	-4.90486400	0.11025600
H	6.29532400	-3.25270000	0.09119400
H	3.27173600	-6.31449800	0.10623900
C	1.07388500	3.97435900	-0.06995100
C	0.09581000	4.98349500	-0.02591500
C	2.43321200	4.35490300	-0.02236900
C	0.44900900	6.32589900	0.06306900
H	-0.94981600	4.70044100	-0.06546700
C	2.79218000	5.68720700	0.06618300
H	3.19448200	3.58428400	-0.05947900
C	1.80388500	6.68653800	0.10970600
H	-0.32955300	7.07845700	0.09408600
H	3.83347200	5.98931900	0.10246900
C	-3.97938400	-1.05732000	-0.06984500
C	-4.36435400	-2.40887500	-0.02577800

C	-4.98859700	-0.07031200	-0.02270100
C	-5.70356400	-2.77411600	0.06277900
H	-3.59642300	-3.17291600	-0.06511700
C	-6.32193500	-0.42551400	0.06543200
H	-4.70179200	0.97425700	-0.05972000
C	-6.69329900	-1.78104800	0.10896900
H	-5.96607900	-3.82462000	0.09382900
H	-7.10422000	0.32523500	0.10137500
O	5.76784900	-5.94014000	0.19789200
O	-8.02902000	-2.02319800	0.19572400
O	2.26205000	7.96435100	0.19681700
C	7.15792800	-5.64874600	0.24186100
H	7.41548900	-5.04275600	1.11927300
H	7.66398500	-6.61251100	0.30928200
H	7.48980900	-5.12849800	-0.66508700
C	1.31501400	9.02272900	0.24263500
H	0.66267700	8.94252300	1.12095100
H	1.89695500	9.94269500	0.30963000
H	0.69722400	9.05056800	-0.66340900
C	-8.47216300	-3.37251900	0.24148300
H	-8.07697700	-3.89726200	1.12005200
H	-9.55987500	-3.32845100	0.30796900
H	-8.18699900	-3.92161300	-0.66435700

References

1. Rabe, E. J.; Corp, K. L.; Huang, X.; Flores, R. G.; Estes, S. L.; Sobolewski, A. L.; Domcke, W.; Schlenker, C. W., Barrierless Heptazine-Driven Excited-State Proton-Coupled Electron Transfer: Implications for Controlling Photochemistry of Carbon Nitrides and Aza-Arenes. *J. Phys. Chem. C.* **2019,** *123,* 29580-29588.
2. Demeter, A.; Mile, V.; Bérces, T., Hydrogen Bond Formation between 4-(Dimethylamino)pyridine and Aliphatic Alcohols. *J. Phys. Chem. A* **2007,** *111* (37), 8942-8949.
3. Demeter, A.; Ravasz, L.; Bérces, T., Influence of Hydrogen Bond Formation on the Photophysics of N-(2,6-Dimethylphenyl)-2,3-naphthalimide. *J. Phys. Chem. A* **2004,** *108* (19), 4357-4364.

Emily Jane Rabe

(847) 651-2303 ● linkedin.com/in/emily-rabe/ ● rabee@uw.edu

SUMMARY

I am passionate about accelerating energy efficient and clean energy technologies towards societal impact. Through years of energy-related research and technical consulting, I am practiced at learning new fields quickly and communicating efficiently within collaborative teams. I am committed to apply my knowledge and skills to further clean energy research

EDUCATION

University of Washington Seattle 2015-August 2020
Ph.D. Candidate in Materials Chemistry **GPA:** 3.82
Fellowships and Awards:

- Graduate Fellow of the Clean Energy Institute
- Torrance Tech Due Diligence Fellow
- NSF Honorable Mention
- PNNL Graduate Fellow
- Excellence in Chemistry Graduate Fellowship
- ARPA-E Student Program Attendee (2017, 2019)

St. Olaf College, Northfield MN 2010-2014
B.A., *magna cum laude*, in Chemistry with Distinction **Major GPA:** 3.89
Fellowships and Awards:

- American Institute of Chemists Award
- American Chemical Society Certification
- Departmental Service Award
- Phi Lambda Upsilon

WORK EXPERIENCE

Graduate Research Assistant *University of Washington* 2015-present

- Investigate photophysical processes in solar harvesting technologies using spectroscopic and electrochemical techniques
- Synthesize organic molecules and design systematic mechanistic studies to probe their photochemistry
- Fabricate novel organic solar devices and characterize efficiencies
- Consolidate and present findings in peer-reviewed journal articles and at international conferences

Senior Venture Analyst *Washington Research Foundation* 2019-present

- Perform initial screenings of companies for investment regarding the technology, market, and competitors
- Model the expected internal rate of return on potential investments
- Compile information and questions into concise reports and presentations monthly

Technical Consultant *E8 Angel Investing Group* 2017-2018

- Investigated clean technology startups with an eye towards intellectual property, technology scalability, and market size
- Wrote due diligence reports highlighting major strengths and concerns regarding each company

Chemist *Argonne National Lab-Energy Systems* 2014-2015

- Collaborated with interdisciplinary teams focused on scaling nanomaterial technologies for energy applications
- Wrote quarterly reports, designed slides for annual reviews, contributed to grant proposals
- Optimized heterogeneous vapor-phase sol-gel polymerization procedures of silica nanoparticles for biofuel adsorption
- Performed electrospinning to produce magnetic nanotubes and fabricated water filtration membranes (**patented**)

Summer Intern *Argonne National Lab-Energy Systems* 2013

- Developed a polymerization method to encapsulate magnetically aligned nanotubes for energy-efficient water filtration
- Prepared and characterized magnetic nanomaterials on the gram-scale for application in electric vehicles
- Assisted in optimization of hydrocyclone protocols for dewatering algae for biofuel applications

Research Assistant *St. Olaf College* 2012-2013

- Investigated human scent composition using gas chromatography-mass spectrometry experiments
- Created and managed large datasets to help assess the viability of human scent as evidence in forensic cases

REU Student *University of Illinois Champagne-Urbana* 2012

- Devised functionalization routes to promote polymer drug encapsulation for targeted delivery
- Synthesized and characterized biocompatible hyperbranched polymers

PATENT

Chen. X.; Iganacio-de-Leon, P.; Rabe, E.; Urgun-Demirtas, M.; Brotzman, R. Magnetic Nanotube Composite Membranes. US 10,022,676

PUBLICATIONS

Peer-Reviewed Articles

Rabe, E J..; Goldwyn, H. J.; Hwang, D.; Masiello, D. J.; Schlenker, C. W. Intermolecular Hydrogen Bonding Tunes Vibronic Coupling in Heptazine Complexes. *In Preparation.for real*

Enright, M.; Dou, F.; Wu, S.; Rabe, E.; et. al. Seeded Growth of Nanoscale Semiconductor Tetrapods: Generality and the Role of Cation Exchange. *Chem. Mater*. **2020**. DOI: 10.1021/acs.chemmater.0c01407

Ehrmaier, E.; Huang, X.; Rabe, E J.; et. al. Molecular Design of Heptazine-based Photocatalysis: Effect of Substituents on Photocatalytic Efficiency and Photostability. *J. Phys. Chem. C.* **2020**, DOI: 10.1021/acs.jpca.0c00488

Corp K. L.; Rabe E. J.; Huang, X; et. al. Control of Excited-State Proton-Coupled Electron Transfer by Ultrafast Pump-Push-Probe Spectroscopy in Heptazine-Phenol Complexes: Implications for Photochemical Water Oxidation. *J. Phys. Chem. C.* **2020**, DOI: 10.1021/acs.jpcc.0c00415 **ACS Editor's Choice**

Rabe, E. J.; Corp, K. L.; Huang, X.; Ehrmaier, J.; Flores, R. G.; Estes, S. L.; et. al. Barrierless Heptazine-Driven Excited State Proton-Coupled Electron Transfer: Implications for Controlling Photochemistry of Carbon Nitrides and Aza-Arenes. *J. Phys. Chem. C.* **2019**, *123* (49), 29580-29588.

Pristash, S. R.; Corp, K. L.; Rabe, E. R.; Schlenker, C. W. Heavy-Atom-Free Red-to-Yellow Upconversion in a Thiosquaraine Composite. *ACS Appl. Ener. Mater.* **2019** DOI: 10.1021/acsaem.9b01808

Ehrmaier, J.; Rabe, E. J., et al. Singlet-Triplet Inversion in Heptazine and in Polymeric Carbon Nitrides. *J. Phys. Chem. A.* **2019**, *123* (38), 8099-8108.

Rabe, E. J.; Corp, K. L.; et. al. Proton-Coupled Electron Transfer from Water to a Model Heptazine-Based Molecular Photocatalyst. *J. Phys. Chem. Lett.* **2018**, *21* (9), 6257-6261.

Sulas, D. B.; Rabe, E. J.; Schlenker, C. W., Kinetic Competition between Charge Separation and Triplet Formation in Small-Molecule Photovoltaic Blends. *J. Phys. Chem. C.* **2017,** *121* (48), 26667-26676.

Ignacio-de Leon, P.A.; Chen, X.; Rabe, E.J.; et. al. Magnetically Aligned Nanotubes in Nanocomposite Membranes for High-Performance Filtration Applications. *TechConnect Briefs: Advanced Materials*, **2016**, Chapter 8, pp. 257 - 260.

Book Chapter

Rabe, E.; Schlenker, C. Excited State Energies Drive Charge Transfer in Organic Semiconductors. In *World Scientific Handbook of Organic Electronics*; So, F.; Rand, B.; World Scientific Publishing.

PRESENTATIONS

Oral Presentations

Exploring Excited-state Manifolds of Photocatalysts Using Pump-push-probe Spectroscopy. ACS Spring Meeting, 2019, Orlando, FL.

Proton-Coupled Electron Transfer in a Model Heptazine-Based Photocatalyst. MRS Fall Meeting, 2018, Boston, MA.

National Labs and Nanoscience. **Invited Seminar**, February 20th, 2015, St. Olaf College; Northfield, MN.

Two Aspects of Green Energy: Biofuels and Water Filtration. SULI Student Program, 2013, Argonne National Lab.

Invited Speech

My Grad School Puzzle: Making connections for clean energy and strong communities. Chemistry Awards Dinner, 2019.

Poster Presentations

Exploring PCET Reactions with Molecular Heptazine. Gordon Research Conference, Easton, MA.

Proton-Coupled Electron Transfer from Water to a Model Heptazine-Based Photocatalyst. CEI Orcas Conference, 2018, San Juan, WA. **Runner-up for Best Poster**

Controlling Exciton-Charge Annihilation via Spectral Polaron Cloaking. CEI Orcas Conference, 2016, San Juan, WA

Synthesis of Functionalized and Clickable HPGs for the Creation of Amphiphilic Molecules, Undergraduate Research Symposium, 2012, Washington University; St. Louis, MO

COMMUNITY INVOLVMENT AND LEADERSHIP

Chemistry Mentorship Network *University of Washington* 2016-present
Co-Founder

- Designed and implemented a voluntary peer mentorship program to foster communication and community
- Over 80% of the incoming students are now involved in the program

Inclusion in Chemical Sciences *University of Washington* 2015-present
Co-President (2019), Vice President (2018), Treasurer (2017)

- Plan and facilitate programs to encourage and support women and minorities in science
- Collaborate with the Diversity in Clean Energy organization to provide annual career development workshops
- Organize and manage budget for all events and prepare a budget proposal for the coming year

Undergraduate Mentor *University of Washington* 2016-present

- Guide undergraduate students in independent scientific projects focused on solar energy conversion (**4 students in total**)
- Engage in discussions regarding research, professional careers, and personal experiences as a woman in STEM